



**HAL**  
open science

# Modern and ancient micrometeorites: Experimental and numerical studies

Giacomo Briani

► **To cite this version:**

Giacomo Briani. Modern and ancient micrometeorites: Experimental and numerical studies. Sciences of the Universe [physics]. Museum national d'histoire naturelle - MNHN PARIS; Università degli studi di Firenze, 2010. English. NNT: . tel-00606512

**HAL Id: tel-00606512**

**<https://theses.hal.science/tel-00606512>**

Submitted on 6 Jul 2011

**HAL** is a multi-disciplinary open access archive for the deposit and dissemination of scientific research documents, whether they are published or not. The documents may come from teaching and research institutions in France or abroad, or from public or private research centers.

L'archive ouverte pluridisciplinaire **HAL**, est destinée au dépôt et à la diffusion de documents scientifiques de niveau recherche, publiés ou non, émanant des établissements d'enseignement et de recherche français ou étrangers, des laboratoires publics ou privés.



UNIVERSITÄ  
**FRANCO  
ITALIENNE**

UNIVERSITÀ  
**ITALO  
FRANCESE**



**ECOLE DOCTORALE « SCIENCES DE LA NATURE ET DE L'HOMME » (ED 227)**

**Année 2010**

**N° attribué par la Bibliothèque**



## **THÈSE**

Préparée en co-tutelle avec  
UNIVERSITÀ DEGLI STUDI DI FIRENZE - ITALIE

Pour obtenir le grade de

## **DOCTEUR DU MUSÉUM NATIONAL D'HISTOIRE NATURELLE**

Discipline : Sciences de l'Univers – Cosmochimie

Présentée et soutenue publiquement par

**Giacomo BRIANI**

Le 23 mars 2010

## **Modern and ancient micrometeorites: Experimental and numerical studies**

Sous la direction de : **Monsieur le Professeur Matthieu GOUNELLE et  
Monsieur Emanuele PACE, Maître de Conférences**

### **JURY**

**M. MORBIDELLI Alessandro – Président**  
**Mme ENGRAND Cécile – Rapporteur**  
**Mme ROTUNDI Alessandra – Rapporteur**  
**M. CHAUSSIDON Marc – Examineur**  
**M. DELLA VENTURA Giancarlo – Examineur**  
**M. AIELLO Santi – Examineur**  
**M. GOUNELLE Matthieu – Directeur de thèse**  
**M. PACE Emanuele – Directeur de thèse**

Directeur de Recherche, Observatoire de la côte d'Azur, Nice (006)  
Chargée de Recherche HdR, Université Paris-Sud 11, Orsay (091)  
Professeure, Università di Napoli Parthenope Napoli (Italie)  
Directeur de Recherche, CRPG, Vandoeuvre-les-Nancy (054)  
Professeur, Università di Roma Tre, Rome (Italie)  
Professeur, Università di Firenze, Florence (Italie)  
Professeur, MNHN, Paris (075)  
Maître de Conférences, Università di Firenze, Florence (Italie)



# Contents

<b>Introduction</b>	<b>5</b>
<b>1 Xenoliths and microxenoliths in H chondrites</b>	<b>10</b>
1.1 The role of xenoliths in meteoritics . . . . .	11
1.2 Review of carbonaceous xenoliths in meteorites . . . . .	12
1.3 Materials and methods . . . . .	21
1.3.1 H chondrite samples . . . . .	21
1.3.2 Searching for xenoliths: instruments and techniques . . . . .	23
1.4 Results: mineralogy and petrography . . . . .	25
1.4.1 Microxenoliths (size < 1 mm) . . . . .	26
1.4.2 Xenoliths (size > 1 mm) . . . . .	33
1.5 Relations with properties of host meteorites . . . . .	35
1.5.1 Relation with host meteorite petrologic type . . . . .	38
1.5.2 Relation with host meteorites cosmic-ray exposure ages . . . . .	40
1.5.3 Relation with brecciated, gas-rich meteorites . . . . .	42
1.5.4 Relation with host meteorite shock degree . . . . .	44
1.6 Discussion . . . . .	44
1.7 Conclusions . . . . .	46
<b>2 Origin of microxenoliths in meteorites: asteroidal or cometary?</b>	<b>48</b>
2.1 Introduction . . . . .	49
2.2 Sources for micrometeorites and micrometeoroids . . . . .	52
2.2.1 Carbonaceous micrometeorites from trans-neptunian objects captured in the asteroid main belt . . . . .	54
2.2.2 Carbonaceous micrometeorites from JFCs . . . . .	55
2.3 Origin of microxenoliths: asteroids or comets? . . . . .	56
2.4 Results . . . . .	63
2.5 Discussion . . . . .	64
2.6 Conclusions . . . . .	66
<b>3 A primordial xenolith in the Isheyev carbonaceous chondrite</b>	<b>68</b>
Abstract . . . . .	68

3.1	Introduction . . . . .	69
3.2	PX18: mineralogy . . . . .	70
3.3	PX18: isotopic composition . . . . .	70
3.4	The carrier phase of the N anomalies . . . . .	76
3.5	Nitrogen fractionation . . . . .	78
3.6	Materials and methods . . . . .	79
3.7	Acknowledgements . . . . .	81
3.8	Supporting Information . . . . .	81
<b>4</b>	<b>Organic matter in Isheyevu microxenoliths</b>	<b>85</b>
4.1	Brief introduction to Raman spectroscopy . . . . .	86
4.2	Application to extraterrestrial organic matter . . . . .	88
4.3	Microxenoliths in Isheyevu . . . . .	89
4.4	Experimental procedures . . . . .	94
4.5	Spectrum fitting and analysis . . . . .	96
4.6	Results . . . . .	100
4.7	Conclusions . . . . .	107
<b>5</b>	<b>Interaction of micrometeoroids with the Earth atmosphere</b>	<b>108</b>
5.1	Introduction . . . . .	109
5.2	The model: properties of micrometeoroids and present-day atmosphere . . . . .	110
5.3	The model equations . . . . .	111
5.4	Numerical integration and validation of our code . . . . .	116
5.5	Results . . . . .	117
5.6	Discussion . . . . .	124
5.7	Application to the early Earth atmosphere . . . . .	126
5.8	Conclusions . . . . .	131
<b>6</b>	<b>Conclusions</b>	<b>133</b>
	<b>Acknowledgements</b>	<b>137</b>
	<b>Appendices</b>	<b>138</b>
<b>A</b>	<b>Meteorite classification</b>	<b>139</b>
<b>B</b>	<b>Principal meteorite minerals</b>	<b>142</b>
	<b>Bibliography</b>	<b>147</b>

# Introduction

Meteoritics is the science that studies extraterrestrial matter. Meteoritics relies on the unique possibility of analysing extraterrestrial matter in laboratories: the most precise analytical techniques and the most recent technologies can be exploited to extract information from extraterrestrial samples, from macroscopic rocks as well as from tiny dust grains. The ultimate goal of meteoritics is the understanding of the origin of the solar system and its evolution. To realize this goal it is essential to connect information obtained from laboratory analyses with those obtained from astronomical observations. This allows to unveil the origin and the evolution not only of the solar system, but, more generally, of any planetary system.

The necessary starting point for meteoritics is the availability of extraterrestrial samples. The first samples to be studied were macroscopic rocks, found on Earth or observed to fall and then recovered. In the late 1960s and in the 1970s, space missions to the Moon added lunar rocks to collections of extraterrestrial samples. Always in the 1970s, extraterrestrial material collections were extended toward samples of smaller dimensions: efficient collection of micrometer-sized particles in the stratosphere began the study of what today are called interplanetary dust particles (IDPs). More recently, samples that fill the gap between micrometer-sized IDPs and macroscopic meteorites have begun to be studied. These samples are micrometeorites. They have been recovered from different places: deep sea sediments, sedimentary rocks, Greenland ice-caps and Antarctica (Engrand and Maurette, 1998; Taylor and Lever, 2001).

Micrometeorites are extraterrestrial samples with size ranging from a few  $\mu\text{m}$  to  $\sim 1$  mm. The great abundance of micrometeorites recovered from Antarctica in the last years allowed an extended and in-depth study of their composition, petrography and mineralogy. An open issue concerning micrometeorites is that of their origin. Several arguments have been presented to support both the hypothesis that micrometeorites originate from asteroids and the hypothesis that they come from comets. Certainly, they are fragments of asteroids and comets, produced by means of collisions and fragmentation, or by the passage of comets in the inner solar system. Indeed, in the inner solar system micrometeorites constitute a very abundant population.

The so-called zodiacal cloud, a disk composed by bodies ranging from sub-micrometer-sized dust grains to cm-sized meteoroids, is largely dominated by objects that have the dimensions of micrometeorites, and that are called micrometeoroids (by definition, a meteorite is a rock that reached the Earth; when it is floating in interplanetary space, it is called meteoroid). Such an abundance of micrometeoroids is attested by several studies. Phenomenological models for size and spatial distribution of zodiacal cloud particles have shown that  $\sim 80\%$  of the zodiacal light is due to particles in the size range  $10 - 100 \mu\text{m}$  ( $\sim 10^{-8} - 10^{-5}$  g) (Grün *et al.*, 1985). Results of a recent dynamical model confirm that particles with size =  $100 \mu\text{m}$  are the most abundant in the zodiacal cloud (Nesvorný *et al.*, 2010). At 1 AU, direct measurements from satellite [performed by the Long Duration Exposure Facility (Love and Brownlee, 1993)] and models based on lunar cratering and measurements of the Pioneer spacecrafts (Grün *et al.*, 1985) showed that the mass distribution is dominated by particles with dimensions of about  $200 \mu\text{m}$ .

However, such an abundance of micrometeoroids does not guarantee an easy access to these extraterrestrial samples. Several space missions have studied micrometeoroids *in situ* (Grün *et al.*, 2001). But space missions specifically aimed at collecting and bringing back to Earth micrometeoroids from interplanetary space have never been realized. At the same time, every micrometeorite recovered on Earth has inevitably suffered the consequences of its passage through the Earth atmosphere. But there is another possibility to study these small extraterrestrial bodies: they can be found embedded in larger meteorites.

It is not rare to find in meteorites inclusions that have characteristics different from those of the host meteorite. The differences in properties like composition, petrography and mineralogy, suggest that these inclusions and their host meteorites have different origins. Such inclusions are called xenoliths. Xenoliths are easily individuated in meteorites when they have dimensions larger than a few mm. Finding out xenolithic inclusions corresponding to micrometeorites and micrometeoroids (i.e. with sub-millimetric size) requires a little more dedication. But microxenoliths are not so rare.

The exact mechanisms by which micrometeoroids are embedded in meteorite parent bodies and become microxenoliths are not known. However, both microxenoliths and xenoliths are observed that do not show alterations due to high-speed, violent impacts. This attests that it is possible, from our laboratories on Earth, to have access to unaltered interplanetary micrometeoroids.

But microxenoliths are more than interplanetary analogues of micrometeorites recovered on the Earth. Microxenoliths and micrometeorites sample the same flux of solar system fragments. However, microxenoliths are samples of more ancient times. On the one hand, this is because micrometeorites, once fallen on the Earth, suffer the effects of the terrestrial geological

activity. The oldest terrestrial ages for meteorites are on the order of 3 Myr (Jull, 2001). On the other hand, several observations, discussed also in chapter 1 of this thesis, suggest that microxenoliths have probably been embedded when the host meteorites were still part of their parent bodies. This means that their embedding happened hundreds of million years ago. In addition, as parent bodies of meteorites are solar system minor bodies (such as asteroids and comets) that undergo limited geological activity, microxenoliths had the possibility of residing in their host meteorites for very long time.

Therefore microxenoliths represent a unique possibility to study ancient micrometeorites. In particular, carbonaceous xenoliths and microxenoliths probably formed in the very first epochs of the solar system evolution, as they are fragments of the same material that constitute carbonaceous chondrites, unanimously considered among the most primordial bodies in the solar system<sup>1</sup>.

This thesis is focused on such samples. The global aim of this work is to exploit the possibility to access these precious extraterrestrial samples to obtain new information about the solar system.

First of all, as microxenoliths are ancient micrometeorites, they allow the study of past epochs of the solar system history, not accessible from micrometeorites recovered on the Earth. This is because microxenoliths are samples of the micrometeoroid flux in very ancient epochs. Therefore, by studying microxenoliths it is possible to estimate if such a flux has always been dominated by carbonaceous chondritic material, as it appears today (Kurat *et al.*, 1994; Engrand and Maurette, 1998; Meibom and Clark, 1999).

This has important consequences also for the evolution of the early Earth. Indeed carbonaceous chondritic material is rich in volatile elements (such as water) and in organic matter (even amino acids and sugars have been detected in carbonaceous chondrites, see Pizzarello *et al.* (2006) for a review). Therefore, small objects like micrometeorites and microxenoliths may have been essential for the pre-biotic matter they delivered on the early Earth (Brinton *et al.*, 1998; Clemett *et al.*, 1998; Matrajt *et al.*, 2004).

In addition, microxenoliths help us to better understand the nature of their parent bodies, i.e. of asteroids and comets. On the one hand, this is because microxenoliths can be samples of parent bodies not represented by larger meteorites, and therefore they could give us complementary information not only with respect to those deciphered from micrometeorites, but also with respect to the information obtained from meteorites. On the other hand, microxenoliths can reveal new insights into the composition of asteroids and comets, and into the relations between these two classes of minor bodies. Structure and composition of asteroids and comets are today in-

---

<sup>1</sup>See Appendix A for a brief description of the principal characteristics of carbonaceous chondrites and of the other meteorites important to this work.

ferred from meteorites, IDPs and micrometeorites. Only one sample return mission, Stardust, succeeded in returning cometary samples to Earth. Basically, microxenoliths represent a “new window” on the solar system minor bodies, because they expand our collections of extraterrestrial material.

Experimental and numerical works presented here concern different issues related to the solar system origin and evolution that can be studied by means of micrometeorites and microxenoliths.

A fundamental work developed during the period of this PhD thesis is the systematic search for new xenoliths and microxenoliths in H chondrites (chapter 1). Such a research is essential in order to characterize the microxenolith population in this group of ordinary chondrites. Up to now, a systematic analysis of xenoliths had been done only for Howardites (Zolensky *et al.*, 1996b; Gounelle *et al.*, 2003). The goal of our work is to determine the xenolith and microxenolith abundance in H chondrites, to analyze their mineralogy in comparison with known groups of meteorites, and to search for possible correlations with physical properties of host meteorites (e.g. petrologic type, cosmic-ray exposure age...). Such a work allows to understand which type of micrometeoroids were the most abundant in the past and which could have been their parent bodies, when microxenoliths have been embedded in their host meteorites and what mechanisms favoured their embedding and their permanence in the hosts.

In chapter 2 our attention focuses on the possible origin of microxenoliths. Namely, the relative contribution of asteroids and comets to the populations of microxenoliths have been evaluated by numerical simulations. The results of these simulations can be compared with microxenolith populations observed in H chondrites (chapter 1) and in Howardites (Zolensky *et al.*, 1996b; Gounelle *et al.*, 2003). Such a direct comparison between observed microxenoliths and modelled relative abundances of asteroidal and cometary microxenoliths is a key tool to understand not only the possible origin of these small samples, but also the actual differences between asteroidal and cometary samples. Indeed, the attempt to reconcile the observed microxenoliths with different possible parent bodies gives us new insights into differences and similarities of asteroids and comets.

In chapter 3 the discovery and the analysis of a primordial microxenolith in the carbonaceous chondrite Isheyevo is described. In this case, with the term “primordial”, we refer to a sample that does not show significant effects of aqueous alteration nor of thermal metamorphism. Such samples are the best candidate for preserving memories of the processes that led to the formation of the solar system. The primordial microxenolith found in the Isheyevo chondrite shed light on the isotopic fractionation of light elements (in particular H, and N), which is supposed to be the result of processes that took place in the interstellar medium before the formation of the solar system, or during the very first epoch of the solar system history.

This same microxenolith, along with four other found in the carbona-

aceous chondrite Isheyevo, have been analyzed by Raman spectroscopy. Raman spectroscopy is a powerful technique to characterize the macromolecular organic matter present in extraterrestrial samples. Preliminary analyses and comparisons with results for organic matter of carbonaceous chondrites are presented in chapter 4.

Chapter 5 is dedicated to the analysis of the interaction between micrometeoroids and the Earth atmosphere. Numerical simulations have been performed in order to analyze what happens when these small bodies approach our planet. The goal is to understand what processes are the most effective in determining the fate of micrometeoroids. In addition, the same numerical simulations have been performed for the interaction of micrometeoroids with modelled early Earth atmospheres. The results contribute to the understanding of the possible role of a large micrometeoroid flux in the evolution of the early Earth.

# Chapter 1

## Xenoliths and microxenoliths in H chondrites

### Summary of Chapter 1

The subject of this chapter is the search and the analysis of xenoliths and microxenoliths in H chondrites. Xenoliths are meteorite inclusions with a different origin from that of their host meteorites. Xenoliths with dimensions between a few  $\mu\text{m}$  and  $\sim 1$  mm can be considered as “meteorite-trapped” analogues of micrometeoroids and micrometeorites. They are relatively common in every group of meteorites, but they are most abundant in Howardites and H chondrites. A systematic analysis of xenoliths and microxenoliths has been done only for Howardites. Here we describe a systematic search for new (micro)xenoliths in H chondrites.

The goal is to determine their abundance in this group of ordinary chondrites, to analyze their mineralogy in comparison with known group of meteorites, and to search for possible correlations with physical properties of host meteorites (e.g. petrologic type, cosmic-ray exposure age...).

The starting point is the extensive collection of H chondrite polished sections of the Muséum National d’Histoire Naturelle (MNHN) in Paris. A first survey of the sections is conducted by optical microscopy to individuate new (micro)xenoliths. The potential new (micro)xenoliths are then imaged by SEM and analysed by energy dispersive X-ray spectroscopy to establish if they are really xenoliths. Then electron microprobe analyses are performed in order to investigate their mineralogy. This allows a classification of the new (micro)xenoliths and their comparison with known meteorites. Finally possible correlations with physical properties of the host meteorites are investigated.

Sixty-six sections from forty meteorites have been analyzed. Twenty four new xenoliths have been discovered. About 87% of them are microxenoliths, only 3 are  $> 1$  mm in their largest dimension. All the new microxenoliths

are fine-grained hydrous (FHG), among the larger ones three are coarse-grained hydrous, two FGH. Among the microxenoliths seven are similar to CI carbonaceous chondrites, three are similar to CM2 and ten to CR2. The three xenoliths  $>1$  mm are clearly of CM2 material. The prevalence of carbonaceous chondritic material among the new xenoliths and microxenoliths indicates that this was the most abundant solar system material even in past epochs. The presence of xenoliths and microxenoliths in H chondrites with petrologic type 4 and 5 shows that their embedding happened after the end of the thermal metamorphism. Exposition to impacts of the host meteorite parent bodies seems to be an essential process for the presence of (micro)xenoliths: all the new xenoliths and microxenoliths have been found in brecciated meteorites.

## 1.1 The role of xenoliths in meteoritics

By definition, a xenolith in a rock is an inclusion which has not the same origin of the host rock. In the case of meteorites this means that it is possible to find meteorite chunks of a certain group embedded in larger meteorites that belong to a different group or class. To make some examples, a piece of H chondrite embedded in an L chondrite, a piece of enstatite chondrite in a H chondrite or carbonaceous inclusions in ordinary chondrites. An important distinction must be made between xenoliths and “cognate clasts”, which are inclusions related to the host rock (e.g. inclusions with a petrologic type different from that of the host meteorites but belonging to the same group), and between xenoliths and “impact melt clasts”, which are fragments that result from impacts. Indeed most of the time xenoliths are little fragments, i.e. with dimensions ranging between a few  $\mu\text{m}$  and a few cm. In this thesis we will use the word xenoliths to designate the largest objects, with size  $>1$  mm, and with microxenoliths we will refer to the smallest of them, with typical size  $<1$  mm.

Xenoliths have long been recognized as an important subject in meteoritics (see e.g. Wahl 1952). The study of xenoliths allows to shed light on different issues concerning meteorites and the solar system:

- xenoliths are supposed to come from different parent bodies with respect to the host meteorites; therefore xenoliths can help to understand the history of relationships between different meteorite parent bodies (see e.g. Wilkening 1977a);
- xenoliths can be samples of meteorites parent bodies that are not present in our collections as whole meteorites, e.g. they can be the only remnant fragments of parent bodies completely destroyed by impacts (the same is true for micrometeorites, see Gounelle *et al.* 2009);

- xenoliths could reveal new classes of parent bodies, namely they could be samples of distant solar system bodies such as comets and Kuiper Belt objects, for which at present we do not have meteoritic samples (Campins and Swindle, 1998; Zolensky *et al.*, 2009).

In quest of new xenoliths and microxenoliths, we chose to concentrate our efforts on H chondrites for two reasons. First, as we will see in the next section, H chondrites appear to be very rich in carbonaceous xenoliths. However no systematic search for and characterization of microxenoliths has been previously performed for this group of meteorites. Second, xenoliths composed of hydrated material (e.g. phyllosilicates) which show little degree of thermal alteration appear quite common in H chondrites. Several xenoliths of this type have already been found in H chondrites (Tab. 1.2) and, as for carbonaceous xenoliths in general, they are more abundant in H chondrites than in L and LL chondrites (Fig. 1.1B). These are the xenoliths that least suffered from shocks during the embedding process in the host meteorite, and therefore they are the most important samples to study the nature of ancient micrometeorites. In other words, we are particularly interested in hydrated/unshocked xenoliths, such as CI-, CR- and CM-like xenoliths.

Our goal is to answer the following questions:

1. Are carbonaceous chondritic xenoliths really widespread in H chondrites?
2. Are there xenoliths related to meteorites other than carbonaceous chondrites?
3. When were xenoliths embedded in H chondrite parent body?
4. What is the origin of xenoliths in H chondrites? Do they share a common origin?
5. Are there “exotic” xenoliths clearly different from known meteorite classes?

The base of this work is necessarily a systematic search for new (micro)xenoliths and their mineralogical characterization. Then the analysis of possible relations between the presence and nature of the new xenoliths and the physical properties of the host meteorites has been conducted. Namely, the meteorite petrologic type, their cosmic-ray exposure age and their brecciated or non-brecciated nature have been considered.

## 1.2 Review of carbonaceous xenoliths in meteorites

Xenoliths are present in almost every class of meteorites, and they can be fragments of several different meteorite groups (Wahl, 1952; Wilkening,

1977a; Lipschutz *et al.*, 1989; Bischoff *et al.*, 2006). Ordinary chondrite xenoliths have been observed in ordinary chondrites as well as in Eucrites, Aubrites, Ureilites. Also enstatite chondrite xenoliths have been observed, namely in the H chondrites Plainview (H5) and Supuhee (H6) and in CR2 carbonaceous chondrite Kaidun (Ivanov *et al.*, 1984). But the most abundant type of xenoliths are carbonaceous xenoliths (Wilkening, 1977a; Meibom and Clark, 1999; Rubin and Bottke, 2009; Zolensky *et al.*, 1996b; Gounelle *et al.*, 2003). In Tab. 1.1 is reported a compilation of known carbonaceous xenoliths.

Table 1.1: meteorites bearing carbonaceous xenoliths.

METEORITE	XENOLITHS	REFERENCES
<b>H chondrites</b>		
Dimmitt (H3.7)	carb. xen.	Wilkening (1977a) Goswami <i>et al.</i> (1984)
Holyoke (H4)	CM xen.	Wilkening (1976) Wilkening (1977a)
Ipiranga (H6)	CM xen.	Rubin and Bottke (2009)
Leighton (H5)	CM xen.	Wilkening (1976) Wilkening (1977a) Goswami <i>et al.</i> (1984)
Plainview 1917 (H5)	CM xen.	Wilkening and Clayton (1974) Fodor and Keil (1976) Goswami <i>et al.</i> (1984) Rubin and Bottke (2009)
Pultusk (H5)	carb. xen.	Wilkening (1976) Wilkening (1977a) Goswami <i>et al.</i> (1984)
Sharps (H3.4)	CM xen.	Wilkening (1976) Wilkening (1977a)
Supuhee (H6)	C1-2 xen.	Leitch and Grossman (1977)
Tysnes Island (H4)	carb. xen.	Wilkening (1976) Wilkening (1977a) Goswami <i>et al.</i> (1984)
Weston (H4)	carb. xen.	Goswami <i>et al.</i> (1984)
Willard (b) (H3.6)	CI xen.	Noguchi <i>et al.</i> (2003)
<b>L chondrites</b>		
Grassland (L4)	carb. xen.	Goswami <i>et al.</i> (1984)
Mezö-Madaras (L3.7)	CM2 xen.	van Schmus (1967) Wilkening (1977a)
Rio Negro (L4)	C3 xen.	Rubin <i>et al.</i> (1982)
Tennasilm (L4)	carb. xen.	van Schmus (1967)
<b>LL chondrites</b>		
Krymka (LL3.2)	carb. xen.	Semenenko <i>et al.</i> (2004) Semenenko <i>et al.</i> (2005) Bischoff <i>et al.</i> (2006)
<b>mixed ordinary chondrites</b>		

continued on next page

Table 1.1: continued.

METEORITE	XENOLITHS	REFERENCES
Abbott (H3-6)	CM xen.	Wilkening (1976) Wilkening (1977a) Goswami <i>et al.</i> (1984)
Bremervörde (H/L3.9)	carb. xen.	van Schmus (1967) Goswami <i>et al.</i> (1984)
Cynthiana (L/LL4)	carb. xen.	van Schmus (1967)
Magombedze (H3-5)	CM xen.	MacPherson <i>et al.</i> (1993)
Tsukuba (H5-6)	CI xen.	Nakashima <i>et al.</i> (2003) Noguchi <i>et al.</i> (2003)
Zag (H3-6)	carb. xen.	Zolensky <i>et al.</i> (2003)
<b>carbonaceous chondrites</b>		
ALH 85085 (CH3)	C1-2 xen.	Greshake <i>et al.</i> (2002)
Allende (CV3)	CM xen.	Gordon <i>et al.</i> (2009)
Al Rais (CR2 anomal.)	CI2 xen.	Zolensky <i>et al.</i> (1989)
Efremovka (CV3)	CM xen.	Krot <i>et al.</i> (1999)
HaH 237 (CBb)	C1-2 xen.	Greshake <i>et al.</i> (2002)
Kaidun (CR2)	CI xen.	Ivanov <i>et al.</i> (1984)
Lancé (CO3.5)	CM xen.	Wilkening (1977a)
Leoville (CV3)	CM xen.	Wilkening (1976) Wilkening (1977a)
Murchison (CM2)	C3, CO, CV xen.	Fuchs <i>et al.</i> (1973) Goswami <i>et al.</i> (1984) Olsen <i>et al.</i> (1988)
QUE 94411 (CBb)	C1-2 xen.	Greshake <i>et al.</i> (2002)
PAT 91546 (CH)	C1-2 xen.	Greshake <i>et al.</i> (2002)
Weatherford (CBa)	C3 xen.	Mason and Nelen (1968)
<b>Aubrites</b>		
Pesyanoe	carb. xen.	Lorenz <i>et al.</i> (2005)
<b>Howardites</b>		
Bholgati	CI1, CM2 and CR2 xen.	Zolensky <i>et al.</i> (1989) Reid <i>et al.</i> (1990) Buchanan <i>et al.</i> (1993) Zolensky <i>et al.</i> (1996b)
EET 87513	CM2 xen.	Buchanan <i>et al.</i> (1993)
Erevan	CM xen.	Nazarov <i>et al.</i> (1993) Nazarov and Ariskin (1993) Nazarov <i>et al.</i> (1994)
G'Day	CM2 xen.	Zolensky <i>et al.</i> (1996b)
Jodzie	CM2 and CR2 xen.	Bunch <i>et al.</i> (1979) Goswami <i>et al.</i> (1984) Zolensky <i>et al.</i> (1996b) Gounelle <i>et al.</i> (2003)
Kapoeta	CM2, CI and CR2 xen.	Wilkening (1973) Goswami <i>et al.</i> (1984) Brearley and Papike (1993) Zolensky <i>et al.</i> (1996b) Gounelle <i>et al.</i> (2003)

continued on next page

Table 1.1: continued.

METEORITE	XENOLITHS	REFERENCES
LEW 87015	CM2 xen.	Zolensky <i>et al.</i> (1996b)
LEW 85441	CM2 xen.	Zolensky <i>et al.</i> (1996b)
Yamato 793497	CR2 xen.	Zolensky <i>et al.</i> (1996b) Gounelle <i>et al.</i> (2003)
<b>Eucrites</b>		
LEW 85300	CV3 xen.	Zolensky <i>et al.</i> (1992) Zolensky <i>et al.</i> (1996b)
LEW 87295	CM2 xen.	Zolensky <i>et al.</i> (1996b)
NWA 5232	CM xen.	Kuehner <i>et al.</i> (2009)
<b>Diogenites</b>		
Ellemeet	CM2 xen.	Mittlefehldt (1994)
<b>Ureilites</b>		
DaG 319	CI-like xen.	Ikeda <i>et al.</i> (2003)
Nilpena	CI xen.	Brearley and Prinz (1992)
Yamato 791834	CR xen.	Buchanan and Zolensky (2003)

Abbreviations: carb. = carbonaceous; xen. = xenoliths.

Meteorite names: ALH = Allan Hills (Antarctica);

DaG = Dar al Gani (Libya); EET = Elephant Moraine (Antarctica);

HaH = Hammadah al Hamra (Libya); LEW = Lewis Cliff (Antarctica);

NWA = North West Africa; PAT = Patuxent Range (Antarctica);

QUE = Queen Alexandra Range (Antarctica).

Carbonaceous xenoliths are indeed very important, for two reasons. First they allow the study of primitive solar system material. Chondritic material is generally recognized as the pristine building material for solids in the solar system, for its chemical composition [the composition of CI chondrites is strikingly similar to the solar composition (Palme and Jones, 2005)] and for the presence of organic matter supposed to be formed in the interstellar medium [see e.g. Yang and Epstein (1983) and Alexander *et al.* (2007)] or in the protosolar disk, during the first stages of the solar system formation (Remusat *et al.*, 2006). Second they are the most similar objects to micrometeorites (Gounelle *et al.*, 2003), i.e. to the most abundant material collected by Earth from space (Love and Brownlee, 1993). However they sample a more ancient micrometeoroid flux than micrometeorites collected on Earth and, above all, they did not suffer the alterations produced by the passage through the atmosphere.

From Tab. 1.1 it is possible to see that the most carbonaceous xenolith-rich classes among meteorites are ordinary chondrites and the HED clan (Howardites-Eucrites-Diogenites, which are breccias usually assumed to originate from the asteroid 4 Vesta). Among ordinary chondrites, H chondrites are the group in which more carbonaceous xenoliths have been found (Fig. 1.1A). However, descriptions of more than 2 or 3 xenoliths in the same meteorite are rare.

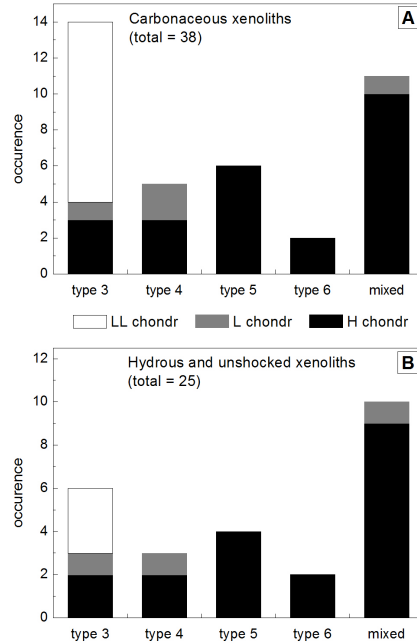


**Figure 1.1:** Distribution of carbonaceous xenoliths in ordinary chondrites as function of petrologic type (data from literature, references are given in Tab. 1.1). A: distribution of carbonaceous xenoliths. B: distribution of hydrated and unshocked (i.e. C1- and C2-like) xenoliths.

In contrast Howardites are very rich in carbonaceous xenoliths: considering only 7 meteorites (Kapoeta, Bholgati, Jodzie, G'Day, LEW 87015, LEW 85441 and Yamato 793497) Zolensky *et al.* (1996b) reported 72 xenoliths. Most important, Howardites are also rich in xenoliths of size  $< 1$  mm, i.e. in microxenoliths. Gounelle *et al.* (2003) described 61 microxenoliths found in Kapoeta, Jodzie and Yamato 793497. But millimeter-sized carbonaceous xenoliths appear to be different from the smaller microxenoliths found in the same meteorites. Among millimeter-sized carbonaceous xenoliths, most are composed of CM2 material (Zolensky *et al.*, 1996b), with a CR2 xenoliths to CM2 xenoliths ratio of 0.18. In contrast, among microxenoliths, CM2 and CR2 microxenoliths have been observed in almost the same quantities, with  $CR2/CM2 = 1.1$  (Gounelle *et al.*, 2003). This suggests that carbonaceous microxenoliths are not fragments of larger objects, as millimeter-sized xenoliths are, but real fossil micrometeorites.

For all these reasons we decided to perform a systematic search of new xenoliths paying particular attention to microxenoliths similar to carbonaceous chondrites. In fact, sizes between a few  $\mu\text{m}$  and 1 mm and structural and compositional properties similar to those of carbonaceous chondrites suggest relations with micrometeorites recovered on Earth. Therefore such microxenoliths are the best samples to investigate the nature of ancient micrometeorites. This does not mean that we ignored larger xenoliths when we found them, nor possible xenoliths different from carbonaceous chondrites. In the rest of this chapter, for the sake of simplicity, xenoliths and

microxenoliths similar to carbonaceous chondrites will be referred to as “carbonaceous chondritic xenoliths” or “carbonaceous xenoliths”. We point out here that this is a somewhat improper language: indeed we did not perform any measurement of the carbon content of the new found xenoliths. The term “carbonaceous xenoliths” reflects only the fact that the main properties of such xenoliths make them similar to known groups of carbonaceous chondrites.

Table 1.2: hydrated and unshocked xenoliths in ordinary chondrites.

<b>H chondrites</b>		
Holyoke (H4)	CM xen.	Wilkening (1976) Wilkening (1977a)
Ipiranga (H6)	1 hydrated unshocked CM xen.	Rubin and Bottke (2009)
Plainview 1917 (H5)	hydrated C2 xen.	Wilkening and Clayton (1974) Fodor and Keil (1976) Goswami <i>et al.</i> (1984) Rubin and Bottke (2009)
Sharps (H3.4)	CM xen.	Wilkening (1976) Wilkening (1977a)
Supuhee (H6)	1 C1-2 hydrated xen.	Leitch and Grossman (1977)
Tysnes Island (H4)	hydrated unshocked CM xen.	Wilkening (1976) Wilkening (1977a) Goswami <i>et al.</i> (1984)
Willard (b) (H3.6)	phyllosilicate rich CI xen.	Noguchi <i>et al.</i> (2003)
<b>L chondrites</b>		
Mezö-Madaras (L3.7)	CM2 xen.	van Schmus (1967) Wilkening (1977a)
Tennasilm (L4)	CM2 xen.	van Schmus (1967)
<b>LL chondrites</b>		
Krymka (LL3.2)	CI xen.	Girich and Semenenko (2001)
<b>mixed ordinary chondrites</b>		
Abbott (H3-6)	hydrated unshocked CM xen.	Wilkening (1976) Wilkening (1977a) Goswami <i>et al.</i> (1984) Rubin and Bottke (2009)
Bremervörde (H/L3.9)	CM2 xen.	van Schmus (1967) Goswami <i>et al.</i> (1984)
Cynthiana (L/LL4)	CM2 xen.	van Schmus (1967)
Magombedze (H3-5)	1 CM xen.	MacPherson <i>et al.</i> (1993)
Tsukuba (H5-6)	phyllosilicate rich CI xen.	Nakashima <i>et al.</i> (2003) Noguchi <i>et al.</i> (2003)
Zag (H3-6)	1 CI1 xen.	Zolensky <i>et al.</i> (2003)

Abbreviations: xen. = xenoliths.

Known carbonaceous xenoliths in ordinary chondrites (Tab. 1.2) have been classified on the basis of their mineralogical, structural and compositional similarities with known groups of carbonaceous chondrites. Therefore

carbonaceous xenoliths are generally referred to as CI-like, CR-like or CM-like (xenoliths similar to other group of carbonaceous chondrites are rare). Here is a brief description of the principal characteristics for each of these groups.

*CI-like xenoliths.* They consist of a fine-grained phyllosilicate-rich matrix, which is a mixture of saponite and serpentine with small grains (100 - 200 nm) of magnetite and sulfides plus minor minerals (ferrhydrite, chromite, olivine and low-Ca pyroxene). Set in the matrix are larger grains of magnetite and sulfides, with size ranging from 1 to  $\sim 30 \mu\text{m}$ . Magnetite is generally abundant, and it is present as plaquettes, spherules or framboidal grains. Pyrrhotite is the most abundant sulfide, while pentlandite and sulfides with intermediate composition between pyrrhotite and pentlandite are rare. Fe-Ni metal grains are present, while no carbonates are observed in these xenoliths (Nakashima *et al.*, 2003; Gounelle *et al.*, 2003). An example of CI-like xenolith is showed in Fig. 1.2 (after Nakashima *et al.* 2003).

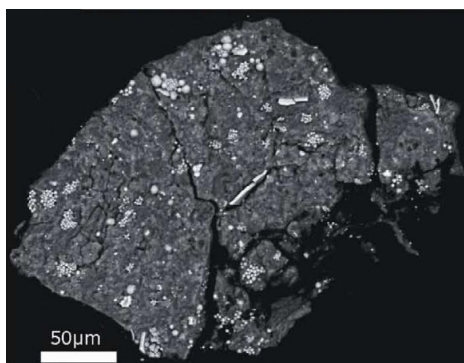


**Figure 1.2:** BSE image of a CI-like xenolith in the Tsukuba H5-6 chondrite, after Nakashima *et al.* (2003)

*CR-like xenoliths.* Xenoliths of this type have not been identified in ordinary chondrites up to now, while they have been observed in Howardites. Their fine-grained phyllosilicate-rich matrix is composed mainly of saponite and serpentine, with minor pyrrhotite, pentlandite and magnetite grains. Magnetite is abundant and present in different forms, as for CI-like xenoliths. Olivine and pyroxene grains are abundant. Olivine is mainly Mg-rich (typically  $\text{Fo}_{>90}$ ). Pyroxene is both Ca-rich (augite and hedenbergite) and Ca-poor (typically Mg-rich pyroxene, with  $\text{En}_{>90}$ ). Carbonates are common, they are principally Ca-carbonates and are frequently associated with magnetite. Among Fe-Ni sulfides, pyrrhotite and pentlandite are common. Fe-Ni metal grains are not observed in these xenoliths. Fig. 1.3 shows a CR-like xenolith, after Gounelle *et al.* (2003).

*CM-like xenoliths.* Once again the fine-grained matrix is dominated by serpentine and saponite, with the presence of tochilinite, often interstratified with serpentine. Matrix hosts olivine grains that are mainly Mg-rich ( $\text{Fo}_{99}$  is the dominant olivine phase) and pyroxene grains of variable composition (high-Ca pyroxene is diopside and augite, low-Ca pyroxene is mainly Mg-

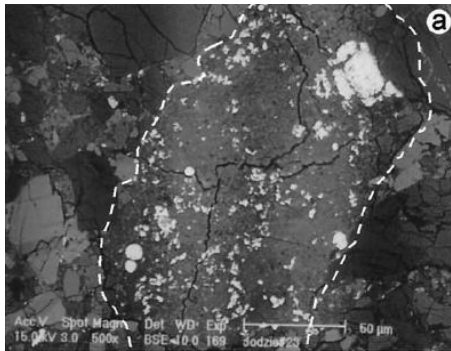


**Figure 1.3:** BSE image of a typical CR-like xenolith in the Jodzie howardite, after Gounelle *et al.* (2003).

rich, ranging from  $En_{87}-Fs_{10}$  to  $En_{98}-Fs_1$ ). Magnetite and metals are rare in these xenoliths. Sulfides have compositions ranging from that of pyrrhotite to that of pentlandite. Ca-carbonates are present, but rarer than in CR xenoliths. A typical CM-like xenolith, described by (Rubin and Bottke, 2009) is shown in Fig. 1.4.

However classifying xenoliths on the basis of their similarities with carbonaceous chondrites or with micrometeorites present some ambiguities. Indeed differences remain between xenoliths and carbonaceous chondrites. For xenoliths in CB and CH chondrites described by Greshake *et al.* (2002), no unambiguous assignment to any certain group of carbonaceous chondrites can have been established, even if these xenoliths clearly have close relationships with C1 and C2 material (such as matrix mineralogy, magnetite morphology and chemical composition of major phases). Gounelle *et al.* (2003) reported differences between CR2 microxenoliths in Howardites and CR2 chondrites. Microxenoliths have abundant matrix, high fayalitic olivine grains, Fe-rich saponite, CAIs and chondrules are absent, metal is rare. Minor differences are instead reported for CM2 microxenoliths with respect to CM2 chondrites: in microxenoliths the pyroxene to olivine ratio

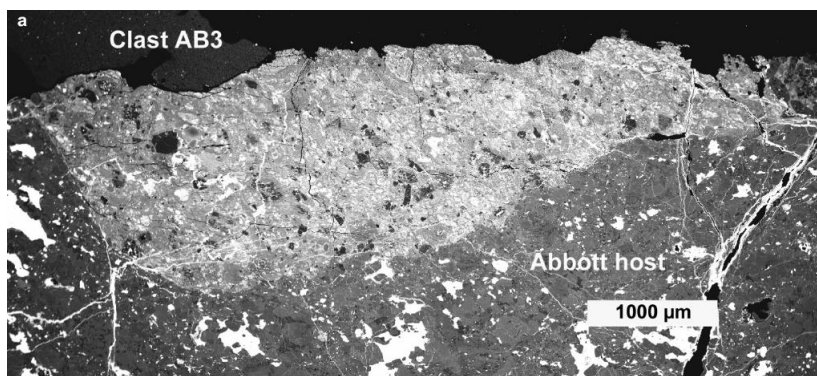


**Figure 1.4:** BSE image of a CM-like xenolith in the Abbott H3-6 ordinary chondrite, after Rubin and Bottke (2009).

is higher, saponite is more abundant, while chondrules and Mg-rich olivines present lower abundances. Rubin and Bottke (2009) described mineralogical and compositional differences between CM-like xenoliths in Abbott and CM chondrites, such as differences in the sulfide modal abundance and in the S/SiO<sub>2</sub> ratio for tochilinite-cronstedtite. Some of these differences may be due to the different size of xenoliths and carbonaceous chondrites (e.g. the limited dimensions of most xenoliths imply chondrules are not so common, when they could facilitate comparison with carbonaceous chondrites). But others may reflect different conditions in the aqueous alteration process (e.g. temperature, pH, water/rock ratio).

In order to solve this problem, alternative classification schemes have been proposed, directly based on xenolith observed properties. Gounelle *et al.* (2005) proposed three groups for microxenoliths in Howardites, defined by the presence or absence of tochilinite, magnetite and olivine. For comparison with the previous classification scheme, tochilinite-rich magnetite-poor microxenoliths are those most similar to CM chondrites. On the other hand, tochilinite-poor magnetite-rich microxenoliths are subdivided in two more groups, based on the abundance of olivine. Olivine-rich microxenoliths are those most similar to CR chondrites, while silicate-poor microxenoliths are CI-like.

In Zolensky *et al.* (2009) the structural properties of xenoliths are used for classification. Xenoliths are therefore divided in fine-grained hydrous (FGH), fine-grained anhydrous (FGA) and coarse-grained hydrous (CGH). Here we report the principal characteristics for each of these groups.

- **FGH:** rather small xenoliths (probably reflecting low-strength) composed of a serpentine and saponite fine-grained matrix with 0.5-10  $\mu\text{m}$  sized Fe-Ni sulfides and magnetite grains. In the larger ones olivine fragments have been observed. Gounelle *et al.* (2003, 2005) have pointed out that these xenoliths are mineralogically most similar to hydrous micrometeorites though some differences are apparent. FGH xenoliths are the most widespread.
- **FGA:** these xenoliths also are quite common, but they have received little detailed characterization. Beside a fine-grained, anhydrous matrix (principally of ferromagnesian silicates) they are composed of coarse (1-100  $\mu\text{m}$ ), generally fragmented grains of olivine, low-Ca pyroxene, Fe-Ni sulfides and microchondrules. Their anhydrous nature suggests possible relations with cometary grains [no phyllosilicates have been found in Wild2 grains, Zolensky *et al.* (2006, 2008)].
- **CGH:** these are significantly larger than FGH xenoliths. They typically consist of fragmented olivine and low-Ca pyroxene, 0.5-10  $\mu\text{m}$  sized Fe-Ni sulfides and partially altered chondrules embedded in a fine-grained matrix of serpentine and lesser saponite. These xenoliths

have long been recognized as being very similar to CM2 in terms of mineralogy (Zolensky *et al.*, 1993a, 1996a,b; Buchanan *et al.*, 1993).

## 1.3 Materials and methods

### 1.3.1 H chondrite samples

The collection of H chondrite sections of the Laboratoire de Minéralogie et Cosmochimie du Muséum at the Muséum National d'Histoire Naturelle in Paris consists of more than 130 samples that are polished or thin sections. Samples with petrologic type from 3 to 6 are present, as well as samples of different shock degree, different cosmic-ray exposure age, samples of brecciated meteorites and of solar gas rich meteorites (see Section 1.5.3 for a description of these meteorite properties). In addition, after a first review of the existing literature about xenoliths, we decided to prepare new sections, in order to study samples of meteorites in which we supposed the presence of xenoliths was probable (e.g. meteorites for which xenoliths had already been described, solar gas-rich meteorites, breccias). In total 15 new sections have been prepared, from Leighton, Plainview 1917, Tysnes Island, Bremervörde, Weston and Dimmitt. All these new sections have been prepared from whole rock samples present in the laboratory collection. After selection of the appropriate portion of rock, we cut it by means of a circular diamond saw, then we embedded the obtained piece in Kōrapox<sup>TM</sup> epoxy (particularly suited for high vacuum analyses) and we polished it using diamond paste of different sizes, from 3  $\mu\text{m}$  down to a 0.25  $\mu\text{m}$  finish. In addition we borrowed a few polished sections from the Astromaterial Research and Exploration Science laboratory at the NASA Johnson Space Center (Houston, Texas), thanks to the collaboration with Michael E. Zolensky. He and his collaborators have been working for years on the search and characterization of xenoliths in meteorites (Zolensky *et al.*, 2009). We have had the possibility to have a few sections in which xenoliths were previously identified, to characterize them in the context of our search for new xenoliths in H chondrites. These sections include samples of Willard (b), Abbott and Sharps. A list of all sections we have analyzed, with their surface, is reported in Tab. 1.3.

Table 1.3: H chondrite sections analyzed searching for new xenoliths.

METEORITE	SECTIONS	SURFACE (mm <sup>2</sup> )
<b>H3 chondrites</b>		
Dimmitt (H3.7)	n.1	200
	2009_06	200
	2009_07	224
Grady 1937 (H3.7)	n.1	104
	n.2	230
Prairie Dog Creek (H3.7)	n.1	65

*continued on next page*

Table 1.3: continued.

METEORITE	SECTIONS	SURFACE (mm <sup>2</sup> )
Sharps (H3.4)	n.1	113
	n.2	203
	USNM 640	170
Willard (b) (H3.6)	n.5	51
<b>Total surface analyzed for H3 chondrites =</b>		<b>1859 mm<sup>2</sup></b>
<b>H4 chondrites</b>		
Cullison	n.1	36
Forest Vale	n.1	56
	USNM 4852	36
Menow	592	110
	50928	140
Monroe	n.1	88
Quenggouk	n.1	110
Sahara 98804	n.1	310
	n.2	240
	n.3	234
Seminole	n.1	37
Ste. Marguerite	n.1	277
Tysnes Island	2009_01	154
	2009_02	136
	2009_03	175
	2009_04	189
	2009_05	176
Weston	2007_24	76
	2007_25	74
	2007_26	120
<b>Total surface analyzed for H4 chondrites =</b>		<b>2774 mm<sup>2</sup></b>
<b>H5 chondrites</b>		
Agen	n.1	81
Allegan	n.1	50
	n.1560	36
Beaver Creek	n.1	90
	n.2	149
Ehole	n.1	60
Faucett	n.1	345
Gao-Guenie	W1	231
	Gao2	56
Leighton	2007_21	51
	2007_22	98
Plainview 1917	2009_09	135
	2009_10	205
Pultusk	n.1	150
Richardton	1280	80
<b>Total surface analyzed for H5 chondrites =</b>		<b>2244 mm<sup>2</sup></b>
<b>H6 chondrites</b>		
Bir Rebaa	n.1	195
Butsura	n.34795	43

*continued on next page*

Table 1.3: continued.

METEORITE	SECTIONS	SURFACE (mm <sup>2</sup> )
	n.5	75
Djati Pengilon	n.1	72
	n.2	76
Galapian	n.1	72
Kernouve	n.1	50
Supuhee	n.1	70
<b>Total surface analyzed for H6 chondrites =</b>		<b>653 mm<sup>2</sup></b>
<b>Mixed H chondrites</b>		
Abbott (H3-6)	7F	106
Bremervörde (H/L3.9)	2007_20	182
Hainaut (H3-6)	n.1	150
Luponnas (H3-5)	n.1	162
Sahara 00181 (H4-6)	n.1	148
Sahara 99070 (H3.8-6)	3867-1	165
	3867-2	180
	n.1	196
Sahara 97179 (H5-6)	n.1	146
Tulia (a) (H3-4)	3383	60
Zag (H3-6)	n.1	260
	n.2	190
	n.3	47
<b>Total surface analyzed for mixed chondrites =</b>		<b>1992 mm<sup>2</sup></b>

### 1.3.2 Searching for xenoliths: instruments and techniques

*First survey: optical microscope.* The systematic search for new (micro)xenoliths starts from the analysis of samples by optical microscopy. By means of an optical microscope, sections are scanned in reflected light searching for inclusions that are potential xenoliths. The most visible characteristic indicating that an inclusion is a potential xenolith is the presence of fine-grained matrix (Fig. 1.5B and C). At this stage xenoliths can be distinguished from the host meteorite “normal” matrix because this is generally diffuse among the meteorite components, while xenoliths have often sharp edges. To locate potential new xenoliths for successive analyses, optical composite maps of the concerned sections are realized. Pictures with a  $\times 2.5$  or  $\times 5$  magnification allow to realize maps with sufficient details in a brief period of time. An example of these maps is given in Fig. 1.5A; new found xenoliths are then reported on the map and numbered.

*Identification: scanning electron microscope.* To definitively ascertain if selected inclusions are xenoliths or not, scanning electron microscopy (SEM) images are realized. These help, for example, to distinguish between real xenoliths and impact melts (inclusions generated by fusion and re-crystallization as consequence of an impact, but with the starting material being that of the host meteorite). In addition to SEM images, energy

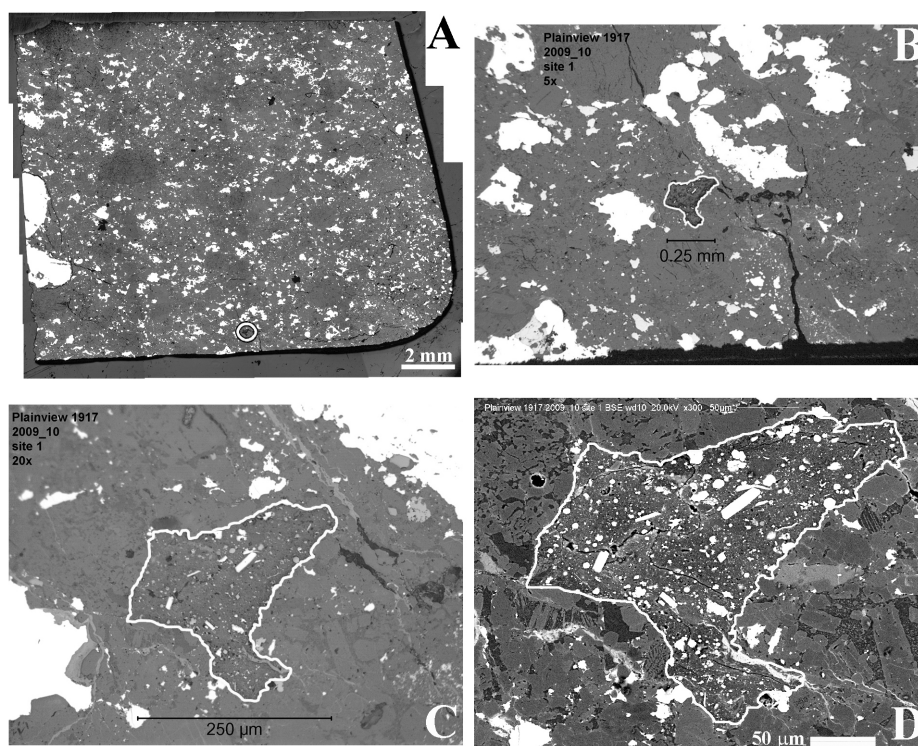


**Figure 1.5:** New discovered microxenolith # 1 in the H5 chondrite Plainview 1917. A: optical microscope composite map of the analyzed Plainview 1917 section: twenty images with magnification  $\times 2.5$  have been used to realize this map. Microxenolith # 1 is encircled near the lower edge of the section. B and C: optical microscopy images, with magnification  $\times 5$  (B) and  $\times 20$  (C). D: Back-scattered electron (BSE) scanning electron microscope image (magnification  $\times 300$ ) of the whole microxenolith. The abundant fine-grained matrix contains phyllosilicates and sub-micrometer-sized magnetite and iron-sulfide grains. Both lath-shaped sulfides and euhedral magnetite grains, with size greater than a few  $\mu\text{m}$ , appear in white.

dispersive X-rays (EDX) analyses are performed to have a first identification of the different phases present in the new xenoliths. SEM and EDX spectral analyses have been performed at the Laboratoire de Minéralogie et Cosmochimie du Muséum of the Muséum National d'Histoire Naturelle (Paris, France) by means of a JEOL JSM 840-A SEM equipped with an EDAX Genesis X-rays detector. For images, a 0.6 nA electron beam accelerated by a 15 kV acceleration voltage was used. Point EDX spectral analyses were performed with a 3 nA electron beam at 20 kV, in order to optimize number of counts and acquisition time. Also EDX spectral maps have been realized for certain xenoliths, in order to determine the nature of small phases (e.g. metals and sulfides). EDX maps are constituted by several images, each representing the spatial distribution of one of the selected elements (that are O, Na, Mg, Al, Si, P, S, Cl, K, Ca, Ti, Cr, Mn, Fe, Ni). These images

are acquired simultaneously, with a map resolution of  $\sim 1 \mu\text{m}/\text{pixel}$ . This is achieved using a grid of  $512 \times 400$  pixels. Acquisition time for each pixel is 600 ms. Moreover, in a few cases high resolution SEM images have been acquired at the University of Paris VI using a Zeiss Supra-55 VP field emission scanning electron microscope, with a 4 nA, 10 kV accelerated primary beam. With the same instrument, EDX spectral analyses of sub-micrometer-sized grains in the matrix of a few xenoliths have been performed.

*Quantitative mineralogy: analytical electron microprobe.* Quantitative analyses for the mineralogical composition of xenolith matrix and components have been obtained with a CAMECA SX-100 electron microprobe at the University of Paris VI. A 10 nA focalized beam, accelerated by a 15 kV acceleration voltage, is used for point analyses of silicates, oxides, sulfides and metals. For silicates and oxides data are collected for the following elements: Na, Mg, Al, Si, P, S, Cl, K, Ca, Ti, Cr, Mn, Fe, Ni. Detection limits range between 300 and 1200 ppm. For metals and sulfides the analyzed elements are: Si, P, S, Ca, Ti, Cr, Mn, Fe, Co, Ni, Zn. In this case detection limits range between 430 and 7000 ppm. For carbonates, to avoid damages to these fragile minerals, we used a 4 nA defocalized beam accelerated by a 15 kV acceleration voltage; the considered elements are: Mg, Al, Si, Ca, Ti, Cr, Mn, Fe, Ni, Sr. Detection limits range between 440 and 5700 ppm. In each case natural and synthetic standards have been used for calibration. Point analyses of matrix have been compared in a Mg-Fe-(Si+Al) ternary diagram to data for CI1 phyllosilicates (Tomeoka and Buseck, 1988), CM2 serpentine (Zolensky *et al.*, 1993b) and CR2 phyllosilicates (Weisberg *et al.*, 1993). When values of S  $\geq 5$  wt% are present, data are considered as due to contamination by a nearby sulfide and hence they are corrected assuming the sulfide is troilite (i.e. stoichiometric FeS).

## 1.4 Results: mineralogy and petrography

We analyzed 66 sections from 40 different meteorites. The total surface analyzed is  $9522 \text{ mm}^2$  (in Tab. 3.3 the surface studied for each section and each H chondrite group is reported). We discovered 26 new xenoliths. Among these, only 5 have a size larger than 1 mm, i.e.  $\sim 80\%$  are microxenoliths. The microxenolith size distribution is reported in Fig. 1.6.

The 21 new discovered microxenoliths belong to the FGH group, i.e. they are dominated by a fine-grained matrix composed of phyllosilicates. Considering the presence of magnetite and anhydrous silicates (simply referred to as silicates in the following) as key reference properties, they have been sub-divided in three groups: “magnetite-poor silicate-rich”, “magnetite-rich silicate-rich” and “magnetite-rich silicate-poor”. These three groups reflect a classification scheme as that proposed by Gounelle *et al.* (2005), based only on directly observed properties of xenoliths, rather than on similarities

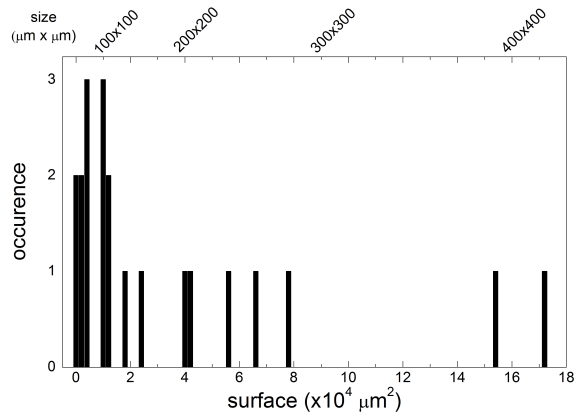


**Figure 1.6:** size distribution of the 21 new microxenoliths discovered in H chondrites.

with known carbonaceous chondrites.

In addition, a tentative association has been made between new microxenoliths and carbonaceous chondrite groups, as described below. This association is based on the presence or absence of anhydrous silicates, magnetite, sulfides, Fe-Ni metals and carbonates. In general, the comparison of xenoliths and microxenoliths to carbonaceous chondrites presents some difficulties. Even only the small size of xenoliths may imply that components characteristic of a certain group of carbonaceous chondrites are not present. For instance, in CI xenoliths previously individuated (Brearley and Prinz, 1992; Nakashima *et al.*, 2003; Gounelle *et al.*, 2003) only one carbonate has been observed, while they are quite common in CI chondrites (Johnson and Prinz, 1993). Here we use also such a classification scheme because it is the most largely diffuse in literature and it allows us to make comparisons with results of previous works.

We report our results starting from microxenoliths that can be associated with known groups of carbonaceous chondrites, and one peculiar microxenolith found in Leighton (H5). We then describe three new xenoliths (with size larger than 1 mm) that show clear similarities to CM chondrites. The main properties of all the new discovered xenoliths are reported in Tab. 1.4.

#### 1.4.1 Microxenoliths (size < 1 mm)

*Magnetite-rich silicate-poor (CI1-like) microxenoliths.* Seven xenoliths are magnetite-rich silicate-poor, and hence they have been associated with CI1 chondrites (Fig. 1.7). They have dimensions ranging between  $60 \times 20 \mu\text{m}^2$  and  $310 \times 255 \mu\text{m}^2$ . For these xenoliths, matrix point analyses gave results that in a Mg-Fe-(Si+Al) ternary diagram plot mainly between the CR2 phyllosilicate field and the CM2 phyllosilicate field, with some points in the CI1 phyllosilicate field (Fig. 1.8A). These xenoliths are rich in magnetite, which is present as spheroidal or hexagonal micrometer-sized grains and as smaller, sub-micrometer-sized framboidal grains. Anhydrous silicate grains

Table 1.4: properties of new discovered (micro)xenoliths.

XENOLITH <sup>a</sup>	SIZE ( $\mu\text{m}$ )	MATRIX <sup>b</sup>	OLIVINE <sup>c</sup>	PYROXENE <sup>d</sup>	SULFIDES <sup>e</sup>	Fe-Ni METALS <sup>f</sup>	MAGNETITE	CARBONATES <sup>g</sup>	DIVERS
<b>Magnetite-rich silicate-poor (CII-like) microxenoliths</b>									
Leighton 2007_21 xen. # 2	120×88	phyll. CR2 CM2	no	no	++ pyrrh.	no	++++	no	
Plainview 2009_10 xen. # 1	310×255	phyll. CR2 CM2	no	no	++ pyrrh.	no	++	+	dolomite
Plainview 2009_10 xen. # 2	90×32	phyll. CR2 CII	no	no	+	no	++	no	
Plainview 2009_10 xen. # 3	50×50	phyll. CR2 CM2	no	no	++ pyrrh. pentl.	no	++	no	
Plainview 2009_10 xen. # 5	60×20	serp. CM2 CR2	no	no	++	no	+	no	
Plainview 2009_10 xen. # 7	145×85	phyll. CII CR2	no	no	+	no	+++	no	
Sahara 00181 xen. # 1	180×30	-	no	no	++++ troil. pyrrh.	no	+++	no	
<b>Magnetite-poor silicate-rich (CM2-like) (micro) xenoliths</b>									
Abbott 7F large xen.	5.4×4.6 mm	phyll. CM2	++++ F <sub>08</sub>	no	+++ pyrrh.	no	no	no	
Abbott 7F small xen.	2×1.5 mm	phyll. CM2	+	no	+	no	++	no	
Leighton 2007_21 xen. # 1	100×200	phyll. CM2	no	+	++ pyrrh.	++ kam.	+	+	chromite grains
Leighton 2007_21 xen. # 3	160×270	phyll. CR2 CM2	++ F <sub>80</sub>	++ En <sub>80</sub> -Fs <sub>19</sub>	++ pyrrh.	+	no	+	chromite grains
Leighton 2007_22 xen. # 4	195×215	phyll. CM2 CR2	+	++ En <sub>75</sub> -Fs <sub>14</sub>	++ pyrr. troil.	++ taen. kam.	no	+	breunn.
Willard (b) n.5 xen. # 1	9×6 mm	phyll. CM2	++++ F <sub>093</sub>	++ En <sub>95</sub> -Fs <sub>3</sub>	+	no	no	+++	

<sup>a</sup> First line is the meteorite name. Second line has section name and xenolith number (xen. = xenolith).

<sup>b</sup> Data reported in a Mg-Fe-(Si+Al) ternary diagram: phyll. = phyllosilicates; CR2 = data in the CR2 phyllosilicate field; CII = data in the CII phyllosilicate field; CM2 = data in the CM2 serpentine field; - = not available data.

<sup>c</sup> +++++ = very abundant; +++ = abundant; ++ = common; + = occurrence. The second line is the mean of measured Fo values.

<sup>d</sup> The second line is the mean of measured En and Fs values. <sup>e</sup>troil. = troilite; pyrrh. = pyrrhotite.

<sup>f</sup> kam. = kamacite; taen. = taenite. <sup>g</sup>calc. = calcite; dolom. = dolomite; breunn. = breunnerite.

Table 1.4: continued.

XENOLITH <sup>a</sup>	SIZE ( $\mu\text{m}$ )	MATRIX <sup>b</sup>	OLIVINE <sup>c</sup>	PYROXENE <sup>d</sup>	SULFIDES <sup>e</sup>	Fe-Ni METALS <sup>f</sup>	MAGNETITE	CARBONATES <sup>g</sup>	DIVERS
<b>Magnetite-rich silicate-rich (CR2-like) microxenoliths</b>									
Leighton 2007_21 xen. # 9	87×55	phyll. CR2	no	+	++ pyrrh.	no	++	++ dolomite	
Leighton 2007_21 xen. # 10	47×36	phyll. CR2	no	+	+++ pyrrh.	no	++	no	
Leighton 2007_21 xen. # 11	285×85	phyll. CR2 CM2	+++ Fo <sub>86</sub>	no	++ pyrrh.	no	++	no	plagioclase grain
Leighton 2007_22 xen. # 2	575×300	phyll. CM2	+++ Fo <sub>98</sub>	+	++ pyrrh.	no	+++	++ calc. dolom.	chromite grains
Leighton 2007_22 xen. # 3a	300×190	phyll. CR2 CM2	no	no	++ pyrrh.	no	++	+	dolom. breunn.
Leighton 2007_22 xen. # 3b	170×70	phyll. CR2 CM2	no	no	++ pyrrh.	no	++	+	breunn.
Sahara 00181 xen. # 3	110×45	-	+	+	++ pyrr.	no	++	no	
Sahara 00181 xen. # 4	400×170	-	+	+	+++ troil. pyrrh.	no	++	++ dolomite	
Tynes Island 2009_02 xen. # 1	110×110	phyll. CR2 CM2	++ Fo <sub>74</sub>	++ En <sub>90</sub> -Fs <sub>6</sub>	++ troil. pyrrh.	small in mx	++	no	chromite grains
Tynes Island 2009_03 xen. # 5	170×60	phyll. CR2 CM2	no	no	++ troil. pyrrh.	+	++	+	breunnerite dolomite
<b>Ungrouped xenoliths</b>									
Leighton 2007_22 xen. # 1	500×310	phyll. CM2	no	no	++ pyrrh.	no	++	++ dolomite	

<sup>a</sup> First line is the meteorite name. Second line has section name and xenolith number (xen. = xenolith).

<sup>b</sup> Data reported in a Mg-Fe-(Si+Al) ternary diagram: phyll. = phyllosilicates; CR2 = data in the CR2 phyllosilicate field; CII = data in the CII phyllosilicate field; CM2 = data in the CM2 serpentine field; - = not available data.

<sup>c</sup> +++++ = very abundant; +++ = abundant; ++ = common; + = occurrence. The second line is the mean of measured Fo values.

<sup>d</sup> The second line is the mean of measured En and Fs values. <sup>e</sup>troil. = troilite; pyrrh. = pyrrhotite.

<sup>f</sup> kam. = kamacite; taen. = taenite. <sup>g</sup>calc. = calcite; dolom. = dolomite; breunn. = breunnerite.

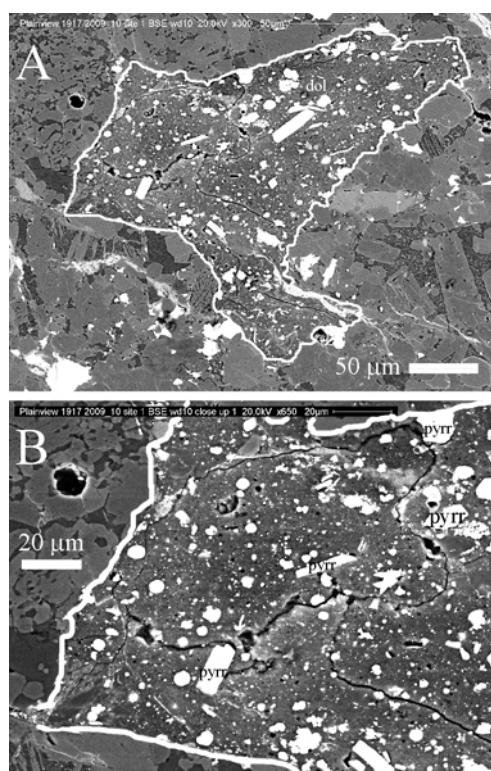


**Figure 1.7:** Magnetite-rich silicate-poor microxenolith from the H5 chondrite Plainview 1917 (microxenolith # 1, section 2009\_10). A: BSE image of the whole microxenolith (magnification  $\times 300$ ). Among the white inclusions two types can be distinguished: lath-shaped pyrrhotite grains and spheroidal magnetite grains. The label “dol” indicates a dolomite grain, the only carbonate we found in seven magnetite-rich silicate-poor microxenoliths. B: BSE close-up of the upper-left part of the microxenolith (magnification  $\times 650$ ). Fractures across the fine-grained matrix reveal its fragile nature. The largest pyrrhotite grains are labelled “pyrr”; spheroidal magnetite grains, from  $\sim 1$  to  $\sim 10 \mu\text{m}$  in size, are widespread, and on the right edge of the figure an aggregate of smaller, framboidal magnetite grains is visible.

are absent, as well as metal grains. Sulfides grains are mainly pyrrhotite, with Ni content around 2 wt%; rare pentlandite grains have been observed. Carbonates are generally absent, but one dolomite grain ( $24 \times 12 \mu\text{m}^2$ ) has been observed in xenolith # 1 of the Plainview section 2009\_10 (Fig. 1.7A).

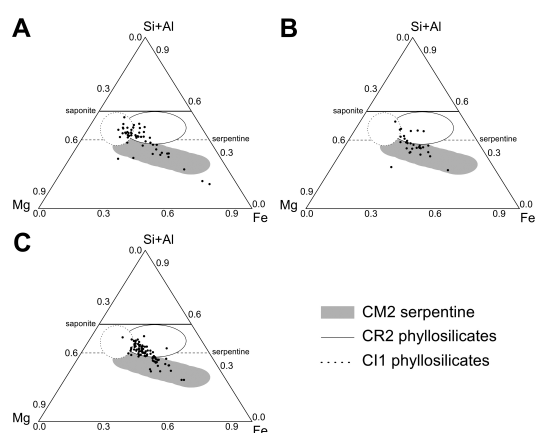


**Figure 1.8:** Mg-Fe-(Si+Al) ternary diagram of electron microprobe point analyses of matrix in the new discovered microxenoliths. A: magnetite-rich silicate-poor microxenoliths. B: magnetite-poor silicate-rich microxenoliths. C: magnetite-rich silicate-rich microxenoliths. Reference fields are indicated in the figure, see text (Materials and methods) for details. The solid and dashed horizontal lines indicate the ideal saponite and serpentine solid solutions, respectively.

*Magnetite-poor silicate-rich (CM2-like) microxenoliths.* We individuated three microxenoliths that are magnetite-poor silicate-rich, and hence similar to CM2 chondrites (Fig. 1.9). They have dimensions ranging between  $100 \times 200 \mu\text{m}^2$  and  $160 \times 270 \mu\text{m}^2$ . Electron microprobe point analyses of

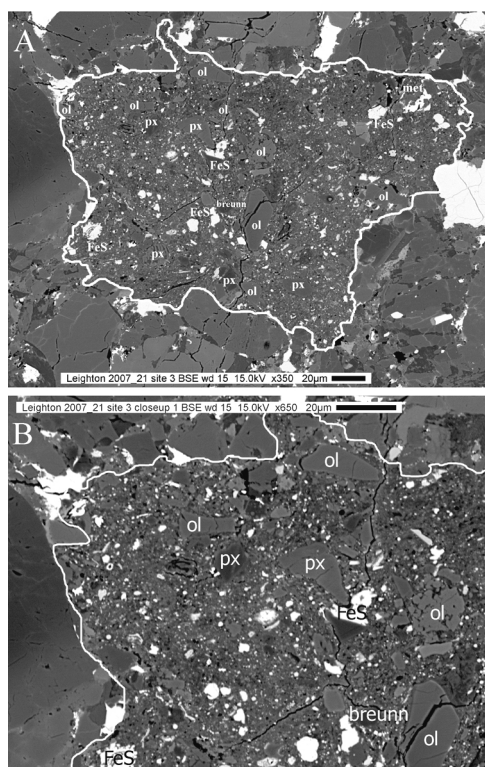


**Figure 1.9:** Magnetite-poor silicate-rich (CM-like) microxenolith from the H5 chondrite Leighton (microxenolith # 3, section 2007\_21). A: BSE image of the whole microxenolith (magnification  $\times 350$ ). The fine-grained nature of the microxenoliths is evident in comparison to the larger grains of the host meteorite. This microxenolith is rich in olivine (“ol”) and pyroxene (“px”) grains. The largest iron sulfides (pyrrhotite in this microxenolith) are labelled “FeS”, while “met” indicates less abundant Fe-Ni metal grains. One Me-Fe carbonate (“breunn” = breunnerite) is present in the center of the microxenolith. B: BSE close-up of the upper-left part of the microxenolith (magnification  $\times 650$ ). In addition to the components present in A, micrometer-sized iron sulfides and Fe-Ni metal grains are visible in the matrix (white dots). Fractures reveal the low-strength nature of the matrix.

matrix in a Mg-Fe-(Si+Al) ternary diagram plot between the field of CM2 serpentine, the serpentine solid solution line and the CR2 phyllosilicates field (Fig. 1.8B). Matrix is rich in S (up to 4 wt%), due to the presence of sub-micrometer-sized sulfides or tochilinite mixed to phyllosilicates. Set in the matrix are common olivine and pyroxene grains, their sizes ranging between few  $\mu\text{m}$  up to 50  $\mu\text{m}$ . They are mainly Mg-rich, with composition ranging between  $\text{Fo}_{74}$  and  $\text{Fo}_{82}$  for olivine (peak at  $\text{Fo}_{80}$ ), and between  $\text{En}_{60}$ – $\text{Fs}_{36}$  and  $\text{En}_{93}$ – $\text{Fs}_6$  for pyroxene. In one xenolith (# 4 in Leighton 2007\_22) two low-K plagioclase ( $\text{Ab}_{92}$ ) grains are present. Sulfides are present as troilite, pyrrhotite and grains with intermediate composition. Fe-Ni metal grains with size of few  $\mu\text{m}$  are present, some of which very rich in Ni (up to 50 wt%). Carbonates are not abundant, but one per microxenolith is present, with size up to 20  $\mu\text{m}$ . They are calcite and breunnerite.

*Magnetite-rich silicate-rich (CR2-like) microxenoliths.* Ten xenoliths are related to CR2 chondrites (Fig. 1.10). Their sizes range between  $47 \times 36 \mu\text{m}^2$  and  $575 \times 300 \mu\text{m}^2$ . Matrix data (Fig. 1.8C) are in or close to the CR2 phyllosilicates field in the Mg-Fe-(Si+Al) ternary diagram, even if sometime tend to the CM2 serpentine field. Matrix analyses have high content of S (up to 4 wt%) probably due to sub-micrometer-sized grains of sulfides. Larger olivine and pyroxene grains, somewhat less abundant than in CM2 microxenoliths, are present in five out of eleven CR2 microxenoliths.

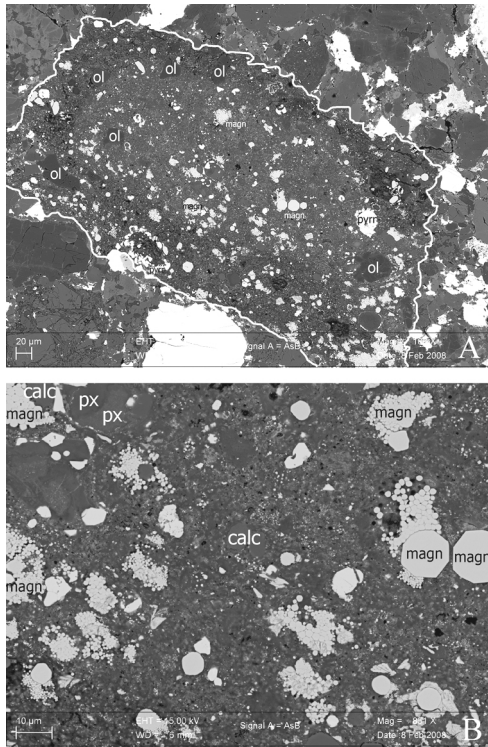


**Figure 1.10:** Magnetite-rich silicate-rich (CR-like) microxenolith from the H5 chondrite Leighton (microxenolith # 2, section 2007\_22). A: BSE image of the whole microxenolith (magnification  $\times 180$ ). This microxenolith is very rich in magnetite (“magn”), present as spheroidal grains, polygonal grains and aggregates of micrometer-sized and smaller grains. Large olivine (“ol”) grains (up to  $57 \times 28 \mu\text{m}^2$ ) are common, pyroxene is present as smaller, micrometer-sized grains. The pyrrhotite (“pyrr”) grain on the right part of the microxenolith is  $38 \mu\text{m}$  in its largest dimension. B: BSE close-up (magnification  $\times 850$ ). Magnetite clearly dominates this part of the microxenolith. In addition, micrometer-sized pyroxene (“px”) and calcite (“calc”) grains are visible.

Olivine composition range between  $\text{Fo}_{68}$  and  $\text{Fo}_{99}$ . Pyroxene grains are also Mg-rich, their composition ranging between  $\text{En}_{88}\text{--Fs}_7$  and  $\text{En}_{96}\text{--Fs}_2$ . Ti-rich phases, such as ilmenite, are present but rare. Sulfides are common, mainly pyrrhotite grains up to few  $\mu\text{m}$  in size, and more rare troilite and grains with intermediate composition. Fe-Ni metals are present as small, micrometer-sized grains dispersed in the matrix. Carbonates, both calcite and dolomite, are more abundant than in CM2 xenoliths, even if xenoliths without carbonates have been observed. Xenolith # 2 in Leighton 2007\_22 contains several calcite grains and abundant magnetite in the form of both aggregates of sub-micrometer-sized framboidal grains and larger spheroidal grains. Xenolith 3a in the same section presents a dolomite grain  $30 \mu\text{m}$  wide in its larger size.

*One ungrouped microxenolith.* One first peculiar microxenolith is xenolith # 1 in section 2007\_22 of Leighton. The absence of anhydrous silicates and the presence of pyrrhotite grains and framboidal magnetite aggregates would suggest it is a CI-like microxenolith. However it contains an impressive amounts of carbonate grains (Fig. 1.11A), rarely observed in CI-like xenoliths. These carbonates are dolomite grains with dimensions ranging from  $\sim 1 \mu\text{m}$  to  $> 10 \mu\text{m}$  (Fig. 1.11B). Their abundance resembles that observed in the carbonate-rich lithology of Tagish Lake (Zolensky *et al.*, 2002), but carbonates in Leighton microxenolith do not show the complex structure (Ca core + Mn-Fe-Mg rims) of the Tagish Lake carbonates. In

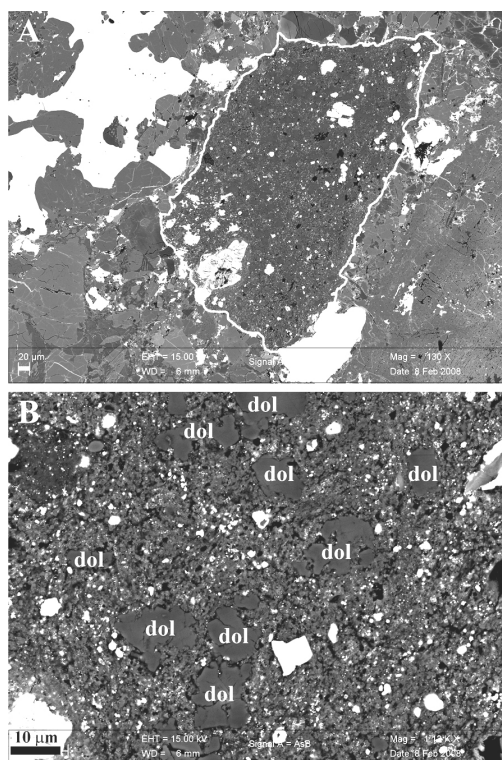


**Figure 1.11:** A: BSE image of microxenolith # 1 in section 2007\_22 of Leighton (H5), highlighted by a white edge. B: BSE image close-up of fine-grained matrix. Widespread dolomite grains are labelled “dol”, see Fig. 1.12 for their composition.

in addition this microxenolith does not present the same characteristics of the carbonate-rich lithology of Tagish Lake: matrix composition is that of CM2 serpentine, while in the carbonate-rich lithology of Tagish Lake is almost only saponite. Magnetite is rare in the carbonate-rich lithology of Tagish Lake, abundant in the Leighton microxenolith. Dolomites of xenolith # 1 in Leighton 2007\_22 have 24.4-27.6 wt% CaO, 16.4-19.9 wt% MgO, 2.5-4.2 wt% FeO and 2.8-6.1 wt% MnO. This composition is similar to that of CI and CM dolomites (Fig. 1.12) and to that of dolomites found in Kaidun (Weisberg *et al.*, 1994). The abundance of carbonates is the reason why we did not include this microxenolith in the CI-like group. At the same time we did not include it in the CR-like group because of the absence of olivine and pyroxene, considering also its size ( $500 \times 310 \mu\text{m}^2$ ). Indeed, in the same section there is the CR-like microxenolith # 2 that has similar size ( $575 \times 300 \mu\text{m}^2$ ), and that contains olivine and pyroxene grains, abundant framboidal magnetite aggregates and carbonate grains (calcite and dolomite). This suggests also that dolomite grains of xenolith # 1 in Leighton 2007\_22 are not due to terrestrial aqueous alteration, otherwise they should be abundant also in microxenolith # 2 and in the other microxenoliths found in the same section (microxenoliths 3a, 3b and # 4 have very few carbonates, some of which are brunnerite).

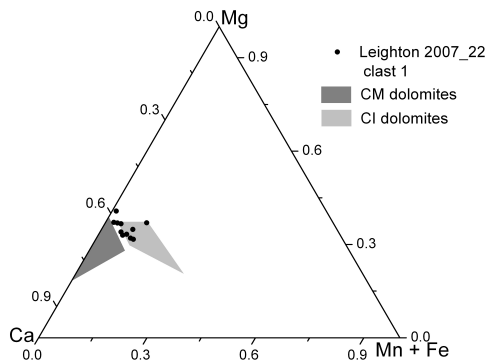


**Figure 1.12:** Mg-Ca-(Mn+Fe) ternary diagram for carbonate composition. Measurements for carbonates in microxenolith # 1 of the Leighton section 2007\_22 are compared to composition of CI and CM dolomite grains (data after Johnson and Prinz 1993).

#### 1.4.2 Xenoliths (size > 1 mm)

*CM-like xenoliths.* Three xenoliths with petrography and mineralogy clearly similar to that of Cm chondrites have been identified in Abbott and Willard (b).

The two xenoliths discovered in Abbott (H3-6) are in the same section, presenting a typical H6 lithology. Their dimensions are 5.4×4.6 mm and 2×1.5 mm. The smallest xenolith (Fig. 1.13) is dominated by a light coloured, fine-grained matrix. Its composition, in a Mg-Fe-(Si+Al) ternary diagram, falls in the CM2 serpentine field. Supported in the matrix are sulfide grains with composition ranging from troilite to pyrrhotite and Ni-rich sulfides with intermediate composition (Ni content is up to 20 at%). Metal grains, magnetite and carbonates are not present. Clearly visible in the xenolith are rounded dark areas composed mainly by fine-grained serpentine. They are interpreted as relict chondrules, i.e. their phyllosilicates are the result of aqueous alteration of chondrule silicates. Embedded in the fine-grained serpentine are micron-sized sulfides and poorly defined iron oxide grains. Such grains, as well as similar, diffuse veins with the same composition and the same low totals in electron microprobe analyses indicate that the xenolith suffered aqueous alteration, probably from terrestrial weathering. Olivine is present in only three grains of size between 30 and 60  $\mu\text{m}$ , their composition being very Mg-rich (from Fo<sub>96</sub> to Fo<sub>99</sub>). Pyroxene grains have not been observed in this xenolith.

The largest xenolith in Abbott (Fig. 1.14) is similar to the previous one. Its matrix has the composition of CM2 serpentine, poorly defined iron oxide grains and veins due to aqueous alteration are abundant, sulfide grains are common, with size up to 45  $\mu\text{m}$  and composition ranging from troilite to pyrrhotite and Ni-rich sulfides (Ni content is up to 28 at%). Metal grains, magnetite and carbonates have not been observed. However this xenolith presents also several chondrules, similar to porphyritic olivine chondrules, composed of olivine crystals alternated to fine-grained serpentine and iron oxide alteration grains, always rimmed by fine-grained serpen-

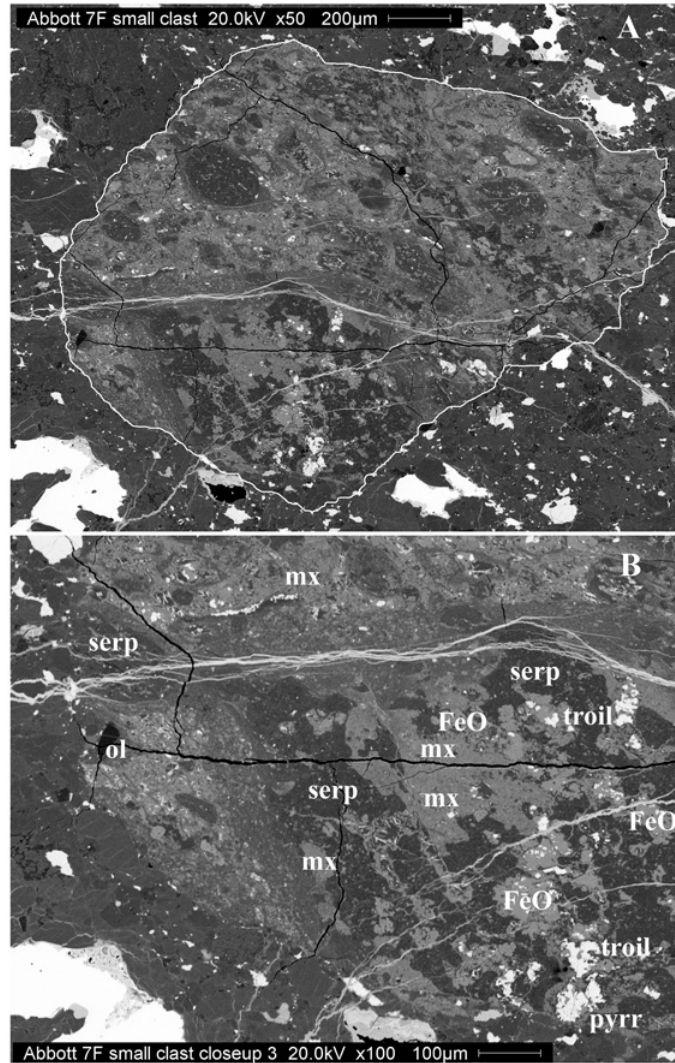


**Figure 1.13:** A: BSE image of the smallest CM2 xenolith found in the H3-6 chondrite Abbott. In the light-colored matrix, rounded, dark areas are evident (the biggest one, in the upper left part of the xenolith, is  $270 \times 200 \mu\text{m}^2$ ). They are fine-grained serpentine-dominated relict chondrules produced by aqueous alteration of silicates. Very few anhydrous silicate grains remain in this xenolith. B: BSE close-up view of the xenolith interior. The Fe-rich (mean FeO wt% = 37.5) light-coloured, fine-grained matrix (“mx”) is intermixed with fine-grained, dark serpentine. An olivine grain is present near the left edge of the xenolith, while on the right side of the image sulfides (“troil” and “pyrr”) are visible, with size up to  $67 \mu\text{m}$ .

tine. The same structure is observed in chondrule fragments scattered in the xenolith. Olivine grains are clearly more abundant than in the smaller xenolith. Considering also those in chondrules, their size range from few  $\mu\text{m}$  up to 77  $\mu\text{m}$  and their compositions are between Fo<sub>44</sub> to Fo<sub>100</sub>, with a marked peak corresponding to forsterite (22 out of 36 grains have Fo<sub>>96</sub>). A large forsterite grain, 730×360  $\mu\text{m}^2$  in size, is included in this xenolith, and presents several fractures filled by iron oxide alteration veins. Once again pyroxene grains are absent. Due to their size, the presence of micrometer-sized sulfides, larger olivine grains and partially altered chondrules, these two xenoliths can be classified as coarse-grained hydrous (CGH), following the classification proposed by Zolensky *et al.* (2009). Their mineralogical and petrological properties are those of CM2 chondritic material.

A third CM2 xenolith has been found in the H3.6 chondrite Willard (b). This xenolith is 9×6 mm. Its fine-grained matrix is characterized by a composition in the CM2 serpentine range in the Mg-Fe-(Si+Al) ternary diagram. Also present are dark areas composed of serpentine, probably produced by aqueous alteration of chondrule silicates, as in the Abbott xenoliths. Indeed these areas form also rims around relict chondrules, as in the largest Abbott xenolith. The Willard (b) xenolith is rich in olivine grains, with a wide size range (from a few  $\mu\text{m}$  to 200  $\mu\text{m}$ ), while only three pyroxene grains have been individuated. Olivine presents a wide composition range, from Fo<sub>48</sub> to Fo<sub>100</sub>, with an evident peak at Fo<sub>99</sub> (30 out of 41 grains have Fo<sub>98–100</sub>). Pyroxene composition varies from En<sub>92</sub>-Fs<sub>5</sub> to En<sub>98</sub>-Fs<sub>1</sub>. One spinel grain is present in this xenolith, with an almost stoichiometric composition: 14.2 at% Mg and 27.8 at% Al. Abundant calcite grains have been observed in this xenolith. Sulfides are present as pyrrhotite and pentlandite, whereas no metal grains and no magnetite grains have been observed.

## 1.5 Relations with properties of host meteorites

In this section we describe possible relations between new discovered xenoliths and properties of the host meteorites. In particular, we consider meteorite petrologic type, cosmic-ray exposure (CRE) age, shock degree, if host meteorites are breccias or not and if they are gas-rich or not. Each of these properties is described in the following subsections, and for each case observed relations between the new discovered xenoliths and the considered meteorite characteristic are discussed. In Tab. 1.5 is reported a summary of the analyzed sections, their properties and number of discovered xenoliths.

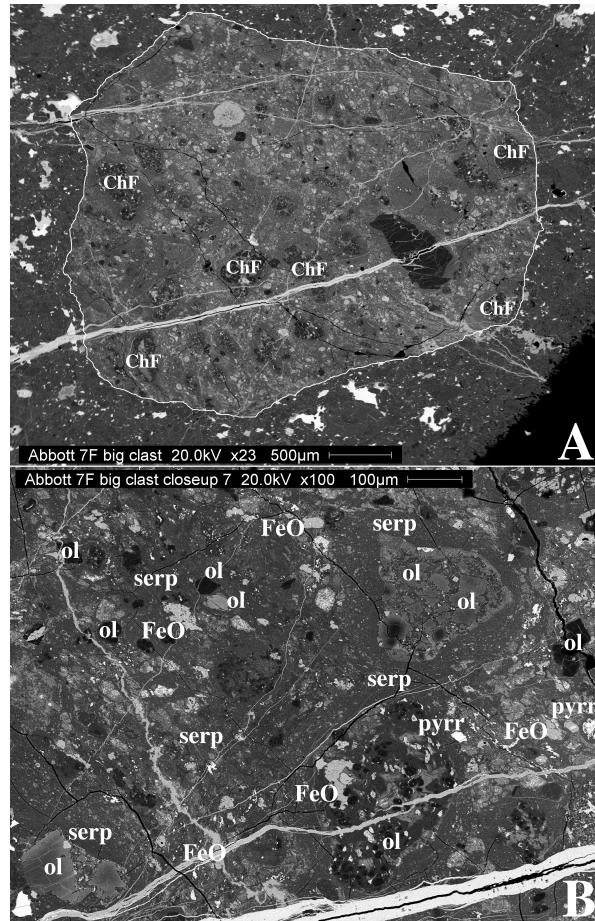


**Figure 1.14:** A: BSE image of the largest CM2 xenolith found in the H3-6 chondrite Abbott. Some of the chondrule fragments are labelled “ChF”. On the right a large,  $730 \times 360 \mu\text{m}^2$ , forsterite grain is visible. The light grey grain in the upper-left part of the xenolith is iron oxide alteration grain, the biggest of many ones present in the xenolith. Also several iron oxide alteration veins are evident. B: BSE close-up view of the xenolith interior. Abundant forsterite (black) grains are scattered in the xenolith, which has also olivine (“ol”) grains with minor Mg content (the large grey grain in the lower left corner). Two pyrrhotite (“pyrr”) grains are visible near the right edge of the image. Two relict chondrules are present, both rimmed by fine-grained serpentine (“serp”), but with different aspect. The uppermost chondrule ( $225 \times 225 \mu\text{m}^2$ ) shows a porphyritic structure, with Fe-rich olivine grains ( $\text{Fo}_{62-81}$ ). The other one ( $367 \times 267 \mu\text{m}^2$ ) has probably suffered a more intense aqueous alteration. It contains forsterite grains ( $\text{Fo}_{90-99}$ ), fine-grained serpentine (the dark matrix between forsterite grains) and iron oxide alteration grains (“FeO”).

Table 1.5: characteristics of analyzed H chondrites.

METEORITE	SHOCK DEGREE <sup>a</sup>	BRECCIA	CRE age (Myr) <sup>b</sup>	XENOLITHS
<b>H3 chondrites</b>				
Dimmitt (H3.7)	S3	reg. breccia - GR	6	no
Grady 1937 (H3.7)	S2	no	6.5	no
Prairie Dog Creek (H3.7)	S2	no	25.9	no
Sharps (H3.4)	S3	no	18.5	no
Willard (b) (H3.6)	–	reg. breccia - GR	–	1 xen.
<b>H4 chondrites</b>				
Cullison	c	breccia	1.9	no
Forest Vale	S2	no	77	no
Menow	S2	no	15.3	no
Monroe	b/c	breccia	12.8	no
Quenggouk	S1/S2	no	22.3	no
Sahara 98804	S1	no	–	no
Seminole	S3	no	7.8	no
Ste. Marguerite	S2	no	31.7	no
Tysnes Island	–	reg. breccia - GR	7.9	2 $\mu$ xen.
Weston	S1/S4	reg. breccia - GR	30	no
<b>H5 chondrites</b>				
Agen	veined	no	5.6	no
Allegan	S1	no	4.8	no
Beaver Creek	S3	no	41.2	no
Ehole	–	no	18.5	no
Faucett	S4	no	5.6	no
Gao-Guenie	S1/S2	breccia	–	no
Leighton	–	reg. breccia - GR	5.7	11 $\mu$ xen.
Plainview 1917	S3	reg. breccia - GR	6	5 $\mu$ xen.
Pultusk	S3	reg. breccia - GR	6.6	no
Richardton	S1/S2 veined	no	23.7	no
<b>H6 chondrites</b>				
Bir Rebaa	S1	no	–	no
Butsura	S3	no	35.9	no
Djati Pengilon	–	no	31.8	no
Galapian	veined	no	–	no
Kernouve	S1 - veined	no	4.5	no
Supuhee	–	breccia	8.2	no
<b>Mixed H chondrites</b>				
Abbott (H3-6)	S3	reg. breccia - GR	–	2 xen.
Bremervörde (H/L3.9)	S2	reg. breccia - GR	14	no
Hainaut (H3-6)	–	reg. breccia - GR	7.1	no
Luponnas (H3-5)	–	breccia	8.4	no
Sahara 00181 (H4-6)	S3	breccia	–	3 $\mu$ xen.
Sahara 99070 (H3.8-6)	S2	breccia	–	no
Sahara 97179 (H5-6)	S4	breccia	–	no
Tulia (a) (H3-4)	b	breccia	4.6	no

*continued on next page*

Table 1.5: continued.

METEORITE	SHOCK DEGREE <sup>a</sup>	BRECCIA	CRE age (Myr) <sup>b</sup>	XENOLITHS
Zag (H3-6)	S2/S4	breccia	5.1	no

<sup>a</sup> Shock degree data are from MetBase v7.2 and the “List of shock classified ordinary chondrites” compiled by Dieter Stöffler.

S1 = unshocked; S2 = very weakly shocked;

S3 = weakly shocked; S4 = moderately shocked (Stöffler *et al.*, 1991);

shock degrees “b” and “c” are based on the Dodd and Jarosewich (1979) classification, see text for details;

veined = presence of shock-produced veins; GR = gas-rich meteorite.

<sup>b</sup> Data after: Graf and Marti (1995); Eugster (1988).

Schultz and Weber (1995); Eugster *et al.* (2007).

### 1.5.1 Relation with host meteorite petrologic type

The petrologic type of a meteorite indicates the degree of alteration suffered by the meteorite. Thermal metamorphism (i.e. changes induced by high temperatures) and aqueous alteration (caused by water) act to alter the original petrographic characteristic of a rock. In 1967, van Schmus and Wood proposed a classification scheme of petrologic types that is still used today. This scheme is based on compositional and structural properties of meteorites (e.g. chondrule and matrix texture, homogeneity of olivine and pyroxene composition) and petrologic types are numbered from 1 to 6. Types 1 and 2 designate aqueously altered meteorites, with type 1 meteorites being the most altered. Meteorites of type 1 or 2 have been observed only among carbonaceous chondrites. Types from 3 to 6, instead, reflects increasing metamorphic grade. All these petrologic types are represented in H chondrites. There are also meteorites that have components of different petrologic type: this is the result of impact and mixing processes, which lead to the formation of a breccia (see Section 1.5.3).

As reported in Tab. 1.5, several meteorites have been analyzed for each petrologic type from 3 to 6. Namely, 10 sections from 5 meteorites of petrologic type 3, 20 sections from 10 meteorites of petrologic type 4, 15 sections from 10 meteorites of petrologic type 5, 8 sections from 6 meteorites of petrologic type 6 and 13 sections from 9 meteorites of mixed petrologic type. We found a total of 26 new xenoliths: their distribution as function of the petrologic type is reported in Fig. 1.15A.

From this figure it is evident that most of the new xenoliths and microxenoliths have been individuated in H5 chondrites (16 out of 26). This holds also when the number of new xenoliths is normalized to the analyzed surface for each petrologic type (Fig. 1.15C). However it has to be noted that all the new xenoliths in H5 chondrites have been individuated in only 2 meteorites, namely Leighton and Plainview 1917. Six microxenoliths have been individuated in the section 2007\_21 of Leighton, five in the section 2007\_22

of the same meteorite and five in the section 2009\_10 of Plainview 1917. One could imagine that such a concentration of xenoliths in a small area is the result of a same impact, i.e. xenoliths individuated in a same section are fragments of a single projectile that impacted the host meteorite. However two observations make this hypothesis problematic. First these xenoliths show differences between each other. All are FGH microxenoliths, but in section 2007\_21 of Leighton three are CR-like, two are CM-like and one is CI-like; in section 2007\_22 of Leighton there is one CM-like microxenolith, three CR-like and a microxenolith different from all the others (see Tab. 1.4 and its description in the previous paragraph). Second, if we imagine a projectile large enough to leave fragments up to  $500 \times 310 \mu\text{m}^2$  in size (xenolith # 1 in Leighton 2007\_22), then it is probable that such a projectile caused a “violent” impact, at least sufficient to cause significant thermal and shock alterations. Such alterations are not observed in these xenoliths, which instead are similar to type 1 and type 2 chondritic material and that, in addition, show a general low-strength aspect, being generally dominated by fine-grained phyllosilicate matrix. We therefore consider as improbable that xenoliths found in a same section come from the same parent projectile, and consider each of them as a distinct sample. H5 chondrites continue to be the most xenolith-rich even considering our results along with those of previous work (Fig. 1.15B). However once again it has to be noted that most of the xenoliths previously found in H5 chondrites (4 out of 6) are concentrated in only one meteorite, which is once again Plainview 1917. Eventually, to confirm that H5 chondrites are really the most xenolith-rich, analyses of more samples (of all petrologic types) are needed.

Our results show that there is not a clear relation between the presence of xenoliths and the petrologic type of their host meteorite. This conclusion holds even when our results are considered along with those of previous works, as shown in Fig. 1.15B. Rather, xenoliths and microxenoliths appear to be common even in H chondrites with relatively high petrologic type, as H4 and H5 chondrites. Therefore we can conclude that the embedding of microxenoliths took place after the metamorphism of the host meteorite parent bodies. Otherwise their fine-grained matrix, rich in hydrous minerals such as phyllosilicates, would not have been preserved.

Moreover, the presence of xenoliths and microxenoliths in H4 and H5 chondrites indicates that these meteorites have been exposed to space after have been metamorphosed. Previous models suggest that the different H chondrite petrologic types are due to the different depth at which these rock were in the parent body (Trieloff *et al.*, 2003). The more deep a rock was, the more it has been heated. Therefore, H4 and H5 chondrites, which were not on the surface of the H chondrite parent body, must have been extracted from the interior of the parent body to have the possibility of embedding xenoliths and microxenoliths. This is consistent with models that suggest a fragmentation and reassembly of the H chondrite parent body (Grimm,

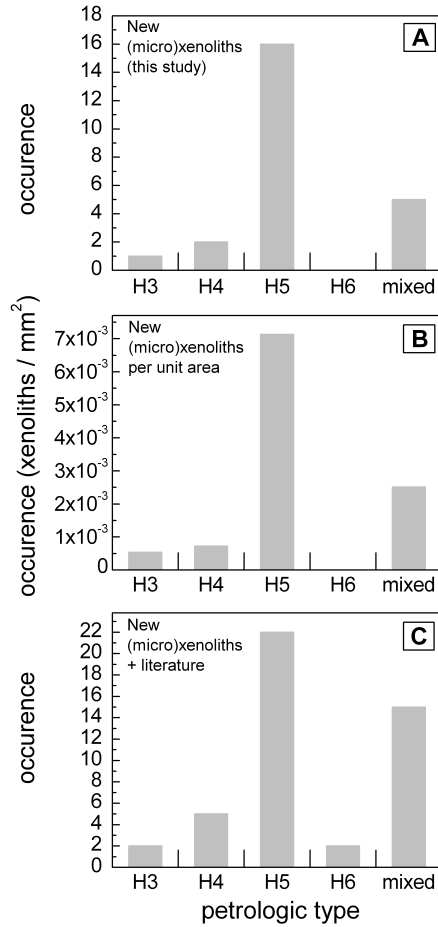


**Figure 1.15:** Distribution of xenoliths and microxenoliths as function of the host meteorite petrologic type. A: (micro)xenoliths discovered in this study. B: (micro)xenoliths discovered in this study per unit analyzed area. C: (micro)xenoliths discovered in this study plus carbonaceous xenoliths described in previous works (see Tab. 1.1).

1985; Grimm *et al.*, 2005).

### 1.5.2 Relation with host meteorites cosmic-ray exposure ages

For most of the meteorites we analyzed, CRE ages are known (Tab. 1.5). CRE ages are a measure of the time a meteoroid spent in interplanetary space as a meter-sized body. During this time it was exposed to several kind of cosmic rays: solar wind particles (with an energy of  $\sim 1$  keV/nucleon), solar energetic particles (1–100 MeV/nucleon) and galactic cosmic rays ( $1\text{--}5 \cdot 10^3$  MeV/nucleon) (Goswami *et al.*, 1984). Particles with different energies penetrate to different depths in meteoritic material. The less energetic are stopped in the first superficial layers, which are easily lost by ablation when a meteoroid enter the Earth atmosphere. More energetic particles can penetrate up to  $\sim 1$  m in the meteoroid (Goswami *et al.*, 1984), reaching material that remains shielded from the external environment for the rest of the time. These particles cause in the meteoroid the accumulation

of stable and radioactive nuclides not originally present (or present in minimal amounts). Radioactive nuclides that have a short half life (with respect to the time the meteoroid takes to reach Earth), decay in stable radiogenic nuclides. Measuring the concentrations of particular nuclides (mainly light noble gases, e.g.  $^3\text{He}$ ,  $^{21}\text{Ne}$ ,  $^{38}\text{Ar}$ ) ascribed to these interactions and coupling such measurements with production rates by cosmic rays, it is possible to estimate CRE ages (Graf and Marti, 1995; Eugster *et al.*, 2006). Usually it is assumed that meteorites CRE ages represents the time a meteoroid spent in interplanetary space after it has been removed from its parent body and until it reached Earth. However a same meteorite (or meteorite component, e.g. chondrules, CAIs) can have had more than one period during which it has been exposed to interplanetary cosmic rays. First in the so-called pre-accretion period, i.e. before the compaction of the rock we observe today. Second during the residence in the parent body, for those rocks that are on the parent body surface. And then after it has been removed from its parent body, during its journey toward the Earth. By means of CRE ages it is not possible to distinguish between these phases in the meteoroid life, but complex exposure histories have been observed [see paragraph 3.4 of Eugster *et al.* (2006) and references therein]. Complex exposure histories can be revealed by inconsistencies between exposure ages obtained by different methods (Graf and Marti, 1995), as for example an exposure age based on long-lived nuclides different from that based on short-lived nuclides (Eugster *et al.*, 2006). However, among H chondrites such complex exposure histories have been observed only for meteorites with low CRE ages ( $T_e < 4$  Myr), which are actually very few (Graf and Marti, 1995). Also in this study only one meteorite presents a CRE age of  $< 4$  Myr (the H4 Cullison, with  $T_e = 1.9$  Myr). Therefore we assume that the CRE ages reported here are representative of the time period spent in interplanetary space by the considered meteorites after their separation from the parent body.

In Fig. 1.16A are reported the distribution of CRE ages (when known) for meteorites analyzed in this work and the distribution of xenoliths found in these meteorites. In Fig. 1.16B the same distributions are showed considering also carbonaceous xenoliths described in previous works. Evident trends of xenoliths number as function of CRE age are not present in these distributions, but in both cases there is a clear prevalence of xenoliths in meteorites with low CRE ages, between 5 and 8 Myr. On one hand this could indicate that xenoliths have been embedded in their host meteorites in very recent times. On the other hand, however, it seems somewhat strange that xenoliths are more abundant in meteorites that took only few Myr to reach the Earth from their parent bodies. If the embedding of xenoliths is a process that happened in the last  $\sim 100$  Myr (the range of measured CRE ages for H chondrites), meteorites that spent more time free floating in space (i.e. those meteorites with larger CRE ages) should be richer in xenoliths than meteorites with low CRE ages. Therefore, our results for the

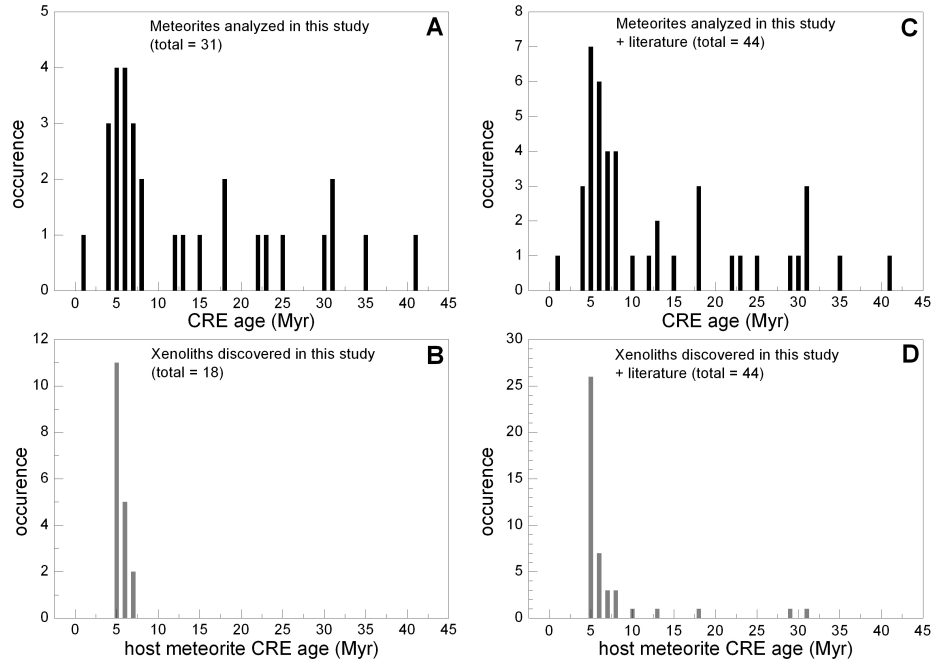


**Figure 1.16:** Carbonaceous xenoliths and host meteorite cosmic-ray exposure (CRE) ages. Panels A and B show data collected in the present study. A: number of analyzed meteorites with the indicated CRE age. B: number of xenoliths found in meteorites indicated in A (i.e., grey bars do not indicate the number of xenoliths with a given CRE age). Panels C and D show data collected in this study plus data obtained from the literature (see Tab. 1.1). In both plots A and C a meteorite with CRE age 77 Myr and without xenoliths is not showed.

abundance of xenoliths in low-CRE-age meteorites might indicate that their embedding happened in very ancient times. One possibility is that such embedding process took place when the meteorite was part of the parent body, if the rock was exposed to space on the parent body surface (see next section about xenoliths in brecciated meteorites). Probably more sections from more meteorites should be analyzed in searching for new xenoliths, to establish a solid relation between the presence of xenoliths and CRE ages.

### 1.5.3 Relation with brecciated, gas-rich meteorites

Of particular interest, in the context of a xenolith study, is considering the role of impacts, essentially for two reasons. First because the origin of xenoliths is intimately related to impacts: xenoliths are fragments detached from their own parent bodies by means of impacts, and then embedded in their host meteorite parent bodies by means of other impacts. Second because impacts are necessary to produce meteoroids that subsequently reach Earth (becoming meteorites). Meteorites show a variety of impact histories,

which necessarily affected also xenoliths, in particular the most fragile carbonaceous ones. Therefore it is essential to consider the shock degree of the analyzed H chondrites, and how many of them are brecciated meteorites.

Breccias are meteorites composed of fragments with different sizes and different characteristics. They are formed by a history of impacts and mixing (Housen and Wilkening, 1982; Keil, 1982; Bunch and Rajan, 1988; Bischoff *et al.*, 2006). Based on their components and on the inferred formation mechanisms, breccias are classified in several groups (see Tab. 1 in Bischoff *et al.* 2006 and Tab. 3.5.2 in Bunch and Rajan 1988). Among these, regolith breccias are good candidates to search for xenoliths: they are formed by lithification of different components from the parent body upper surface, and contain solar-flare tracks and solar-wind gases. They are also called gas-rich meteorites, because their concentrations of light noble gases are well above a normal meteoritic value (Goswami *et al.*, 1984; Bischoff *et al.*, 2006). Indeed, these meteorites are formed by impacts that cause limited shock effects, but at the same time induce melting of grain boundaries, cementing the fragments together (Bischoff *et al.*, 2006). When collisions are more violent, impact-melted components are evident. In other words the characteristics of regolith breccias testify their exposure to the external environment.

A striking result of this study is that all the new xenoliths and microxenoliths have been found in brecciated meteorites. In total, we analyzed samples from 20 brecciated meteorites. In 6 of these there are xenoliths. Also for non brecciated meteorites samples from 20 meteorites have been analyzed. Considering carbonaceous xenoliths described in previous works (see Tab. 1.1 and Fig. 1.1A), in only three cases the host meteorite is not a breccia: the already cited H3.4 Sharps (Fredriksson *et al.*, 1968; Wilkening, 1977b), the H4 Holyoke (McCall, 1973; Wilkening, 1977b) and the H6 Ipiranga (Rubin and Bottke, 2009). In contrast there are 13 H chondrite breccias that contain carbonaceous xenoliths. These data indicate that the probability of finding a carbonaceous xenolith is clearly larger in a brecciated than in a non-brecciated H chondrite.

Considering only regolith breccias, i.e. gas-rich meteorites, we have analyzed samples from 10 gas-rich meteorites: Dimmitt (H3), Willard (b) (H3.6), Tysnes Island (H4), Weston (H4), Leighton (H5), Plainview 1917 (H5), Pultusk (H5), Abbott (H3-6), Bremervörde (H/L3.9) and Hainaut (H3-6). In 5 of these (Willard (b), Tysnes Island, Leighton, Abbott and Plainview 1917) we found xenoliths. Also, xenoliths have been previously found in Weston (Noonan *et al.*, 1976), Dimmitt, Bremervörde (Goswami *et al.*, 1984) and Pultusk (Wilkening, 1977b; Goswami *et al.*, 1984). Therefore gas-rich H chondrites appear as very probable xenolith-bearing meteorites (but it is difficult to estimate what percentage of gas-rich meteorites contain xenoliths, because we do not know in how many gas-rich meteorites xenoliths have ever been searched for).

#### 1.5.4 Relation with host meteorite shock degree

The most common classification of impact degrees for meteorites is that proposed by Stöffler *et al.* (1991) based on observation of olivine and plagioclase in transmitted light. Six progressive grades of shock are used, from S1 (unshocked) to S6 (very strongly shocked). A precedent classification scheme for shocks was described by Dodd and Jarosewich (1979). Also in this case six progressive grades of shock are proposed, and they are labelled with letters from “a” (the least shocked case) to “f” (the most shocked case).

Among the H chondrites we analyzed, excluding breccias (which clearly suffered important shocks) shock degrees are somewhat low: they range between S1 and S4, i.e. from unshocked to moderately shocked, or are “b” and “c” following the Dodd and Jarosewich (1979) classification. Limiting the analysis to non-brecciated meteorites, our results do not allow to investigate possible relations between the presence of xenoliths and host meteorite shock degree. In fact we did not find any non-brecciated meteorite that contains xenoliths. Neither literature help us in this case, because only three cases of non-brecciated meteorites bearing carbonaceous xenoliths have been reported: Sharps (Fredriksson *et al.*, 1968; Wilkening, 1977b) and Ipiranga (Rubin and Bottke, 2009), whose shock degree is S3, and Holyoke (McCall, 1973; Wilkening, 1977b) for which we did not find any shock degree determination.

### 1.6 Discussion

In order to classify the new xenoliths and microxenoliths discovered in H chondrites, we adopted a classification scheme based on the abundance of olivine, pyroxene and magnetite (Section 1.4). Among the 21 new microxenoliths, seven are magnetite-rich silicate-poor (CI-like), ten are magnetite-rich silicate-rich (CR-like), three are magnetite-poor silicate-poor (CM-like) and one is ungrouped. The three new xenoliths (size > 1 mm) are magnetite-poor silicate-rich (CM-like).

This classification highlights a fundamental result: carbonaceous chondritic xenoliths and microxenoliths are by far the most common in meteorites. Our systematic search for new xenoliths was not biased toward this particular class of objects, but different xenoliths have not been found. This is consistent with the abundance of carbonaceous chondritic particles among micrometeorites collected on Earth. Micrometeorites represents the major part of the extraterrestrial matter flux that annually enter the Earth atmosphere (Love and Brownlee, 1993). Among them, ~84% has carbonaceous chondritic properties (Genge, 2006b; Levison *et al.*, 2009).

Considering the new carbonaceous microxenoliths discovered in this work, the ratio between CR-like and CM-like microxenoliths is  $10/6 = 1.67$ . Among millimeter-sized carbonaceous xenoliths (Zolensky *et al.*, 1996b) the CR/CM

xenoliths ratio is 0.18. For microxenoliths in howardites  $CR/CM = 1.1$  (Gounelle *et al.*, 2003). Our result is clearly different from that for millimeter-sized xenoliths, and therefore reinforces the idea that carbonaceous microxenoliths are not fragments of larger objects, but rather the same objects that, once reached the Earth surface, are called micrometeorites.

A very interesting result is that all the new xenoliths and microxenoliths have been found in brecciated meteorites. On one hand, this is consistent with the history of brecciated meteorites. They are formed by collisions and impacts; in other words, by encounters between distinct bodies in interplanetary space. Therefore it is easy to imagine that there they can contain xenoliths. Conversely, one can imagine that non-brecciated meteorite parent bodies never encountered other objects in space (the only exception can be the one that caused the detachment of the observed meteorites). On the other hand, collisions and impacts also act to destroy fragile components such as carbonaceous xenoliths and microxenoliths. Indeed, of the 20 brecciated meteorites we analyzed only 6 contain xenoliths. Instead, if we consider the more restricted group of regolith breccias, also called gas-rich meteorites, we find that 5 meteorites out of 10 have xenoliths. In addition, in four of the gas-rich H chondrites where we did not find xenoliths (Weston, Dimmitt, Bremervörde and Pultusk) carbonaceous xenoliths have been previously observed. This indicates that gas-rich H chondrites are very probably xenolith-bearing meteorites. Therefore our results indicate that a long exposition to space of the host meteorites on the surface of the parent body is the key aspect to embed xenoliths.

An essential point to explain the presence of carbonaceous xenoliths in H chondrites is also the speed at which xenoliths have been embedded in their host meteorites. All our new xenoliths, and especially microxenoliths, show large amount of fine-grained, hydrous matrix, while evident shock effects or melt pockets are absent. To preserve such a structure, the embedding of xenoliths in the host meteorites must have occurred at low velocity (Gounelle *et al.*, 2003; Rubin and Bottke, 2009). As described above (Section 1.5.3) regolith breccias are formed by impacts that cause limited shock effects. This is consistent with the idea that the parent body surface is where the embedding of xenoliths more probably took place.

The scenario in which xenoliths and microxenoliths are embedded in host meteorites when these are still part of their parent bodies is also consistent with our results on host meteorites CRE ages. CRE ages are a measure of the time a meteorite spent in space as meter-sized meteoroid, i.e. after it has been removed from its parent body. If xenoliths were embedded mainly in this time period, one should expect that meteorites with the most elevated CRE ages are those that contain more xenoliths. In contrast with this hypothesis, our results show that H chondrites with low CRE ages (between 5 and 8 Myr) are the most xenolith-rich (Fig. 1.16).

## 1.7 Conclusions

In this chapter we described our systematic search for new xenoliths and microxenoliths in H chondrites. Particular attention has been dedicated to microxenoliths similar to carbonaceous chondrites, because they are the “meteorite-trapped” analogues of micrometeorites recovered on Earth. However, our research was not biased against larger or non-carbonaceous inclusions.

This work is based on the analysis of 66 polished sections from 40 meteorites present in the collection of the Laboratoire de Minéralogie et Cosmochimie du Muséum (MNHN, Paris), comprising samples with different petrologic type, CRE age, brecciated and non-brecciated meteorites and gas-rich meteorites. On the one hand, our results show that xenoliths and microxenoliths in H chondrites are not isolated oddities, even if they are not very common. Xenoliths are present in 10 out of 66 sections, corresponding to 7 out of 40 meteorites. Therefore  $\sim 17\%$  of the analyzed H chondrites hosts xenoliths. On the other hand, as all the new discovered xenoliths and microxenoliths are composed of carbonaceous chondritic material and  $\sim 80\%$  of the new discovered xenoliths are microxenoliths, our results show that carbonaceous chondritic microxenoliths are by far the most common in H chondrites.

All the new microxenoliths belong to the fine-grained hydrous group (FGH), i.e. they are dominated by a fine-grained matrix mainly composed of phyllosilicates. The larger xenoliths contain abundant chondrules or chondrule fragments of several hundreds of  $\mu\text{m}$  in size, set in a phyllosilicate fine-grained matrix: such xenoliths belong to the coarse-grained hydrous group.

The new xenoliths and microxenoliths have been classified on the basis of their directly observed properties. In particular, the abundance of olivine, pyroxene and magnetite. We associated magnetite-rich silicate-poor xenoliths with CI carbonaceous chondrites, magnetite-rich silicate-rich xenoliths with CR carbonaceous chondrites, and magnetite-poor silicate-rich xenoliths with CM carbonaceous chondrites. Among the 21 new microxenoliths, seven are magnetite-rich silicate-poor (CI-like), ten are magnetite-rich silicate-rich (CR-like), three are magnetite-poor silicate-poor (CM-like) and one is ungrouped. The three new xenoliths (size  $> 1$  mm) are magnetite-poor silicate-rich (CM-like).

We investigated possible relations between the presence of (micro) xenoliths and host meteorite properties. Xenoliths and microxenoliths are present in meteorites with petrologic type from 3 to 5. This shows that their embedding happened after alterations due to thermal metamorphism. Also, the presence of microxenoliths in H4 and H5 chondrites attests that these meteorites, probably altered by high temperatures in the interior of their parent body, have subsequently been exposed to space.

At the same time, xenoliths and microxenoliths are more abundant in meteorites with low CRE ages than in meteorites with high CRE ages. This suggests that their embedding took place during the residence onto the parent body, rather than during their transfer toward the Earth.

This is confirmed by the fact that all the new xenoliths and microxenoliths have been found in brecciated meteorites. Such a result highlights the key role of low-velocity collisions in favouring the mixing of genetically distinct material in the solar system.

A last point concerns xenoliths that have not been found. In particular, we showed that almost all the new discovered xenoliths have similarities with known groups of carbonaceous chondrites. This means that new types of xenoliths, radically different from known meteorites, and hence with parent bodies possibly different from asteroids, have not been individuated. Such a result can be explained in two ways: either sources different from asteroids (e.g. comets and trans-neptunian objects) are far less important to produce fragments that later become xenoliths, or the distinction between solar system minor body populations, asteroids on one hand, comets on the other hand, is not as sharp as believed. This problem is the object of the next chapter.

## Chapter 2

# Origin of microxenoliths in meteorites: asteroidal or cometary?

### Summary of Chapter 2

In chapter 1 we have seen that most of the xenoliths and microxenoliths we found in H chondrites have similarities with known types of carbonaceous chondrites. This holds also for the majority of xenoliths described in previous works. Such similarities suggest that both meteorites and their xenoliths come from the same class of parent bodies, namely asteroids.

In chapter 3 we will describe a particular, primordial microxenolith discovered in the Isheyev carbonaceous chondrite, having properties which make it different from other, more common xenoliths. Microxenolith PX-18 in Isheyev appears more similar to interplanetary dust particles (IDPs) and comet Wild2 grains than to carbonaceous chondrites. Indeed, chondritic porous IDPs are considered cometary samples. For micrometeorites too it has been proposed a cometary origin. Such samples attest that material in the inner solar system can originate from different parent bodies.

The issue of possible different parent bodies for microxenoliths in meteorites is the object of this chapter. Our aim is to investigate what population of micrometeoroids, between cometary and asteroidal, has the larger probability of producing microxenoliths in meteorites. The interest in doing this is that asteroids and comets are clearly distinct from a dynamical point of view. Hence, also the fragments they produce (as results of collisions or, for comets, of passages in the inner solar system) undergo different dynamical evolutions. Our goal is to understand if this initial dynamical difference result in different contributions to the inventory of microxenoliths in meteorites. We therefore evaluate, by means of numerical simulations, the ratio of asteroidal to cometary micrometeoroids that collide at low velocity with

selected targets in the asteroid main belt.

## 2.1 Introduction

In the previous chapter we described xenoliths and microxenoliths in meteorites from an experimental point of view. Different measurements have been performed to investigate the composition and structure of xenoliths and their components. We now turn our attention on the question of the microxenoliths origin, i.e. we focus on the possible sources of fragments with dimensions between a few  $\mu\text{m}$  and 1 mm. Namely, our aim is to evaluate if one of the two populations between main belt asteroids and Jupiter family comets (JFCs) is a dominant source of xenoliths (other groups of minor bodies, such as long period comets, are assumed to supply a negligible amount of micrometeoroids to the asteroid main belt, see sections 2.2 and 2.3 for details).

To reach our goal, we performed numerical simulations of the orbital evolution of micrometeoroids, choosing the appropriate initial conditions that correspond to fragments generated by main belt asteroids and JFCs, and calculating their probability to encounter selected targets in the asteroid main belt at low velocity.

Before describing the details of the problem, let us start with a brief introduction to the physics of micrometeoroids orbital evolution in the interplanetary space. The orbital motion of these small bodies is determined by the gravitational force of the Sun and the planets, the radiation pressure, and the drag due to the solar wind and the Poynting-Robertson effect. The presence of the planets causes gravitational perturbations to the keplerian motion of a micrometeoroid around the Sun. Considering the eight solar system planets, the gravitational forces on a micrometeoroid of mass  $m$  can be written:

$$\mathbf{F}_g = - \left[ \frac{GM_\odot m}{r_s^2} \right] \hat{\mathbf{r}}_s - \sum_{n=1}^8 \frac{GM_n m}{r_n^2} \hat{\mathbf{r}}_n \quad (2.1)$$

where  $\hat{\mathbf{r}}_s$  is the micrometeoroid unit position vector with respect to the Sun,  $M_\odot$  is the mass of the Sun,  $M_n$  and  $\hat{\mathbf{r}}_n$  are the mass of the  $n^{\text{th}}$  planet and the micrometeoroid unit vector with respect to that planet.

An important effect on the orbits of minor bodies due to the presence of planets is that of resonances. When orbiting at particular distances from the Sun, an object can have an orbit that corresponds to a “mean motion resonance” with a planet. This means that the ratio between their orbital periods can be expressed as a ratio between integer number (e.g. 2:1, 3:4 and so on). A second type of resonances is represented by the “secular resonances”. In this case two bodies have orbits with the same (or very close) precession. Resonances are particularly important for the orbital evolution of micrometeoroids (and in general for all minor bodies) because they act

to change orbital inclination and eccentricity. Just to give some examples, a mean motion resonance can cause the rise of eccentricity, in some cases up to the expulsion of the involved body from the solar system. Secular resonances may favour the approach of objects in the asteroid belt toward the Earth: the  $\nu_6$  secular resonance with Saturn (around 2.05 AU) can cause fragments to reach Earth-crossing orbits in  $\sim 10^6$  yr (Scholl and Froeschle, 1991).

The primary non-gravitational force acting on micrometeoroids is the radiation pressure, which is independent from the micrometeoroid velocity and can be expressed as (Gustafson, 1994)

$$\mathbf{F}_{\text{rad}} = \frac{S_0 A Q_{\text{pr}}}{c r_s^2} \hat{\mathbf{r}}_s \quad (2.2)$$

where  $S = S_0/r_s^2$  is the solar energy flux density ( $S_0$  is the energy flux at 1 AU, i.e. the ‘‘solar constant’’),  $A = \pi s^2$  is the micrometeoroid cross section,  $c$  is the speed of light,  $Q_{\text{pr}}$  is the radiation pressure coefficient. The effect of radiation pressure is easily seen by introducing the dimensionless parameter  $\beta$ , defined as the ratio of the radiation pressure force to the gravitational force. Considering for simplicity only the Sun gravity, we have:

$$\beta = \frac{S_0 A Q_{\text{pr}}}{c r_s^2} \frac{r_s^2}{GM_{\odot} m} = \frac{S_0 Q_{\text{pr}}}{c GM_{\odot}} \pi s^2 \frac{3}{4\pi s^3 \rho} \propto 1/s\rho$$

where  $s$  and  $\rho$  are the particle radius and density, respectively. This allows to write the combined effect of Sun gravity and radiation pressure as

$$\begin{aligned} \mathbf{F} &= - \left[ \frac{GM_{\odot} m}{r_s^2} \right] \hat{\mathbf{r}}_s + \frac{GM_{\odot} m}{r_s^2} \left[ \frac{r_s^2}{GM_{\odot} m} \frac{S_0 A Q_{\text{pr}}}{c r_s^2} \right] \hat{\mathbf{r}}_s = \\ &= - \left[ \frac{GM_{\odot} m}{r_s^2} \right] \hat{\mathbf{r}}_s + \frac{GM_{\odot} m}{r_s^2} \beta \hat{\mathbf{r}}_s = - \frac{G(1-\beta)M_{\odot} m}{r_s^2} \hat{\mathbf{r}}_s \end{aligned} \quad (2.3)$$

Therefore the radiation pressure is such that a micrometeoroid behaves as if it were orbiting around a central mass  $(1-\beta)M_{\odot}$ .

The last term to be considered for the micrometeoroid dynamics are the drag forces, due to Poynting-Robertson effect and solar wind. The Poynting-Robertson effect is caused by the micrometeoroid motion at speed  $\mathbf{v}$  in the Sun radiation field. This means that in the rest frame of a micrometeoroid, photons have a velocity component in a direction different from the Sun-micrometeoroid direction. Therefore, when photons hit the micrometeoroid, there is a momentum transfer in a direction perpendicular to that of the Sun gravity force. Instead, in the Sun inertial reference frame, Poynting-Robertson effect is attributed to Doppler-shift (Kortenkamp and Dermott, 1998), and it can be expressed as (Liou *et al.*, 1996)

$$\mathbf{F}_{\text{PR}} = - \frac{S A Q_{\text{pr}}}{c} \left[ \frac{\mathbf{v} \cdot \mathbf{r}_s}{c r_s} \hat{\mathbf{r}}_s + \frac{\mathbf{v}}{c} \right]. \quad (2.4)$$

As this expression has been derived also in a corpuscular formulation (Gustafson, 1994; Klacka, 1992) it can be also applied to solar wind drag, substituting the speed of solar wind particles  $\mathbf{v}_{\text{sw}}$  for the speed of light  $c$ . Combining the two expressions, drag forces can be written as

$$\mathbf{F}_{\text{drag}} = -\frac{SAQ_{\text{pr}}}{c}(1 + sw) \left[ \frac{\mathbf{v} \cdot \mathbf{r}_s}{cr_s} \hat{\mathbf{r}}_s + \frac{\mathbf{v}}{c} \right] \quad (2.5)$$

where  $sw$  represents the ratio of solar wind drag to Poynting-Robertson drag. Both Poynting-Robertson and solar wind drag act to reduce micrometeoroid semi-major axis and eccentricity. Therefore micrometeoroids approach the Sun on more and more circular orbits.

Eventually, the complete equation of motion for a spherical micrometeoroid with cross section  $A$ , velocity vector  $\mathbf{v}$  and mass  $m$  is:

$$\begin{aligned} m\dot{\mathbf{v}} = \mathbf{F}_g + \mathbf{F}_{\text{rad}} + \mathbf{F}_{\text{drag}} = & - \left[ \frac{GM_{\odot}m}{r_s^2} \right] \hat{\mathbf{r}}_s - \sum_{n=1}^8 \frac{GM_n m}{r_n^2} \hat{\mathbf{r}}_n + \\ & + \frac{SA}{c} Q_{\text{pr}} \left[ \left( 1 - (1 + sw) \frac{\mathbf{v} \cdot \mathbf{r}_s}{cr_s} \right) \hat{\mathbf{r}}_s - (1 + sw) \frac{\mathbf{v}}{c} \right]. \end{aligned} \quad (2.6)$$

Under the combined effect of gravity, radiation pressure and drag forces, the different behaviours of fragments orbiting the Sun is determined by their size and mass. The smallest particles, with mass  $\leq 10^{-13}$  g, are pushed out of the solar system by the radiation pressure. Particles with mass between  $10^{-13}$  and  $10^{-7}$  g are the most influenced by drag forces. For greater particles, with mass  $\geq 10^{-5}$  g (diameter  $\geq 100 \mu\text{m}$  for density =  $3 \text{ g/cm}^3$ ) life time is determined by a process different from the previous ones, namely collisions (Grün *et al.*, 1985; Grün *et al.*, 2004). Collisions change the size of the involved objects. The smallest fragments produced by collisions are easily pushed out of the solar system by radiation pressure. For the other ones, changing size and mass, it also changes the effect of processes described in equation 2.6 and therefore the evolution of their orbits. In Tab. 2.1 the dominant processes for meteoroid of different size at 1 AU from the Sun are indicated, along with Poynting-Robertson life-time ( $\tau_{\text{PR}}$ ) and collisional life-time ( $\tau_{\text{coll}}$ ).

In the inner solar system, bodies from sub-micrometer-sized dust grains to cm-sized meteoroids form the so-called zodiacal cloud, visible in a clear night sky as the zodiacal light. Forces described in equation 2.6 and collisions act to shape this complex of small objects. Phenomenological models for size and spatial distribution of zodiacal cloud particles have shown that  $\sim 80\%$  of the zodiacal light is due to particles in the size range  $10 - 100 \mu\text{m}$  ( $\sim 10^{-8} - 10^{-5}$  g) (Grün *et al.*, 1985). Results of a recent dynamical model confirm that particles with diameter =  $100 \mu\text{m}$  are the most abundant in the zodiacal cloud (Nesvorný *et al.*, 2010). At 1 AU, direct measurements

**Table 2.1:** Poynting-Robertson life-time ( $\tau_{\text{PR}}$ ) and collisional life-time ( $\tau_{\text{coll}}$ ) for meteoroid of different size. Data refer to 1 AU and are for a density of 3 g/cm<sup>3</sup> [after Leinert *et al.* (1983)].

Radius	Mass (g)	$\tau_{\text{PR}}$ (yr)	$\tau_{\text{coll}}$ (yr)	dominant process
<1 $\mu\text{m}$	< $10^{-11}$	–	–	radiation pressure
1 $\mu\text{m}$	$1.3 \times 10^{-11}$	$2.2 \times 10^3$	$\sim 10^7$	PR drag
10 $\mu\text{m}$	$1.3 \times 10^{-8}$	$2.1 \times 10^4$	$1.2 \times 10^6$	PR drag
100 $\mu\text{m}$	$1.3 \times 10^{-5}$	$2.1 \times 10^5$	$1.4 \times 10^5$	collisions
1 mm	$1.3 \times 10^{-2}$	$2.1 \times 10^6$	$4.1 \times 10^4$	collisions
1 cm	$1.3 \times 10^{-1}$	$2.1 \times 10^7$	$8.3 \times 10^5$	collisions

from satellite [performed by the Long Duration Exposure Facility (Love and Brownlee, 1993)] and models based on lunar cratering and measurements of the Pioneer spacecrafts (Grün *et al.*, 1985) showed that the mass distribution is dominated by particles with a diameter of 200  $\mu\text{m}$ .

However, as indicated in Tab. 2.1, micrometeoroids with size  $\gtrsim 100 \mu\text{m}$  have a life-time determined by collisions. In particular, such objects are destroyed by collisions at a rate that is about 10 times the rate at which particles of the same size are produced by collisions (Grün *et al.*, 1985). This means that larger bodies, such as asteroids and comets, represent efficient sources of micrometeoroid-sized objects, and allow to maintain the observed steady state of the zodiacal cloud.

## 2.2 Sources for micrometeorites on Earth and micrometeoroids in the inner solar system

Our aim is to evaluate which minor body group, between main belt asteroids and JFCs, dominates as source of microxenoliths in meteorites. Therefore, an estimation of the amount of matter provided by main belt asteroids and JFCs to the zodiacal cloud is necessary. Moreover, it is necessary to evaluate the orbital distribution of micrometeoroids in the asteroid main belt region. Indeed, the collision probability between micrometeoroids and selected asteroids is determined by the micrometeoroid orbital distribution and by the orbital properties of the target asteroids.

A parallel problem is that of the individuation of the micrometeorite sources. However, differences are present between the case in which the Earth is the target and the case in which asteroids are the targets. This is due to several reasons: 1) micrometeoroids can have different orbital distributions in the asteroid main belt and near the Earth; 2) Earth is far larger than asteroids, and therefore it has a far larger cross section; 3) asteroids

can have different orbital properties (e.g. larger eccentricity and inclination) with respect to Earth and this affects the collision probability with micrometeoroids.

Usually, to understand which minor body population can be the most effective in supplying micrometeoroid-sized fragments to the inner solar system, both the observed properties of the zodiacal cloud (such as particle size and spatial distribution, amount of scattered light and thermal emission) and the abundance of different types of micrometeorites (e.g. carbonaceous chondritic and ordinary chondritic particles) are used as constraints.

In particular, the relative abundance of carbonaceous and ordinary chondritic material among micrometeorites has recently been the object of two papers, Levison *et al.* (2009) and Nesvorný *et al.* (2010), that propose two different scenarios.

Carbonaceous chondritic micrometeorites represent  $\sim 84\%$  of all micrometeorites (Genge, 2006b; Levison *et al.*, 2009). This fraction is very different with respect to that of carbonaceous chondritic material among meteorites: the London Natural History Museum “Catalogue of meteorites”<sup>1</sup> lists 656 carbonaceous chondrites and 17641 ordinary chondrites, i.e. carbonaceous chondrites represent less than 4% of all chondrites. To explain such a difference between meteorites and micrometeorites, it has been proposed that meteorites principally sample the inner asteroid main belt, rich in ordinary chondritic material, while micrometeorites represent a more uniform sampling of the whole main belt (Genge *et al.*, 1997; Meibom and Clark, 1999). However, this hypothesis is not supported by results of Levison *et al.* (2009). They estimated the ratio of ordinary to carbonaceous material (O/C) in micrometeorites, assuming carbonaceous material originate from C-, D- and P-type asteroids, and ordinary material come from S-type asteroids, in proportions relative to the relative abundances of these bodies. The resulting O/C ratio is not smaller than 0.4, while it is  $\sim 0.16$  in micrometeorites. Also, they discard the possibility that micrometeorites are produced by comets, because cometary particles usually enter the Earth atmosphere with too high velocity to survive as unaltered micrometeorites (Flynn, 1995a; Levison *et al.*, 2009).

In the following sections we describe two recent papers: the first is focused on the collisional evolution of trans-neptunian objects captured in the asteroid main belt (Levison *et al.*, 2009); the second concerns the origin of micrometeoroids that compose the zodiacal cloud (Nesvorný *et al.*, 2010). Both these papers propose an explanation for the abundance of carbonaceous chondritic material among micrometeorites.

---

<sup>1</sup><http://www.nhm.ac.uk/research-curation/research/projects/metcat/>

### 2.2.1 Carbonaceous micrometeorites from trans-neptunian objects captured in the asteroid main belt

In Levison *et al.* (2009) numerical simulations have been performed in order to track the evolution of planetesimals originally formed in the trans-neptunian disk and later evolved in the inner solar system. This work is based on the so-called Nice model, which successfully explains several features of the present solar system: the present-day orbits of the giant planets (Tsiganis *et al.*, 2005), the origin of the Trojans asteroids (Morbidelli *et al.*, 2005; Nesvorný and Vokrouhlický, 2009), the Kuiper belt structure (Levison *et al.*, 2008b) and the origin and timing of the Late Heavy Bombardment (Gomes *et al.*, 2005). In particular, the Nice model assumes that the giant planets formed on nearly circular orbits with semi-major axis between 5 and 17 AU from the Sun, and that a planetesimal disk of comet-like objects with total mass 30–35 Earth masses was present beyond Neptune. The mutual gravitational interaction of the planets and the planetesimal disk caused the outward migration of the giant planets. After  $\sim 600$  Myr, Jupiter and Saturn crossed their 1:2 mean motion resonance (i.e. the configuration in which the Saturn revolution period is twice that of Jupiter) and this caused Uranus and Neptune to enter the planetesimal disk. A period of instability followed, during which the trans-neptunian, comet-like planetesimals were scattered throughout the solar system, causing the enormous amount of impacts on inner solar system bodies known as Late Heavy Bombardment.

Levison *et al.* (2009) focus their attention on trans-neptunian, comet-like planetesimals captured in the asteroid main belt after they had been scattered from their original disk. They compared the results of numerical simulations for the orbital evolution of these planetesimals with observed orbits of primitive asteroids (Trojans, Hildas and D-type asteroids<sup>2</sup>): their results successfully reproduce the distributions of orbital eccentricity and inclination.

Once captured in the asteroid main belt, the size and orbital distributions of trans-neptunian planetesimals have been affected by collisions, both among themselves and with indigenous main belt asteroids. Levison *et al.* (2009) simulated such collisional evolution of captured comet-like planetesimals along with that of indigenous main belt asteroids, assuming captured objects have a lower density ( $1 \text{ g/cm}^3$ ) than indigenous ones ( $2.7 \text{ g/cm}^3$ ). In order to reproduce the size frequency distribution of present-day Trojans, Hildas and outer-main belt asteroids (i.e. of those objects supposed to be derived from captured planetesimals) Levison *et al.* (2009) had to assume

---

<sup>2</sup>Trojans are asteroids orbiting on the same orbit of Jupiter, preceding and following it in correspondence of its L4 and L5 Lagrangian points. Hildas are asteroids with semi-major axis around 4 AU that form a dynamical family: they are close to the 2:3 mean motion resonance with Jupiter (that is, their orbital periods are 2/3 that of Jupiter). D-type asteroids have low-albedo and featureless spectra.

that the captured planetesimals are weaker than main belt asteroids. This has important implications for the delivery of micrometeorites to Earth. Indeed, in this model the disruption of captured objects produces more than 15 times more fragments per unit mass than indigenous main belt asteroids. As captured objects are assumed to have carbonaceous chondritic properties, this enormous production of fragments can explain the dominance of carbonaceous chondritic material among micrometeorites. At the same time larger meteorites produced by the disruption of captured trans-neptunian objects are rare for two reasons: the captured trans-neptunian objects reside in a region of the asteroid main belt that is unlikely to be a source of meteorites, and their weak nature implies a lower probability to survive the atmospheric passage.

### 2.2.2 Carbonaceous micrometeorites from Jupiter family comets

A scenario that favours a cometary origin for zodiacal cloud particles and carbonaceous chondritic micrometeorites is the one that proposed by Nesvorný *et al.* (2010). Their work is based on numerical simulations of the dynamical evolution of particles (with diameter between 10 and 1000  $\mu\text{m}$ ) originated from different sources. Namely, the analyzed particle sources are: 1) individual asteroid families, such as the Karin, Veritas and Beagle family; 2) the whole asteroid main belt; 3) active JFCs; 4) old dormant JFCs (i.e. comets dynamically evolved beyond the period they are supposed to be active); 5) Halley-type comets and 6) Oort cloud comets. All minor bodies in these groups can produce fragments the size of a micrometeoroid. The first fragments production mechanism, which concerns all the listed bodies, is represented by collisions. In addition, active comets are efficient producer of dust and micrometeoroid-sized fragments when they pass through the inner solar system, because of the sublimation of their volatile components. However, Nesvorný *et al.* (2010) propose that spontaneous disruption of JFCs is the main mechanism for supplying particles to the zodiacal cloud. This is possible because collisions disrupt the initial mm- and cm-sized fragments to sub-millimeter particles in  $\lesssim 10^4$  yr.

The dynamical simulations of Nesvorný *et al.* (2010) are primarily intended to reproduce observations of the zodiacal cloud made by IRAS, and hence to deduce what fraction of zodiacal cloud particles is supplied by the considered sources. The satellite IRAS observed the infrared emission of the zodiacal cloud at four different wavelengths: 12, 25, 60 and 100  $\mu\text{m}$  (Hauser *et al.*, 1984; Low *et al.*, 1984). To reproduce such observations, Nesvorný *et al.* (2010) adopted the following strategy: they defined the initial orbital distribution of particles for each source, simulated the orbital evolution of these particles (in each simulation all particles have the same size; considered particle diameters are 10, 30, 100, 200, 300 and 1000  $\mu\text{m}$ ), determined

the infrared emission corresponding to the particle final orbital distributions and modelled the detection of such emission by IRAS.

The best agreement between simulations and observations is found when three micrometeoroid sources are considered at the same time. Based on their best results, Nesvorný *et al.* (2010) propose that the zodiacal cloud is composed for  $\gtrsim 90\%$  by JFC particles, with  $\lesssim 20\%$  due to asteroidal sources and  $\lesssim 10\%$  to particles from Oort cloud comets.

Additional results of Nesvorný *et al.* (2010) include an estimation of the relative contribution of asteroids and comets to the mass influx on the Earth and an estimation of the relative abundance of carbonaceous and ordinary chondritic material among micrometeorites. The annual influx of extraterrestrial matter on Earth is dominated by JFC particles: the Earth should receive  $\sim 10^8$  kg/yr of cometary material and  $\sim 15 \times 10^6$  kg/yr of asteroidal particles, i.e. asteroidal material is  $\sim 15\%$  of the total mass influx.

The prevalence of cometary particles in the terrestrial accretion rate of micrometeoroids also implies that most micrometeorites have a cometary origin. As described in the previous section, the main problem with a cometary origin of micrometeorites is that such particles should enter the Earth atmosphere at high velocities, such that they burn in the atmosphere or are totally melted to form cosmic spherules (Flynn, 1995a; Levison *et al.*, 2009). However, Nesvorný *et al.* (2010) found that the mean entry speed for 200  $\mu\text{m}$ -diameter JFC particles is  $\approx 14.5$  km/s, only slightly higher than the value of  $\approx 12.5$  km/s calculated for asteroidal particles. Therefore they conclude that the high fraction of carbonaceous chondritic material among micrometeorites ( $\sim 84\%$ ) is due to particles coming from JFCs.

## 2.3 Origin of microxenoliths: asteroids or comets?

Carbonaceous xenoliths are the most abundant type of xenoliths observed in meteorites (Wilkening, 1977a; Meibom and Clark, 1999; Rubin and Bottke, 2009). Results presented in the previous chapter for H chondrites and study of microxenoliths in Howardites (Gounelle *et al.*, 2003) indicate this is true also for microxenoliths. Therefore, it appears that the prevalence of carbonaceous material is common to both micrometeorites and microxenoliths. We have seen in the previous section that different explanations have been proposed to account for such observation in micrometeorites.

Here we analyze the same issue focusing on the origin of microxenoliths. Our aim is to evaluate if one of the two populations between main belt asteroids and JFCs is a dominant source of microxenoliths. We choose these two populations of minor bodies because JFCs are the most important sources of zodiacal cloud particles (Nesvorný *et al.*, 2010) and we want to compare the flux of JFC micrometeoroids with that of micrometeoroids directly originated in the asteroid main belt. Also, both primitive asteroids (Levison

*et al.*, 2009) and JFCs (Nesvorný *et al.*, 2010) have been proposed as the dominant source of carbonaceous micrometeorites.

It is important to note that, if both these minor body populations can be proposed as source of carbonaceous chondritic micrometeorites, it is for their similar structural and compositional properties. Indeed, it has been suggested that asteroids and comets form a continuum population of solar system objects, rather than have sharply distinct structure and composition Campins and Swindle (1998); Lodders and Osborne (1999); Gounelle *et al.* (2006, 2008); Genge *et al.* (2008). This implies that also the distinction between asteroidal and cometary microxenoliths could be more complicated than expected. At present, two different microxenolith (or xenolith) populations, radically distinct on the basis of their structure and composition, have never been observed. However, main belt asteroids and JFCs have different dynamical properties (i.e. different orbital characteristics) that are inherited by the fragments they produce. We want to understand if such initial difference has observable consequences on microxenoliths in meteorites.

Numerical simulations have been performed in order to calculate the probability of low-speed impacts of main belt asteroid and JFC fragments on selected targets in the asteroid main belt. For targets represented by main belt asteroids, the mass influx and the relative contributions of asteroidal and JFC micrometeoroids are expected to be different from results obtained by Nesvorný *et al.* (2010) for Earth. First because, even if the zodiacal cloud is dominated by JFC micrometeoroids, main belt asteroids are, by definition, in the main belt, i.e. where asteroidal micrometeoroids originate. And

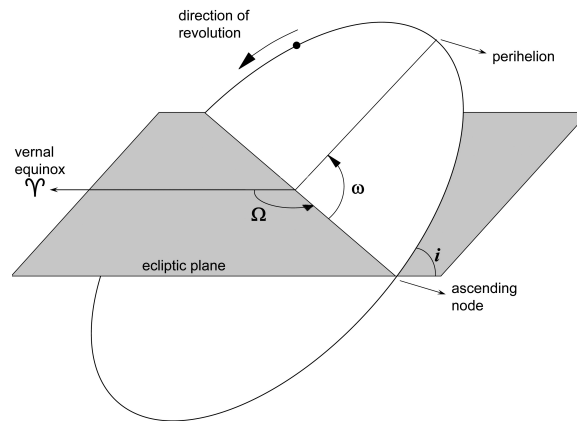


**Figure 2.1:** parameters that define an orbit. The inclination ( $i$ ) is the angle between the reference plane (in the solar system, the ecliptic plane) and the orbit plane. The argument of periastron ( $\omega$ ) is the angle, on the orbit plane, between the ascending node and the semi-major axis. The longitude of the ascending node ( $\Omega$ ) is the angle, on the ecliptic plane, between the point of the vernal equinox and the ascending node. They are indicated in the figure. The mean anomaly is defined as  $M = (2\pi/P)(t - t_0)$  where  $P$  is the orbital period and  $t$  is the time from the passage to perihelion at time  $t_0$ .

then because, as asteroids are far smaller than Earth, only a limited range of orbital parameters allows actual collisions between micrometeoroids and asteroids.

Orbital distributions for micrometeoroid-sized fragments generated by main belt asteroids and JFCs represent the initial conditions for our simulations. The parameters we need to know are those that characterize every orbit (Fig. 2.1): semi-major axis ( $a$ ), eccentricity ( $e$ ), inclination ( $i$ ), argument of periapsis ( $\omega$ ), longitude of the ascending node ( $\Omega$ ), and mean anomaly ( $M$ ). For asteroidal micrometeoroids we chose two sets of initial conditions. Both have been composed starting from asteroid orbital elements obtained from the Jet Propulsion Laboratory (JPL) Small-Body database<sup>3</sup>. The first set is composed by C-, D- and P-type asteroids (i.e., by those asteroids supposed to be composed of carbonaceous chondritic material) of any size and magnitude. S-type asteroids, the second most abundant in the asteroid main belt, are thought to be composed of ordinary chondritic material, and therefore they have not been considered in this first set. We obtained orbital elements for 310 C-, D- and P-type asteroids from the JPL Small-Body database. From these we extrapolated 1000 orbits, varying the mean anomaly  $M$ . Namely, for each original orbit, three or four more orbits have been obtained uniformly varying  $M$  over  $360^\circ$ . The second set consists of the first 1000 asteroids with a diameter  $>15$  km (from 1 Ceres to 1259 Ogyalla), chosen among all main belt asteroids without preferences for any particular type. In Fig. 2.2 the initial values of semi-major axis, eccentricity and inclination for asteroidal micrometeoroids are reported. For JFC micrometeoroids (Fig. 2.3) we used initial orbital elements for 1000 bodies that represent the steady state distribution of JFCs. This list has been compiled by D. Nesvorný (personal communication).

The orbits of the first 1000 asteroids  $>15$  km have been assumed as proxy for the steady state orbital distribution of asteroidal micrometeoroids. Instead, to obtain the steady state orbital distribution of particles from C-, D-, P-type asteroids and JFCs we performed numerical simulations of their orbital evolution, assuming density  $2 \text{ g/cm}^3$  and particle diameter  $100 \mu\text{m}$ . Numerical simulations have been performed with the `swift_rmvs3_pr` code (Nesvorný *et al.*, 2006). The code integrates the orbits of massless particles considering the forces described in equation 2.6, i.e. under the action of gravity of the Sun and seven planets (Venus to Neptune), radiation pressure, solar wind and Poynting-Robertson drag. The numerical integration of a particle orbit is stopped if that particle collide with a planet or if it is ejected from the solar system or if it drifts to within 0.04 AU (we set 0.04 AU as inferior limit to the particle distance from the Sun because at 0.04 AU the orbital period is comparable to our integration step of 0.041 yr). We set the duration of our simulations to 10 Myr, a period after which almost

---

<sup>3</sup>[http://ssd.jpl.nasa.gov/sbdb\\_query.cgi](http://ssd.jpl.nasa.gov/sbdb_query.cgi)

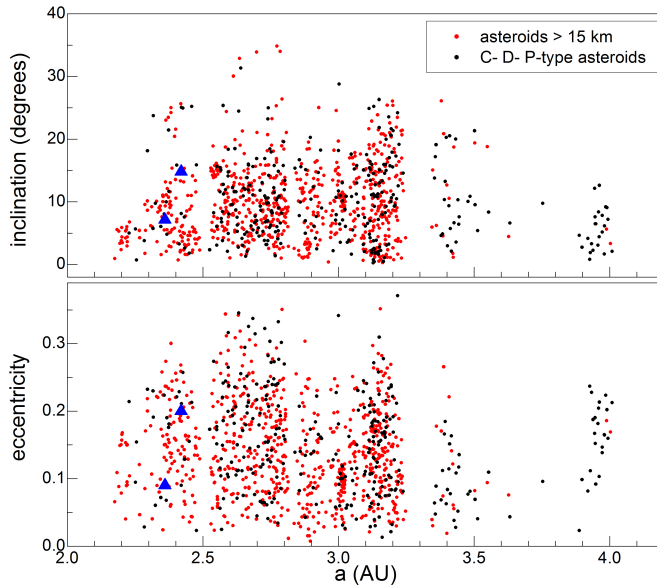


**Figure 2.2:** initial orbital inclination (top panel) and eccentricity (bottom panel) as function of semi-major axis for the two sets of micrometeoroids originated from asteroids. Vesta and Hebe inclination and eccentricity are reported as blue triangles.

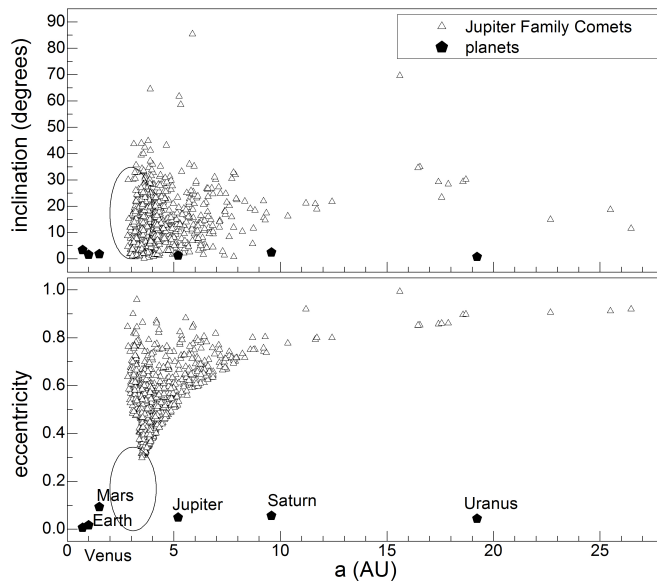


**Figure 2.3:** initial orbital inclination (top panel) and eccentricity (bottom panel) as function of semi-major axis for micrometeoroids originated from JFCs. Ellipses indicate inclination and eccentricity range for asteroidal micrometeoroids of Fig. 2.2. Inclination and eccentricity of six planets (Venus to Uranus) are reported. Neptune is beyond the right edge, at  $a = 30.1$  AU.

**Table 2.2:** orbital characteristics of asteroids 4 Vesta and 6 Hebe.

	$q$ (AU)	$Q$ (AU)	$a$ (AU)	$e$	$i$ ( $^\circ$ )	$\Omega$ ( $^\circ$ )	$\omega$ ( $^\circ$ )	$M$ ( $^\circ$ )
4 Vesta	2.15	2.57	2.36	0.09	7.13	103.9	149.8	253.5
6 Hebe	1.93	2.92	2.42	0.20	14.8	138.7	239.5	279.5

Data from the JPL Small-Body database.

$q$  = perihelion;  $Q$  = aphelion.

all the orbit integrations have been stopped. The effects of collisions are neglected in these simulations. This can be an important approximation. However, results of Nesvorný *et al.* (2010) show that IRAS observations of the zodiacal cloud are well reproduced when values  $\geq 6 \times 10^5$  yr are assumed for the collisional life time of particles. Nesvorný *et al.* (2010) conclude that such a collisional life time is long enough to allow Poynting-Robertson drag to significantly affect the orbital distribution of micrometeoroids with diameter 100  $\mu\text{m}$ .

As result of our simulations we obtain the orbital evolution of each particle, from its initial orbit to the moment when integration is stopped. Such a collection of orbits is assumed as the steady state orbital distribution of the considered set of particles. This require the assumption of a constant rate of particle production.

In order to calculate the micrometeoroid impact probability with main belt asteroids, we selected as targets the asteroids 4 Vesta and 6 Hebe. 4 Vesta is the best candidate to be the parent body of meteorites belonging to the Howardites-Eucrites-Diogenites (HED) clan (Binzel and Xu, 1993). 6 Hebe was proposed as possible parent body of H chondrites (Farinella *et al.*, 1993; Migliorini *et al.*, 1997; Gaffey and Gilbert, 1998). More recent studies have highlighted that Hebe is unlikely the parent body of H chondrites and that ordinary chondrites groups (e.g. H, L, LL chondrites) more probably derive from asteroid families (see Rubin and Bottke (2009) for a critical and detailed discussion). In particular, Rubin and Bottke (2009) suggest some asteroid families as possible H chondrite parent bodies: the Maria, Koronis, Eunomia and Flora families. Orbital inclinations and eccentricities of the four asteroids from which these families take their names are reported in Fig. 2.4, along with those of Vesta and Hebe. It is possible to see that Hebe is the asteroid with both the highest inclination and the highest eccentricity, while Koronis is that with both the lowest inclination and the lowest eccentricity. This suggest that impact probabilities and mean collision velocities could be different for Hebe and Koronis, given their different orbital parameters. However, Koronis has inclination and eccentricity more close to those of Vesta, and hence we expect minor differences between two targets as Vesta and Koronis. Therefore, we selected as targets Vesta because it is the most probable parent body of HED meteorites, and Hebe because its

orbital properties are quite different from those of Vesta. In particular both values of eccentricity and inclination differ for a factor  $\sim 2$  (see Tab. 2.2 and Fig. 2.2).

Once obtained the steady state orbital distribution of asteroidal and cometary particles, it is possible to calculate their collision probability with Vesta and Hebe, as well as their mean collision velocity. In doing this, the gravitational focusing exerted by the target asteroids has been taken into account. Hence the collision velocity is calculated as

$$v_{\text{coll}} = \sqrt{v_{\infty}^2 + v_{\text{esc}}^2}$$

where  $v_{\infty}$  is the micrometeoroid velocity on its orbit and  $v_{\text{esc}}$  is the escape velocity of the target. The value of  $v_{\infty}$  is calculated from the orbital elements obtained as results of the numerical integrations by the `swift_rmvs3_pr` code.

The probabilities of collision between micrometeoroids and target asteroids are calculated considering those orbits of micrometeoroids that intersect the target orbits. For each couple of intersecting orbits, we calculate the collision probability  $P_i$ , following the procedure described by Wetherill (1967). Indeed, orbits of micrometeoroids are known at intervals of  $10^4$  yr, because this is the interval between results of the orbital evolution simulations. Therefore, each  $P_i$  is relative to a time period of  $10^4$  yr. The total collision probability is the sum of all  $P_i$ . Eventually, we calculate the mean collision probability as the mean probability of collision for all particles present between 2 and 4 AU. This allows us to consider the mass of asteroidal and JFC micrometeoroids between 2 and 4 AU (see below for details) as calibration to calculate the mass influx on the selected targets.

The mean collision velocity for a given set of micrometeoroids is obtained as mean of collision velocities of each impact weighted with the collision probability. This means that impacts happening at a given speed have little effect on the mean collision velocity if they have a little impact probability.

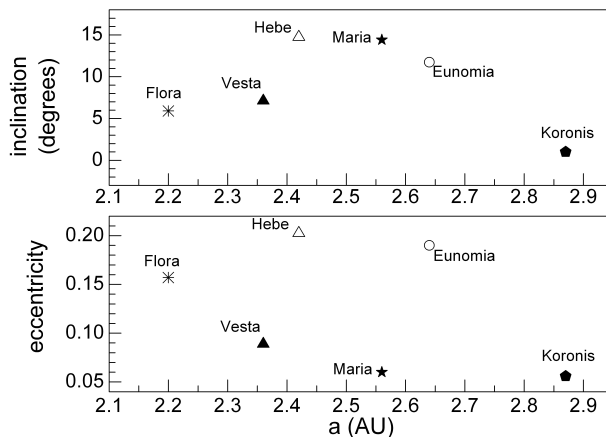


**Figure 2.4:** orbital inclination (top panel) and eccentricity (bottom panel) of the 7 asteroids cited in the text.

An essential parameter is the maximum velocity at which micrometeoroids can be embedded in asteroids without suffering significant alterations. Laboratory experiments have shown that for an impact speed of 1.8 km/s, ordinary chondritic projectiles launched in quartz sand produce intact fragments that have up to 3.7% of the projectile mass (Bland *et al.*, 2001). In these experiments, for impact speeds between 1.4 and 1.8 km/s, the largest fragments recovered have a dimension of several hundreds  $\mu\text{m}$ , i.e. those of microxenoliths. However, carbonaceous material has probably lower strength than ordinary chondritic material. Indeed, Gounelle *et al.* (2003), performing numerical simulations similar to those presented here, assumed 1 km/s as maximum velocity to avoid alterations caused by the increase of temperature and shocks. In Chappelow and Sharpton (2006) the adopted value is 1.5 km/s. A more conservative value, 300 m/s, is indicated in Rubin and Bottke (2009). It is easy to imagine that the maximum value of speed at which significant alterations are avoided strongly depends on the projectile and target properties and also on the angle of impact. As here we do not treat in detail these aspects we assume a conservative value of 1.5 km/s as threshold velocity. This means that, for the evaluation of the impact probabilities, we do not consider those micrometeoroids that collide at speed  $>1.5$  km/s. Therefore a large part of collisions is excluded from our analysis. A comprehensive study of collisions, considering the distribution of impact velocities, is planned for a future, more detailed work.

To evaluate the amount of asteroidal and JFC material that collide with the selected targets at low velocity, we use recent estimates of the mass of the zodiacal cloud. On the basis of the numerical simulations described in section 2.2, Nesvorný *et al.* (2010) propose for the total mass of the zodiacal cloud the value of  $5.2 \times 10^{19}$  g. This value is uncertain by a factor of  $\sim 2$ , because it depends on the assumed size and density of the zodiacal cloud particles. The value quoted above is for simulations that concern spherical particles with diameter 200  $\mu\text{m}$  and density 2 g/cm<sup>3</sup>. In this case Nesvorný *et al.* (2010) report that  $\sim 30\%$  of JFC particles, equivalent to  $1.6 \times 10^{19}$  g, is within 4 AU from the Sun, and that  $\sim 10\%$  ( $5.2 \times 10^{18}$  g) is within 2 AU. For asteroidal particles, the mass within 4 AU from the Sun is  $1.3 \times 10^{18}$  g, that within 2 AU  $5.3 \times 10^{17}$  g. These values are summarized

**Table 2.3:** mass (in  $10^{19}$  g) of asteroidal and JFC particles in the inner solar system. Data after Nesvorný *et al.* (2010).

	R<2 AU	R<4 AU	2<R<4 AU
JFC part.	0.52	1.6	1.08
asteroidal part.	0.053	0.13	0.077
ratio	9.8	12.3	14

R is the distance from the Sun.

in Tab. 2.3. Therefore, as calibration for the amount of mass present in the asteroid main belt, where our targets reside, we assume the values proposed by Nesvorný *et al.* (2010) for the mass between 2 and 4 AU:  $1.08 \times 10^{19}$  g are due to JFC material,  $7.7 \times 10^{17}$  g originate from asteroids. These values are obtained assuming asteroidal particles contribute by 15% to the zodiacal cloud mass. Indeed this ratio has an uncertainty of a factor  $\sim 2$ , as Nesvorný *et al.* (2010) obtain good fits to the zodiacal cloud infra-red emission considering asteroidal contributions varying between 0 and 22%.

## 2.4 Results

With the assumptions described above, we calculated the probability that asteroidal and JFC micrometeoroids collide on the target asteroids Vesta and Hebe at velocity  $< 1.5$  km/s. The results for the collision probability and for the mean impact velocity of each impactor population (asteroids with diameter  $> 15$  km, C-, D- and P-type asteroids and JFCs) are reported in Tab. 2.4. These values are preliminary results. Given the limited number of simulations we performed and the limited sets of different initial conditions we explored, we estimate our results have an uncertainty of a factor  $\sim 2$ .

**Table 2.4:** collision probabilities and mean impact velocity.

source	target	collision probability ( $\times 10^{-20}$ km $^{-2}$ yr $^{-1}$ )	mean impact speed (km/s)
D $>15$ km asteroids	Vesta	3.8	0.2
	Hebe	0.31	0.1
C-, D-, P-type asteroids	Vesta	8.7	0.2
	Hebe	0.76	0.09
JFC	Vesta	0.27	0.2
	Hebe	0.09	0.09

Asteroidal particles, either coming from the whole asteroid main belt or only from primordial asteroids, have greater collision probability than cometary particles. For Vesta the ratio between the collision probability of micrometeoroids from D $>15$  km asteroids and that of particles from JFCs is  $\sim 14$ . Micrometeoroids originated from primordial asteroids have a probability of collision with Vesta  $\sim 32$  times that of JFC micrometeoroids. In the case of Hebe, these two ratios are  $\sim 3.5$  and  $\sim 8.5$ , respectively.

Considering the zodiacal cloud mass estimations described in the previous section and the radii of Vesta and Hebe (265 km and 92.5 km, respectively; data obtained from the JPL Small Body Database) we obtain

the results reported in Tab. 2.5 for the mass of micrometeoroids impacting on Vesta and Hebe. It can be seen that Vesta is supplied with more asteroidal than cometary material. In particular, the ratio of mass coming from primordial asteroids to the mass derived from JFCs is  $\sim 2.3$ . The situation is inverted for Hebe, which receives more mass from comets than from asteroids, with a ratio of 4:1 when JFC micrometeoroids are compared to micrometeoroids originated from  $D > 15$  km asteroids.

**Table 2.5:** micrometeoroid mass influx on Vesta and Hebe.

source	target	mass influx (kg/yr)
D>15 km asteroids	Vesta	2080
	Hebe	21
C-, D-, P-type asteroids	Vesta	4720
	Hebe	50
JFC	Vesta	2070
	Hebe	84

## 2.5 Discussion

Results in Tab. 2.4 show that the mean impact speed of collisions between micrometeoroids and target asteroids are very low. We note again (as described in section 2.3) that such values are calculated without considering collisions for which the impact speed is  $> 1.5$  km/s. However, collisions selected with such a threshold happen at very low speed, always  $\leq 200$  m/s. This makes us confident that such impacts can produce microxenoliths as the unshocked microxenoliths observed in H chondrites (chapter 1) and in Howardites (Gounelle *et al.*, 2003).

Results for the micrometeoroids mass influx on target asteroids (Tab. 2.5) show that, for each source population, Vesta receives annually more mass than Hebe. The rate of mass received by Vesta is  $\sim 100$  times that for Hebe considering micrometeoroids coming from asteroids  $> 15$  km, and also when micrometeoroids originate from primitive asteroids, while it is  $\sim 25$  times that of Hebe considering JFC micrometeoroids. Such mass influx ratios are in part due to the different size of Vesta and Hebe (265 km and 92.5 km in radius, respectively). However, the ratio between their cross sections, corrected for the gravitational focusing<sup>4</sup>, can not reach values as high as 100. Therefore, the difference in the rate of micrometeoroid mass

<sup>4</sup>Assuming the target asteroid has a spherical shape, if  $S = \pi r^2$  is the asteroid cross

accreted by Vesta and Hebe is also due to their different orbital properties. Namely to the greater inclination and eccentricity of Hebe.

An interesting observation is that also studies of microxenoliths in Howardites and H chondrites show that Vesta received more micrometeoroids than the H chondrite parent body. Namely, in chapter 1 we described 21 new microxenoliths found analyzing a total H chondrite surface of  $95.2 \text{ cm}^2$ , that is  $\sim 0.2$  microxenoliths per  $\text{cm}^2$ . And Gounelle *et al.* (2003) reported the observation of 71 microxenoliths in Howardites, for a total analyzed surface of  $3.8 \text{ cm}^2$ , that is  $\sim 18.7$  microxenoliths per  $\text{cm}^2$ .

Differences between results relative to  $D > 15 \text{ km}$  asteroids and results relative to C-, D-, P-type asteroids are probably caused by their different initial orbital distributions. Because of our selection criteria for the list of 1000 asteroids with  $D > 15 \text{ km}$ , we consider very few asteroids with semi-major axis  $> 3.3 \text{ AU}$ , while primordial asteroids are abundant beyond this distance (Fig. 2.2). Further simulations will be performed in the future to investigate the dependence of our results on initial micrometeoroid orbital distributions.

The ratio between the mass influx rate from  $D > 15 \text{ km}$  asteroids and the mass influx rate from JFCs is  $\sim 1$  for Vesta. Instead, micrometeoroids originated from primordial asteroids annually supply Vesta with a mass  $\sim 2.3$  times that provided by JFC micrometeoroids. Conversely, for Hebe, the mass influx rate from JFCs is  $\sim 4$  times that from  $D > 15 \text{ km}$  asteroids, and  $\sim 1.7$  times that from C-, D- and P-type asteroids. These results suggest two different populations could be present between microxenoliths of Vesta and Hebe. However, our results are uncertain by a factor  $\sim 2$  and the same holds for the amounts of asteroidal and cometary mass in the zodiacal cloud taken from Nesvorný *et al.* (2010). Therefore, differences of a factor 2 or 4 in the micrometeoroid mass influx are not sufficient to claim for a clear domination of asteroidal microxenoliths on cometary microxenoliths, or vice versa. For the same reason, we think that mass influx rates for different target asteroids (as those belonging to the Flora, Maria, Eunomia and Koronis families) would have been similar to results presented here for Vesta and Hebe.

It is interesting to compare our results to the observed populations of carbonaceous chondritic microxenoliths (and xenoliths) in HED meteorites and H chondrites. Namely, the ratios between the mass influx rates of micrometeoroids originated from C-, D-, P-type asteroids and those coming from JFCs suggest that two groups of carbonaceous chondritic microxenoliths, “asteroidal” and “cometary”, should be observed in meteorites. However,

---

section (with  $r =$  radius of the asteroid) then the gravitational cross section is

$$S_{\text{grav}} = S \left( 1 + \frac{v_{\text{esc}}^2}{v_{\infty}^2} \right)$$

where  $v_{\text{esc}}$  is the target asteroid escape velocity and  $v_{\infty}$  is the speed of the approaching micrometeoroid.

this is not the case. Certainly, carbonaceous chondritic xenoliths and microxenoliths observed in both Howardites (Zolensky *et al.*, 1996b; Gounelle *et al.*, 2003, 2005) and in H chondrites (see chapter 1) present petrographic and mineralogical differences. Indeed, they can be subdivided in different groups, usually on the basis of similarities with carbonaceous chondrite groups. However such differences do not suggest a sharp distinction between parent bodies, as the possible difference between asteroids and comets. A possible explication is that primordial asteroids and JFCs can be bodies that share a common origin. Bodies such as D- and P-type asteroids are trans-neptunian, comet-like bodies captured and disrupted in the asteroid main belt after they have been scattered from the Kuiper belt during the Late Heavy Bombardment (Levison *et al.*, 2009). And Levison and Duncan (1997) showed that JFCs mainly derive from trans-neptunian objects scattered by planets in the inner solar system. Therefore, even if clearly distinct from a dynamical point of view, D-, P-type asteroids and JFCs would have similar structure and composition.

The interesting point here is that C-type asteroids, the most abundant in the asteroid main belt and commonly assumed as parent bodies of carbonaceous chondrites, do not derive from trans-neptunian, comet-like bodies. Rather, they are indigenous main belt asteroids. This should imply a clear difference in composition and structure with respect to D-, P-type asteroids and JFCs, difference that should be present also in xenoliths and microxenoliths. As such a clear difference is not observed, the distinction between indigenous main belt asteroids and comets, clear on a dynamical basis, it is not so sharp from a compositional and structural point of view. Instead, our results support the idea of a continuum between asteroids and comets (Campins and Swindle, 1998; Lodders and Osborne, 1999; Gounelle *et al.*, 2006, 2008; Genge *et al.*, 2008).

## 2.6 Conclusions

In this chapter we analyzed possible different sources for microxenoliths in meteorites. We performed numerical simulations to calculate the collision probability of micrometeoroids originated from asteroids and JFCs with targets represented by the two main belt asteroids Vesta and Hebe. To quantify the mass supplied to Vesta and Hebe by micrometeoroids, we used recent estimations of the zodiacal cloud mass and of the relative contributions of asteroids and JFCs to it.

Our results suggest that two groups of carbonaceous chondritic microxenoliths, “asteroidal” and “cometary”, could be present between microxenolith of Vesta and Hebe. In particular, the annual mass received by Vesta from asteroidal micrometeoroids is about twice that received from cometary micrometeoroids. Conversely, for Hebe the ratio of cometary to asteroidal

micrometeoroid mass influx rate is  $\sim 4$ . However, given the uncertainties present in our simulations, these values do not indicate a clear prevalence of asteroids or comets as source of microxenoliths. Instead, both populations of microxenoliths should be present on Vesta and Hebe.

This is somewhat in contrast with observations of microxenoliths (and xenoliths) in meteorites: two different populations, clearly distinct by their composition, structure and mineralogy, have never been observed. In most cases xenoliths and microxenoliths have similarities with known group of carbonaceous chondrites, as we have seen in chapter 1 for those found in H chondrites. Indeed, differences among microxenoliths are present, such that it is possible to classify them as CI-like, CM-like and CR-like. But such differences do not suggest these microxenoliths derive from parent bodies as different as asteroids and comets. Therefore, our results suggest that differences in structure and composition between C-type asteroids (that are indigenous main belt asteroids), D-, P-type asteroids (supposed to be trans-neptunian, comet-like bodies captured in the asteroid main belt) and comets could be less sharp than previously thought.

## Chapter 3

# A primordial xenolith in the Isheyevu carbonaceous chondrite

### Foreword

Text and figures of this chapter have been published as a paper in the Proceedings of the National Academy of Science. The complete reference is:

Briani G., Gounelle M., Marrocchi Y., Mostefaoui S., Leroux H., Quirico E. and Meibom A.

“Pristine extraterrestrial material with unprecedented nitrogen isotopic variation”

PNAS, volume 106 (no. 26), 10522-10527, 2009.

### Abstract

Pristine meteoritic materials carry light element isotopic fractionations that constrain physiochemical conditions during solar system formation. Here we report the discovery of a unique xenolith in the metal-rich chondrite Isheyevu. Its fine-grained, highly pristine mineralogy has similarity with interplanetary dust particles (IDPs), but the volume of the xenolith is more than 30,000 times that of a typical IDP. Furthermore, an extreme continuum of N isotopic variation is present in this xenolith: from very light N isotopic composition ( $\delta^{15}\text{N}_{\text{AIR}} = -310 \pm 20\%$ ), similar to that inferred for the solar nebula, to the heaviest ratios measured in any solar system material ( $\delta^{15}\text{N}_{\text{AIR}} = 4900 \pm 300\%$ ). At the same time, its hydrogen and carbon isotopic compositions exhibit very little variation. This object poses serious challenges for existing models for the origin of light element isotopic anomalies.

### 3.1 Introduction

Physical and chemical conditions during the earliest stages of Solar System evolution can be studied in chondritic meteorites and Interplanetary Dust Particles (IDPs), believed to be among the most primordial objects left over from the formation of the Solar System some 4.567 billion years ago (Bouvier *et al.*, 2007). In this work we describe the unaltered mineralogy and light element (i.e. hydrogen, carbon and nitrogen) isotopic composition of a primordial xenolith in the chondrite Isheyevo. Isheyevo is a Fe-Ni metal rich (60 vol% on average) chondrite with two dominant lithologies that resemble CB and CH chondritic material (Ivanova *et al.*, 2008). Apart from Fe-Ni metal grains, this rock is composed of chondrules, rare Ca-Al rich inclusions (CAIs) and hydrated lithic clasts, but does not otherwise contain fine-grained matrix, which separates high-temperature components in most other types of chondritic materials (Ivanova *et al.*, 2008; Krot *et al.*, 2007; Bonal *et al.*, 2008). In a survey of two polished sections of Isheyevo (the CH lithology), representing a total area of about 400 mm<sup>2</sup>, we identified more than 100 lithic clasts. Their mineralogy has been studied by Energy Dispersive X-ray (EDX) spectroscopy, Analytical Electron Microprobe (AEM), Scanning Electron Microscope (SEM) and Transmission Electron Microscope (TEM). In general, these lithic clasts show a high degree of aqueous alteration, consistent with previous reports (Krot *et al.*, 2007; Bonal *et al.*, 2008). This indicates that they are not genetically related to the high-temperature components in Isheyevo, which do not show effects of in situ aqueous alteration (Krot *et al.*, 2007; Bonal *et al.*, 2008). Lithic clasts found in our two sections range in size between 50 and 750  $\mu\text{m}$ . Their mineralogical properties are broadly similar to matrix material of CI, CM or CR carbonaceous chondrites, i.e. dominated by a fine-grained matrix composed of sub- $\mu\text{m}$ -size phases, mainly phyllosilicates with variable amount of Fe-Ni sulfides and magnetite. Matrix AEM point analyses show high contents of S (between 2 and 15 wt%), due to the presence of either tochilinite and/or Fe-Ni sulfides. Anhydrous silicates such as olivine and pyroxene, present either as isolated crystals in the matrix or as microchondrules ( $\sim 30\text{-}60$   $\mu\text{m}$  in diameter), are less abundant. Olivine is mainly Mg-rich, with compositions ranging from Fo<sub>98</sub> and Fo<sub>84</sub>, with a mean value of Fo<sub>89</sub> [Fo is defined as the mol% ratio Mg/(Mg+Fe)]. Pyroxene ranges in composition between En<sub>63-98</sub> Wo<sub>0-4</sub> Fs<sub>1-36</sub> [En = Mg/(Mg+Fe+Ca) mol%; Wo = Ca/(Mg+Fe+Ca) mol%; Fs = Fe/(Mg+Fe+Ca)]. Magnetite is very abundant in some lithic clasts, and absent in others. Carbonates are rare, but have been identified in some cases. Sulfide grains are mostly pyrrhotite, with some rare grains of pentlandite. Metal is present as small,  $\mu\text{m}$ -sized grains associated with sulfides. Among the  $\sim 100$  lithic clasts studied here, one stood out by its distinct textural and mineralogical properties and for its extreme variation in N isotopic composition. We describe here the discov-

ery of this primordial xenolith (hereafter named PX-18) and the implications concerning models for light element fractionation.

### 3.2 PX18: mineralogy

PX-18 is a dark xenolith ( $\sim 380 \times 470 \mu\text{m}^2$ ) dominated by a very fine-grained matrix, mainly composed of anhydrous Mg-rich silicates, with tiny Fe-Ni sulfides grains and magnetite (Fig. 3.1A). High resolution SEM images and EDX spectral analyses revealed a matrix composed of sub- $\mu\text{m}$ -sized crystals, including Mg-rich olivine and pyroxene crystals ( $\text{Fo}_{84-89}$ ;  $\text{En}_{89-95}$   $\text{Wo}_{0-4}$ ) with sizes of about 1-2  $\mu\text{m}$ , Fe-Ni metal grains, magnetite and very rare carbonates grains. TEM examination confirmed that PX-18 matrix is primarily composed of crystalline, anhydrous silicate grains, mainly Mg-rich pyroxene, with a few,  $\mu\text{m}$ -sized, forsterite ( $\text{Fo}_{97-99}$  grains (Fig. 3.1B).

Low-Ca pyroxene grains show a wide compositional range ( $\text{En}_{63-100}$ ,  $\text{Wo}_{0-5}$ ) but enstatite clearly dominates (36% of analyzed grains has  $\text{En}_{99-100}$ ). The most fine-grained phase (labelled “mx” in Fig. 3.1B) contains abundant Fa-rich olivine (grain size 20-100 nm) with compositions ranging from  $\text{Fo}_{24}$  to  $\text{Fo}_{70}$ , and an average around  $\text{Fo}_{40}$ . Small Fe-Ni metal and Fe-oxide grains are present as minor components between silicates. Importantly, high resolution TEM observations did not yield any occurrence of layered phyllosilicates, which seem to be absent from PX-18. These observations indicate that PX-18 is mineralogically similar to other primitive material, such as chondritic porous IDPs (Bradley, 2003) and comet 81P/Wild2 samples returned by the Stardust mission (Zolensky *et al.*, 2006). Clearly, PX-18 has avoided the extensive aqueous alteration that affected the other xenoliths in Isheyevo (Ivanova *et al.*, 2008) and therefore represents a more pristine sample, which might have better preserved isotopic anomalies of light elements.

### 3.3 PX18: isotopic composition

We performed isotopic composition analyses of PX-18 and four other xenoliths, covering a total area of 30400  $\mu\text{m}^2$ . The isotopic ratios D/H,  $^{13}\text{C}/^{12}\text{C}$  and  $^{15}\text{N}/^{14}\text{N}$  were imaged by multi-collection secondary ion mass spectrometry, using a CAMECA NanoSIMS N50. We report our results in the  $\delta$ -notation, which expresses the deviation in parts per thousand from terrestrial standards (i.e. the SMOW value for the D/H ratio, the atmospheric  $^{15}\text{N}/^{14}\text{N}$  ratio for N and the PDB value for  $^{13}\text{C}/^{12}\text{C}$ ). NanoSIMS imaging of the H isotopic composition in the five xenoliths yielded homogeneous distributions with average  $\delta\text{D}_{\text{SMOW}}$  values ranging between  $-70 \pm 20\text{‰}$  and  $420 \pm 50\text{‰}$ . In other words, the bulk D/H ratios obtained are generally higher than the SMOW value, but no extreme D/H ratios were observed,

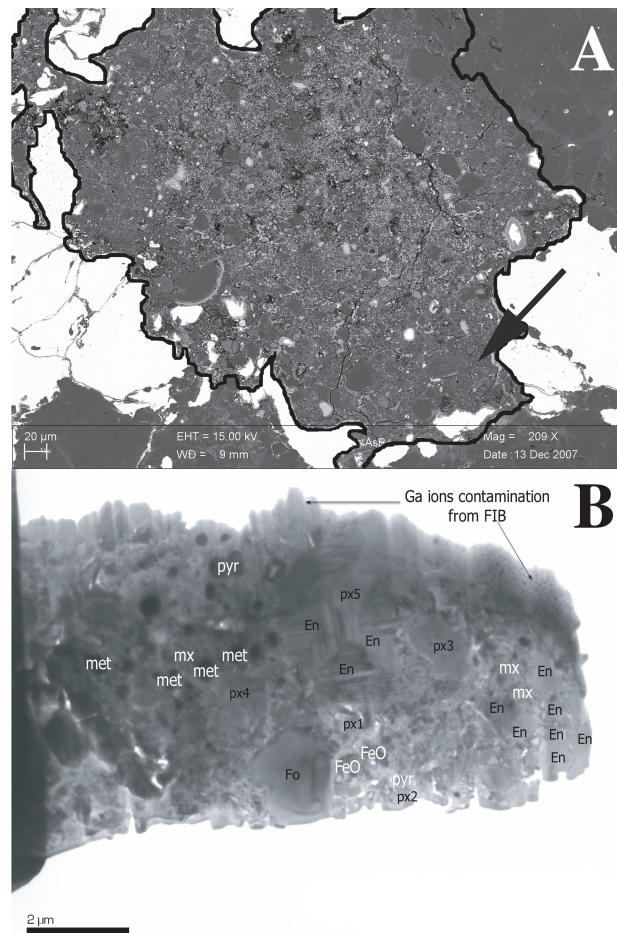


**Figure 3.1:** PX-18 in the Isheyevo chondrite. (A) High resolution SEM image. The minimum and maximum dimensions of PX-18 are  $380 \mu\text{m}$  and  $470 \mu\text{m}$  respectively. This xenolith is clearly dominated by matrix, but some large olivine and pyroxene grains are also visible. White inclusions are metal grains. The black arrow indicates the point from which the TEM thin section showed in (B) has been extracted. (B) TEM bright-field micrograph of a thin section extracted by focused ion beam (FIB) technique from PX-18 in Isheyevo. Individual analyses made by TEM are reported in the figure. A large olivine grain ( $\text{Fo}_{100}$ ) is visible at the bottom of the section. En labels indicate pyroxene grains with  $\text{En}_{98-100}$ . The other pyroxene grains analyzed are: px1 ( $\text{En}_{87} - \text{Wo}_1$ ); px2 ( $\text{En}_{91} - \text{Wo}_1$ ); px3 ( $\text{En}_{63} - \text{Wo}_1$ ); px4 ( $\text{En}_{95} - \text{Wo}_1$ ); px5 ( $\text{En}_{93} - \text{Wo}_1$ ). Fe-Ni metal grains (met) are visible in the left part of the section. Two grains of pyrrhotite are also present (pyr). Labels mx indicate a very fine-grained matrix, composed of tiny crystals and minor amorphous material, with average composition frequently close to olivine  $\text{Fo}_{60}$ .

neither in bulk nor as individual hotspots, compared to previous studies of IDPs Floss *et al.* (2006) and insoluble organic matter (IOM) extracted from primitive chondritic meteorites Busemann *et al.* (2006). Carbon isotopic compositions were also found to be relatively homogeneous within individual xenoliths with values ranging from  $\delta^{13}\text{C}_{\text{PDB}} = -35 \pm 3\%$  to  $-17 \pm 2.5\%$ ,

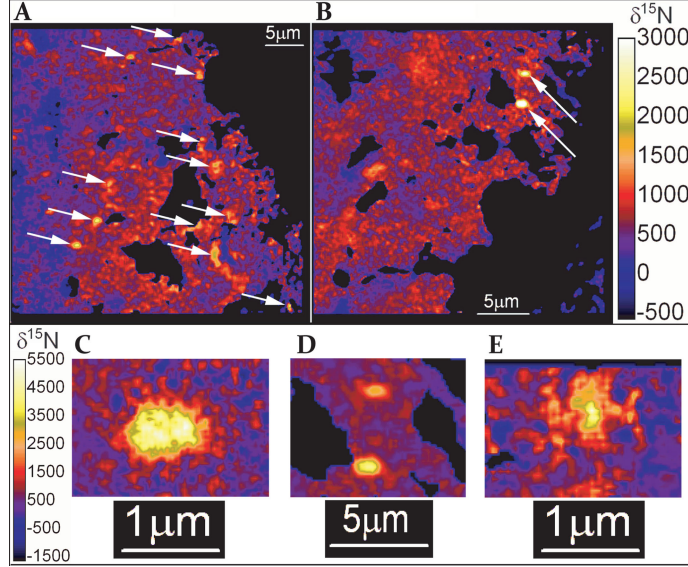
**Isotopic measurements for eight 40×40- $\mu\text{m}^2$  images from PX-18.**

Image name	Area ( $\mu\text{m}^2$ )	Average $\delta^{15}\text{N}_{\text{AIR}}$ (‰)	$\delta^{15}\text{N}_{\text{AIR}} > 250\text{‰}$ (% area)	$\delta^{15}\text{N}_{\text{AIR}} < 0\text{‰}$ (% area)	Number of hotspots
g_31	394.6	140 $\pm$ 13	34.26	27.42	3
g_32	541.2	630 $\pm$ 20	92.63	1.05	10
g_33	507.6	700 $\pm$ 17	95.76	0.79	2
g_41	1218.9	220 $\pm$ 9	35.89	29.95	7
g_42	1082.9	640 $\pm$ 11	89.67	1.45	16
g_48	888.6	110 $\pm$ 20	23.48	43.18	7
g_49	601.4	30 $\pm$ 22	28.78	52.63	0
g_53	995.8	80 $\pm$ 17	28.26	46.67	1

**Table 3.1:** The column labelled “Area” reports the fraction of each ratio image that has a number of  $^{14}\text{N}$  counts at least equal to 5% of the  $^{14}\text{N}$ -image maximum. Average  $\delta^{15}\text{N}_{\text{AIR}}$  values are evaluated only on these image portions. These same regions also define for each image the basic area to which percentages of  $\delta^{15}\text{N}_{\text{AIR}} > 250\text{‰}$  and  $\delta^{15}\text{N}_{\text{AIR}} < 0\text{‰}$  refer.

comparable to bulk C isotopic composition of chondritic meteorites (Pearson *et al.*, 2006) and IOM (Alexander *et al.*, 2007). The N isotopic compositions yielded a dramatically different data set. For all five xenoliths, systematic bulk enrichments in  $^{15}\text{N}$  were observed, with  $\delta^{15}\text{N}_{\text{AIR}}$  ranging from  $110 \pm 10\text{‰}$  to  $318 \pm 16\text{‰}$ . Even larger N isotopic anomalies were found in the mineralogically primitive PX-18. The main characteristics of the N isotopic distribution in PX-18 are: 1) large areas with a diffuse, but substantial enrichment in  $^{15}\text{N}$  over the surrounding material (Fig. 3.2A); 2) extremely  $^{15}\text{N}$ -enriched, localized anomalies (hereafter called hotspots, Fig. 3.2B); 3) areas with negative  $\delta^{15}\text{N}_{\text{AIR}}$  values, comparable to those of the solar nebula (11-13). A total of 13 NanoSIMS images were obtained from PX-18, covering an area of  $\sim 12800 \mu\text{m}^2$ . These images have average  $\delta^{15}\text{N}_{\text{AIR}}$  values that range between  $30 \pm 20\text{‰}$  and  $700 \pm 20\text{‰}$ , indicating a highly heterogeneous distribution of the  $^{15}\text{N}/^{14}\text{N}$  ratio in PX-18 (Table 3.1). In three images obtained on PX-18 (each  $40 \times 40 \mu\text{m}^2$ ) more than 90% of the surface is characterized by  $\delta^{15}\text{N}_{\text{AIR}} \geq 250\text{‰}$  and very elevated average  $\delta^{15}\text{N}_{\text{AIR}}$  values ( $630 \pm 20\text{‰}$ ,  $640 \pm 11\text{‰}$  and  $700 \pm 17\text{‰}$ ). These high values are not due to the presence of only a few small anomalously  $^{15}\text{N}$ -rich regions, but rather to the occurrence of a diffuse  $^{15}\text{N}$ -rich component, present in large fractions of the images (Fig. 3.2A; Table 3.1). This is demonstrated by the frequency distribution of  $\delta^{15}\text{N}_{\text{AIR}}$  values obtained from a grid of  $600 \times 600 \text{ nm}^2$  squares laid over each  $\delta^{15}\text{N}_{\text{AIR}}$  image. The resulting frequency distributions (Fig. 3.3) clearly show continuous and broad ranges of  $\delta^{15}\text{N}_{\text{AIR}}$  values, centered on the  $\delta^{15}\text{N}_{\text{AIR}}$  average value obtained for each image.

In addition to the diffuse distribution of  $^{15}\text{N}$ -enriched material, forty-six  $^{15}\text{N}$  hotspots with extremely high  $\delta^{15}\text{N}_{\text{AIR}}$  were observed in PX-18 (Fig. 3.2B). These hotspots, with areas of  $\sim 1 \mu\text{m}^2$ , are distinct from the afore-



**Figure 3.2:** Results of NanoSIMS measurements on PX-18: the  $\delta^{15}\text{N}_{\text{AIR}}$  distribution of two  $40 \times 40 \mu\text{m}^2$  regions (A, B) and hotspots with internal structures (C, D, E). Color scale has been changed for images C to E in order to better show internal structures of hotspots. In all the images, the black areas are regions in which precise isotopic ratios could not be determined. These pixels have therefore been removed from each image. (A) Region with average  $\delta^{15}\text{N}_{\text{AIR}} = 640 \pm 11\text{‰}$ . About 90% of this image is characterized  $\delta^{15}\text{N}_{\text{AIR}} \geq 250\text{‰}$  (Table 3.1). Several hotspots are also visible (indicated by white arrows). (B) Area with average  $\delta^{15}\text{N}_{\text{AIR}} = 700 \pm 17\text{‰}$ . Two hotspots, approaching  $\delta^{15}\text{N}_{\text{AIR}} = 4000\text{‰}$ , are indicated by arrows. (C) The hotspot is  $0.598 \mu\text{m}^2$  ( $\sim 773 \times 773 \text{ nm}^2$ ) in size and has  $\delta^{15}\text{N}_{\text{AIR}} = 3200 \pm 150\text{‰}$ . The yellow internal region has a surface of  $0.251 \mu\text{m}^2$  ( $\sim 500 \times 500 \text{ nm}^2$ ) and  $\delta^{15}\text{N}_{\text{AIR}} = 4110 \pm 200\text{‰}$ .  $^{15}\text{N}$ -richer, white areas are visible. They have  $\delta^{15}\text{N}_{\text{AIR}} = 4900 \pm 300\text{‰}$ , and a total surface of  $0.0967 \mu\text{m}^2$  ( $\sim 310 \times 310 \text{ nm}^2$ ). This is the only case in which is possible to define two internal structures in the same hotspot. (D) For the larger isotopic anomaly ( $1.29 \mu\text{m}^2$ ,  $\delta^{15}\text{N}_{\text{AIR}} = 2600 \pm 170\text{‰}$ ) an internal hotspot corresponding to the yellow region can be defined, with  $\delta^{15}\text{N}_{\text{AIR}} = 3700 \pm 300\text{‰}$  and a surface of  $0.467 \mu\text{m}^2$  ( $\sim 683 \times 683 \text{ nm}^2$ ). For the smaller isotopic anomaly ( $1.1 \mu\text{m}^2$ ,  $\delta^{15}\text{N}_{\text{AIR}} = 1700 \pm 110\text{‰}$ ), the internal hotspot has an area of  $0.124 \mu\text{m}^2$  ( $\sim 352 \times 352 \text{ nm}^2$ ), with  $\delta^{15}\text{N}_{\text{AIR}} = 3000 \pm 300\text{‰}$ . (E) Again, the yellow region represents the internal hotspot, corresponding to  $\delta^{15}\text{N}_{\text{AIR}} = 3100 \pm 470\text{‰}$  with a surface of  $0.079 \mu\text{m}^2$  ( $\sim 280 \times 280 \text{ nm}^2$ ) [for the entire hotspot the size is  $0.896 \mu\text{m}^2$  ( $\sim 946 \times 946 \text{ nm}^2$ ) and  $\delta^{15}\text{N}_{\text{AIR}} = 1800 \pm 160\text{‰}$ ].

mentioned, broad  $^{15}\text{N}$ -enriched zones, because their  $\delta^{15}\text{N}_{\text{AIR}}$  values minus a  $3\sigma$  error bar (where  $\sigma$  is the error on the hotspot  $\delta^{15}\text{N}_{\text{AIR}}$  value) are higher than the average  $\delta^{15}\text{N}_{\text{AIR}}$  value for the image plus  $3\sigma_{\text{av}}$  (where  $\sigma_{\text{av}}$  is the error on the average  $\delta^{15}\text{N}_{\text{AIR}}$  value of the entire image). These hotspots are highly heterogeneously distributed. For example, one NanoSIMS image ( $40 \times 40 \mu\text{m}^2$ ) contains no hotspots, while other areas in PX-18 of similar size have between 2 and 10 hotspots, and one image contains as much as 16 hotspots (Table 3.1). All the  $^{15}\text{N}$  hotspots have sizes larger than  $300 \times 300 \text{ nm}^2$ , up to  $\sim 2 \times 2 \mu\text{m}^2$ . The highest  $\delta^{15}\text{N}_{\text{AIR}}$  for a single hotspot is  $3200 \pm$

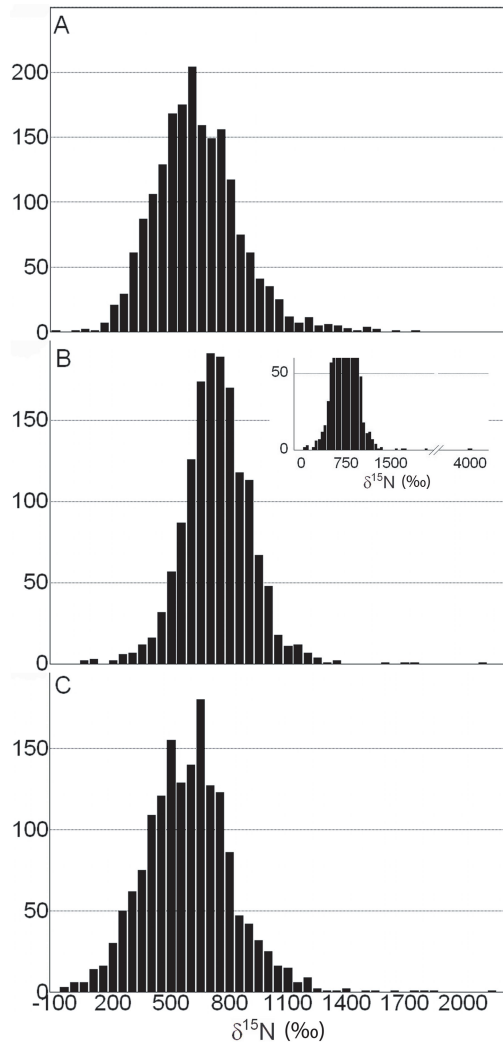


**Figure 3.3:** Frequency distribution for  $\delta^{15}\text{N}_{\text{AIR}}$  values of three  $40 \pm 40 \mu\text{m}^2$  images from PX-18. These distributions are obtained from a grid of  $600 \times 600 \text{ nm}^2$  regions of interest (ROIs) laid over each NanoSIMS image in areas for which  $^{12}\text{C}^{14}\text{N}$  signal was at least 5% of the image maximum. See Table 3.1 for average values of each image. Vertical scale is the number of square ROIs in each  $\delta^{15}\text{N}$  bin. The right-hand tails of these distributions are due to hotspots, but the correspondence between ROIs and hotspots is only partial, because the randomly distributed,  $600 \times 600 \text{ nm}^2$  ROIs do not exactly match hotspots. (A) Image g\_32, the distribution is obtained from a total surface of  $410.45 \mu\text{m}^2$ . (B) Image g\_33, the distribution is obtained from a total surface of  $325.5 \mu\text{m}^2$ . The distribution also contains a hotspot at  $\delta^{15}\text{N}_{\text{AIR}} = 3900\text{‰}$  (visible in the inset). (C) Image g\_42, the distribution is obtained from a total surface of  $639.45 \mu\text{m}^2$ .

150‰.

However, several hotspots exhibit distinct internal structures, i.e. small internal regions with even higher values of  $\delta^{15}\text{N}_{\text{AIR}}$ . Four such cases have been identified (Fig. 3.2C, 3.2D, 3.2E), in which the averages  $\delta^{15}\text{N}_{\text{AIR}}$  values for each hotspot are  $1700 \pm 110\text{‰}$ ,  $1800 \pm 160\text{‰}$ ,  $2600 \pm 170\text{‰}$  and  $3200 \pm 150\text{‰}$ , and in which there are sub-regions with higher  $\delta^{15}\text{N}_{\text{AIR}}$  values of  $3000 \pm 300\text{‰}$ ,  $3100 \pm 500\text{‰}$ ,  $3700 \pm 300\text{‰}$  and  $4900 \pm 300\text{‰}$  respectively. These hotspot sub-regions are the highest  $\delta^{15}\text{N}_{\text{AIR}}$  values ever measured in Solar System material:  $3700 \pm 300\text{‰}$  and  $4900 \pm 300\text{‰}$  (Fig. 3.4).

We stress here that these are results obtained by *in situ* measurements, and hence they represent an isotopic composition that is a mix of the  $^{15}\text{N}$ -rich phase with other,  $^{15}\text{N}$ -poor phases. This implies that our highest  $\delta^{15}\text{N}_{\text{AIR}}$  values are a lower limit for the  $^{15}\text{N}$  enrichment in the carrier phase.

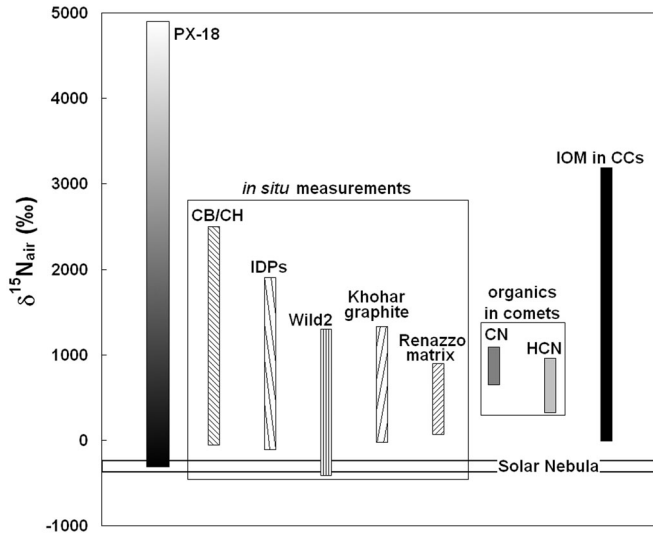


**Figure 3.4:**  $\delta^{15}\text{N}_{\text{AIR}}$  values measured in PX-18, compared with other data for Solar System materials. Ranges reported in the figure comprise results from bulk measurements as well as from hotspots. The mean  $\delta^{15}\text{N}_{\text{AIR}}$  for the whole PX-18 is  $318 \pm 16\text{‰}$ . Bulk  $\delta^{15}\text{N}_{\text{AIR}}$  values for the other materials reported in the figure range between  $-52.5\text{‰}$  and  $2500\text{‰}$  for CB/CH chondrites (31-33), between  $-108 \pm 9\text{‰}$  and  $500 \pm 20\text{‰}$  for IDPs (7), between  $-54\text{‰}$  and  $452\text{‰}$  for Wild2 samples [more negative values are due to the presence of  $^{15}\text{N}$ -poor,  $^{13}\text{C}$ -rich hotspots (34)] and between  $-66 \pm 3\text{‰}$  and  $415 \pm 2\text{‰}$  for IOM extracted from carbonaceous chondrites (8, 10). The in situ measurements, and those on IOM, have been obtained by SIMS techniques. Stepped combustion has been performed for CB/CH chondrites. For HCN molecules in comets, astronomical spectroscopy measurements (35) yielded values of  $\delta^{15}\text{N}_{\text{AIR}} = 330 \pm 450\text{‰}$  (for comet Hale-Bopp) and  $960 \pm 370\text{‰}$  (for comet 17P/Holmes). For CN molecules in comets,  $\delta^{15}\text{N}_{\text{AIR}}$  values range between  $650 \pm 400\text{‰}$  and  $1100 \pm 450\text{‰}$  (35, 36). The values of the N isotopic composition for the solar nebula are obtained from measures on: 1) ammonia in the Jupiter atmosphere analysed by the Galileo spacecraft [ $\delta^{15}\text{N}_{\text{AIR}} = 370 \pm 80\text{‰}$ , (13)]; 2) solar wind N implanted in lunar regolith grains [ $\delta^{15}\text{N}_{\text{AIR}} \leq 240\text{‰}$ , (12)]; 3) an osbornite (TiN) inclusion in a CAI of Isheyevo [ $\delta^{15}\text{N}_{\text{AIR}} = 359 \pm 5\text{‰}$ , (11)].

Regions with negative  $\delta^{15}\text{N}_{\text{AIR}}$  values have been also identified in PX-18. In some case they represent up to 52% of the analysed surface (Table 3.1). The global mean  $\delta^{15}\text{N}_{\text{AIR}}$  value evaluated from all the image fractions with negative  $\delta^{15}\text{N}_{\text{AIR}}$  is  $-150 \pm 30\text{‰}$ , and the minimum value measured for a single image is  $\delta^{15}\text{N}_{\text{AIR}} = -310 \pm 20\text{‰}$  (Fig. 3.4). This latter value is consistent with values inferred for the solar nebula (11-13) from previous measurements (see Fig. 3.4 for details). The large range of  $\delta^{15}\text{N}_{\text{AIR}}$  values observed in PX-18 from Isheyevo (Fig. 3.4) greatly expands the range of N isotopic composition for a single extraterrestrial object or type of material (e.g. IOM). On one hand, the heaviest N isotopic compositions observed ( $\delta^{15}\text{N}_{\text{AIR}} = 3700 \pm 300\text{‰}$  and  $4900 \pm 300\text{‰}$ ) are enriched in  $^{15}\text{N}$  by factors of 4.7 and 5.7, respectively, compared to terrestrial atmospheric N and even more (factors of 7.3 and 9.1, respectively) when compared to the best

estimate for the N isotopic composition of the solar nebula Meibom *et al.* (2007). On the other hand, negative  $\delta^{15}\text{N}_{\text{AIR}}$  values ( $\delta^{15}\text{N}_{\text{AIR}} = -310 \pm 20\%$ ) similar to those of the solar nebula and corresponding to the lowest observed values, have also been measured. This, combined with PX-18 unique mineralogy, is consistent with the notion that only the most pristine, unaltered material can preserve primordial isotopic compositions in light elements.

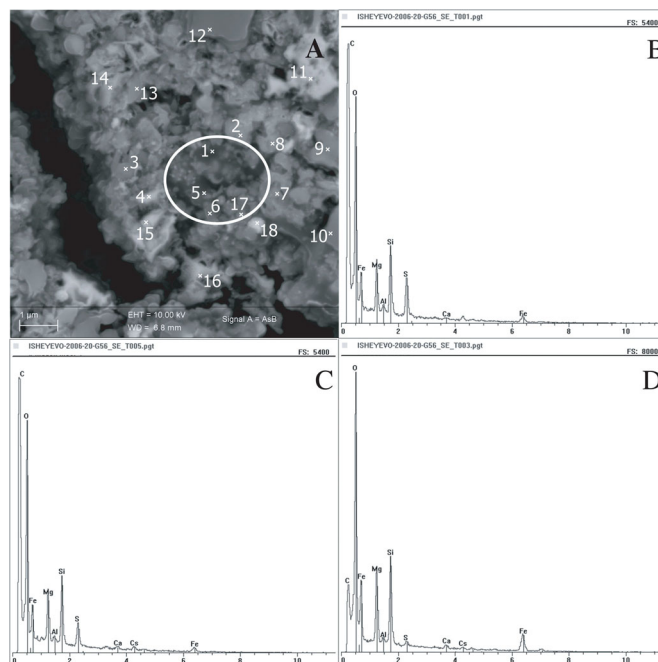


**Figure 3.5:** (A) High-resolution SEM image of a PX-18 matrix area corresponding to one hotspot, indicated by the green ellipse. Red crosses labelled with numbers are the points analysed by EDX spectroscopy. (B, C) EDX spectra of points number 1 and 5 respectively. The first peak on the left is that of carbon, clearly evident in these two spectra. (D) EDX spectrum of point number 3. In this case the C peak is smaller, corresponding to the background signal due to the section carbon coating.

### 3.4 The carrier phase of the N anomalies

To verify whether  $^{15}\text{N}$  hotspots in PX-18 are associated with specific carriers it is possible to exploit the high spatial resolution of the NanoSIMS images (100 - 200 nm). By comparing NanoSIMS images with high resolution SEM images (Fig. S1), the site of the  $^{15}\text{N}$  hotspots in PX-18 were located in the matrix and studied in more detail. Several important observations were made: i) hotspots have linear dimensions substantially larger than the size of typical matrix grains (see Fig. 3.5 for an example), ii) typically, hotspot regions contain abundant, sub- $\mu\text{m}$ -sized grains of Mg-rich

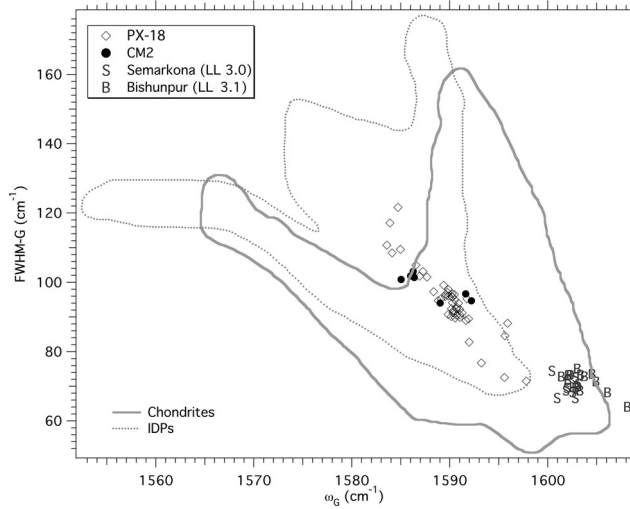


**Figure 3.6:** G-diagram for results of Raman analyses on PX-18: the spectral parameter FWHM-G plotted against the peak position  $\omega_G$ . This diagram reflects the degree of thermal metamorphism and structural order of the organic matter. The solid and dashed lines show the range of values for chondritic meteorites and IDPs respectively (Sandford *et al.*, 2006). CM measurements were obtained from matrix of Murchison (CM2) and Cold Bokkeveld (CM2).

pyroxene and magnetite, iii) EDX spectra of hotspot regions show a general enrichment in C with respect to spectra obtained in other regions of PX-18 (Fig. 3.5).

Presolar SiC grains or nanoglobules (Nakamura-Messenger *et al.*, 2006) can be excluded as the carrier phase of the N isotopic anomalies because a) they generally have smaller size than the diffuse  $^{15}\text{N}$  enrichments observed here, b) if  $^{15}\text{N}$  hotspots were due to presolar grains or nanoglobules, they would be identified in high resolution SEM images at the hotspots locations (or in TEM observations) c) organic nanoglobules have D enrichments (Nakamura-Messenger *et al.*, 2006), not measured in PX-18 and d) most SiC grains carry with them large anomalies in C, which are not observed (Nittler, 2003). Together, these observations lead to the conclusion that  $^{15}\text{N}$  hotspots in PX-18 are due to the presence of organic matter (OM). The spatial extension of  $^{15}\text{N}$ -rich regions in PX-18 suggests the presence of a diffuse component as carrier of these anomalies. Indeed, macromolecular OM has been identified in PX-18 by Raman spectroscopy. PX-18 was analyzed together with matrix fragments extracted from pristine chondrites that were used as standards: Murchison (CM2), Cold Bokkeveld (CM2), Semarkona (LL3.00) and Bishunpur (LL3.15). The spectra exhibit the first-order carbon bands D and G, superimposed onto a fluorescence background indicating that the macromolecular OM is widespread and abundant. Inspection of the combined set of spectra (Fig. S2) shows that in PX-18 these

two bands are wider and more overlapping than in the type 3 ordinary chondrites Semarkona and Bishunpur. This suggests a lower degree of thermal metamorphism in PX-18 macromolecular OM. The Lorentz-Breit-Wigner-Fano (LBWF) fit analysis confirmed the visual analysis of the spectra. The values of the spectral parameter FWHM-D (D band full width at half maximum), which is a sensitive tracer of thermal metamorphism (Bonal *et al.*, 2007), rule out the presence of significant thermal metamorphism. Raman spectra from PX-18 have mean FWHM-D of  $268 \pm 8 \text{ cm}^{-1}$  (Fig. S3), a value between those of the metamorphosed chondrite Bishunpur ( $170 \pm 20 \text{ cm}^{-1}$ ) and Semarkona ( $250 \pm 3 \text{ cm}^{-1}$ ) and those of the little metamorphosed Cm<sup>2</sup> Cold Bokkeveld ( $282 \pm 12 \text{ cm}^{-1}$ ). To characterize highly disordered carbonaceous matter, the most suitable spectral parameters are FWHM-G and  $\omega_G$  (G band peak position). A rough comparison can be made with data from IDPs and chondrites (Sandford *et al.*, 2006), keeping in mind that different experimental conditions have been used. The G-diagram (Fig. 3.6) indicates that the macromolecular OM in PX-18 has a degree of thermal metamorphism lower than that of the Bishunpur and Semarkona chondrites and comparable to that of organic matter present in IDPs.

### 3.5 Nitrogen fractionation

Excluding a stellar nucleosynthesis origin (i.e. related to presolar grains) for the observed N isotopic anomalies, processes such as self-shielding and low-temperature ion-molecules reactions can be considered. Self-shielding (Thiemens and Heidenreich, 1983) is still being explored as an explanation for O fractionation in early solar nebula (Lyons and Young, 2005; Clayton, 2002; Yurimoto and Kuramoto, 2004) and it has been proposed to be effective also for N in the protosolar accretion disk (Clayton, 2002). However, quantitative models for N fractionation due to self-shielding have not been developed and the extent of N isotopic fractionation by this process is unknown. Models for isotopic fractionation by low-temperature ion-molecule reactions can produce values of  $\delta^{15}\text{N}_{\text{AIR}}$  as high as those observed in PX-18. In the most recent model (Rodgers and Charnley, 2008), which invokes chemical reactions with N-containing molecules under dark molecular cloud conditions, values for  $\delta^{15}\text{N}_{\text{AIR}}$  of  $> 9000\%$  for external layers of NH<sub>3</sub> ice accreted on dust grains are obtained. Transfer of fractionated N from NH<sub>3</sub> ice to organic matter is achieved by UV-induced transformations into polycyclic aromatic hydrocarbons (PAHs). PAHs are abundant in the gas phase where N fractionation take place and they can condense on dust grains and form ice (Bernstein *et al.*, 2002). Experiments on various coronene-ice mixtures at low temperature (15 K) and low pressure have shown that -NH<sub>2</sub> functional groups present in the ice can be added to PAHs by the action of UV photolysis (Bernstein *et al.*, 2002).

However, a fundamental problem is that low temperature ion-molecule reactions are also predicted to produce strong deuterium enrichments in organic matter (Bernstein *et al.*, 2002; Roberts *et al.*, 2003), which are not found in PX-18 or any other xenolith in Isheyevo. Other previous studies [e.g. Ivanova *et al.* (2008); Pearson *et al.* (2006); Alexander *et al.* (2007)] have also found that H and N anomalies are decoupled in extraterrestrial matter. These results call for a new theoretical and experimental approach, which must be able to provide an explanation for the decoupling of these light element isotopic variations. The primitive mineralogy of PX-18, in combination with the extreme range of N isotopic variation and the unmetamorphosed organic matter it preserves, indicate that PX-18 represents a new class of extremely pristine extra-terrestrial material, which might sample little processed outer Solar System bodies. A Kuiper Belt parent body is a likely possibility. The presence of outer Solar System material in an asteroidal body is a natural consequence of the idea that xenoliths represent samples of primordial matter scattered throughout the Solar System during the Late Heavy Bombardment (Briani and Gounelle, 2008). In the context of global scattering and mixing of bodies (Gomes *et al.*, 2005), objects composed of more fragile and/or unconsolidated material, such as primordial chondritic planetesimals, comets and Kuiper Belt objects, are greatly affected by collisions (Levison *et al.*, 2008a), and can produce fragments that are scattered throughout the Solar System and become embedded in meteorite parent bodies.

### 3.6 Materials and methods

To search for primordial xenoliths, preliminary SEM and EDX spectral analyses of two Isheyevo polished sections have been performed at the Laboratoire de Minéralogie et Cosmochimie du Muséum of the Muséum National d'Histoire Naturelle (Paris, France) by means of a JEOL JSM 840-A SEM equipped with an EDAX Genesis X-rays detector, using a 3 nA primary beam accelerated by a 15 kV potential difference. High resolution SEM images have been acquired at the University of Paris VI using a Zeiss Supra-55 VP field emission SEM, with a 4 nA, 10 kV accelerated primary beam. By the same instrument, EDX spectral analyses of sub- $\mu\text{m}$ -sized grains in the matrix of PX-18 have been performed. Quantitative analyses for the mineralogical composition of xenoliths have been obtained with a CAMECA SX-100 electron microprobe at the University of Paris VI. A 10 nA focalized beam, accelerated by a 15 kV potential difference, is used for point analyses of xenoliths silicates, oxides and metals. For TEM analyses two thin sections have been extracted from PX-18 by focused ion beam technique at the Institut d'Électronique, de Microélectronique et de Nanotechnologie (Lille, France). Individual matrix grains have been analyzed by a Philips CM 30 at

the Laboratoire de Structure et Propriétés de l'Etat Solide of the Université des Sciences et Technologies (Lille, France). The accelerating voltage was 300 kV. EDX microanalyses have been realized by a Noran detector. Raman measurements have been performed at the Laboratoire de Sciences de la Terre (ENS Lyon, France) with a Labram spectrometer (Horiba-Jobin-Yvon), equipped with a Spectra Physics Argon ion laser using 514.5 nm excitation. The laser beam was focused by a microscope equipped with a long distance working objective (x50), leading to a 2-3  $\mu\text{m}$  spot. The reproducibility of Raman measurements on poorly ordered macromolecular organic matter is controlled by atmospheric conditions, irradiation time and power on the sample, due to heating and photo-oxidation effects during irradiation (Quirico *et al.*, 2005). Hence spectra have been acquired under strictly constant experimental conditions: power at the sample surface was  $400 \pm 5 \mu\text{W}$ , exposure time of each measurement was 90 s and under an inert argon atmosphere. A 600 gr/mm grating has been used and provided with spectra in the spectral region 500 - 2200  $\text{cm}^{-1}$ , recovering the first and second order carbon bands. Raman spectra have been quantitatively analyzed by fitting the first-order carbon bands using a Lorentzian profile for the D peak, and a Breit-Wigner-Fano one for the G peak [LBWF fit: see Ferrari and Robertson (2000) for a discussion regarding the choice of these profiles]. The spectral parameters derived from the LBWF fit are the width of the bands FWHM-G and FWHM-D and their peak position  $\omega_G$  and  $\omega_D$ . Secondary ion mass spectrometry analyses were performed with a NanoSIMS CAMECA N50 at the Laboratoire de Minéralogie et Cosmochimie du Muséum of the Muséum National d'Histoire Naturelle of Paris. We have used a Cs+ primary beam in two sessions. The first session for detection of H- and D- (with a current on the sample of  $\approx 40$  pA) and the second one for  $^{12}\text{C}^-$ ,  $^{13}\text{C}^-$ ,  $^{12}\text{C}^{14}\text{N}^-$  and  $^{12}\text{C}^{15}\text{N}^-$  (current on the sample  $\approx 4$  pA). In each case an electron beam has been used to compensate for charging effects. For H isotopes measurements, the experimental set up was such that the mass resolution was  $\Delta M/M$  greater than or equal to 2000. For C and N isotopes a larger mass resolution is needed, so the machine was set up to yield  $\Delta M/M$  between 7500 and 8000. This is necessary in order to prevent possible interferences between different isotope masses, e.g.  $^{11}\text{B}^{16}\text{O}^-$  on  $^{12}\text{C}^{15}\text{N}^-$ . To determine the instrumental mass fractionation (IMF) we have used as standard reference a type III kerogen, with known isotopic compositions of H, C and N in the same reference sample. The IMF was on the order of  $-315 \pm 5\%$  for H,  $-50 \pm 1\%$  for C, and  $-6 \pm 4\%$  for N. We selected for isotopic analysis a few  $40 \times 40 \mu\text{m}^2$  matrix-dominated regions from five xenoliths of Isheyevo. These regions were exposed to high Cs+ current ( $\sim 1$  nA) for 15-20 minutes before analyses, in order to reach sputtering equilibrium. Measurements were made in scanning imaging mode. For each selected region, between 7 and 35 plans composed of  $256 \times 256$  pixels were collected. Measurement time was 65.536 seconds per plan in the case of H

isotopes, 327.68 seconds per plan for C and N isotopes. Where hotspots were found, close-up analyses on  $\sim 10 \times 10 \mu\text{m}^2$  areas have been performed. Details for data reduction can be found in the on-line Supporting Information. Here we stress our criteria to define hotspots in  $^{15}\text{N}/^{14}\text{N}$  ratio images. A selected region of interest (ROI) in one image is defined as a hotspot if: 1)  $(\delta^{15}\text{N}_{\text{AIR}})_{\text{hotspot}} - \sigma_{\text{hotspot}} > (\delta^{15}\text{N}_{\text{AIR}})_{\text{av}} + 3\sigma_{\text{av}}$ , where  $\sigma_{\text{hotspot}}$  is the error on the  $(\delta^{15}\text{N}_{\text{AIR}})_{\text{hotspot}}$  value of the selected ROI and  $(\delta^{15}\text{N}_{\text{AIR}})_{\text{av}}$  and  $\sigma_{\text{av}}$  are the average  $\delta^{15}\text{N}_{\text{AIR}}$  value and error for the entire image; 2) the hotspot is larger than the image spatial resolution (all potential hotspots with size smaller than  $250250 \text{ nm}^2$  have been discarded); 3) each individual plan that composes the image has a  $^{15}\text{N}/^{14}\text{N}$  ratio that differs no more than  $3\sigma_{\text{mean}}$  from the mean  $^{15}\text{N}/^{14}\text{N}$  ratio (where  $\sigma_{\text{mean}}$  is the standard deviation calculated from the all set of isotopic ratios relative to the same ROI). The errors reported in the text express a  $2\sigma$  confidence level.

### 3.7 Acknowledgements

We gratefully acknowledge three anonymous reviewers that carefully went through the manuscript and suggested corrections and improvements. This study was funded by the Programme Nationale de Planetologie (PNP) and the European grant ORIGINS [MRTN-ct-2006-035519]. The National NanoSIMS facility at the Muséum National d’Histoire Naturelle was established by funds from the CNRS, Région Île de France, Ministère délégué à l’Enseignement supérieur et à la Recherche, and the Muséum itself.

### 3.8 Supporting Information

#### Materials and methods

For the measured isotopic compositions, we report our results in the d-notation, which expresses the deviation in parts per thousand from terrestrial standards. For example, the  $^{15}\text{N}/^{14}\text{N}$  isotopic ratio is expressed as  $\delta^{15}\text{N}_{\text{AIR}}$ , defined by

$$\delta^{15}\text{N}_{\text{AIR}} = \left( \frac{(^{15}\text{N}/^{14}\text{N})_{\text{measured}}}{(^{15}\text{N}/^{14}\text{N})_{\text{air}}} - 1 \right) \times 1000.$$

In order to evaluate the isotopic ratios of the xenoliths analyzed areas we adopted the following procedure. Before calculations of the different isotopic ratios, individual plans of the same region have been added together after shift correction. Average values of  $\delta\text{D}_{\text{SMOW}}$ ,  $\delta^{13}\text{C}_{\text{PDB}}$  and  $\delta^{15}\text{N}_{\text{AIR}}$  have been evaluated for each isotopic image after selection of the image portion with sufficient counts (5% of the image maximum) of the denominator isotope involved. Only N ratio images of PX-18 show isotopic anomalies. They

were more extensively analyzed, first to investigate the presence of diffuse isotopic anomalies (i.e. on areas of several  $\mu\text{m}^2$ ). For each N ratio image the fraction with  $\delta^{15}\text{N}_{\text{AIR}} > 250\text{‰}$  has been evaluated as a measure of general  $^{15}\text{N}$  enrichment (Table 3.1). To verify the presence of large zones with high isotopic ratio, a complementary procedure has been used. Starting from images of  $^{14}\text{N}$  distribution, all the image pixels with counts above 5% of image maximum are divided into small square regions of interest (ROIs) (with area of  $600 \times 600 \text{ nm}^2$ , i.e. substantially larger than the spatial resolution of the NanoSIMS) for which isotopic ratios are evaluated. In this case no effort is made to identify the highest isotopic ratios, and the presence of a large, isotopic anomalous region is confirmed if a continuous distribution on a wide range of  $\delta^{15}\text{N}_{\text{AIR}}$  values is found (Fig. 3.3). To evaluate the presence of hotspots in ratio images, taking into account that different images present different average  $\delta^{15}\text{N}_{\text{AIR}}$  values, we searched for ROIs with  $\delta^{15}\text{N}_{\text{AIR}} > (\delta^{15}\text{N}_{\text{AIR}})_{\text{av}} + 3\sigma_{\text{av}}$  (i.e. more than the image average value + 3 times the error) (Table 3.1). In addition, we also verify if the  $\delta^{15}\text{N}_{\text{AIR}}$  of these ROIs, with its own  $3\sigma$  error bars, is larger than  $(\delta^{15}\text{N}_{\text{AIR}})_{\text{av}} + 3\sigma_{\text{av}}$ . To summarize, a hotspot must have  $(\delta^{15}\text{N}_{\text{AIR}})_{\text{hotspot}} - 3\sigma_{\text{hotspot}} > (\delta^{15}\text{N}_{\text{AIR}})_{\text{av}} + 3\sigma_{\text{av}}$ . This is the first condition required to define a hotspot, i.e. a region with  $^{15}\text{N}/^{14}\text{N}$  ratio beyond the range of statistical fluctuations of the isotopic distribution in the analyzed area. The second condition is that a hotspot must be larger than the image spatial resolution, determined by the NanoSIMS primary beam size. With the setup adopted to detect C and N isotopes, the primary beam size is between 100 and 200 nm. As a conservative estimate, all potential hotspots with size smaller than  $250 \times 250 \text{ nm}^2$  have been discarded. Third, the  $^{15}\text{N}/^{14}\text{N}$  ratio of each individual plan (i.e. calculated from a single pair of  $^{15}\text{N}$  and  $^{14}\text{N}$  images) for which  $|\frac{^{15}\text{N}}{^{14}\text{N}} - \frac{^{15}\text{N}}{^{14}\text{N}}_{\text{mean}}| > 3\sigma_{\text{mean}}$  has been rejected (here  $\sigma_{\text{mean}}$  is the standard deviation calculated from the all set of isotopic ratios relative to the same ROI). With these criteria, we identified forty-six hotspots, and there are four cases in which all these three conditions are fulfilled by areas that are completely enclosed in larger hotspots (Fig. 3.2C, 3.2D, 3.2E). Finally, in order to consider minimum spatial scales larger than the resolution of the NanoSIMS, hotspots have been identified in smoothed images (i.e. in images where the value of a pixel is the mean of a box whose area is larger than the NanoSIMS spatial resolution). Errors have been evaluated as follows: for each image and each ROI, the error of the average isotopic ratio has been assumed to be the greatest between errors due to counting statistics and errors due to measure dispersion among successive cycles that form the image. Combining these errors from measures on samples and on standards, and taking into account the IMF correction, we obtained errors for d values. The final values reported in the text express a  $2\sigma$  confidence level.

## Supporting figures

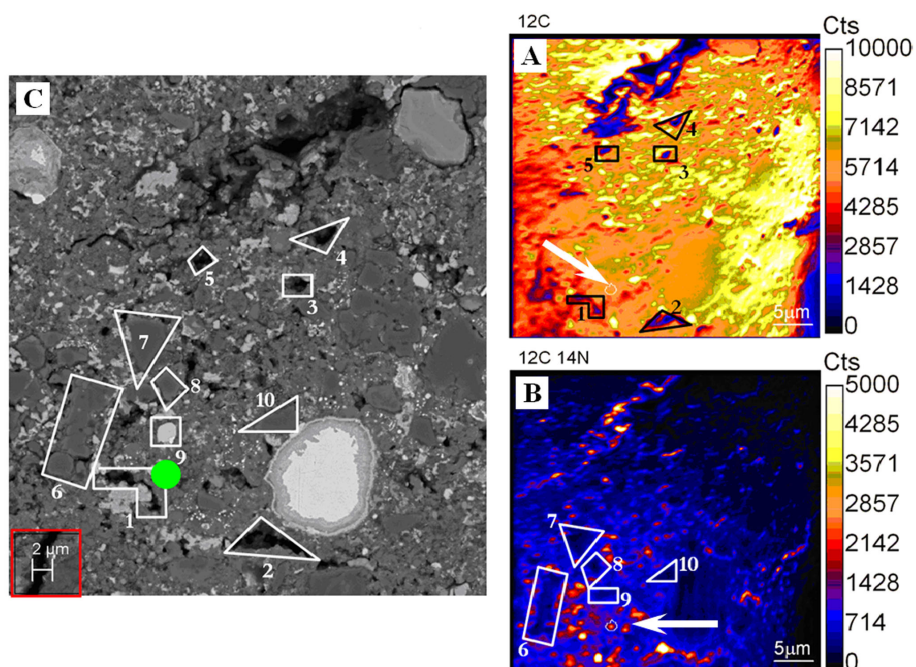


**Figure S1:** comparison between two NanoSIMS (A and B, on the right) and a high resolution SEM (C, on the left) images of the same region of PX-18. The two different techniques by which these images have been obtained imply sampling at different depth in PX-18. NanoSIMS analyses are based on sputtering of sample atoms, and only the very superficial atomic layers are concerned. With a measure time of 327.68 s/image and a 4 pA beam current, as in this work, a thickness of only a few nm is removed per image. High resolution SEM images have been acquired with an electron beam accelerated by a 10 kV potential difference, i.e. the interaction with the sample extends to a depth of 2  $\mu\text{m}$ . Notwithstanding these differences, it is possible to identify some common features (here indicated by numbers) and therefore to find the hotspot location. (A) NanoSIMS image for  $^{12}\text{C}$ , the hotspot is indicated by a white arrow and a white ring, lower left, near the area labelled # 1. (B) NanoSIMS image is for  $^{12}\text{C}^{14}\text{N}$ , the hotspot (white arrow) is below area # 9. In the SEM (C) image the hotspot location is indicated by the green spot. This type of comparison has been done for five  $10 \times 10 \mu\text{m}^2$  and two  $40 \times 40 \mu\text{m}^2$  different areas from PX-18. In no case there are individual mineral phases corresponding to hotspot locations. Rather, hotspots are in matrix dominated area, and their sizes are always larger than those of matrix mineral grains (Fig. 3.5 in the main text).

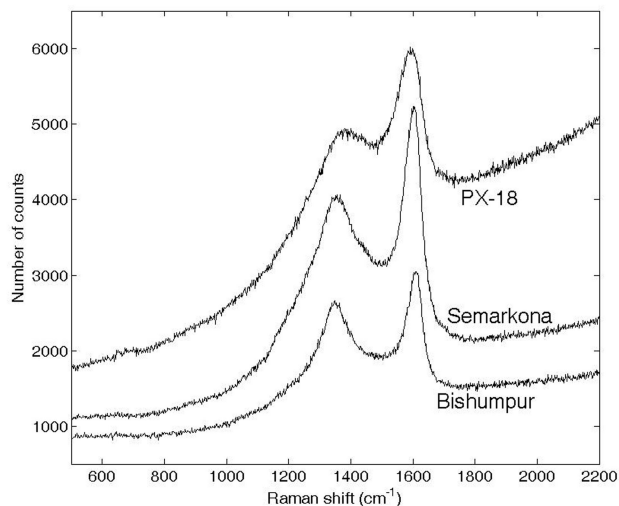


**Figure S2:** typical Raman spectra of PX-18 and matrix fragments from Semarkona (LL 3.00) and Bishunpur (LL 3.15). Raman spectra of PX-18 exhibit significant fluorescence background, indicating abundant organic matter.

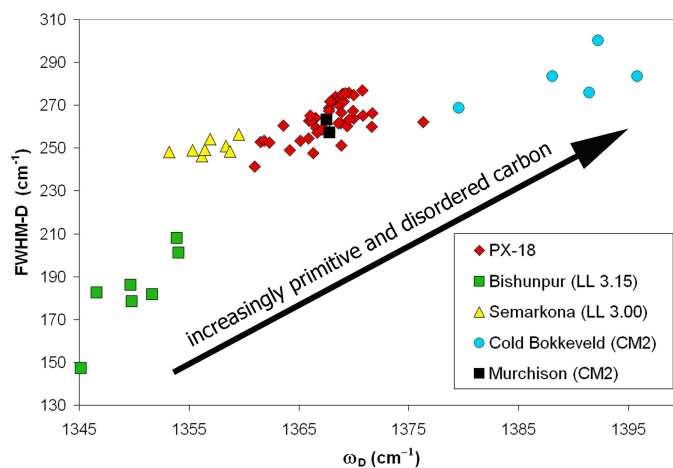


**Figure S3:** D-diagram for results of Raman analyses on PX-18: the spectral parameter FWHM-D plotted against the peak position  $\omega_D$ . This diagram reflects the degree of thermal metamorphism of the organic matter, as indicated by the arrow. All the spectra presented in this figure have been acquired with identical experimental conditions. For this reason a direct comparison between spectra is possible, to evaluate the relative degree of thermal metamorphism suffered by the samples. The D-diagram clearly shows that the Raman spectra of the PX-18 organic matter are between those of type 3 ordinary chondrites and those of less metamorphosed CM2 carbonaceous chondrites.

## Chapter 4

# Organic matter in Isheyevo microxenoliths

### Summary of Chapter 4

Raman spectroscopy is a powerful technique to characterize organic matter in extraterrestrial samples. In the case of metamorphosed chondrites (petrologic type 3), the organic matter structure is interpreted in terms of degree of metamorphism (Quirico *et al.*, 2003; Bonal *et al.*, 2006, 2007). In the case of unmetamorphosed objects, slight structural differences have been differently interpreted depending on the sample, e.g. as due to oxidation in Antarctic micrometeorites (Dobrică *et al.*, 2009), to short duration heating in metamorphosed CM chondrites (Quirico *et al.*, 2009b), to the heterogeneity of the precursors accreted by carbonaceous chondrites and IDPs/Antarctic micrometeorites: (Quirico *et al.*, 2008a; Dobrică *et al.*, 2009). However, the interpretation is generally more difficult and less concluding.

The typical Raman spectrum of chondritic organic matter exhibits two dominant peaks, called first-order G and D carbon bands. They provide information on the nature and structure of the material (e.g. amorphous vs polyaromatic) and/or the degree of structural order, when considering samples within a coherent series exhibiting a continuous evolution.

Following results described in the previous chapter for the primordial microxenolith PX-18, we report in this chapter a Raman spectroscopy analysis of organic matter contained in five microxenoliths of the carbonaceous chondrite Isheyevo, along with that of insoluble organic matter (IOM) extracted from several carbonaceous chondrites, in order to compare both types of samples. We collected Raman spectra using three different excitation wavelengths (244, 457.9 and 514.5 nm) to take advantage of the so-called dispersion effect, i.e. the analysis of how spectral parameters change with excitation wavelength. This approach is expected to provide more

unambiguous data than analyses based on spectra collected with only one excitation wavelength. Indeed, for very disordered macromolecular organic matter, distinct samples can exhibit similar Raman spectra at a given excitation wavelength. Analysis of Raman spectra based on the dispersion effect has been successfully applied to various synthetic carbon films (Ferrari and Robertson, 2001), and seems powerful to go further in the investigation of pristine extraterrestrial samples (Quirico *et al.*, 2008b, 2009a).

Our preliminary results suggest that organic matter in Isheyevo microxenoliths is dissimilar to IOM extracted from C1-C2 carbonaceous chondrites. Also, they confirm that the structure of IOM in the metamorphosed CM chondrites (MCMs) PCA 91008 and WIS 91600 is the fingerprint of a thermal event distinct from thermal metamorphism which occurred in type 3 chondrites. However, any of the Isheyevo microxenoliths has Raman features similar to those of MCMs, suggesting that a similar heating process can not account for the differences observed in Isheyevo microxenolith organic matter with respect to unmetamorphosed CI and CM chondrites. New Raman analysis along with experimental simulations are planned to further investigate this issue.

## 4.1 Brief introduction to Raman spectroscopy

Raman spectroscopy is based on inelastic scattering of photons interacting with the analyzed sample. In general, when light is scattered by an atom or molecule only a small fraction of the scattered light [approximately 1 in  $10^5$  photons (Ferraro *et al.*, 2003)] is inelastically scattered, while most photons are elastically scattered. Inelastic scattering implies a change in the photon energy, and therefore in their frequency and wavelength also. For molecules, such a difference corresponds to a variation in their vibrational energy.

When an energy exchange happens between an incident photon and a target molecule (i.e. when inelastic scattering happens) two cases are possible:

- the photon loses energy and the molecule changes from a lower to an upper energy level (Stokes scattering);
- the photon gains energy and the molecule changes from an upper to a lower energy level (anti-Stokes scattering).

Considering only two fixed energy levels, both the above processes are simultaneously possible. Therefore, given a flux of incident monochromatic photons, the spectrum of scattered light contains photons of larger and smaller energy, both shifted of the same quantity with respect to the frequency of the incident light. When incident photons are elastically scattered by target atoms or molecules, changes in frequency do not occur. Therefore, the

complete spectrum of scattered photons is composed by a prominent central peak corresponding to elastic scattering, and symmetric peaks of higher and smaller frequency due to inelastic Raman scattering. The intensity of Stokes and anti-Stokes peaks depends on the number of molecules occupying the different energy levels. When the molecules of the target sample are in thermal equilibrium, these numbers are given by the Boltzmann distribution, which states that lower energy levels are more populated. This implies that Stokes peaks are more intense than anti-Stokes peaks. Usually, Raman spectroscopy is based on the analysis of the Stokes peaks of the spectrum.

When atoms or molecules are bound in a solid, complex features arise in the Raman spectrum. Indeed, in the case of macromolecular organic matter, the incident photon is first absorbed, and subsequently scattered. The absorption leads to a resonant process, which enhances the Raman scattering cross-section by several orders of magnitudes. Because the moieties composing the macromolecular organic matter absorb photons with different frequencies, the incident photons probe only a fraction of this solid and Raman spectra depend on the excitation wavelength. Therefore the dispersion effect appears as a serious advantage for characterizing complex disordered organic samples (Ferrari and Robertson, 2001; Ferrari *et al.*, 2003). Such an enhancement of the Raman cross-section also accounts for the lack of detection of minerals bands when samples mixing organic matter and minerals are investigated, as it is the case for matrix of chondrites or stratospheric IDPs (Rotundi *et al.*, 2008).

In pristine chondrites, organic matter consists of a soluble fraction (small molecules soluble in current solvents) and an insoluble fraction (called insoluble organic matter, IOM). The latter represents about 75-99% of the whole organic content (Alexander *et al.*, 2007). It is a polyaromatic material, based on the assemblage of small polyaromatic units (1-3 rings) held together by short highly branched aliphatic chains, with the presence of significant amount of heteroatoms such as O, H (major elements) and N, S (minor elements) (Becker and Epstein, 1982; O'D. Alexander *et al.*, 1998; Remusat *et al.*, 2005; Robert and Derenne, 2006; Derenne and Robert, 2009).

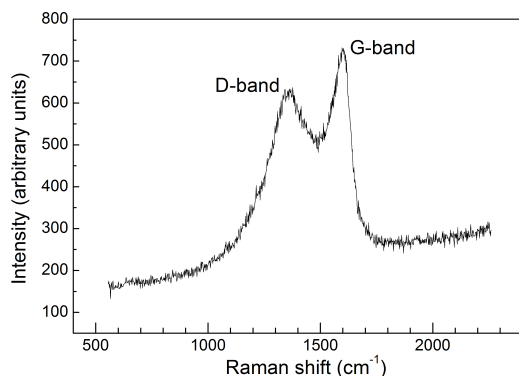


**Figure 4.1:** a typical Raman spectrum of macromolecular organic matter (measured on a xenoliths of the carbonaceous chondrite Isheyevo). D and G bands are indicated. The slope of the spectrum baseline is due to fluorescence.

Raman spectra of amorphous carbons and disordered organic matter, including IOM, are dominated by two peaks, called the G and D bands (Fig. 4.1). The G band peaks in the range 1580-1600  $\text{cm}^{-1}$ , and the D band at  $\sim 1355 \text{ cm}^{-1}$  (Ferrari and Robertson, 2000). It is noteworthy that these two peaks dominate Raman spectra of organic matter samples that have various ordering degree and  $sp^2$  structures, i.e. from amorphous carbon to nano-crystalline carbon and graphite (Ferrari and Robertson, 2000, 2001). In graphite, the G band (G stands for graphite) is related to the  $E_{2g2}$  vibration mode in rings. In disordered and amorphous carbonaceous materials, this band is more generally induced by in-plane bond-stretching modes of  $sp^2$  bonded carbon atom pairs (Fig. 4.2A). In contrast, the D band does not appear in the Raman spectrum of graphite, but it is present in any carbonaceous material with disorder in its structure. This band is induced by a breathing mode in rings ( $A_{1g}$  symmetry; Fig. 4.2B), forbidden in perfect graphite but induced by disorder (D stands for disorder).

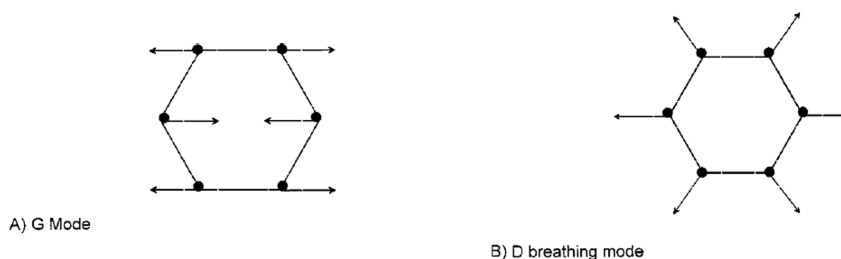


**Figure 4.2:** motion of carbon atoms in the G mode (A) and in the D mode (B). Figure adapted from Ferrari and Robertson (2000).

## 4.2 Application to the study of extraterrestrial organic matter

IOM appears to be ubiquitous in extraterrestrial samples. It has been studied in carbonaceous chondrites (Cody *et al.*, 2005; Remusat *et al.*, 2005, 2006; Thomen *et al.*, 2008, 2009), ordinary and enstatite chondrites (Bonal *et al.*, 2006; Alexander *et al.*, 2007; Cody *et al.*, 2008; Quirico *et al.*, 2008c; Piani *et al.*, 2009), in IDPs (Wopenka, 1988; Keller *et al.*, 2004; Flynn *et al.*, 2004; Quirico *et al.*, 2005; Rotundi *et al.*, 2007), in cometary grains recovered by the Stardust mission (Sandford *et al.*, 2006; Rotundi *et al.*, 2008) and in Antarctic micrometeorites (Matrajt *et al.*, 2001; Suzuki *et al.*, 2005; Dobrică *et al.*, 2008; Wilson *et al.*, 2008).

IOM is generally believed to carry memories of processes that happened in the interstellar medium from which the solar system formed. The hypothesis of an interstellar, presolar origin of the IOM is mainly based on similarities in infrared spectra of diffuse interstellar and meteoritic organic matter

(Ehrenfreund *et al.*, 1991) and on the presence of hydrogen and nitrogen isotopic anomalies in IOM (see e.g. Robert and Epstein 1982; Busemann *et al.* 2006). However, the improvement of astronomical observations has shown that the refractory carbon material in diffuse interstellar medium is mostly similar to a hydrogenated amorphous carbon and not to IOM (Dartois and Muñoz-Caro, 2007). Other recent studies questioned the interpretation of the D and  $^{15}\text{N}$  enrichments, and proposed that fractionation mechanisms affected IOM after its formation, possibly in the protoplanetary disk or even in the parent body (Remusat *et al.*, 2006; Alexander *et al.*, 2007; Thomen *et al.*, 2008; Alexander *et al.*, 2009; Cody *et al.*, 2009). This is also the case of the results presented in chapter 3, based on the difference in hydrogen and nitrogen isotopic composition of the primordial microxenolith PX-18 in the Isheyevo carbonaceous chondrite.

Whatever the place and formation processes, IOM has suffered also from thermal metamorphism and/or aqueous alteration on the meteorite, IDP and micrometeorite parent body.

We report in this chapter our *in situ* Raman spectroscopy analyses of the organic matter present in five carbonaceous microxenoliths of the Isheyevo chondrite. The study of organic matter not separated from its mineral carriers was possible directly on polished sections because intense G and D bands were found to largely dominate the Raman spectra, and spectral features of minerals were not observed.

### 4.3 Microxenoliths in the CB/CH chondrite Isheyevo

Isheyevo (Fig. 4.3) is a recent discovered (Russel *et al.*, 2005) carbonaceous chondrite, classified as a CBb/CH chondrite. As described in chapter 3, Isheyevo is a Fe-Ni metal rich (60 vol% on average) chondrite with two dominant lithologies similar to CB and CH chondritic material (Ivanova *et al.*, 2008). In addition to Fe-Ni metal grains, Isheyevo contains chondrules, rare Ca-Al rich inclusions and hydrated lithic clasts, but does not present fine-grained matrix, which separates high-temperature components in most other types of chondritic materials (Ivanova *et al.*, 2008; Krot *et al.*, 2007; Bonal *et al.*, 2008).

In a survey of the two polished sections MNHN 2006\_04 and MNHN 2006\_20 of Isheyevo (the CH lithology), representing a total area of about 400 mm<sup>2</sup>, we identified more than 100 lithic clasts. They are indeed xenoliths, as they show a high degree of aqueous alteration (also described in previous works, Krot *et al.* 2007; Bonal *et al.* 2008). This indicates that they are not genetically related to the high-temperature components in Isheyevo, which do not show effects of *in situ* aqueous alteration (Krot *et al.*, 2007; Bonal *et al.*, 2008). Five of these xenoliths, among which PX-18 described

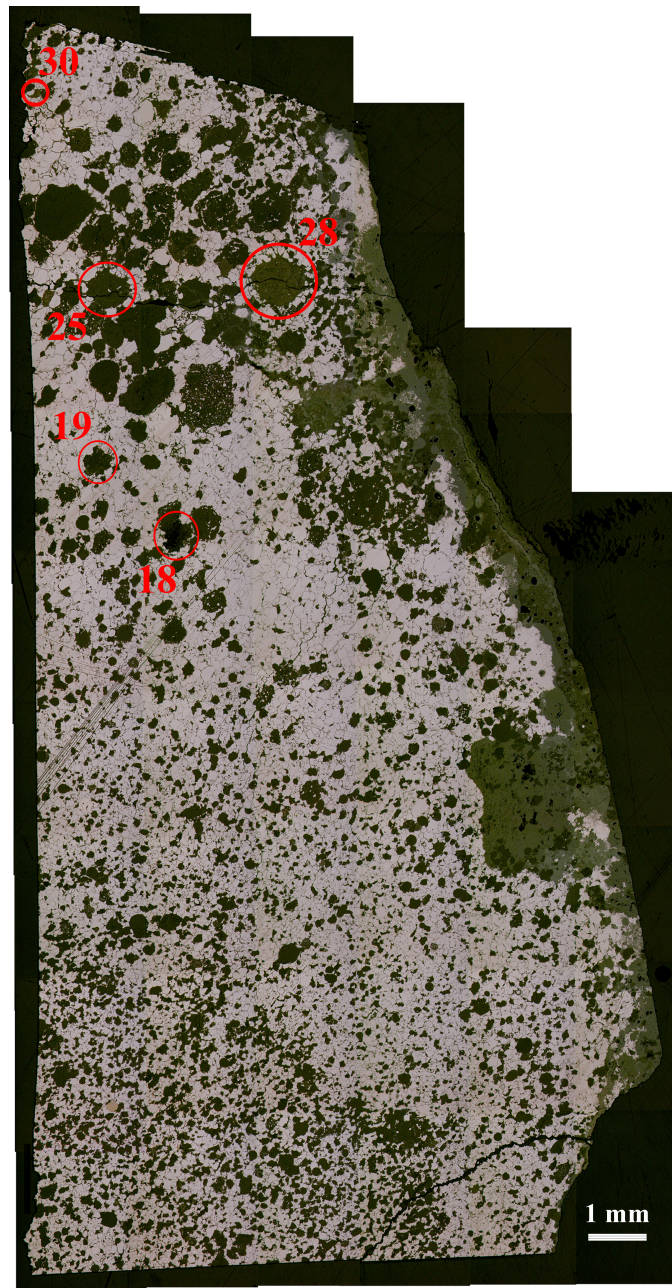


**Figure 4.3:** composite optical microscope map (magnification x5) of section MNHN 2006\_20 of the Isheyevo carbonaceous chondrite. The five xenoliths selected for Raman spectroscopy analyses are indicated.

in chapter 3, have been selected for Raman spectroscopy analyses. In the following they will be called xenolith # 19, # 25, # 28 and # 30. We report here their mineralogy and petrography, determined by SEM imaging,

**Table 4.1:** properties of Isheyevo xenoliths selected for Raman spectroscopy analyses.

	<b>PX-18</b>	<b><math>\mu</math>xen. # 19</b>	<b><math>\mu</math>xen. # 25</b>	<b><math>\mu</math>xen. # 28</b>	<b><math>\mu</math>xen. # 30</b>
SIZE ( $\mu$ m)	380×470	420×220	550×650	710×740	110×170
MATRIX <sup>a</sup>	sil. CM2	phyll. CM2-CR2	?	sil. CM2	?
OLIVINE <sup>b</sup>	++ Fo <sub>86</sub>	+ Fo <sub>97</sub>	++ Fo <sub>90</sub>	++ Fo <sub>90</sub>	+ Fo <sub>90</sub>
PYROXENE <sup>b</sup>	++ En <sub>92</sub> -Fs <sub>6</sub>	+ En <sub>92</sub> -Fs <sub>4</sub>	++ En <sub>88</sub> -Fs <sub>8</sub>	+++ En <sub>87</sub> -Fs <sub>10</sub>	no
SULFIDES <sup>c</sup>	no	++ pyrrh. pentl.	++ pyrrh. troil.	++ pyrrh.	++ troil.
Fe-Ni METALS	++ kam.	+ kam.	++ kam.	++ kam.	++
MAGNETITE	no	++++	++	no	no
CARBONATES <sup>d</sup>	no	no	++ dol. breunn.	no	no
DIVERS			3 plagio Ab <sub>10</sub> -An <sub>90</sub>	metamorph. silicates	

<sup>a</sup> sil. = anhydrous silicates; phyll. = phyllosilicates; ? = matrix not analysed by TEM. Data reported in a Mg-Fe-(Si+Al) ternary diagram. CR2 = data in the CR2 phyllosilicate field; CI1 = data in the CI1 phyllosilicate field; CM2 = data in the CM2 serpentine field.

<sup>b</sup> ++++ = very abundant; +++ = abundant; ++ = common; + = occurrence. Second line is the mean composition.

<sup>c</sup> pyrrh. = pyrrhotite; troil. = troilite; pentl. = pentlandite.

<sup>d</sup> dol. = dolomite; breunn. = breunnerite.

<sup>e</sup> kam. = kamacite

EDX spectroscopy and electron microprobe analyses (as explained in detail in section “Materials and methods” of chapter 1). In addition, preliminary transmission electron microscopy (TEM) analyses have been performed on matrix grains extracted from microxenoliths # 19 and # 28. TEM images and EDX analyses have been realized by a JEOL JEM-2500SE transmission electron microscope at the NASA Johnson Space Center (Houston, USA), with an accelerating voltage of 200 kV.

A detailed description of PX-18 has already been presented in chapter 3. Like PX-18, the other four xenoliths are largely dominated by fine-grained matrix (Fig. 4.4). This is a fundamental property to perform *in situ* Raman spectroscopy of organic matter, as organic matter is essentially associated with fine-grained matrix (Quirico *et al.*, 2003; Bonal *et al.*, 2006, 2007). We decided to perform Raman spectroscopy analyses on these microxenoliths after the first interesting results obtained for PX-18 (see chapter 3). The other four xenoliths have been selected because their fine-grained matrix show differences in composition and structure (their principal properties are summarized in Tab. 4.1).

Principal structural differences have been revealed between microxenoliths # 19 and 28 by preliminary transmission electron microscopy (TEM) analyses (Fig 4.5). Matrix of microxenolith # 19 is largely dominated by

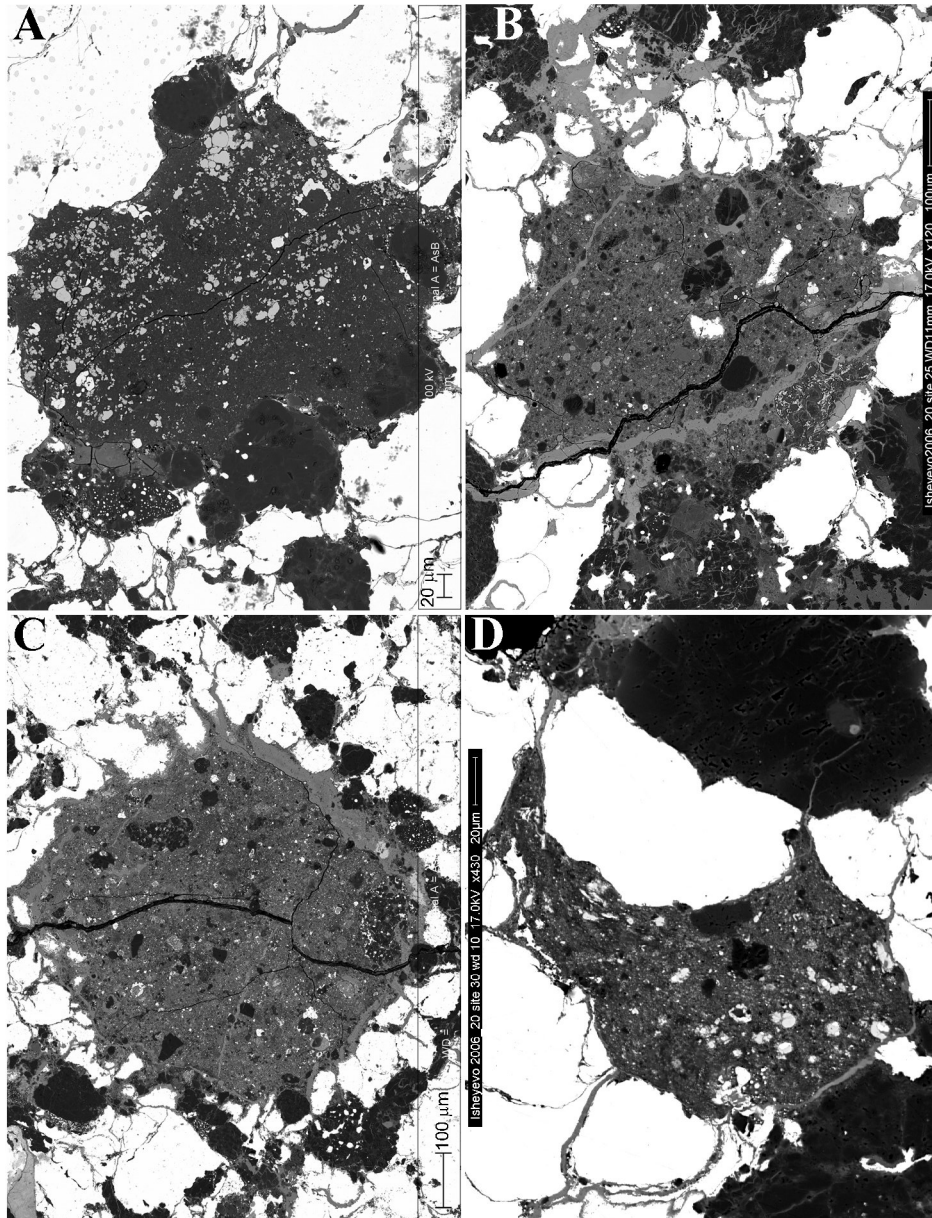


**Figure 4.4:** Back scattered electron images of Isheyevu xenoliths selected for Raman spectroscopy analyses. A: microxenolith # 19. B: microxenolith # 25. C: microxenolith # 28. D: microxenolith # 30. See text and Tab. 4.1 for their description.

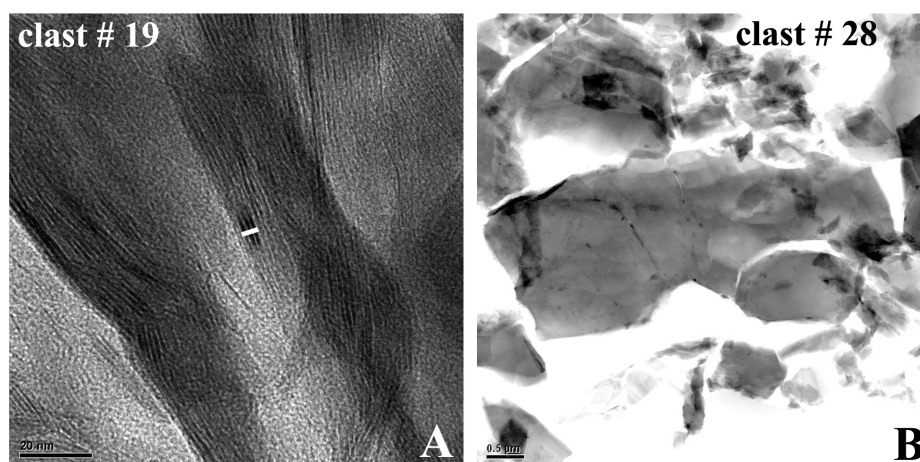


**Figure 4.5:** TEM bright field images of matrix grains extracted from microxenoliths # 19 (A) and # 28 (B). A: layered structures typical of phyllosilicates. The white line in the center covers three layers and it is 3.9 nm, indicating this is saponite with a 1.3 nm interlayer spacing. B: the large central grain is olivine, with Fe-Ni metal on the left edge (black) and small FeS inclusions (black droplets).

phyllosilicates (in particular saponite, with minor amount of serpentine), while that of microxenolith # 28 has a structure mainly composed by sub-micrometer-sized to micrometer-sized grains of olivine and pyroxene, with minor Fe sulfides and Fe-Ni metal grains. Phyllosilicates are apparently absent in microxenolith # 28, as in PX-18 matrix (see Fig. 3.1B in chapter 3).

Elemental composition of matrix has been reported on a (Si+Al)-Mg-Fe ternary diagram (Fig. 4.6). Most of the data are in the field of CM2 serpentine, but with clear differences in Fe content. Matrix of PX-18 is the most Fe rich, while results for microxenolith # 30 are the least Fe rich and are mostly in the field of CII phyllosilicates. Differences have been also observed in the S content. Microxenolith # 28 matrix is the most rich in S, with values between 2.6 and 11.9 at%. This is ascribed to the presence of sub-micrometer-sized sulfide grains. Matrix of microxenolith # 30 shows similar S content (up to 7.4 at%), and also similar high total values of electron microprobe analyses (mean total values are 95.7 wt% for microxenolith # 30, 94.2 wt% for microxenolith # 28). These data suggest that also microxenolith # 30 may have a matrix mainly composed by anhydrous silicates and Fe sulfides rather than a phyllosilicate-dominated matrix.

The situation is clearly different for microxenolith # 19: its phyllosilicate-dominated matrix shows S values always below 2.7 at%. Similar S content and total values have been obtained for matrix of microxenolith # 25 (mean total is 86.4 wt% for microxenolith # 19, 87.6 wt% for microxenolith # 25).

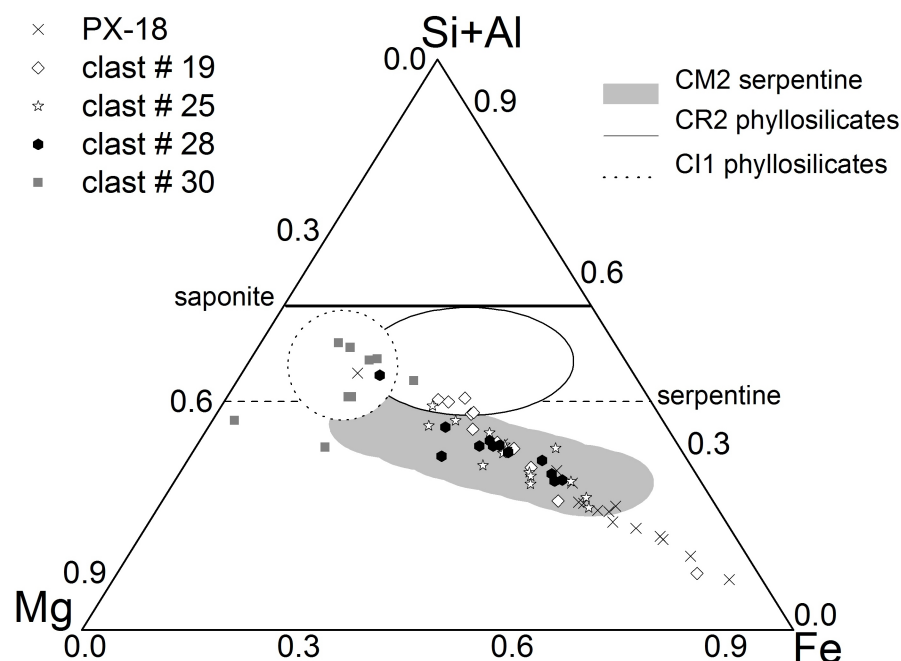


**Figure 4.6:** Electron microprobe point analyses of matrix in the five Isheyevo microxenoliths selected for Raman spectroscopy.

However, microxenolith # 19 contains far more magnetite (as spheroidal grains and framboidal aggregates), while microxenolith # 25 has more anhydrous silicate grains, up to  $77 \mu\text{m}$  in size.

In summary, all the five Isheyevo microxenoliths selected for Raman spectroscopy analyses suffered a low degree of thermal alteration. Among them, PX-18 and microxenolith # 28 (and possibly microxenolith # 30) appear to be the less modified by aqueous alteration, given the absence of phyllosilicates in their matrix. Indeed, microxenolith # 28 is the only one to show features probably related to thermal metamorphism. Namely, two large ( $315 \times 150 \mu\text{m}^2$  and  $200 \times 109 \mu\text{m}^2$ ) pyroxene grains show FeS-filled fractures and dispersed, angular pyrrhotite and troilite grains, similar to those typically observed in ordinary chondrites with higher petrologic type.

#### 4.4 Raman spectroscopy on Isheyevo microxenoliths: experimental procedures

The five carbonaceous microxenoliths of the CH/CBb chondrite Isheyevo described above were analyzed by *in situ* Raman spectroscopy. Results were compared to those obtained for IOM extracted from the following carbonaceous chondrites: Renazzo (CR2), Orgueil (CI1), Tagish Lake (ungrouped)

C2), Wisconsin Range (WIS) 91600 (C2), Murchison (CM2), Murray (CM2) and Pecora Escarpment (PCA) 91008 (CM2). These meteorites provide samples of both unmetamorphosed and metamorphosed carbonaceous chondrites. In particular, PCA 91008 and WIS 91600 are unusual CM chondrites, which show effects of thermal alteration which is not similar to long duration thermal metamorphism. For these two meteorites, a short duration thermal event, possibly induced by shock metamorphism, has been proposed (Hiroi *et al.*, 1997; Wang and Lipschutz, 1998; Tonui *et al.*, 2002; Yabuta *et al.*, 2008).

IOM samples have been provided by Eric Quirico of the Laboratoire de Planétologie de Grenoble, Université Joseph Fourier (France). Raman measurements were performed at the Laboratoire de Sciences de la Terre (ENS-Lyon, France). Unpolarized Raman spectra were excited with an argon-ion laser (Spectra Physics) and collected in back scattering geometry at room temperature by a micro spectrometer LabRam HR800 (Horiba Jobin-Yvon) implemented with a single dispersive grating. Two excitation wavelengths were used for visible Raman spectroscopy: 514.5 nm (green light) and 457.9 nm (blue light). For calibration, the peak of a Si semiconductor sample at  $521\text{ cm}^{-1}$  has been used. Unpolarized UV Raman spectra were excited by the 244 nm wavelength of a frequency doubled argon-ion laser (Spectra Physics) and collected with a LabRam HR800 (Horiba Jobin-Yvon) designed for UV radiation. Calibration has been made using the  $1332\text{ cm}^{-1}$  peak of diamond. Coupling Raman analyses performed with visible and UV excitation wavelengths is particularly useful to investigate the maturity of IOM in low-metamorphosed samples, as type 1 and 2 chondrites (Quirico *et al.*, 2008c; Dobrică *et al.*, 2008; Quirico *et al.*, 2009a).

Raman spectrometer were coupled with optical microscopes. This coupling allows precise focusing of the laser beam on the sample, making possible working with small grains of IOM and selecting different points in the Isheyevo microxenoliths. An Olympus X80 objective lens was used for analyses with visible light, with a spot size of 2-3  $\mu\text{m}$  across. For UV light an Olympus OFR X40 objective was employed, providing spot size diameters of 4-5  $\mu\text{m}$  across.

For each Isheyevo microxenolith 3 sets of measurements were performed, with different excitation wavelength. For each set, measurements on IOM extracted from selected meteorites were performed, in order to compare these spectra with those of organic matter in Isheyevo microxenoliths. The experimental conditions of the 3 sets of measurements are reported in Tab. 4.2.

The reproducibility of Raman measurements on poorly ordered material (like IOM) is a very complex issue. Sample heating and photostability (annealing, photo-oxidation, and photolysis) appear to be critical problems which cannot be fully resolved. Reproducibility is controlled by atmospheric conditions, irradiation time, and power on the sample, due to heating and

**Table 4.2:** samples and experimental set up

	excitation wavelength (nm)		
	244	458	514.5
Counting time (s)	30 & 150	2×40	3×60
Power on the sample ( $\mu$ W)	200	100	100
Atmosphere	air	air	air
Microscope objective	x40	x80	x80
Laser spot size ( $\mu$ m)	4 – 5	2 – 3	2 – 3
Grating (gr/mm)	600	600	600
Filter	no	D1	D3
	Samples		
Isheyevo xenoliths	PX-18, # 19, # 25, # 28, # 30		
IOM	Orgueil	Orgueil	Orgueil
	Tagish Lake	Tagish Lake	Tagish Lake
	Murray	Murray	Murray
	WIS 91600	WIS 91600	Murchison
	PCA 91008	PCA 91008	Renazzo

photo-oxidation effects during irradiation. Bonal *et al.* (2006), in the attempt of extending Raman characterization of IOM performed by Quirico *et al.* (2003), showed that their set of measurements correlate well with those of Quirico *et al.* (2003), but the slope of the regression line was not equal to one. Consequently, only Raman spectra acquired under the same experimental conditions can be safely compared.

The UV Raman measurements on Isheyevo polished sections do not allow to optimize the standard sample preparation, which consists in crushing a raw sample onto a glass slide. This operation generally optimizes heat dissipation. With an acquisition time of 2×150 s, we observed a decrease of the signal intensity beyond 150 s. Therefore, the UV Raman measurements have been carried out with an acquisition time of 30 s on Isheyevo microxenoliths, and with acquisition times of 30 s and 150 s on carbonaceous chondrite IOM. The data collected with acquisition time 30 s were definitely more noisy than the others.

## 4.5 Spectrum fitting and analysis

A total of 461 spectra have been acquired, considering the three different wavelengths and all samples. However, some spectra present high levels of noise and fluorescence background. The fluorescence background can have different intensity for different Raman shift. Usually it appears as an inclination of the spectrum baseline. Quirico *et al.* (2005) suggested that for *in situ* measurements fluorescence is induced by the same organic matter rather than by other components (e.g. minerals). Both noise and fluorescence cause the D and G bands to be less evident. Therefore, in order

to avoid difficulties in the fitting process, spectra with particularly high level of noise or fluorescence have not been considered for data reduction: 64 spectra have been rejected in this first selection. In the remaining spectra, the fluorescence background has been subtracted assuming a linear baseline (Quirico *et al.*, 2005; Bonal *et al.*, 2006, 2007; Quirico *et al.*, 2009a). Also, spectra are normalized, assuming the maximum value of the G band equals 1. A second selection of spectra has been performed after the fitting procedure. Indeed, in some cases, and in particular for UV spectra, we noted high values of the D band peak position. We attributed such high values to problems in the fitting procedure due to poorly defined D bands. Therefore we rejected all spectra for which the distance between the D and G peak was less than half the full width at half maximum of the D peak. The total number of spectra remaining after the second selection was 344.

Many fitting models of Raman spectra have been proposed in the literature, using various numbers and types of spectral profiles (Beny-Bassez and Rouzaud, 1985; Beyssac *et al.*, 2002; Quirico *et al.*, 2003; Sadezky *et al.*, 2005). In this study we used a 2-band fit model (Fig. 4.7), with a Lorentzian profile for the D peak and a Breit-Wigner-Fano profile for the G peak (LBWF fit). There is no physical justification for choosing these profiles, given that the physical mechanisms controlling the first-order carbon bands are not yet fully understood (Ferrari and Robertson, 2000). However the LBWF fit is a good choice for spectra of samples with different structure, from graphite to amorphous carbon (Ferrari and Robertson, 2000). The spectral parameters obtained by the fitting process are peak position  $\omega$ , full width at half maximum FWHM and intensity  $I$ . They are labelled  $\omega_D$ ,  $\text{FWHM}_D$ ,  $I_D$  for the D band,  $\omega_G$ ,  $\text{FWHM}_G$ ,  $I_G$  for the G band. D and G bands are readily quantified when noise and fluorescence are not too large. This is not always the case in our data: sometime the D band is poorly distinct from the G band. As a consequence, the values of  $\omega_D$  and  $\text{FWHM}_D$  obtained from spectrum fits are generally less accurate than the same values for the G band (Ferrari and Robertson, 2000).

An important issue is that of sample degradation, particularly for UV excitation wavelengths. When we started measurements on Isheyevo microxenoliths with excitation wavelength 244 nm, our first choice for the counting time was 300 s. However, performing such measurements in two steps of 150 s or 5 steps of 60 s, we noted a progressive degradation of the spectrum. Namely, the G band was lesser and lesser evident. Therefore we decided to acquire the UV spectra on a limited time interval of 30 s. The consequence is that spectra have a lower signal to noise ratio and that in some cases it is difficult to individuate and properly fit the D band. To evaluate the accuracy of 30 s UV spectra, we performed also measurements with counting time 150 s on samples of IOM extracted from Tagish Lake, Murray, Orgueil, PCA 91008 and WIS 91600. UV spectra acquired on IOM with counting time 150 s do not show the evident degradation observed for spectra acquired on Isheyevo

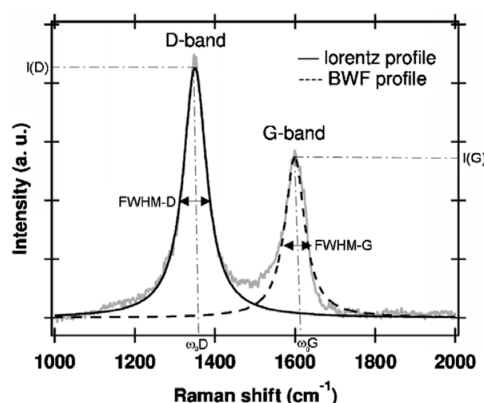


**Figure 4.7:** a typical Raman spectrum of polyaromatic organic matter, dominated by the D and G bands [after Bonal *et al.* (2006)]. The spectral parameter  $\omega_G$ ,  $\text{FWHM}_G$ ,  $\omega_D$ ,  $\text{FWHM}_D$ ,  $I_D$  and  $I_G$  are obtained by fitting the D band with a Lorentzian profile and the G band with a Breit-Wigner-Fano profile.

microxenoliths with counting time 300 s. This observation is likely due to the fact that IOM samples had been carefully crushed onto a glass slide, thus enhancing heat dissipation. This was not possible for organic matter in Isheyev microxenoliths, because measurements were performed *in situ* on polished sections. Matrix areas selected for measurements are composed of sub-micrometer-sized mineral grains, with a significant microporosity, which does not favour heat dissipation.

Both spectra acquired with counting time of 30 s and spectra acquired with counting time of 150 s exhibit low level of fluorescence, but 150 s spectra have higher signal to noise ratios. For each spectrum, the signal to noise ratio has been evaluated as the following: first we selected those points of the spectrum that belong to the baseline. As in UV spectra both first order carbon bands (around 1355 and 1600  $\text{cm}^{-1}$ ) and second order carbon bands (around 2900 and 3200  $\text{cm}^{-1}$ ) are present, we selected as baseline the points in the three intervals 500-1100  $\text{cm}^{-1}$ , 1900-2700  $\text{cm}^{-1}$  and 3400-4000  $\text{cm}^{-1}$ . The mean values of the spectrum baseline is assumed as the value of the signal. The root mean square of the baseline fluctuations (i.e., the differences between two adjacent points) is assumed as noise. Following this procedure, UV Raman spectra acquired with counting time 30 s have a signal to noise ratio of 11, while for those acquired with counting time 150 s the signal to noise ratio is 16.

Fig. 4.8 reports the relations between D and G band parameters obtained from 30 s spectra and those obtained from 150 s spectra. For  $\omega_G$ ,  $\text{FWHM}_G$  and  $\omega_D$  there is a good correlation (Fig. 4.8A, B, C). A linear fit of these data is obtained with slope values and correlation coefficients close to 1. This makes us confident that even with a limited counting time (30 s) it is possible to obtain good spectra, that can be used to evaluate the spectral

parameters  $\omega_G$ ,  $\text{FWHM}_G$  and  $\omega_D$ . The situation is different for values of  $\text{FWHM}_D$  and the  $I_D/I_G$  ratio (Fig. 4.8D, E). In this case there is no good correlation between data obtained with different counting times. Therefore we did not consider the values of these latter parameters in our analysis. Noise and the weak intensity of the D band likely perturb the evaluation of these parameters.

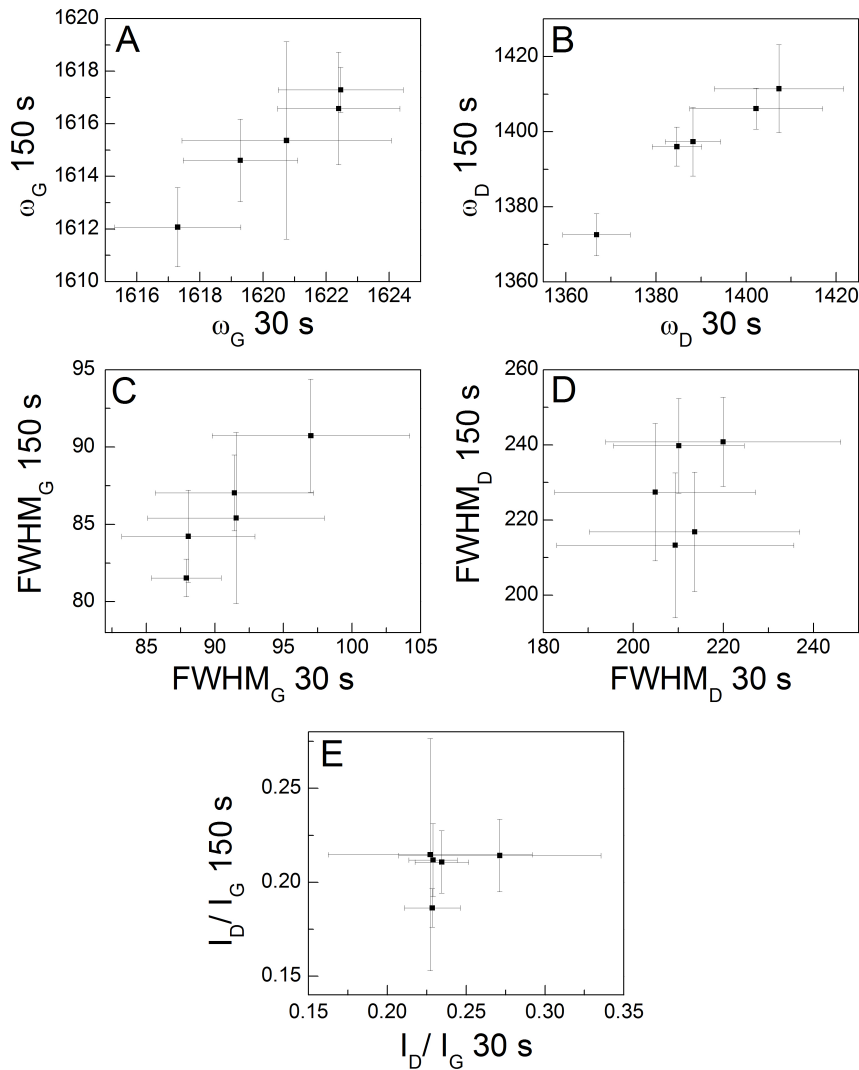


**Figure 4.8:** comparison between spectral parameters from spectra acquired with different counting time.

## 4.6 Results

All the analyzed samples show Raman spectra dominated by the first order G and D bands (Fig. 4.9). The fluorescence background only slightly affects UV spectra, but it can be very important for visible spectra. In general the fluorescence background is homogeneous within spectra of a same sample, but it varies significantly among spectra of different samples. Spectra collected with excitation wavelength 458 nm appear to be the most affected by noise. Indeed, both fluorescence and noise are very high for spectra of Orgueil IOM acquired with excitation wavelength 458 nm. We cannot use these spectra for the result analysis, and therefore they do not appear in Fig. 4.9. For both visible excitation wavelengths, we note similar signal intensity and signal to noise ratio between spectra of Isheyev microxenoliths PX-18, # 19 and # 25 and spectra of IOM. They suggest that these three Isheyev microxenoliths have a high content of organic matter. At the same time, it is evident that there are two distinct groups of spectra among Isheyev microxenoliths. Spectra of xenoliths # 28 and # 30 have far lower intensity than spectra of the three previous xenoliths. Note that none of Isheyev microxenoliths exhibits the signature of a significant degree of long duration thermal metamorphism, as observed in type 3 chondrites (Bonal *et al.*, 2006, 2007).

Subtraction of the fluorescence background and normalization give the spectra reported in Fig. 4.10. Normalized spectra of Isheyev microxenoliths # 28 and # 30 collected with visible excitation wavelengths have D bands more intense than the spectra of the other Isheyev microxenoliths, and they are also more distinct from the G band. Instead, in the UV spectra the D band is more easily visible in spectra of microxenoliths # 19, # 25 and PX-18, while it is less evident for microxenoliths # 28 and # 30.

We report here a preliminary analysis of our Raman spectra. Our first aim is to exploit spectra collected using different excitation wavelengths. For each sample and excitation wavelength, the value of a given spectral parameter has been estimated as the mean value of all the measured spectra. Our results are described below.

*Dispersion of  $\omega_G$ .* Our data (Fig. 4.11) show that dispersion of  $\omega_G$  is less important for spectra of Isheyev microxenoliths than for spectra of IOM extracted from carbonaceous chondrites. Hence, organic matter in Isheyev microxenoliths has apparently a different structure from IOM of carbonaceous chondrites. This result is particularly obvious in the case of the microxenoliths # 28 and # 30, on the basis of the UV spectra which are readily discriminated with the naked eye.

In Tab. 4.3 we report a tentative classification of our samples on the basis of the  $\omega_G$  dispersion, evaluated as the slope of a linear fit.

*Dispersion of  $\omega_D$ .* Two groups of samples can be identified (Fig. 4.12): PX-18, microxenolith # 19, microxenolith # 25 and IOM from Orgueil,

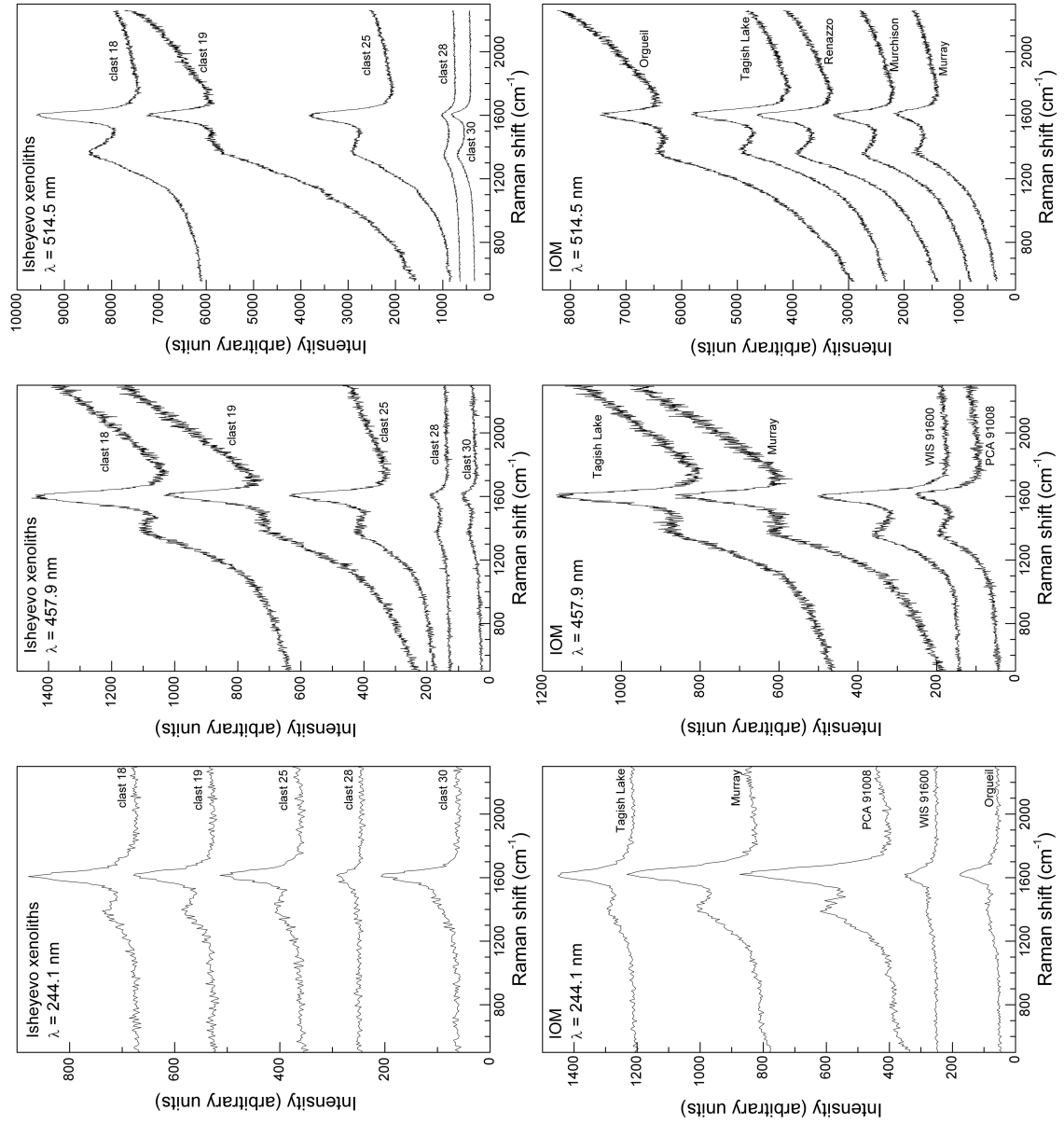


Figure 4.9: examples of Raman spectra

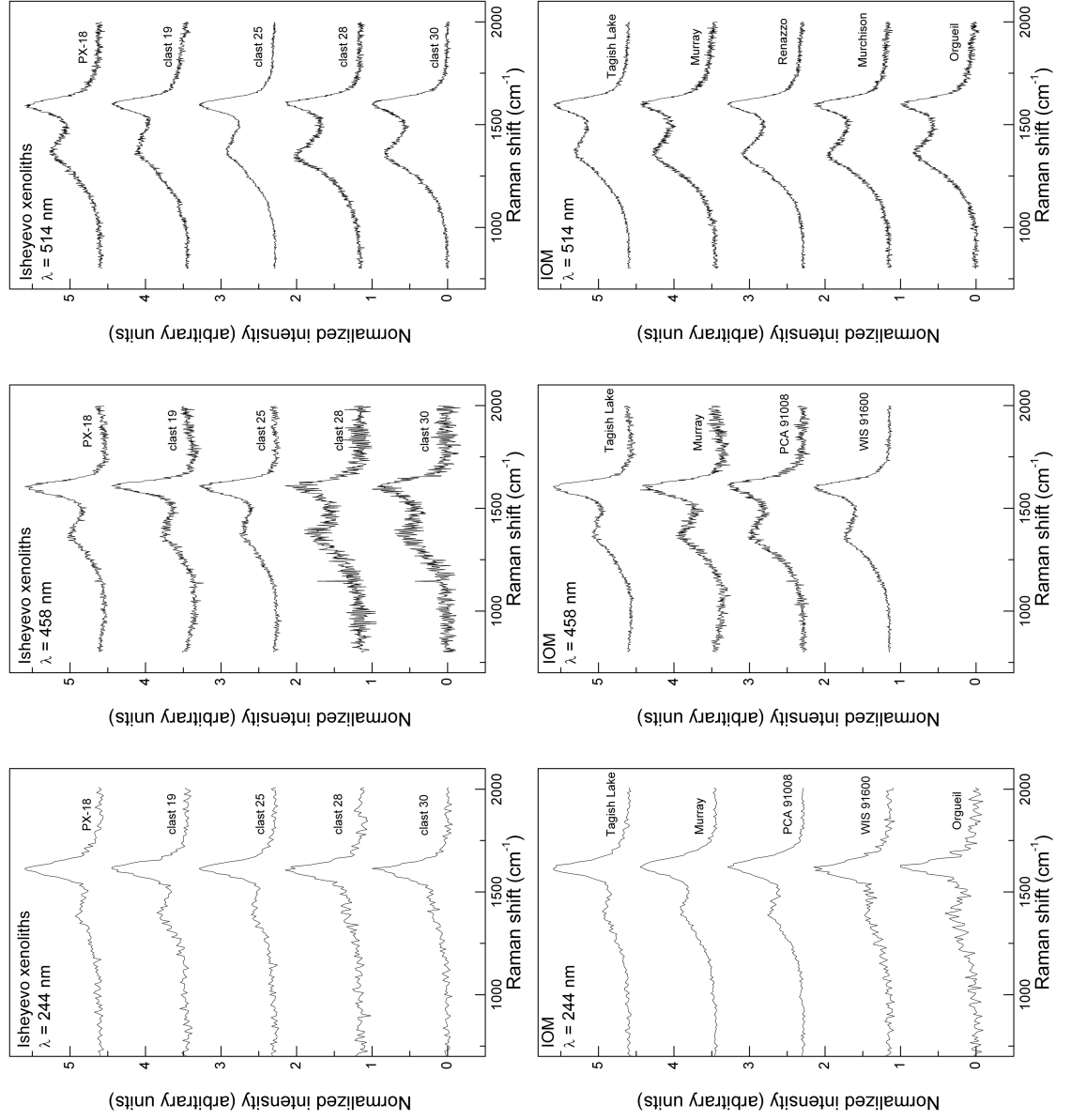
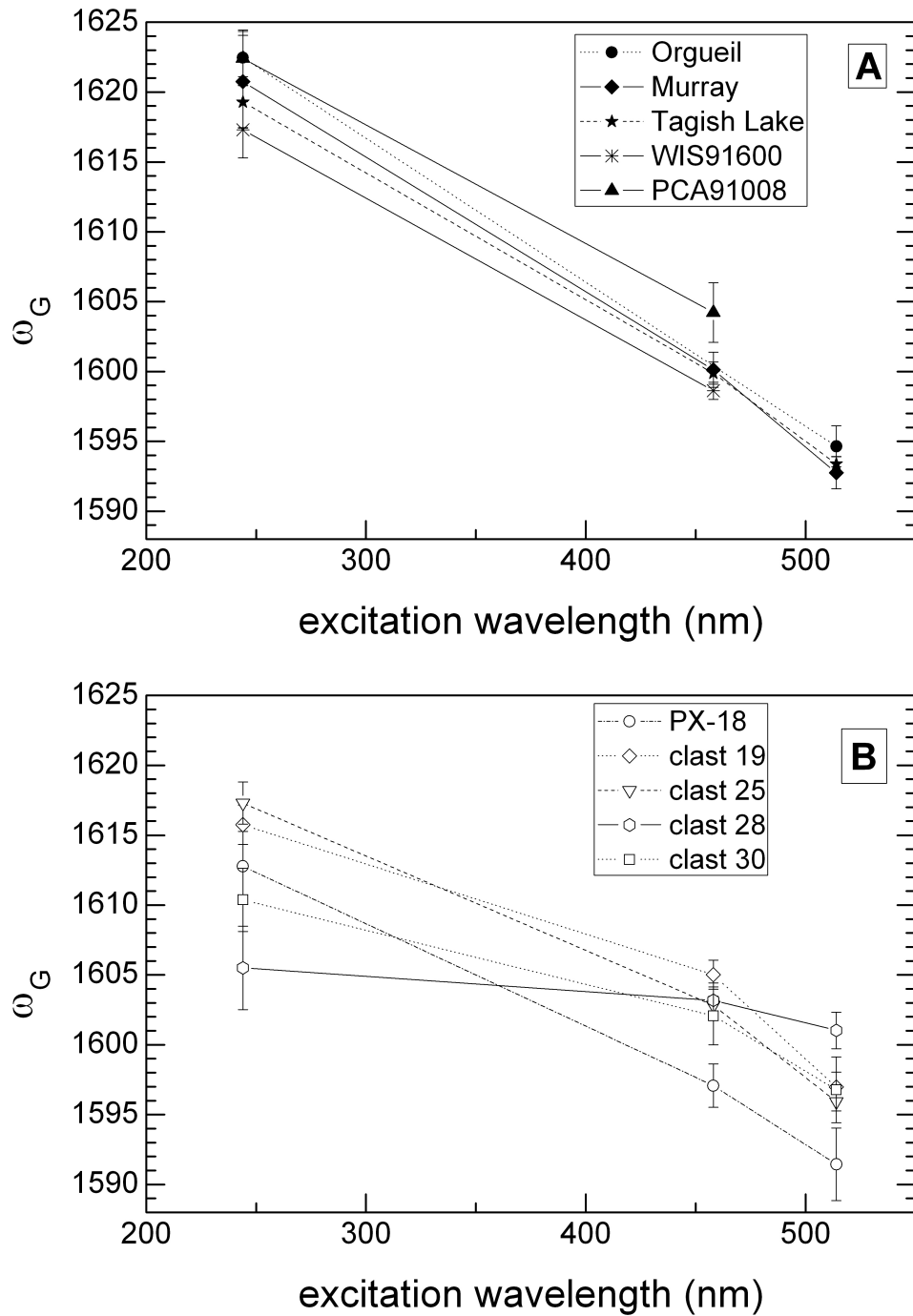
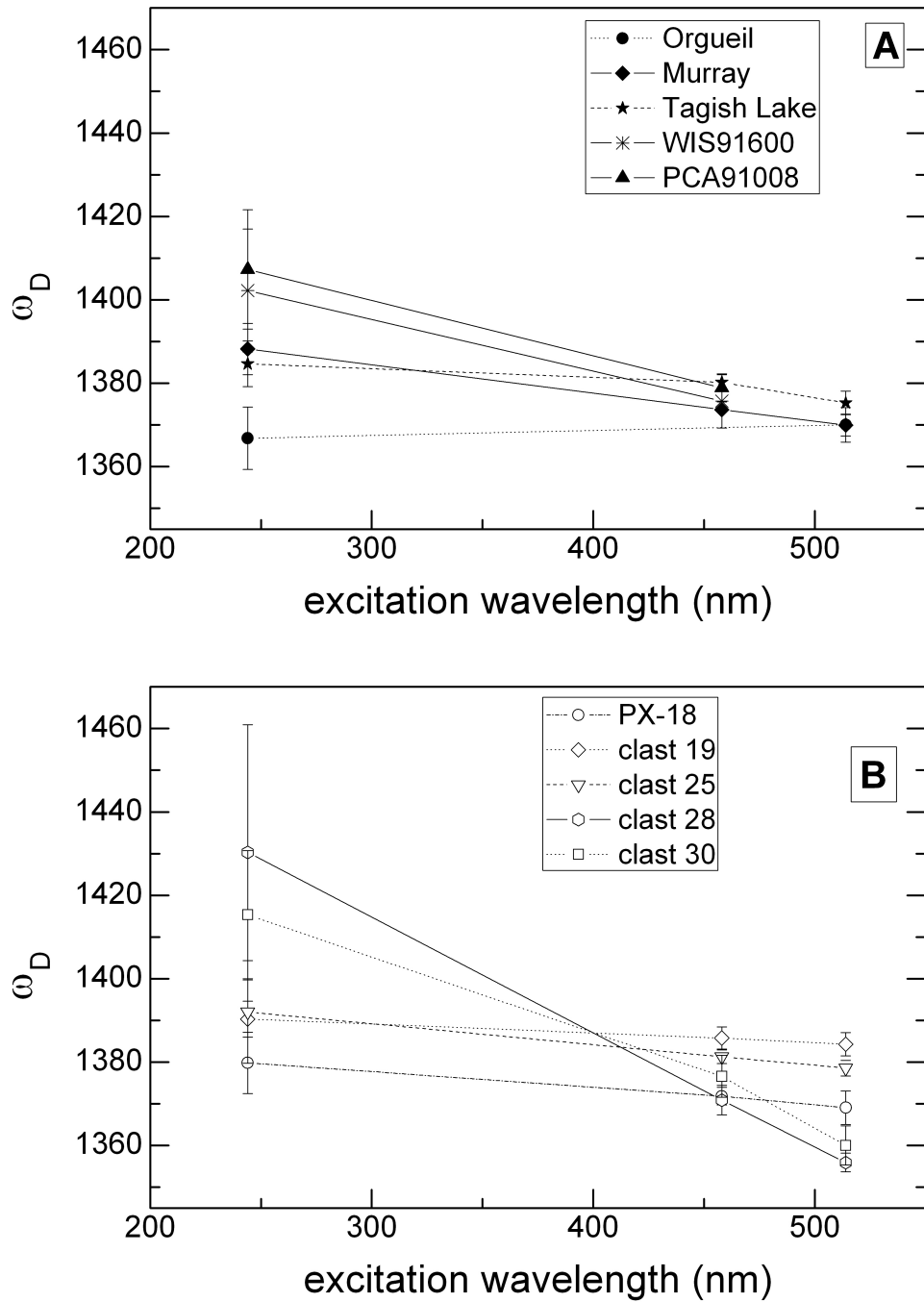


Figure 4.10: normalized Raman spectra



**Figure 4.11:** dispersion of  $\omega_G$  for A: carbonaceous chondrite IOM; and B: Isheyev microxenoliths. Each point is the mean value of all spectra measured for a given sample at a given excitation wavelength; error bars are the standard deviation.



**Figure 4.12:** dispersion of  $\omega_D$  for A: carbonaceous chondrite IOM; and B: Isheyevu microxenoliths. Each point is the mean value of all spectra measured for a given sample at a given excitation wavelength; error bars are the standard deviation.

**Table 4.3:** dispersion of spectral parameters  $\omega_G$  and  $\omega_D$ .

sample	$\omega_G$ disp. <sup>a</sup> ( $\times 10^{-3}$ )	sample	$\omega_D$ disp. <sup>a</sup> ( $\times 10^{-3}$ )
Murray	$-106 \pm 13$	Orgueil	12
Orgueil	-103	$\mu$ xen. 19	$-22 \pm 19$
Tagish Lake	$-98 \pm 7$	Tagish Lake	$-35 \pm 23$
WIS 91600	-87	PX-18	$-40 \pm 31$
PCA 91008	-85	$\mu$ xen. 25	$-49 \pm 34$
$\mu$ xen. 25	$-81 \pm 6$	Murray	$-68 \pm 25$
PX-18	$-76 \pm 12$	WIS 91600	-124
$\mu$ xen. 19	$-66 \pm 6$	PCA 91008	-133
$\mu$ xen. 30	$-47 \pm 11$	$\mu$ xen. 30	$-217 \pm 57$
$\mu$ xen. 28	$-17 \pm 12$	$\mu$ xen. 28	$-270 \pm 64$

<sup>a</sup> values without errors are evaluated using 2 points.

Tagish Lake, Murray, show little dispersion of  $\omega_D$ , while microxenolith # 28, microxenolith # 30 and IOM from PCA 91008 and WIS 91600 present a higher dispersion. The structure of organic matter is clearly different in these two groups of samples. In Tab. 4.3 we report the dispersion of  $\omega_D$  evaluated as the slope of a linear fit: it is possible to note the relatively large variation in  $\omega_D$  dispersion between Murray IOM ( $\omega_D$  dispersion =  $-68 \pm 25$ ) and WIS 91600 IOM ( $\omega_D$  dispersion = -124).

The trend depicted by dispersion of  $\omega_D$  does not correspond to that established by dispersion of  $\omega_G$ . However in both cases the two most distinct samples are organic matter in Isheyev microxenoliths # 28 and # 30. Also, IOM from the metamorphosed carbonaceous chondrites PCA 91008 and WIS 91600 results as the most altered among IOM samples.

*Dispersion of  $FWHM_G$ .* The dispersion of  $FWHM_G$  in our spectra (Fig. 4.13) is not monotonic, and appears less defined than the dispersion of  $\omega_G$  and  $\omega_D$ . Linear fits of these data (in order to establish a classification, as for dispersion of  $\omega_G$  and  $\omega_D$ ) have thus not been realized. However, we note that the Murray IOM exhibits a different value of  $FWHM_G$  with respect to that of Orgueil, though their IOM are expected to be fairly similar. This parameter was expected to be very reliable, because the G band is more intense than the D band, and therefore its width is expected to be unperturbed by the D band. The evaluation of these data needs to be revisited.

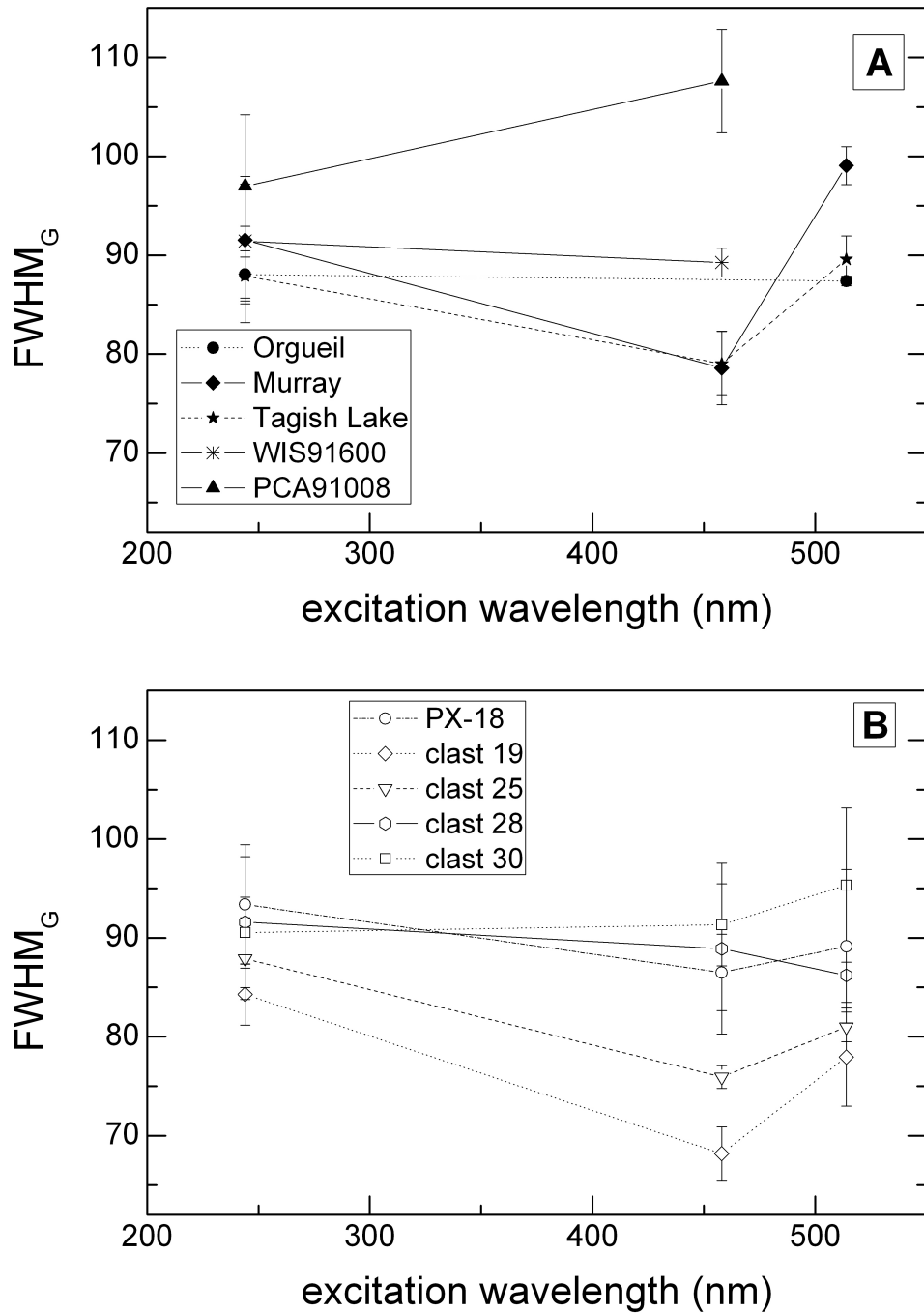


**Figure 4.13:** dispersion of  $FWHM_G$  for A: carbonaceous chondrite IOM; and B: Isheyevu microxenoliths. Each point is the mean value of all spectra measured for a given sample at a given excitation wavelength; error bars are the standard deviation.

## 4.7 Conclusions

Results obtained in this work for the dispersion of the spectral parameters  $\omega_G$  and  $\omega_D$  are reported in Tab. 4.3 and presented in Fig. 4.14. They demonstrate that the microxenoliths # 28 and # 30 have an organic matter different from that of PX-18 and microxenoliths # 19, # 25. The dispersion of the G and D band positions also suggests that the organic matter of the analyzed Isheyevite microxenoliths is not similar to carbonaceous chondrite IOM.

PCA 91008 and WIS 91600, which are classified as metamorphosed CM chondrites, have Raman features distinct from that of unmetamorphosed CM chondrites. However, their IOM is different from organic matter of Isheyevite microxenoliths. It is thus not possible to interpret these structural differences between Isheyevite and normal C1/C2 chondrites in terms of alteration processes or accretion of different precursors. Further measurements to complete and expand the present set of data, along with laboratory experiments, have been planned.

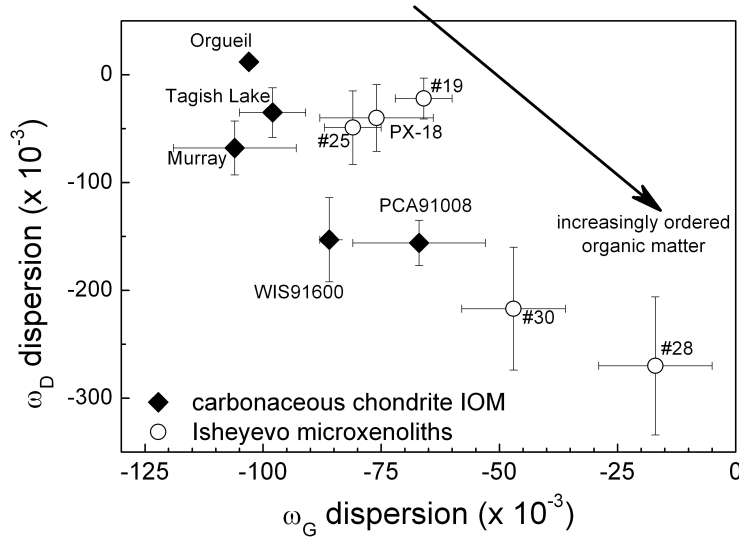


**Figure 4.14:** dispersion of spectral parameters  $\omega_G$  and  $\omega_D$  in organic matter of Isheyevite microxenoliths and in IOM extracted from carbonaceous chondrites.

## Chapter 5

# Interaction of micrometeoroids with the Earth atmosphere

### Summary of Chapter 5

A fundamental problem in astrobiology is the emergence of life on earth. For Astrophysics the question is if and how organic molecules abundant in space could have reached the Earth by means of extraterrestrial bodies. If this is the case, what extraterrestrial bodies were the carriers? And could their organic molecules have survived the atmospheric passage? Submillimetric micrometeoroids dominate the annual extraterrestrial mass flux toward the Earth. They show an unexpected ability to survive the atmospheric passage. We investigate the physical processes occurring when micrometeoroids cross the Earth atmosphere, to assess micrometeoroids possibility to reach the surface and to individuate the most effective processes that determine their fate, depending on entry conditions. Moreover we investigate the micrometeoroids-atmosphere interaction in early-Earth-like atmospheres, to understand if micrometeoroids could have contributed to the organic material inventory of the early Earth. We develop a general numerical model for the micrometeoroids-atmosphere interaction. Equation of motion, energy and mass balance are simultaneously solved with different entry conditions (micrometeoroids sizes, entry speeds and entry angles). The effects of physical processes are evaluated analysing their temporal evolutions and comparing their contributions to the energy and mass balance. The model is then applied to two early-Earth-like models of atmosphere and to the atmosphere of Titan, principally to test the role of different atmospheric density profiles. Low entry velocities and entry angles far from the vertical allow micrometeoroids to reach Earth surface. Among micrometeoroids that survive, our model individuate those that are not totally melted (unmelted

or partially melted micrometeorites) and those that are totally melted (cosmic spherules). Melting is the most effective mechanism to avoid extremely high temperatures. Sputtering is negligible for mass loss. Peak temperatures and final sizes are similar in the two early-Earth-like atmospheres and in the present day atmosphere. In contrast micrometeoroids survive more easily in the Titan atmosphere.

## 5.1 Introduction

Micrometeoroids (MMs) with dimensions between 25 and 500  $\mu\text{m}$  represent, by mass, the absolute majority in the Solar System minor bodies population at a distance of 1 AU from the Sun (Grün *et al.*, 1985) and in the flux of extra-terrestrial matter that enter the Earth's atmosphere in 1 year [ $4 \pm 2 \times 10^7$  kg/yr, Love and Brownlee (1993)]. Furthermore, micrometeoroids show an unexpected ability to survive to the interaction with the atmosphere, as demonstrated by the large number ( $\geq 10^5$ ) of micrometeorites recovered in Antarctica during the last 20 years (Engrand and Maurette, 1998; Duprat *et al.*, 2007). In addition, many of the recovered samples show a lower degree of alteration than what was expected: unmelted micrometeorites account for between 10 and 30% for particles  $>100 \mu\text{m}$ ,  $\sim 50\%$  for sizes between 50 and 100  $\mu\text{m}$  and up to 78% in the size range 25-50  $\mu\text{m}$  (Genge *et al.*, 2008).

Of special interest is that these objects could have been involved in the emergence of life on Earth. Micrometeoroids are rich in C and N, and the distributions of these elements in recovered samples suggest they are bound together in organic matter (Matrajt *et al.*, 2003). Thus, micrometeoroids may have been the dominant source of organic carbon on the primitive Earth. Moreover, the total amount of volatiles (N, Ne, H<sub>2</sub>O, CO<sub>2</sub> and SO<sub>2</sub>) released by micrometeoroids in the atmosphere during the  $\sim 100$  My of the so-called sterilization period (after the Earth formation 4.45 Gy ago) have been calculated (Maurette *et al.*, 2000, 2001; Maurette, 2006, 2009). For this, critical assumptions are that the early micrometeorite flux is proportional to the lunar impact cratering rate and that this rate has decreased exponentially since the time of Earth formation (this exponential decreasing is still matter of debate, see e.g. Chapman *et al.* 2007). The resulting estimates of micrometeoroid-delivered volatiles are sufficient to explain the amounts of these elements observed today. Assuming a more conservative micrometeoroid flux between 4.4 and 3.8 Gy ago, and with new data for the N content of micrometeorites, Marty *et al.* (2005) evaluated that micrometeoroids delivered  $\sim 10\%$  of the present N to Earth. This support the idea that micrometeoroids could have contribute to the formation of terrestrial atmosphere and oceans. The possible role of micrometeoroids as conveyors of amino acids and nucleo-bases is less clear. Thus far only one extrater-

restrial amino acid,  $\alpha$ -amino isobutyric acid, has been found in antarctic micrometeorites (Brinton *et al.*, 1998; Matrajt *et al.*, 2004). The absence of amino acids in other samples may be due to the heating they experienced during atmospheric entry, when micrometeoroid temperatures reach values at which organic species sublime or decompose. On the other hand experiments have demonstrated that amino acids present in micrometeoroid-analogues (i.e., grains from the CM chondrite Murchison) can be released from micrometeoroids as their temperature rises, and hence they can survive to the atmospheric entry (Glavin and Bada, 2001).

In light of these considerations it seems worthwhile to investigate the processes occurring during the passage of micrometeoroids through the atmosphere. The complexity of a comprehensive treatment, that include physical, mineralogical and bio-chemical aspects, appears to be the reason why a general and detailed model of the micrometeoroids-atmosphere interaction has not yet been realized. We approach this problem in a holistic way, considering those processes that can be the most important and highlighting their relative contributions with different atmospheric entry conditions. To evaluate the importance of the atmosphere properties (and in particular of the density profile) we use two models of the early Earth atmosphere and the atmosphere of Titan [from the Huygens probe, see e.g. Fulchignoni *et al.* (2005) and Aboudan *et al.* (2008)]. This work is, however, not an exhaustive analysis of the micrometeoroids-atmosphere interaction: our goals are (a) to highlight the necessity of a general study (b) to propose a model that includes different physical processes and to analyse their respective contributions (c) to delineate the most critical aspects of the problem and (d) to evaluate the possibility for micrometeoroids to reach the surface of the early Earth.

## 5.2 The model: properties of micrometeoroids and present-day atmosphere

We treat micrometeoroids as spheres, with radius  $r_{\text{MM}}$ . Their initial radii are assumed to be between  $25 \mu\text{m}$  and  $500 \mu\text{m}$ . The upper limit of  $500 \mu\text{m}$  is due to the hypothesis of isothermal micrometeoroids, i.e. we assume that a micrometeoroid is sufficiently small to reach at every moment in its flight a uniform temperature  $T_{\text{MM}}$  by heat conduction. Actually thermal gradients develop within micrometeoroids due to endothermic reactions [e.g. phase transitions, see Flynn (1995b)] and are observed in recovered micrometeorites (Toppani *et al.*, 2001; Genge, 2006a). But a treatment of micrometeoroids internal temperature distribution is beyond the goals of the present work. The minimum radius chosen in the simulations is  $5 \mu\text{m}$ , i.e. if the radius become less that  $5 \mu\text{m}$  simulations are stopped. This value follows from the emission properties of micrometeoroids: namely, in

order to characterize micrometeoroids with a constant emissivity, their dimensions must be larger than the wavelength of the emitted and adsorbed radiation. Since a micrometeoroid generally absorbs radiation in the VIS - UV range (200 - 800 nm) and emits IR radiation (at temperatures of  $\sim 1000$  K) with  $\lambda \approx 3 \mu\text{m}$  (Coulson and Wickramasinge, 2003), simulations end if  $r_{\text{MM}}$  reaches  $5 \mu\text{m}$ . For micrometeoroids structure and composition, being very difficult to reproduce their particular characteristics and all the mineralogical processes that happen during the atmospheric passage (Greshake *et al.*, 1998; Genge *et al.*, 2008), we assume that they are composed entirely of silicates and phyllosilicates, the major component observed in Antarctic micrometeorites. We choose consequently the values of the micrometeoroid thermodynamic parameters, as described below. In addition, we assume that organic matter is present in micrometeoroids, and that its fraction remains constant during the interaction with the atmosphere. Hence, surviving micrometeoroids are considered to deliver their organic content to Earth. However, here we do not treat in detail the role of organic matter in the micrometeoroids-atmosphere interaction [see e.g. Flynn (1995b)] nor its fate once on Earth. The micrometeoroid density  $\rho_{\text{MM}}$  is assumed to be constant during the atmospheric flight. We tested two different values for  $\rho_{\text{MM}}$ , 3 and 1 g/cm<sup>3</sup>, measured for compact coarse-grained micrometeorites and porous micrometeorites, respectively (Genge *et al.*, 2008). Similar values are adopted in some recent models (Campbell-Brown and Koschny, 2004; Rogers *et al.*, 2005).

The properties of the present day Earth atmosphere (the profiles of density and the concentration of neutral components as height function), are taken from the MSISE-90 model (Hedin, 1991). We include 6 species of atmospheric particles: N<sub>2</sub>, O, O<sub>2</sub>, Ar, He, H (adding CO<sub>2</sub> and CH<sub>4</sub> for the primordial atmosphere, see section 5.7). The atmospheric properties determine also how a micrometeoroid moves in the atmosphere: because the mean free path of an atmospheric particle, at heights between 60 and 200 km (those of interest in this work), is always longer than the micrometeoroid radius, we apply the free molecular flow regime. In other words, micrometeoroids always interact with single atmospheric atoms and molecules, and there is not a gas layer that protects them from collisions (Sorasio *et al.*, 2001; Campbell-Brown and Koschny, 2004). The characteristics of the models adopted for the early Earth atmosphere and of the Titan atmosphere will be described in section 5.7.

### 5.3 The model equations

The two dimensional micrometeoroid trajectory is described by  $h$  (height from the Earth surface) and  $z$  (angle with respect to the zenith direction).

The equations that describe their evolution are:

$$\frac{dh}{dt} = -v_{\text{MM}} \cos z \quad (5.1)$$

and

$$\frac{dz}{dt} = -\frac{\sin z}{v_{\text{MM}}} \left( g(h) - \frac{v_{\text{MM}}^2}{R_{\oplus} + h} \right) \quad (5.2)$$

where  $v_{\text{MM}}$  is the micrometeoroid velocity,  $g(h)$  is the gravitational acceleration at height  $h$  and  $R_{\oplus}$  is the Earth radius. The initial value of  $h$  for simulations in the present-day atmosphere is 400 km: above this height the atmospheric density is low enough to be negligible. For the entry angle, different values have been tested ( $0^\circ$ ,  $45^\circ$  and  $70^\circ$ ). For entry angle larger than  $70^\circ$ , micrometeoroids tend to be skip back in space. The initial value ( $v_{\text{in}}$ ) of the micrometeoroid velocity  $v_{\text{MM}}$  is a free parameter: it can be between 11.2 km/s and 72.8 km/s (Ceplecha *et al.*, 1998).

Collisions with atmospheric atoms and molecules determine the micrometeoroid velocity  $v_{\text{MM}}$ . To evaluate this effect we neglect the thermal velocity of atmospheric particles ( $\sim 370$  m/s for  $T_{\text{atm}} = 160$  K at  $h = 100$  km) with respect to  $v_{\text{MM}}$ . Including also the Earth gravitational attraction  $g(h)$ , we obtain the following equation:

$$\frac{dv_{\text{MM}}}{dt} = -\frac{\Gamma}{M_{\text{MM}}} S \rho_{\text{atm}}(h) v_{\text{MM}}^2 + g(h) \cos z \quad (5.3)$$

where  $S = \pi r_{\text{MM}}^2$  is the micrometeoroid transverse section,  $M_{\text{MM}}$  is the micrometeoroid mass,  $\rho_{\text{atm}}(h)$  is the atmospheric density as a function of altitude and  $\Gamma$  is the drag coefficient, that describes the momentum fraction transferred to a micrometeoroid in a single collision. Its value can be between 0 and 2 (2 for elastic collisions) and we assume  $\Gamma = 1$  (Campbell-Brown and Koschny, 2004; Rogers *et al.*, 2005).

The heart of our model is the description of how micrometeoroids acquire energy and of the processes triggered by this energy. Micrometeoroids acquire energy by collisions with atmospheric atoms and molecules. As described above, the thermal motion of these particles is negligible with respect to the micrometeoroid speed  $v_{\text{MM}}$ . Hence the heating rate is:

$$\frac{dE_{\text{coll}}}{dt} = \frac{\Lambda}{2} S \rho_{\text{atm}}(h) v_{\text{MM}}^3 \quad (5.4)$$

where  $\Lambda$  is the heat transfer coefficient, that describes the fraction of the kinetic energy of an incoming particle that is transferred to the target. Its value depends on the micrometeoroid temperature and on the ratio of the micrometeoroid velocity  $v_{\text{MM}}$  to the atmospheric particle thermal velocity  $v_{\text{th}}$  (Hood and Horanyi, 1991; Melosh and Goldin, 2008). However, in the

limit  $v_{\text{MM}} \gg v_{\text{th}}$ ,  $\Lambda$  remains close to unity (see section 5.6 for a discussion) and we therefore assume  $\Lambda = 1$ , as also in recent models for the atmospheric entry of small meteoroids (Campbell-Brown and Koschny, 2004; Rogers *et al.*, 2005). A second possible source of energy for micrometeoroids can be the radiation coming from the Sun [as proposed in Moses (1992); McAuliffe and Christou (2006)] and from the atmosphere itself. We did not include this term in our energy balance because for meteoroids small as micrometeoroids it is negligible. We estimated the contribution of Sun and atmosphere radiation for  $r_{\text{in}} = 500 \mu\text{m}$ ,  $v_{\text{in}} = 11.2 \text{ km/s}$ ,  $z_{\text{in}} = 45^\circ$ ,  $\rho_{\text{MM}} = 3 \text{ g/cm}^3$ . Energy acquired by radiation is dominant only in the first part of the micrometeoroid flight (by 3 orders of magnitude at the very beginning) but it becomes negligible, as in previous models (Moses, 1992), when denser atmospheric layers are reached, i.e. when the collision rate increases. The result is that micrometeoroid temperature is determined by energy acquired from collisions: peak temperature and final size of micrometeoroids do not change when energy acquired by radiation is considered.

As a micrometeoroid acquires energy from collisions with atmospheric particles its temperature increases. This causes the onset of processes like evaporation and melting of the micrometeoroid material, which determine a reduction of its mass and dimensions. Here the word evaporation refers to the direct passage of micrometeoroid material from solid to gas phase. Evaporated mass is assumed to be immediately lost. Also, we assume that the evaporation process begins as soon as micrometeoroids start to acquire energy from collisions (Moses, 1992; Campbell-Brown and Koschny, 2004; Rogers *et al.*, 2005). For this reason we describe the rate of mass loss by evaporation as a function of the micrometeoroid temperature using the Knudsen-Langmuir formula (Bronshten, 1983):

$$\left(\frac{dM_{\text{MM}}}{dt}\right)_{\text{evap}} = S \sqrt{\frac{\mu}{2\pi k_{\text{B}} T_{\text{MM}}}} \times 10^{(A-B/T_{\text{MM}})} \quad (5.5)$$

where  $k_{\text{B}}$  is the Boltzmann constant. Here the relation  $\log_{10}(p_{\text{sat}}) = A - B/T_{\text{MM}}$  (solution of the Clausius-Clapeyron equation) is used to evaluate the micrometeoroid pressure of saturated vapour as function of their temperature. For the coefficients A and B the values  $A = 10.6$  and  $B = 13500 \text{ K}$  have been assumed (Love and Brownlee, 1991). We adopt  $\mu = 45 \text{ amu}$  for the mean atomic mass of micrometeoroid components. This is the value estimated for micrometeoroids with chondritic composition (Love and Brownlee, 1991).

Dimensions of micrometeoroids are reduced also by loss of melted portions of their mass. When high temperatures (between  $\sim 1500$  and  $\sim 2000 \text{ K}$ ) are reached, portions of the micrometeoroid material undergo the passage from solid to liquid phase. Here we assume that the melted mass is completely lost. We have to point out that the very complex composition of

micrometeoroids means also that their different components have different melting points. Therefore, different portions of a micrometeoroid can start to melt when others remain solid. To account for such a mass loss we use a term proportional to the energy acquired by micrometeoroids, as suggested by Campbell-Brown and Koschny (2004). We want the rate of mass loss due to melting to be effectively different from zero only if  $T_{\text{MM}} \approx T_{\text{melt}} =$  micrometeoroid melting temperature. Hence we use the parametric coefficient  $P_{\text{spall}}$ , defined as

$$P_{\text{spall}} = 0.5 + \frac{\arctan(T_{\text{MM}} - T_{\text{fus}})}{\pi} \quad \text{for } T_{\text{MM}} < T_{\text{melt}}$$

$$P_{\text{spall}} = 0.5 + \frac{\arctan[4(T_{\text{MM}} - T_{\text{fus}})]}{4\pi} \quad \text{for } T_{\text{MM}} > T_{\text{melt}}.$$

This coefficient has been introduced by Campbell-Brown and Koschny (2004), but in their work its value rapidly reaches 1 for  $T_{\text{MM}} > T_{\text{melt}}$ , which is equivalent to assume that all the incoming energy is used to melt the micrometeoroid mass. To take into account that melting always has to share the incoming energy with the other processes included in the energy balance, we adopt a form of  $P_{\text{spall}}$  which allows to limit its value to 0.625 (the two different expression make  $P_{\text{spall}}$  a continuous function of  $T_{\text{MM}}$ , this avoids problems in the numerical integration). The assumed value for the micrometeoroid melting temperature is  $T_{\text{melt}} = 1623$  K. This is similar to values adopted in previous works (Bonny and Balageas, 1990; Love and Brownlee, 1991; Flynn, 1992; Scarsi, 2004) and is the melting point of silicates that represent the dominant phases in micrometeoroids. The rate of mass loss caused by melting is thus described by

$$\left( \frac{dM_{\text{MM}}}{dt} \right)_{\text{melt}} = \frac{P_{\text{spall}}}{H_{\text{melt}}} \left( \frac{dE_{\text{coll}}}{dt} \right) \quad (5.6)$$

where  $H_{\text{melt}} = 2.65 \times 10^5$  J/kg is the latent heat of melting for stony meteoroids (Love and Brownlee, 1991).

The third process by which micrometeoroids can lose mass is sputtering, which is the removal of atoms or molecules (targets) by collisions with incident particles (projectiles) of sufficient energy. This mechanism has been proposed to explain high altitude meteors (Brosch *et al.*, 2001) and previous works suggest it can cause significant mass loss (Rogers *et al.*, 2005). In order to evaluate the amount of mass lost by sputtering, we must evaluate the sputtering yield  $Y$ , i.e. the number of target atoms or molecules removed by each projectile impact. To calculate  $Y$  we chose a semi-empirical formula suggested by Draine and Salpeter (1979), again using  $\mu = 45$  amu as mass of the target particles and  $U_0 = 5.7$  eV as the binding energy per atom/molecule [this value is that indicated for a silicate compound in

Draine and Salpeter (1979)]. Indicating by  $s$  the total number of atmospheric species considered, the rate of mass loss by sputtering is:

$$\left(\frac{dM_{\text{MM}}}{dt}\right)_{\text{sputt}} = \mu S v_{\text{MM}} \sum_{i=1}^s n_i Y_i \quad (5.7)$$

where  $n_i$  is the number density of the  $i^{\text{th}}$  atmospheric species.

The three processes described above (evaporation, melting and sputtering) are properly considered in the energy balance, i.e. the equation that allows us to track the micrometeoroid temperature evolution. As emphasized by Love and Brownlee (1991), it is essential to include these terms in the energy balance to properly evaluate the micrometeoroid temperature evolution. An important feature of our model is that the contributions of melting and evaporation are treated separately.

To insert sputtering in the energy balance the problem is to evaluate the fraction  $\eta$  of the incoming energy that is used for sputtering and not for the other processes. Popova *et al.* (2007) estimated that particles removed by sputtering have a kinetic energy varying from 0% of the energy supplied by collisions (when the micrometeoroid entry velocity is  $< 20$  km/s) to 20% (when micrometeoroids enter the atmosphere at 70 km/s), and that the rest of the energy contributes to the rise of micrometeoroid temperature, which causes the emission of radiation and ablation processes. Based on this, and considering that, in addition to the kinetic energy of the sputtered particles, a part of the incoming energy must be used to remove these particles, we assume  $\eta = 0.15$  for every value of the micrometeoroid entry speed.

Beyond processes responsible for the mass loss, the rise of micrometeoroid temperature causes also an intense emission of radiation, which is fundamental for the micrometeoroid thermal balance, unlike for larger meteoroids. As described in section 5.2, we assume micrometeoroids have a constant emissivity; its value is  $\epsilon = 0.9$ , as suggested in Campbell-Brown and Koschny (2004).

Finally we add to the energy balance a term for the kinetic energy of the ablated mass. As proposed in Campbell-Brown and Koschny (2004), we assume that the ablated micrometeoroid mass moves away with a velocity determined by the micrometeoroid temperature  $T_{\text{MM}}$ . The energy balance is thus given by:

$$\begin{aligned} \frac{\Lambda}{2} S \rho_{\text{atm}}(h) v_{\text{MM}}^3 &= c M_{\text{MM}} \frac{dT_{\text{MM}}}{dt} + 4\pi r_{\text{MM}}^2 \epsilon \sigma T_{\text{MM}}^4 + H_{\text{evap}} \left(\frac{dM_{\text{MM}}}{dt}\right)_{\text{evap}} + \\ &+ H_{\text{melt}} \left(\frac{dM_{\text{MM}}}{dt}\right)_{\text{melt}} + \frac{\Lambda}{2} S v_{\text{MM}}^3 \sum_{i=1}^s (\eta_i n_i m_i) + \frac{1}{2} \left(\frac{dM_{\text{MM}}}{dt}\right)_{\text{abl}} \frac{3k_{\text{B}} T_{\text{MM}}}{\mu} \end{aligned} \quad (5.8)$$

where  $\sigma$  is the Stefan-Boltzmann constant,  $\eta_i$ ,  $n_i$  and  $m_i$  are the sputtering coefficient, number density and mass, respectively, of the six atmospheric components considered. Such expression for the energy used in sputtering takes into account that, depending on the collision velocity, sputtering can be caused only by some of the atmospheric species, and not always by all of them. For the thermodynamic properties of micrometeoroids we adopt values suggested in Bronshten (1983) and Love and Brownlee (1991) for stony meteoroids:  $c = 10^3$  J/(kg K) is the micrometeoroid specific heat,  $H_{\text{evap}} = 6.05 \times 10^6$  J/kg is the latent heat of vaporization.

The value of each term present in equation 5.8 is tracked all along the numerical integrations. In this way it is possible to understand which of these terms are the most effective in determining the micrometeoroid fate and how their roles change with different entry conditions.

## 5.4 Numerical integration and validation of our code

Numerical integrations were performed using the RK4 method with an adaptive stepsize. For each quantity calculated (i.e., micrometeoroid height, angle with respect to the vertical, speed, radius, mass and temperature) at every integration step we require a minimum relative variation of  $5 \times 10^{-5}$ , and the maximum relative variation allowed is  $10^{-3}$ . If relative variations are too small then the integration stepsize is doubled for the next calculation (with a superior limit of 1 s imposed); if variations are too large then the calculated values are rejected and the integration stepsize is divided by 2 for the next calculation (with a inferior limit of  $10^{-10}$  s imposed).

With our numerical code we were able to reproduce results of previous works. In Love and Brownlee (1991) several micrometeoroid temperature vs time profiles are showed. Due to differences in micrometeoroid initial temperature and in atmospheric properties with respect to that work, we choose the difference between micrometeoroid peak temperatures as parameter for a comparison (i.e. the difference between the peak temperatures of micrometeoroids that have equal entry speed, angle and density, but with different initial size). Introducing the set of equations of Love and Brownlee (1991) in our numerical code, we obtain peak temperature differences that differ from the original ones for less than 9%.

A second comparison has been made with results presented in Rogers *et al.* (2005), which focus on mass lost by sputtering. The fractional mass lost by sputtering for asteroidal micrometeoroids ( $\rho_{\text{MM}} = 3$  g/cm<sup>3</sup>) and for cometary micrometeoroids ( $\rho_{\text{MM}} = 1$  g/cm<sup>3</sup>) with value of entry speed ranging between 20 and 70 km/s has been calculated by our numerical code using the same set of equations of Rogers *et al.* (2005). The maximum difference between our results and those of Rogers *et al.* (2005) is 6%.

**Table 5.1:** Maximum values of entry velocity for which micrometeoroids are able to survive and reach the Earth surface.

$r_{\text{in}}$ ( $\mu\text{m}$ )	$v_{\text{in}}^{\text{max}}$ (km/s)			
	$\rho_{\text{MM}} = 3 \text{ g/cm}^3$		$\rho_{\text{MM}} = 1 \text{ g/cm}^3$	
	$z_{\text{in}} = 0^\circ$	$z_{\text{in}} = 45^\circ$	$z_{\text{in}} = 70^\circ$	$z_{\text{in}} = 45^\circ$
25	16	17	22	22
50	15	16	21	21
100	13	14	20	20
200	12	13	18	18
300	11.2	12	16	16
400	-	12	15	15
500	-	11.2	14	14

## 5.5 Results

Our simulations highlight how decisive entry conditions are. Tab. 5.1 summarizes the maximum values of  $v_{\text{in}}$  that allow the survival of micrometeoroids with different entry radii, angles and densities. It is evident that 1) smaller micrometeoroids can have higher values of entry speed than larger micrometeoroids; 2) low density micrometeoroids can have higher values of entry speed than denser micrometeoroids and 3) micrometeoroids with shallow entry angle (i.e. far from the vertical) can have larger values of entry speed than micrometeoroids with steep entry angle (i.e. close to the vertical).

In Fig. 5.1 (all figures refer to micrometeoroids with  $\rho_{\text{MM}} = 3 \text{ g/cm}^3$ ) it is shown the size evolution of a  $50 \mu\text{m}$  initial radius micrometeoroid that enter the atmosphere with different values of  $v_{\text{in}}$ : it is clear that for larger values of the initial velocity smaller final radii are attained. For  $v_{\text{in}} = 11.2 \text{ km/s}$  the final micrometeoroid size is  $28 \mu\text{m}$ , i.e. the micrometeoroid lost  $\sim 82\%$  of its initial mass, while for  $v_{\text{in}} = 16 \text{ km/s}$  the final micrometeoroid radius is  $7 \mu\text{m}$  (the mass lost is  $99\%$ ). This happens because for higher initial velocities micrometeoroids acquire more energy from collisions with atmospheric atoms and molecules, so they reach higher temperatures and also sustain larger mass loss. Another important feature evident in Fig. 5.1 is that micrometeoroids shrink from their initial to their final size in a limited height interval ( $\sim 15 \text{ km}$  for the cases reported Fig. 5.1). Such a height interval corresponds to a time period of only few seconds. The same is true for the time evolution of micrometeoroid velocity. After a first phase in which the velocity remains almost constant, micrometeoroids are suddenly decelerated when they encounter sufficiently dense atmospheric layers. The height at which micrometeoroids start to be decelerated is higher for larger entry radii and velocities. But the time interval in which micrometeoroids

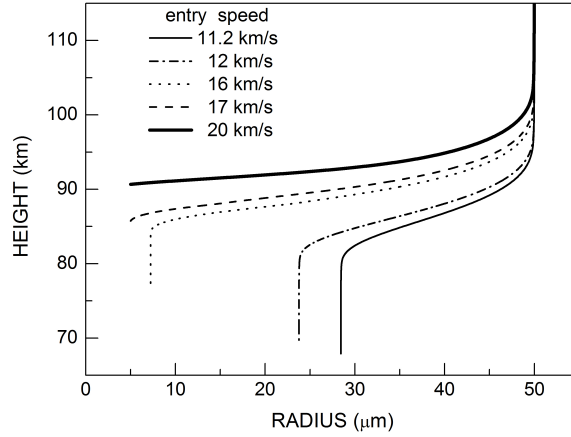


**Figure 5.1:** Evolution of micrometeoroid radius with height. For an initial radius of  $50 \mu\text{m}$  and an entry angle of  $45^\circ$ , different values of the entry speed are considered. For  $v_{\text{in}} < 16 \text{ km/s}$  micrometeoroids are not destroyed and reach their final radius at a height of  $\sim 80 \text{ km}$ , i.e. at this height they settled in the atmosphere and then they can reach Earth surface. For larger entry speed, micrometeoroids are destroyed before they can be decelerated.

change from their initial to their final velocity is generally small. A micrometeoroid with  $r_{\text{in}} = 50 \mu\text{m}$ ,  $v_{\text{in}} = 11.2 \text{ km/s}$ ,  $z_{\text{in}} = 45^\circ$  and  $\rho_{\text{MM}} = 3 \text{ g/cm}^3$  is slowed down to  $1 \text{ km/s}$  in  $\sim 4 \text{ s}$ , and then reaches its final velocity of  $\sim 100 \text{ m/s}$  in  $\sim 30 \text{ s}$ . For  $r_{\text{in}} = 300 \mu\text{m}$ ,  $v_{\text{in}} = 12 \text{ km/s}$ ,  $z_{\text{in}} = 45^\circ$  and  $\rho_{\text{MM}} = 3 \text{ g/cm}^3$  a micrometeoroid is slowed down to  $1 \text{ km/s}$  in only  $\sim 2.5 \text{ s}$ .

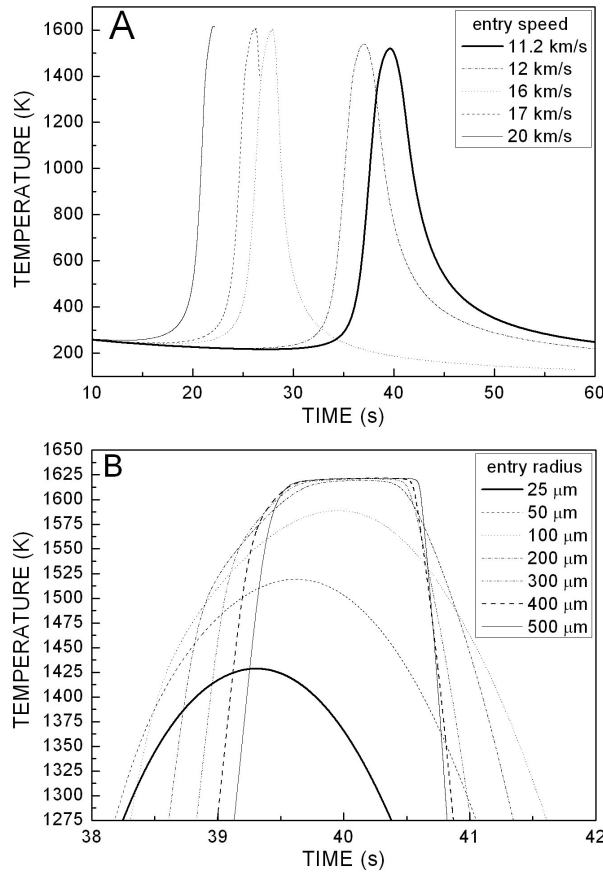
The effects of the atmospheric entry are attenuated for micrometeoroids that have grazing trajectory (i.e. with large angles with respect to the vertical) or a lesser density. When a micrometeoroid has a trajectory far from the vertical, it is decelerated more gradually. In particular, its velocity (and therefore the rate of collisions) is reduced before the beginning of intensive ablation. Hence the maximum temperature is smaller and the final radius is larger than in the case of steeper entry angle. Similarly, micrometeoroids with low density values ( $1 \text{ g/m}^3$ ) are decelerated at higher altitude where the atmospheric density is low, which is why their final radius is larger.

Analyzing the thermal evolution of micrometeoroids during the atmospheric passage is essential for understanding the alterations they suffer and also to check whether the organic molecules they include can survive. Typical temperature histories are shown in Fig. 5.2A: the shape of each curve is that of a pulse heating, i.e. a temperature rise as rapid as the following cooling, with the whole process lasting only few seconds. The initial slight decrease is due to the efficiency of radiation emission and to the scarcity of collisions in the high layers of the atmosphere (micrometeoroid temperature would not decrease in the first phases of atmospheric entry if we included energy from radiation of Sun and atmosphere in the energy balance. However this contribution has negligible effects on micrometeoroid peak temperatures and final sizes, as explained in section 5.3). When micrometeoroids arrive in denser atmospheric layers ( $h \sim 100 - 120 \text{ km}$ ) their temperature

rapidly rises because of the increased number of collisions with atmospheric particles. After the maximum,  $T_{\text{MM}}$  decreases very rapidly because the collisional heating is reduced as micrometeoroids slow down and shrink. The temperature increase as well as the heating pulse are more rapid for larger initial speeds. Taking the full width at half the maximum temperature as parameter to evaluate the duration of the heating pulse, micrometeoroids in Fig. 5.2A suffered heating pulses of 5.78 s (for  $v_{\text{in}} = 11.2$  km/s), 5.25 s (for  $v_{\text{in}} = 12$  km/s) and 3.15 s (for  $v_{\text{in}} = 16$  km/s). Fig. 5.2A shows that for increased entry velocities peak temperatures are reached earlier. However, the height of peak temperature is about the same: 86 km for  $v_{\text{in}} = 11.2$  km/s, 88 km for  $v_{\text{in}} = 16$  km/s. Fig. 5.2A and B show that higher entry speeds as well as larger initial radii imply larger values of peak temperature. However differences in peak temperatures are somewhat limited. Comparing Fig. 5.2A and B with Fig. 5.1 it is clear that the value of final radius is more sensitive to differences in entry speed. Such results are due to the action of the melting process that, on one hand, limits the maximum temperature values (Fig. 5.2B) and, on the other hand, implies significant mass loss.

Fig. 5.2B shows temperature profiles for different values of the initial radius (with  $v_{\text{in}} = 11.2$  km/s). Again, for larger  $r_{\text{in}}$  higher peak temperatures are reached. In Fig. 5.2B it is also visible a clear difference between two classes of profiles. For  $r_{\text{in}} \leq 100 \mu\text{m}$  the temperature curves have a regular, rounded shape. In contrast, for  $r_{\text{in}}$  between 200 and 500  $\mu\text{m}$  the top of the curves is clearly flattened. This flattening is due to melting of micrometeoroid material: when micrometeoroid temperatures approach the melting point, the term relative to melting in the energy balance becomes important and prevents further temperature increments. This is a general characteristic of our results, and it is not linked only to different entry radii, but it appears for several combinations of entry conditions. These two classes of temperature profiles can be interpreted as two different fates for micrometeoroids. When the peak temperature is clearly below the melting point and the temperature profile does not flatten, then the corresponding micrometeoroid survive and can reach the Earth surface without been totally melted. These micrometeoroids are therefore those that are recovered as unmelted micrometeorites [see e.g. Genge *et al.* (2008)]. The other class of temperature profiles, with flatten peak near the melting point, correspond to micrometeoroids that do survive to the atmospheric passage, but that are totally melted. These are therefore recovered as cosmic spherules.

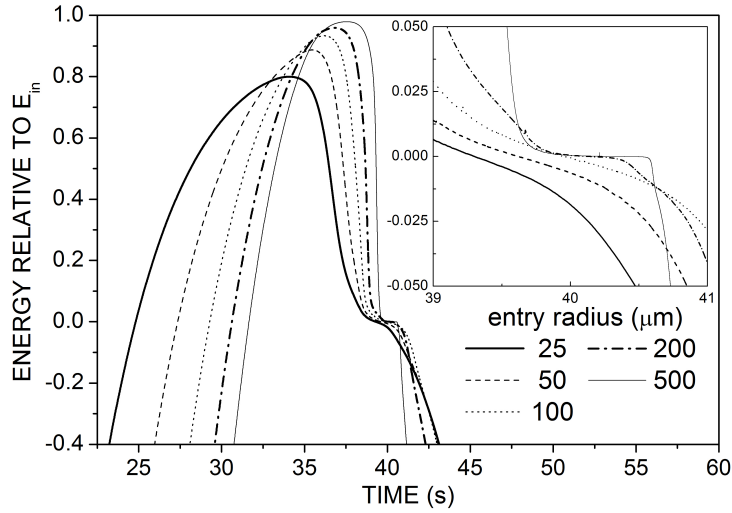
The difference between these two classes can be seen also analyzing the time evolution of the energy used for micrometeoroid temperature variation, i.e. the term  $cM_{\text{MM}}(dT_{\text{MM}}/dt)$  included in the energy balance. In Fig. 5.3 this term normalized to the incoming energy (equation 5.4) is shown for the same cases of Fig. 5.2. These curves cross zero around 41 s, i.e. when the micrometeoroid temperatures reach their peak value and then start to de-



**Figure 5.2:** Typical time evolution of the micrometeoroid temperature. A: Results for  $r_{\text{in}} = 50 \mu\text{m}$ ,  $z_{\text{in}} = 45^\circ$  and  $\rho_{\text{MM}} = 3 \text{ g/cm}^3$ . The truncated dashed and solid curves correspond to micrometeoroids that do not survive to the atmospheric entry. B: Results for  $v_{\text{in}} = 11.2 \text{ km/s}$ ,  $z_{\text{in}} = 45^\circ$  and  $\rho_{\text{MM}} = 3 \text{ g/cm}^3$ . The flattening of the temperature profile witnesses a phase of intensive melting. A  $r_{\text{in}} = 100 \mu\text{m}$  micrometeoroid clearly escapes total melting. For  $r_{\text{in}} = 200 \mu\text{m}$  intensive melting begins to be significant (see also Fig. 5.3).

crease. From the inset in Fig. 5.3 it is clear that when micrometeoroids are completely melted there is a time interval during which no energy is used to vary their temperature. In contrast, curves corresponding to micrometeoroids that are not completely melted vary smoothly.

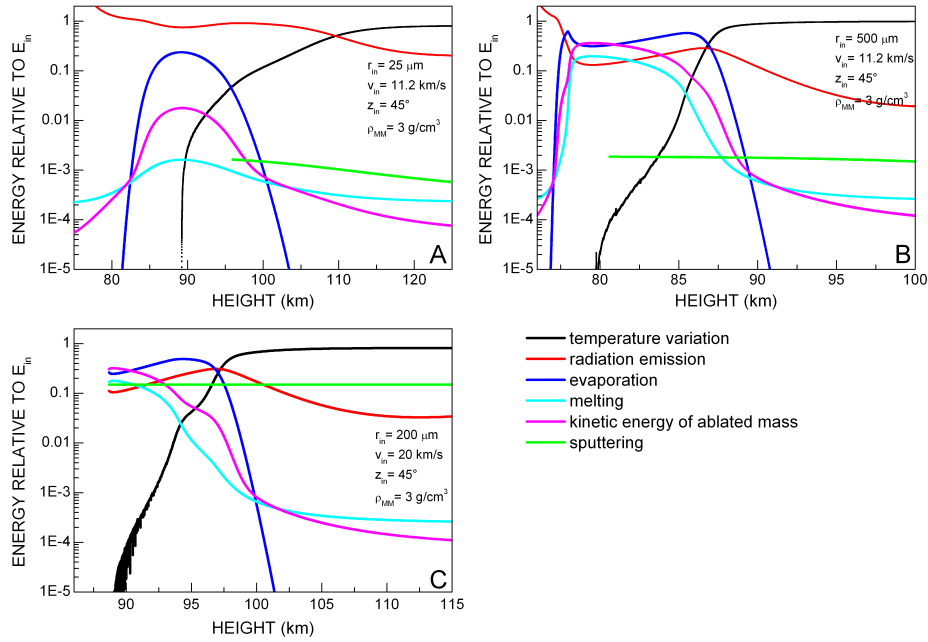
A more general analysis of how the physical processes that determine the fate of micrometeoroids evolve is presented in Fig. 5.4, which shows the distribution of the energy that micrometeoroids gain from collisions with atmospheric particles in the different processes considered in the energy balance. In the first part of the atmospheric trajectory most of the energy is used to rise the temperature of micrometeoroids (black line). When temperature reaches high values ( $\gtrsim 1000 \text{ K}$ ) ablative processes (evaporation and melting) become important and therefore also the kinetic energy of the ablated mass. However, it is clear that the relative roles of the different processes included in the energy balance change on the basis of the entry conditions. For the smallest micrometeoroids (Fig. 5.4A) the most important process is radiative emission. Energy lost in this way cannot be used to reduce the micrometeoroid mass, so these small bodies can survive.



**Figure 5.3:** Fraction of the incoming energy spent to change the micrometeoroid temperature. These curves are proportional to  $dT_{MM}/dt$  therefore negative values mean that temperature is decreasing, positive values that it is increasing. Particularly important is the passage from positive to negative values reported in the inset, happening here around 40 s. This passage correspond to attainment of the peak temperature value and to the begin of micrometeoroid cooling, i.e. a period of intense ablation. The flattening of these curves reveals a period during which the micrometeoroid temperature does not change. The curve for  $r_{in} = 300$  and  $400 \mu\text{m}$ , present in Fig. 2, are not reported here for sake of clarity.

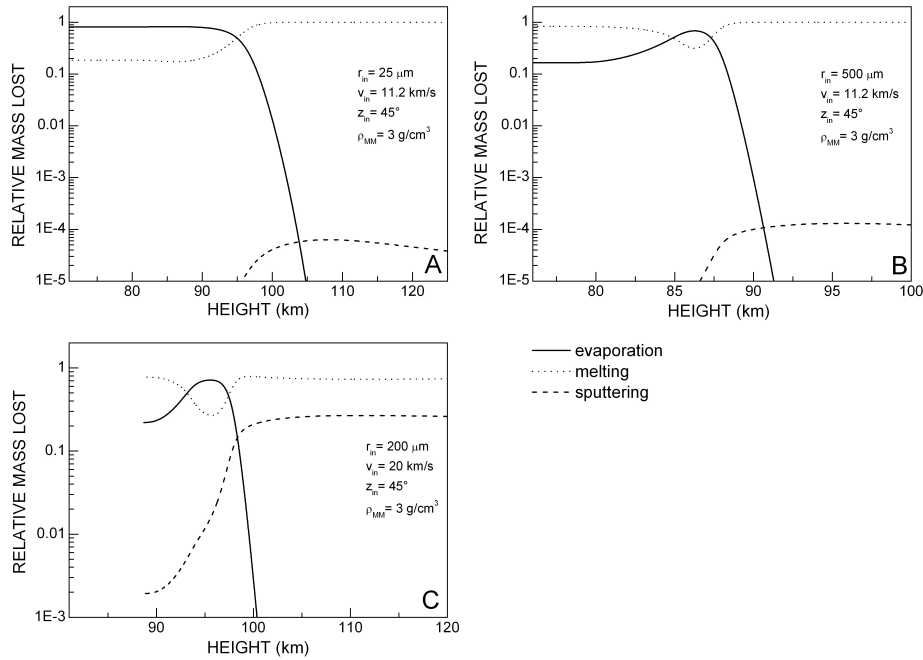
The ratio of the energy used in radiative emission to the energy acquired by collisions can be larger than unity. This happens in two phases of the micrometeoroids-atmosphere interaction. First at the very beginning (this phase is not showed in Fig. 5.4) when micrometeoroids are in low-density atmospheric layers and suffer relatively few collisions, but their temperature ( $T_{in} = 330 \text{ K}$ ) yields significant emission of radiation, and second when the micrometeoroid speed and radius are greatly reduced so that the energy acquired by collisions is consequently reduced; in this case the micrometeoroid temperature is near its peak values, so the radiative emission dominates.

Fig. 5.4A represents the typical situation for micrometeoroids that survive the atmospheric passage without been totally melted. In this case melting accounts for only about 1‰ of the incoming energy, while more energy is clearly spent in evaporation (that reaches  $\sim 25\%$ ). Sputtering is also negligible in this case, reaching about 1‰ of the incoming energy and terminating abruptly when micrometeoroids are slowed down (when the energy involved in collisions between micrometeoroids and atmospheric particles falls below the threshold energy required to remove micrometeoroid atoms and molecules, then sputtering is stopped). In contrast, looking at the case of micrometeoroids that survive but that are totally melted (Fig. 5.4B) it



**Figure 5.4:** Evolution of the energy spent in different processes relative to the incoming energy. A: micrometeoroid not completely melted. The sputtering line ends when the micrometeoroid is decelerated, i.e. when the energy of collisions is no more sufficient to remove micrometeoroid atoms or molecules. B: micrometeoroid totally melted. Evaporation and melting are clearly more important than in A and reach values comparable to those of radiative emission. Major mass loss implies a larger quantity of energy is present as kinetic energy of the ablated mass. C: micrometeoroid completely destroyed. Sputtering is more important than in A and B, due to the larger value of entry speed. Noise in the black lines is due to the numerical integration and occurs when the calculation is performed on very small stepsizes (of the order of  $10^{-5}$  s, used when micrometeoroid size, velocity and temperature vary significantly).

is clear that the ablative processes (evaporation and melting) are more important than in the previous case. Indeed there is a time interval during which both evaporation and melting demand more energy than radiation emission. As a consequence more mass is lost (see Fig. 5.5) and therefore also the kinetic energy of the ablated mass become important in the energy balance. Instead the importance of sputtering is still limited, also because of the low initial velocity ( $v_{\text{in}} = 11.2$  km/s in Fig. 5.4B). The contribution of sputtering is very sensitive to micrometeoroid entry speed. Already for  $v_{\text{in}} = 14$  km/s (with  $r_{\text{in}} = 500$   $\mu\text{m}$ ,  $z_{\text{in}} = 70^\circ$  and  $\rho_{\text{MM}} = 3$  g/cm<sup>3</sup>, another case of micrometeoroid completely melted) we observe a change of about two order of magnitude, with energy spent in sputtering that reaches  $\sim 10\%$  of the incoming energy. This is also the case for micrometeoroids that do not survive atmospheric passage, as shown in Fig. 5.4C. Here again sputtering accounts for more than 10% in the energy balance, and melting and



**Figure 5.5:** Relative contribution to the mass loss of processes present in the mass balance. A: a case of micrometeoroid not completely melted, for which evaporation is the principal mechanism of mass loss, accounting for 80% of the total mass lost. The final mass of this micrometeoroid is 47% of the initial mass. B: a micrometeoroid that has been totally melted. In this case melting is the principal mechanism of mass loss. Here the total mass lost is 99%. C: micrometeoroid completely destroyed by the interaction with the atmosphere. Melting is still the dominant mechanism for mass loss. The contribution of sputtering is more important than in A and B but still negligible.

evaporation become more important than radiative emission.

The analysis of the mass balance (Fig. 5.5) confirms what we see from the energy balance. In the case of Fig. 5.5A (micrometeoroids not totally melted) melting accounts for  $\sim 20\%$  of the total mass lost. For these micrometeoroids the principal cause of mass loss is evaporation, while sputtering is negligible. The situation is opposite for micrometeoroids that survive but are totally melted (Fig. 5.5B): melting is the principal mechanism by which they lose mass, while evaporation causes a limited mass loss ( $\sim 16\%$  for the case of Fig. 5.5B). As said above, sputtering become important for larger entry velocities. Nevertheless it is hardly decisive as mechanism for mass loss. In the case of Fig. 5.5C sputtering is responsible of the loss of  $< 1\%$  of the total mass lost. Even in the most severe case, when micrometeoroids enter the atmosphere with very high speed ( $v_{in} = 70 \text{ km/s}$ ) and have a large surface exposed to collisions ( $r_{in} = 500 \mu\text{m}$ ) sputtering contribute for a modest 1% to mass loss.

## 5.6 Discussion

Our results show how the different physical processes involved in the micrometeoroids-atmosphere interaction are related to each other, and in what conditions one can prevail on the others. To this end it is a key issue to analyze the choice of the values for the most important parameters present in our model and of the equations describing the processes of interest.

We have assumed that both the drag coefficient  $\Gamma$  (equation 5.3) and the heat transfer coefficient  $\Lambda$  (equation 5.4) equal 1. These values are justified when the micrometeoroid flight happens in a free molecular flow regime [see e.g. Sorasio *et al.* (2001) and Popova *et al.* (2007)], as is the case for micrometeoroids treated in this work. Actually their values are not constant during the micrometeoroids flight, because they depend on the micrometeoroid temperature and on the ratio of the micrometeoroid velocity  $v_{\text{MM}}$  to the atmospheric particle thermal velocity  $v_{\text{th}}$  (Hood and Horanyi, 1991; Melosh and Goldin, 2008). However for micrometeoroids in free molecular flow regime and in the limit  $v_{\text{MM}} \gg v_{\text{th}}$  (as in this work) their value is always close to unity. To test the sensitivity of our model on these parameters we have done simulations with  $\Gamma \neq 1$  and  $\Lambda \neq 1$  (but still constant). We tested different values of  $\Gamma$  and  $\Lambda$  for  $r_{\text{in}} = 100 \mu\text{m}$ ,  $v_{\text{in}} = 12 \text{ km/s}$ ,  $z_{\text{in}} = 45^\circ$  and  $\rho_{\text{MM}} = 3 \text{ g/cm}^3$ . On one hand when  $\Gamma$  increases ( $\Gamma = 2$  is the value for elastic collisions) micrometeoroids are slowed down more efficiently, so they are less heated by collisions, reach lower maximum temperatures (peak temperature for  $\Gamma = 2$  is 55 K lower than for  $\Gamma = 1$ ) and have greater final radii ( $r_{\text{fin}} = 67 \mu\text{m}$  for  $\Gamma = 2$ , while  $r_{\text{fin}} = 30 \mu\text{m}$  for  $\Gamma = 1$ ). On the other hand, low values of  $\Gamma$  imply less deceleration and therefore a more severe heating. For  $\Gamma < 0.6$  our test micrometeoroid is destroyed; for  $\Gamma = 0.6$  its peak temperature is 15 K higher than in the case  $\Gamma = 1$  and the final radius is  $6 \mu\text{m}$ . Varying  $\Lambda$  produces more important variation on micrometeoroid temperature and final size. Decreasing  $\Lambda$  from 1 to 0.1 causes the peak temperature to be lowered from 1604 K to 1255 K. Final radius is  $99 \mu\text{m}$  for  $\Lambda = 0.1$ , i.e. micrometeoroid size is unaffected by the interaction with the atmosphere. Variations on  $\Lambda$  appear therefore more influential than variation on  $\Gamma$ , as reported also in Campbell-Brown and Koschny (2004). However low values of  $\Lambda$  are not probable for the cases treated in this work. To estimate what  $\Lambda$  would be when micrometeoroids suffer the most intense alteration, we use the expression of Hood and Horanyi (1991):

$$\Lambda = 1 - \frac{1}{2(v_{\text{MM}}/v_{\text{th}})^2} \left( \frac{\gamma + 1}{\gamma - 1} \right) T_{\text{MM}}/T_{\text{air}}$$

where  $\gamma$  is the ratio of the specific heat of the terrestrial atmospheric gases at constant pressure to that at constant volume ( $= 7/5$ ),  $T_{\text{air}}$  is the atmospheric temperature and  $v_{\text{th}}$  is the atmospheric thermal velocity. Since  $v_{\text{th}}$

is computed as  $v_{\text{th}} = \sqrt{3k_{\text{B}}T_{\text{air}}/m_{\text{avg}}}$  ( $k_{\text{B}}$  = Boltzmann constant and  $m_{\text{avg}}$  = mean mass of atmospheric particles) the value of  $\Lambda$  is determined by the ratio  $T_{\text{MM}}/v_{\text{MM}}^2$ . In our simulations the maximum value of  $T_{\text{MM}}$  is always reached before  $v_{\text{MM}}$  is significantly reduced, and when  $v_{\text{MM}}$  decreases,  $T_{\text{MM}}$  decreases too. As consequence,  $\Lambda$  remains close to 1. This is illustrated in Tab. 5.2.

	Test case 1	Test case 2	Test case 3
$r_{\text{in}}$ ( $\mu\text{m}$ )	50	100	500
$v_{\text{in}}$ (km/s)	16	12	11.2
$T_{\text{MM}}^{\text{max}}$ (K)	1606	1603	1622
$v_{\text{MM}}$ when $T_{\text{MM}}^{\text{max}}$ (km/s)	12.45	9.65	10.0
$h$ when $T_{\text{MM}}^{\text{max}}$ (km)	88.0	84.1	79.5
$T_{\text{air}}(h)$ (K)	176.2	181.4	191.6
$v_{\text{th}}(h)$ (m/s)	392	398	409
$\Lambda$	<b>0.973</b>	<b>0.955</b>	<b>0.958</b>

**Table 5.2:** Values of the heat transfer coefficient  $\Lambda$  for three test case micrometeoroids with  $z_{\text{in}} = 45^\circ$  and  $\rho_{\text{MM}} = 3 \text{ g/cm}^3$ . Simulations performed in the present-day atmosphere.

The value of  $\eta$ , the fraction of the incoming energy we assume is spent for sputtering is also important. It is clear that for larger values of  $\eta$ , sputtering in the energy balance (and for the mass loss) increases. Actually choosing a value for  $\eta$  is very difficult. Theoretical (e.g. Sigmund 1981) and experimental (e.g. Nakles 2004) studies on this argument have treated sputtering in detail, but always as an isolated process. In addition, the mean molecular mass of micrometeoroid atoms and their bounding energy are important parameters in determining the value of the sputtering yield  $Y$ , and thus of the sputtering contribution to the energy balance. Therefore a simplified treatment of the structural and compositional properties of micrometeoroids, as in this work, implies that we have a first approximation of the sputtering contribution. Nonetheless, this process could be more important for micrometeoroids less compact than those treated here, as recently found Antarctic micrometeorites (Duprat *et al.*, 2007).

The case of sputtering is a good example to show also how choices made to characterize physical processes can be decisive. There are several critical points: the evaluation of the different processes that cause the removal of a particle from a solid body (May *et al.*, 2000), the sputtering yield dependence on the projectiles incidence angle (Jurac *et al.*, 1998), which type of particles are emitted from the target (atoms? molecules? both? See Tielens *et al.* 1994) and the speed at which these particles leave the target (Popova *et al.*, 2007). In Coulson (2002) a Maxwellian distribution for the speed of particles

removed by sputtering is assumed, and this implies an increment of a factor 11 in the momentum transferred to micrometeoroids with respect to the case in which only collisions are considered, with consequent large decrease of the micrometeoroids speed, peak temperature and ablation. In our model the momentum transferred to micrometeoroids by removed fragments is not considered, even if we include the kinetic energy of these fragments in the energy balance. This is why we assume that ablated mass moves away isotropically. So the net momentum transferred is zero.

Another fundamental issue is that of atmospheric properties. This point will be treated in major details in the next paragraph. Here we want to highlight the influence of atmospheric components number density on sputtering. In our results mass lost by sputtering is always a little fraction ( $\leq 1\%$ ) of the total mass lost. This is in contrast with results of Rogers *et al.* (2005), where sputtering is responsible for up to  $\sim 40\%$  of mass loss for asteroidal micrometeoroids ( $\rho_{\text{MM}} = 3 \text{ g/cm}^3$ ) and up to  $\sim 50\%$  for cometary micrometeoroids ( $\rho_{\text{MM}} = 1 \text{ g/cm}^3$ ). We think their results are due to an overestimation of the number densities of the atmospheric components, which are systematically larger, by two order of magnitude, than those we obtained from the MSISE-90 model.

## 5.7 Application to the early Earth atmosphere

Among the atmospheric properties, the density profile  $\rho_{\text{atm}}(h)$  is certainly the most important, as it determines the speed evolution of micrometeoroids (equation 5.3) and the rate of incoming energy (equation 5.4). Indeed, the micrometeoroids-atmosphere interaction is effective only for a few seconds (see Fig. 2A), starting when micrometeoroids reach sufficient dense layers. Therefore it is important to know what happens when different atmospheric density profiles are considered. Previous works have studied micrometeoroid atmospheric entry for planets other than the Earth, such as Neptune (Moses, 1992), Venus (McAuliffe and Christou, 2006) and also the Saturn satellite Titan (Ip, 1990; English *et al.*, 1996). These works were aimed to investigate the meteoric contribution to composition and chemistry of the considered atmosphere (Ip, 1990; Moses, 1992; English *et al.*, 1996) or to analyze meteor properties (McAuliffe and Christou, 2006). Therefore they were focused on issues different from those of the present paper. Here we investigated the passage of micrometeoroids through two atmosphere models for the early Earth and to the atmosphere of Titan, considered as possible analogue of a  $\text{CH}_4$ -rich primordial atmosphere. This is of major interest for astrobiology since micrometeoroids were probably an important component in the primordial accretion of extraterrestrial matter on the early Earth (Maurette *et al.*, 2000, 2001; Maurette, 2009).

We adopted two simple models for the primordial atmosphere considering different possible compositions, temperature profiles and the enhanced X-UV flux of the early sun. We point out here that these models are not intended to precisely characterize the primordial atmosphere. They are used as test-cases for the micrometeoroids-atmosphere interaction and provide two different density profiles that should bracket the conditions found on Earth upper atmosphere about 3.5 Gy ago. The first model (Early Atmosphere 1 - EA1) is for a composition of 80% N<sub>2</sub> and 20% CO<sub>2</sub>, a surface pressure of 1.1 bar and a mean surface temperature similar to the present one. These conditions, which assume that the carbonate-silicate cycle resulted in an enhanced CO<sub>2</sub> level compensating for the lower solar luminosity (Walker *et al.*, 1981), represent the *standard model* for the Earth atmosphere after the end of the Late Heavy Bombardment around 3.9 Gy ago (Kasting, 1993; Selsis *et al.*, 2002). The temperature profile  $T_{EA1}$  is based on the following assumptions: the troposphere temperatures (0-15 km) are the same as in the present atmosphere (it should be slightly different as consequence of the enhanced concentration of CO<sub>2</sub> that changes the adiabatic lapse rate, but this does not affect the micrometeoroids-atmosphere interaction, which always happens at higher heights); for the stratosphere (15-80 km) we estimated the temperature based on recent calculations (von Paris *et al.*, 2008); for the thermosphere (80-300 km) we considered the X-UV flux of the sun 3.5 Gy ago (6 times the present day value, see Ribas *et al.* 2005) and recent calculations by Kulikov *et al.* (2007) for the heating of the thermosphere. In addition, to take into account that above 100 km different atomic and molecular species are stratified as a function of their mass, we made the approximate assumption that the mean molecular mass drops off linearly from 32 g/amu at 100 km to 15 g/amu at 300 km. The resulting temperature profile is reported in Fig. 6A.

The second model (Early Atmosphere 2 - EA2) represents a low-CO<sub>2</sub> case. Due to its efficient radiative cooling and its heavy weight CO<sub>2</sub> has a critical impact on the temperature profile in the thermosphere (Kulikov *et al.*, 2007). This effect can be illustrated by the thermospheric temperature of the present Earth, that reaches 800 to 1600 K depending on solar activity, while the thermospheric temperature of Mars and Venus atmosphere (both CO<sub>2</sub>-rich) remains below 300 K. A N<sub>2</sub>-rich early atmosphere, with no or little CO<sub>2</sub> would have a hot and extended thermosphere with high scale heights, providing extremely different conditions for the entry of micrometeoroids. This scenario implies that either the mean surface temperature was significantly below 273 K or there was another efficient greenhouse gas at work. The case for a permanent frozen early Earth contradicts geological records for most of the Archean (Martin *et al.*, 2006), but for the few so-called snowball events, during which the mean surface temperature drops down to several tens of degrees below the freezing point (Schrag *et al.*, 2002). It is, however, a plausible scenario at epochs earlier than about 3.5

Gyr, for which reliable constraints are scarce (see for instance Sleep and Zahnle 2001). The case for alternate greenhouse gases has been studied by several groups who considered candidates such as  $\text{CH}_4$  (Haqq-Misra *et al.*, 2008) or sulfur compounds (Ueno *et al.*, 2009). In a fully consistent work, one should of course study how these gases affect the upper atmosphere but, at the present stage, we simply want to study how micrometeoroids interact with such an extended and hot thermosphere. We thus considered a 0.8 bar  $\text{N}_2$ -rich atmosphere, with 0.02%  $\text{CO}_2$ . As the lowest part of the atmosphere does not affect the entry of micrometeoroids, we used a present-day mean surface temperature. The mean molecular mass drops off linearly from 28 g/amu at 100 km to 14 g/amu at 400 km. The temperature profile  $T_{\text{EA2}}$  results from the same assumption described above for  $T_{\text{EA1}}$ , and it is reported in Fig. 6A. The low level of  $\text{CO}_2$  assumed for the EA2 model results in a smaller mean molecular mass and a thermosphere warmer than in the first case (with temperatures  $>5000$  K above 180 km); this implies that the scale factor  $H = TR_{\text{gas}}/mg$  ( $g$  = gravitational acceleration,  $m$  = mean molecular mass of atmospheric components,  $R_{\text{gas}}$  = gas constant,  $T$  = atmospheric temperature) is larger, which means a density profile less steep than in the case of the EA1 model (Fig. 6B).

Starting from  $T_{\text{EA1}}$  and  $T_{\text{EA2}}$  the density profiles were calculated using the barometric formula  $\rho(h) = \rho_0 \exp(-gmh/TR_{\text{gas}})$ . Fig. 6B shows the two profiles  $\rho_{\text{EA1}}$  and  $\rho_{\text{EA2}}$ :  $\rho_{\text{EA1}}$  is quite similar to the present day density profile, while  $\rho_{\text{EA2}}$  has larger density values and a less steep gradient above  $h \sim 100$  km.

In Fig. 6A and 6B are reported also the temperature and density profiles, respectively, for the atmosphere of Titan. These are estimated from data collected by the Huygens probe (Fulchignoni *et al.*, 2005; Aboudan *et al.*, 2008). The density profile of the Titan atmosphere has density values always larger than those of the terrestrial cases, but a less steep gradient, with the exception of the EA2 model above  $h \sim 150$  km. For the Titan atmosphere we assumed the measured composition of 98.6%  $\text{N}_2$  and 1.4%  $\text{CH}_4$ .

For all the simulations the entry height  $h_{\text{in}}$  is such that the initial atmosphere density value is the same ( $3.6 \times 10^{-13}$  g/cm<sup>3</sup>) except for the EA2 model, which has a slightly larger density ( $4.6 \times 10^{-13}$  g/cm<sup>3</sup>) at  $h_{\text{in}} = 1000$  km. Also, we have to point out that for the initial micrometeoroid temperature we assumed only one value for the four atmospheres, the value corresponding to the temperature of a micrometeoroid at 1 AU from the sun. This implies an initial decrease of the micrometeoroid temperature in the Titan case, as observed for simulations in the present-day atmosphere (see section 5.5 and Fig. 5.2A). If we consider the real distance of Titan from the sun, the appropriate micrometeoroid initial temperature is 107 K. Consequently, the emission of radiation is less effective, and the initial decrease in the micrometeoroid temperature is not observed.

Our results (Fig. 5.7) evidence that the micrometeoroids-atmosphere

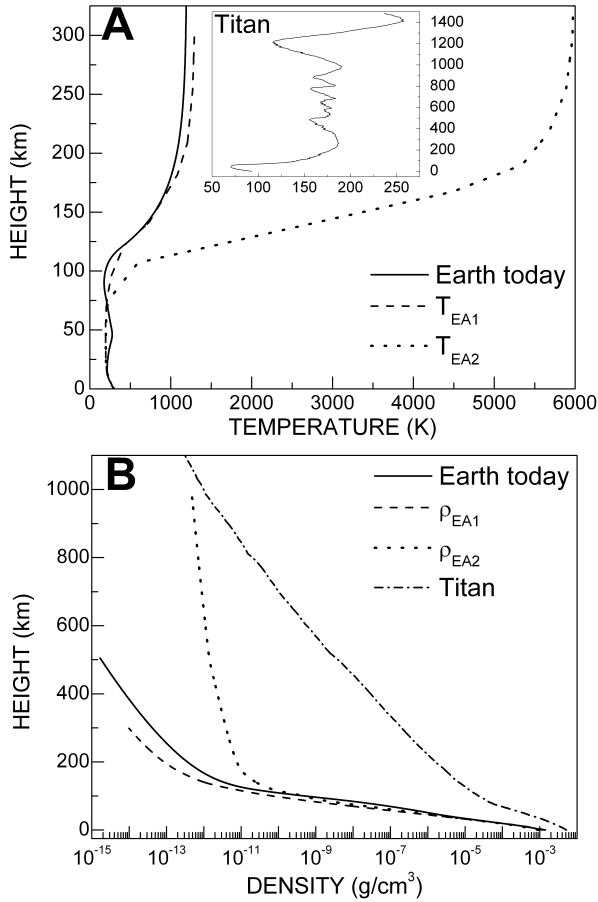


**Figure 5.6:** A: temperature profiles of the atmospheres considered for the simulations. The  $T_{EA1}$  and  $T_{EA2}$  models for the primordial atmosphere are obtained as described in the text. Titan temperature is from Fulchignoni *et al.* (2005). B: density profiles obtained from the temperature profiles in A via the barometric formula (see text)

interaction is similar in the present-day atmosphere and in the EA1 model: maximum temperatures, final velocities and final radii are quite the same. In the EA2 model micrometeoroids are slightly less affected by the passage through the atmosphere: they attain larger final radii and peak temperatures are lower than in the two other terrestrial atmospheres. In contrast, the situation is clearly different for the Titan atmosphere. In particular, final radii are far larger (Fig. 7A) and peak temperatures are lower (Fig. 7B). In the case of a micrometeoroid with entry radius of  $100 \mu\text{m}$  ( $v_{\text{in}} = 12 \text{ km/s}$ ,  $z_{\text{in}} = 45^\circ$ ,  $\rho_{\text{in}} = 3 \text{ g/cm}^3$ ) there is a small difference between its final size in the present day atmosphere ( $29 \mu\text{m}$ ), in the EA1 model ( $31 \mu\text{m}$ ) and in the EA2 model ( $35 \mu\text{m}$ ), but the final radius is clearly larger when the simulation is done for the Titan atmosphere ( $96 \mu\text{m}$ ). For the same micrometeoroid, peak temperatures are very similar in the three Earth cases, but once again clearly different from that obtained in the Titan atmosphere, where the maximum temperature is  $\sim 400 \text{ K}$  lower. In addition, the same is true for the timing of the interaction. In general the variations of temperature, speed and size are completed in just few seconds for the three terrestrial cases, while more

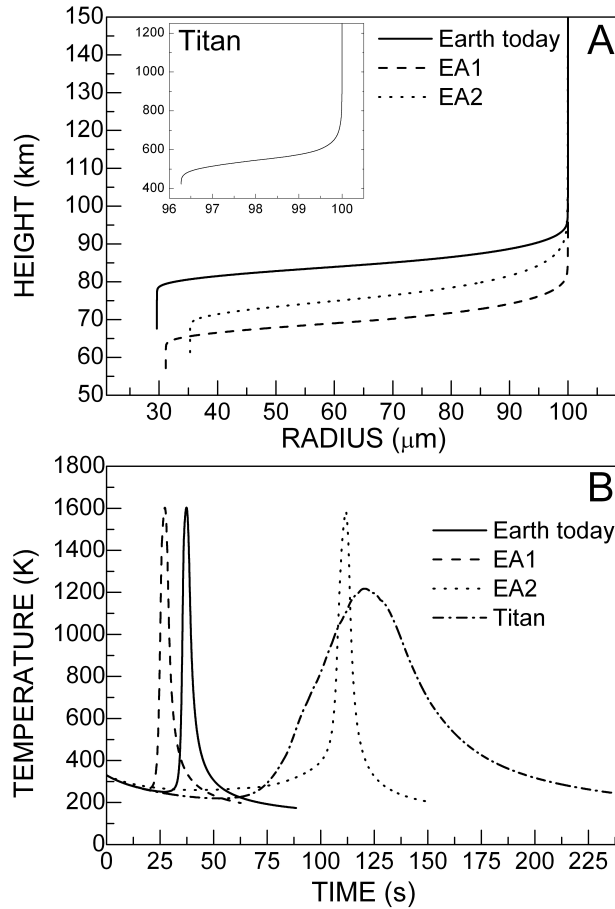


**Figure 5.7:** Size and temperature evolution of a micrometeoroid with  $r_{in} = 100 \mu\text{m}$ ,  $v_{in} = 12 \text{ km/s}$ ,  $z_{in} = 45^\circ$ ,  $\rho_{MM} = 3 \text{ g/cm}^3$  in four different atmospheres. A: evolution of radius as function of height. The change in size happens over an interval of few km and few seconds. Note the difference in final size between the Earth cases and the Titan case. B: temperature evolution as function of time. The difference in maximum temperature between the three terrestrial atmospheres and the Titan case is  $\sim 400 \text{ K}$ . It is evident also the different timing of the micrometeoroids-atmosphere interaction.

time is required in the Titan atmosphere (Fig. 7B).

The importance of a different density gradient for the considered atmosphere is highlighted also in the analysis of the evolution of micrometeoroids temperatures, velocities and radii as function of the atmospheric density. The three Earth cases are once again similar: velocity changes in a narrow range of density values between  $10^{-9}$  and  $5 \times 10^{-8} \text{ g/cm}^3$ . In the Titan atmosphere, the passage from the initial to the final value of velocity happens over a density range of 3 order of magnitude (between  $3 \times 10^{-11}$  and  $5 \times 10^{-8} \text{ g/cm}^3$ ). Similar differences are observed for the evolution of micrometeoroids radii and temperatures.

Results for the EA2 model confirm that high low-density layers (e.g.  $\geq 200 \text{ km}$ ) do not affect the micrometeoroids-atmosphere interaction. To see if a low density gradient (as in the high layers of EA2) allows the micrometeoroids surviving even with larger density values, we ran one simulation with a density profile  $\rho_{EA2} \times 1000$ , such that the initial density value is close to those at which the important part of the interaction take place. In this case a micrometeoroid with  $r_{in} = 100 \mu\text{m}$ ,  $v_{in} = 12 \text{ km/s}$ ,  $z_{in} = 45^\circ$  and  $\rho_{MM} = 3$

$\text{g/cm}^3$  is unaffected by the atmospheric passage. It is gradually slowed down over a time period of  $\sim 500$  s, its temperature rises of only 100 degrees and its size does not change. Therefore, even if the density is increased by 3 orders of magnitude, the very low gradient prevent the micrometeoroid destruction. In conclusion, the results of our simulations show that the density gradient is a crucial parameter: for the same values of atmospheric density, a less steep density gradient implies that micrometeoroids have more chance to survive and reach the Earth surface.

## 5.8 Conclusions

Our work evidences the general characteristics of the micrometeoroids-atmosphere interaction through the analysis of the evolution of intervening physical processes. This allows to understand how the importance of these processes changes in response to different entry conditions. Entry conditions are essential. For a given initial radius, a higher entry velocity and a steeper entry angle (i.e. closer to the vertical direction) imply a more severe heating for micrometeoroids, and therefore a less probability of surviving. For fixed entry velocity and angle, the larger is the radius, the larger is the mass loss. Different entry radii also imply that different processes dominate the micrometeoroids energy balance. For the smallest micrometeoroids simulated in this work ( $r_{\text{in}} = 25\mu\text{m}$ ), radiative emission is the dominant process, allowing the survival of these small micrometeoroids. For larger micrometeoroids ablation processes are more important, i.e. these micrometeoroids lose a fraction of mass larger than small micrometeoroids. The probability of surviving the atmospheric passage is greatly reduced for larger micrometeoroids, and only low entry velocities and grazing entry angles can allow them to reach Earth surface.

In our results, among those cases in which micrometeoroids are not completely destroyed, two general classes can be identified. The first corresponds to micrometeoroids that are not completely melted during atmospheric flight and therefore reach Earth surface as unmelted or partially melted micrometeorites; the second corresponds to completely melted micrometeoroids, recovered on Earth as cosmic spherules. The difference between these two classes is in the importance that the process of melting assumes in the energy and in the mass balance, being clearly more important for micrometeoroids that end as cosmic spherules.

Application of our model to the interaction of micrometeoroids with possible early Earth atmospheres show that the atmosphere density gradient is a key feature. In case of a density gradient lower than that of the present day atmosphere, micrometeoroids are able to survive and reach the surface more easily.

The model described in this work is a first step to study the physics

of the micrometeoroids-atmosphere interaction in a general way. The basic idea is to treat this problem holistically. We have underlined that there are many elements that must be carefully analyzed: micrometeoroids composition and structure, characterization of physical processes, parameters values, entry conditions. It is necessary to consider all them in order to highlight their interconnections and their respective roles in determining the micrometeoroids fate. For this reason, it would be useful to study this problem in a multidisciplinary context, i.e. not only from a physical point of view, but also mineralogical (for the alteration that micrometeoroids suffer crossing the atmosphere). Finally, the analysis of the biochemical aspects related to this subject, i.e. related to the organic molecules present in micrometeoroids, could help to better understand the micrometeoroids role in the emergence of Life on Earth.

## Chapter 6

# Conclusions

In this thesis experimental and numerical studies of microxenoliths in meteorites and of micrometeorites have been presented. Particular attention has been dedicated to the characterization of microxenoliths. As they represent the best proxy of interplanetary micrometeoroids, they offer unique possibilities of studying one of the most abundant population of extraterrestrial matter. In addition, microxenoliths sample the solar system micrometeoroid flux at more ancient times than micrometeorites. Therefore they allow to characterize the past micrometeoroid population. Also, microxenoliths can reveal new insights into the nature of asteroids and comets, their more probable parent bodies.

The different experimental and numerical works realized for this PhD thesis attest the richness and variety of information that can be obtained from the analysis of microxenoliths. Here are reported the principal results achieved during this PhD thesis.

As the main goal of this thesis was to exploit the studying of microxenoliths in meteorites to unveil new insights into the solar system origin and evolution, a fundamental task was to obtain samples to analyze. This has been realized by performing a systematic search of new xenoliths and microxenoliths in H chondrites (chapter 1). This group of ordinary chondrites has been selected for its richness in xenoliths, attested by works in the literature. Twenty six new xenoliths have been discovered in sixty-six sections from forty meteorites. Our results show that  $\sim 80\%$  of the new discovered xenoliths have dimensions smaller than 1 mm, i.e. they are microxenoliths, and only 5 have size larger than 1 mm. Most of the new discovered xenoliths and microxenoliths are similar to known groups of carbonaceous chondrites, namely CM, CR and CI. They are present in meteorites of petrographic type from 3 to 5: this indicates that their embedding happened after the metamorphism of the host meteorites. Almost all the new xenoliths (24 out of 26) have been found in brecciated meteorites. These results suggest that exposure of meteorite parent body surface to space favours the embedding

of xenoliths, instead of destroying already existing xenoliths.

In order to evaluate the importance of main belt asteroids and Jupiter Family comets (JFCs) as sources of carbonaceous microxenoliths, we performed numerical simulations for the collision probability of asteroidal and cometary micrometeoroids with selected targets in the asteroid main belt (chapter 2). Our results show that fragments originated from asteroids and those originated from JFCs have a similar probability to hit our selected targets Vesta and Hebe. Hence, two populations of carbonaceous microxenoliths should have been (and still being) present in Vesta, Hebe and probably in the other asteroids candidate to be the H chondrite parent bodies. Therefore two populations of microxenoliths should co-exist in HED and H chondrites. However, our observations about xenoliths and microxenoliths in H chondrites and results of previous works on xenoliths in HED did not show two radically distinct populations of microxenoliths. This suggests that, if both asteroidal and cometary carbonaceous microxenoliths are actually present in HED and H chondrites, they have similar structure and composition. Therefore, while asteroids and comets are clearly distinct from a dynamical point of view, their structures and compositions are probably not as distinct as previously thought.

The peculiar xenolith PX-18 found in the carbonaceous chondrite Isheyev (described in chapter 3) carries unprecedented nitrogen isotopic variations. At the same time, it lacks a significant hydrogen fractionation. The most recent models for the nitrogen fractionation explain high values of the  $^{15}\text{N}/^{14}\text{N}$  ratio as the result of low-temperature ion-molecule reactions in dense cloud cores. However, in the same conditions, also a high H fractionation should be produced. Therefore, the N and H fractionations observed in PX-18 are not consistent with such models. Rather, these data suggest fractionation of light elements could be happened not only in the interstellar medium before the formation of the solar system, but even in the protoplanetary disk. Also, processes other than low-temperature ion-molecule reactions can be responsible of such fractionation, as the self-shielding.

PX-18 and four other microxenoliths found in the carbonaceous chondrite Isheyev have been analyzed by Raman spectroscopy (chapter 4). This technique is particularly suited to investigate the structure of the macromolecular organic matter. In this thesis we presented preliminary results principally based on the comparison of spectra obtained using both visible and UV excitation wavelengths. As reference we collected Raman spectra of insoluble organic matter (IOM) extracted both from unmetamorphosed carbonaceous chondrites (Orgueil, Renazzo, Murchison, Murray and Tagish Lake) and from metamorphosed carbonaceous chondrites (PCA 91008 and WIS 91600). Our results confirm the higher metamorphic degree of PCA 91008 and WIS 91600. Organic matter in the five Isheyev microxenoliths show different Raman properties from those of carbonaceous chondrite IOM. In particular, Isheyev microxenoliths # 28 and # 30 have clearly different

Raman spectra with respect to those of the other samples. Such a difference can be due to a different degree of thermal metamorphism or to different precursors of the organic matter.

Eventually, we addressed the question of the interaction between micrometeoroids and the Earth atmosphere (chapter 5). A comprehension of the alterations suffered by micrometeoroids during the passage through the atmosphere is essential to understand their origin and if they could have significantly supplied the Earth with pre-biotic organic compounds. Our work evidences the general characteristics of the micrometeoroids-atmosphere interaction through the analysis of the evolution of the intervening physical processes. This allows to understand how the importance of these processes changes in response to different entry conditions. In our results, among those cases in which micrometeoroids are not completely destroyed, two general classes can be identified. The first corresponds to micrometeoroids that are not completely melted during the atmospheric flight and therefore reach the Earth surface as unmelted micrometeorites; the second corresponds to completely melted micrometeoroids, recovered on the Earth as cosmic spherules. The difference between these two classes is in the importance that the process of melting assumes in the energy and in the mass balance, being clearly more important for micrometeoroids that end as cosmic spherules. The application of our model to the interaction of micrometeoroids with modelled early Earth atmospheres shows that the atmosphere density gradient is a key feature. In case of a density gradient lower than that of the present day atmosphere, micrometeoroids are able to survive and reach the surface more easily.

*E quindi uscimmo a riveder le stelle.*  
Dante, Inferno, canto XXXIV, 139



# Acknowledgements

I am deeply grateful to the persons that led me and helped me during these three years of PhD. It was a great experience, and this is thanks to the persons I worked with. I had the chance to meet many persons always available and open to discussions, explications, corrections and suggestions. All this has been an invaluable example.

I want to thank my three advisors (right, three for one thesis!), who gave me the possibility of working in the field of meteoritics. Emanuele Pace, for his support since the very beginning. Santi Aiello, for his generosity and his many advice, not only concerning astrophysics. Matthieu Gounelle, who introduced me to meteorites and always encouraged me to work harder. In particular I want to thank all them for their availability and for their dedication to this work.

Many thanks to the persons who accepted to be in the committee for the dissertation of my thesis: Alessandro Morbidelli, Marc Chaussidon, Alessandra Rotundi, Cécile Engrand and Giancarlo Della Ventura.

I am equally grateful to all persons that collaborated to the success of this work, in each of the many places I had the chance to visit.

A special thanks to Michèle Denise, for her patience in explaining me the mineralogy and the petrography of meteorites, and who taught me how to prepare beautiful sections from beautiful meteorites.

I am very grateful to Steven Shore, Anders Meibom, François Robert and Jean Duprat for many fruitful discussions and for their many advice.

I would like to thank Yves Marrocchi and Smail Mostefaoui, who let me work with the marvellous NanoSIMS.

It has been a pleasure to work at the LMCM also thanks to Laurent Remusat, Brigitte Zanda, Chistine Fiéni, Jean-Jacques Pantel, Remy Duhamel, Madeleine Selo, Elisabeth Malassis, Catherine Caillet, Claude Perron, Michel Serrano, Roger Hewins and Philippe Irisson.

I am deeply grateful to Michael Zolensky, that received me at the NASA Johnson Space Center, and to Loan Le, Keiko Nakamura-Messenger, Georg Ann Robinson, Motoo Ito and Scott Messenger that worked with me and supported me during my stay at JSC.

A special thank to Eric Quirico, who introduced me to Raman spectroscopy, and also for his corrections to this work up to the last day; to

Hugues Leroux for his TEM measurements, Omar Boudouma for his great FESEM pictures, and to Alessandro Morbidelli, who introduced me in the realm of solar system dynamics simulations; to Gilles Montagnac, for his assistance with Raman spectrometers; and to David Troadec, who prepared two beautiful FIB sections.

I want to thank Alessandra Giannini, for her technical assistance in many different fields throughout all these years.

I had the chance of sharing the PhD experience with many friends. Maurizio Pancrazzi and Alessandro Gherardi since the very beginning (and even before), Giulia Talini during the many, intense days of redaction. Special thanks to the LMCM group of students: Aurélien Thomen, Manuel Petitat, Chloé Brahmi, Laurette Piani, Celine Defouilloy, Christophe Kopp and Emmanuel Jacquet. The “martians” of the MNHN, whit which I spent several funny nights in Paris!

I am grateful to Antonio De Sio, Lisa Gambicorti and Mauro Focardi for their continuous help and support.

I would like to thank Luigi Folco, who first suggested the possibility of working in Paris, and the first to show me a real micrometeorite.

A special thanks to Guy Dubarry, Lisetta Pinzauti and Michela Graziani, for their corrections of my English mistakes. This thesis has also been supported by the 2008 Vinci grant of the French-Italian University, that partially founded my stay in Paris.

My greatest gratitude goes to my parents, Adalberto and Marzia, for their constant, invaluable support.

At the end, a very special thanks to Aude, who waited for me all this time.

## Appendix A

# Meteorite classification

Fig. A1 reports a simplified scheme of meteorites classification. Meteorites particularly important in this thesis are highlighted.

Here their principal characteristics are summarized.

**Undifferentiated meteorites** are rocks originated from parent bodies that have not been heated enough to undergo differentiation. Differentiation is the separation, inside a meteorite parent body, of the denser phases (e.g. metals) from the lighter ones (e.g. silicates).

The name **chondrites** is due to the fact that these meteorites contain chondrules. Chondrules are millimetric and sub-millimetric spheroidal grains that crystallized after have been formed as totally or partially melted droplets in space. Chondrites are among the most ancient rocks in the solar system. As they have never been melted, they preserve large part of the structure and composition acquired during primordial accretion.

**Carbonaceous chondrites** are the meteorites with the chemical composition most similar to that of the Sun. In particular, meteorites belonging to the CI group have a chemical composition that strikingly matches the solar composition. Carbonaceous chondrites are generally more rich in carbon than other meteorites. Most of the carbon is in the form of organic compounds, present as macromolecular organic matter and as soluble compounds like amino acids and hydrocarbons. Carbonaceous chondrites are the most volatile-rich meteorites, suggesting they formed far from the Sun, in low-temperature regions of the solar system. They formed in oxidizing condition, i.e. in O-rich regions of the solar system. This implies that most of the metal is present not in its free, reduced form, but in silicates, oxides and sulfides. Most of the carbonaceous chondrites clearly suffered low thermal metamorphism, but intense aqueous alteration, as attested by their richness in water-bearing minerals like phyllosilicates. Among the eight groups of carbonaceous chondrites, CI and CM chondrites are the most aqueously altered, the most rich in carbon and in volatile elements. CR, CH and CB

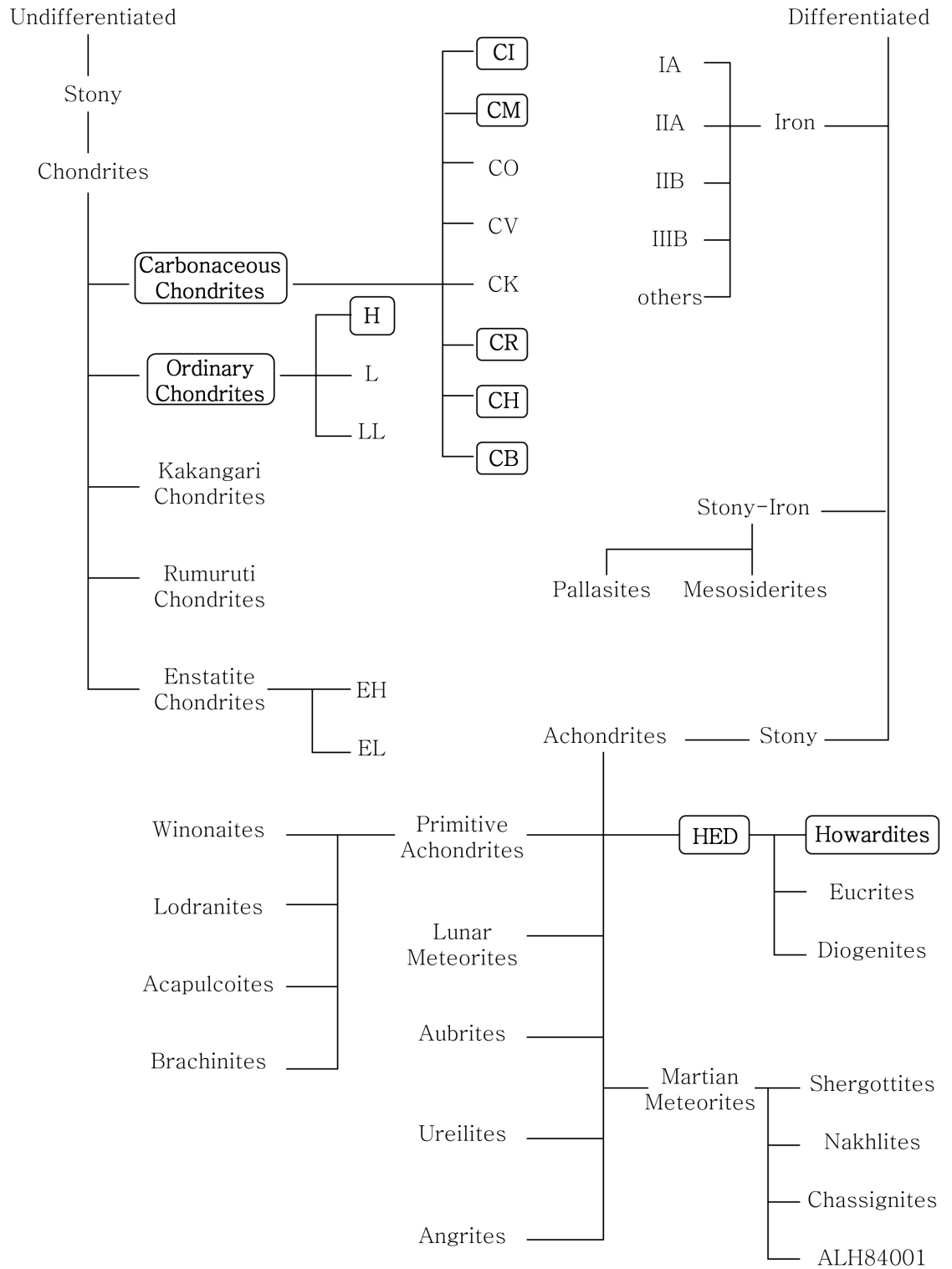


**Figure A1:** classification of meteorites.

chondrites are distinct from the other groups for their larger abundance of Fe-Ni metal, with CH and CB chondrites being by far the most metal-rich among carbonaceous chondrites.

**Ordinary chondrites** are the most common chondrites, representing ~80 % of the observed fall. They are composed by chondrules and Fe-Ni metal grains uniformly distributed in a fine-grained matrix. They generally suffered more intense thermal metamorphism than carbonaceous chondrites, but less significant or no aqueous alteration. The three ordinary chondrites groups, H, L and LL, are distinct on the basis of their Fe and metal content (metal indicate here reduced Fe, in contrast to oxidized Fe as that present in silicates). H chondrites are the most rich in both Fe (25–30 wt%) and metal (15–19 wt%), followed by L chondrites (20–23 wt% of Fe and 1–10 wt% of metal) with LL chondrites being the most Fe- and metal-poor (19–22 wt% and 1–3 wt%, respectively).

**Howardites**, Eucrites and Diogenites are basaltic (i.e., solidified from a magma) achondrites originated on the asteroid 4 Vesta. Eucrites are supposed to be samples of rocks formed by flows that erupted on the surface of Vesta. These flows would have covered a layer of rocks from which Diogenites originated. Collisions mixed these two types of rocks, and the regolith-formation process induced by micrometeorites, cosmic rays and solar wind compacted them in breccias represented today by Howardites. Howardites are particularly rich in chondritic xenoliths.

## Appendix B

# Principal meteorite minerals

Here is a list with the composition of the principal minerals found in meteorites.

**Albite** [NaAlSi<sub>3</sub>O<sub>8</sub>]

Sodium end member of the plagioclase solid solution series.

**Anorthite** [CaAl<sub>2</sub>Si<sub>2</sub>O<sub>8</sub>]

Calcium end member of the plagioclase solid solution series.

**Augite** [(Ca,Mg,Fe)SiO<sub>3</sub>]

Calcium-rich iron magnesium pyroxene.

**Breunnerite** [(MgFe)CO<sub>3</sub>]

Iron magnesium carbonate.

**Calcite** [CaCO<sub>3</sub>]

Calcium carbonate.

**Carbonate**

Class of minerals containing the carbonate ion CO<sub>3</sub><sup>2-</sup>.

**Chromite** [FeCr<sub>2</sub>O<sub>4</sub>]

Iron chromium oxide.

**Corundum** [Al<sub>2</sub>O<sub>3</sub>]

Aluminium oxide.

**Diopside** [(Ca,Mg)Si<sub>2</sub>O<sub>6</sub>]

Calcium-rich magnesium pyroxene.

**Dolomite** [CaMg(CO<sub>3</sub>)<sub>2</sub>]

Calcium magnesium carbonate.

**Enstatite** [MgSiO<sub>3</sub>]

Magnesium end member of the orthopyroxene solid solution series.

**Fayalite** [Fe<sub>2</sub>SiO<sub>4</sub>]

Iron end member of the olivine solid solution series.

**Ferrosilite** [FeSiO<sub>3</sub>]

Iron end member of the orthopyroxene solid solution series.

**Forsterite** [Mg<sub>2</sub>SiO<sub>4</sub>]

Magnesium end member of the olivine solid solution series.

**Hedenbergite** [(Ca,Fe)Si<sub>2</sub>O<sub>6</sub>]

Calcium-rich iron pyroxene.

**Kamacite** [(Fe,Ni)]

Iron nickel metal, with nickel content up to 7.5 wt%.

**Magnetite** [Fe<sub>3</sub>O<sub>4</sub>]

Iron oxide.

**Olivine**

Silicate solid solution between Forsterite (Mg<sub>2</sub>SiO<sub>4</sub>) and Fayalite (Fe<sub>2</sub>SiO<sub>4</sub>). Olivine composition is usually indicated as Fo<sub>x</sub> where x is the value of the ratio Fo = Mg/(Mg+Fe) expressed in mol%, which varies between 100 for pure Forsterite and 0 for pure Fayalite.

**Osbornite** [TiN]

Titanium nitride.

**Pentlandite** [(Fe,Ni)<sub>9</sub>S<sub>8</sub>]

Iron nickel sulfide with Fe:Ni ratio close to 1.

**Phyllosilicates**

Silicate minerals containing the hydroxyl group OH and with typical structure organized in parallel sheets. The most common in meteorites are phyllosilicates of the Serpentine group and Smectite group.

**Plagioclase**

Silicate minerals ranging in composition between Albite (NaAlSi<sub>3</sub>O<sub>8</sub>) and Anorthite (CaAl<sub>2</sub>Si<sub>2</sub>O<sub>8</sub>).

**Pyroxene**

Group of silicate minerals. The orthopyroxenes range in composition between Enstatite ( $\text{MgSiO}_3$ ) and Ferrosilite ( $\text{FeSiO}_3$ ). Their composition is usually indicated as  $\text{En}_x\text{-Fs}_y$ , where  $x$  is the value of the ratio  $\text{En} = \text{Mg}/(\text{Mg}+\text{Fe}+\text{Ca})$  mol%, and  $y$  is the value of the ratio  $\text{Fs} = \text{Fe}/(\text{Mg}+\text{Fe}+\text{Ca})$  mol%. The calcium-rich pyroxenes are Diopside [ $(\text{Ca},\text{Mg})\text{Si}_2\text{O}_6$ ], Augite [ $(\text{Ca},\text{Mg},\text{Fe})\text{SiO}_3$ ] and Hedenbergite [ $(\text{Ca},\text{Fe})\text{Si}_2\text{O}_6$ ].

**Pyrrhotite** [ $(\text{Fe},\text{Ni})_{1-x}\text{S}$ ]

Iron nickel sulfide (with  $x = 0$  to 0.2).

**Serpentine** [ $\text{Mg}_3\text{Si}_2\text{O}_5(\text{OH})_4$ ]

Hydrous silicates produced by aqueous alteration of magnesium silicates.

**Siderite** [ $\text{FeCO}_3$ ]

Iron carbonate.

**Smectite**

Clay-like minerals including Montmorillonite  $((\text{Na},\text{Ca})_{0.3}(\text{Al},\text{Mg})_2(\text{Si}_4\text{O}_{10})(\text{OH})_2 \cdot n\text{H}_2\text{O})$  and Saponite  $((\text{Ca},\text{Na})_{0.3}(\text{Mg},\text{Fe}^{+2})_3(\text{Si},\text{Al})_4\text{O}_{10}(\text{OH})_2 \cdot 4\text{H}_2\text{O})$ .

**Spinel** [ $\text{MgAl}_2\text{O}_4$ ]

Magnesium aluminium member of the mineral group with composition  $\text{A}^{2+}\text{B}_2^{3+}\text{O}_4^{2-}$ .

**Sulfide**

Minerals containing the ion  $\text{S}_2^-$ . Iron sulfides as Troilite ( $\text{FeS}$ ), Pyrrhotite ( $(\text{Fe}_{1-x}\text{S})$ ) and Pentlandite  $((\text{Fe},\text{Ni})_9\text{S}_8)$  are common in meteorites.

**Taenite** [ $(\text{Fe},\text{Ni})$ ]

Iron nickel metal, with nickel content greater than 20 wt%.

**Troilite** [ $\text{FeS}$ ]

Iron sulfide.

**Wollastonite** [ $\text{CaSiO}_3$ ]

Calcium end member in the  $\text{CaSiO}_3\text{-MgSiO}_3\text{-FeSiO}_3$  pyroxene composition system.

# List of publications associated with my PhD thesis

## Publications on refereed journals

G. Briani, M. Gounelle, Y. Marrocchi, S. Mostefaoui, H. Leroux, E. Quirico, A. Meibom, *Pristine extraterrestrial material with unprecedented nitrogen isotopic variation*, Proceedings of the National Academy of Science, 106, 10522-10527, 2009

## Not-refereed proceedings

G. Briani, M. Gounelle, M. E. Zolensky, *(Micro)xenolith systematics in H chondrites*, Meteoritics and Planetary Science Supplement, abstract # 5120, 44, A41, 2009

M. E. Zolensky, G. Briani, M. Gounelle, T. Mikouchi, K. Oshumi, M. K. Weisberg, L. Le, W. Satake, T. Kurihara, *Searching for chips of Kuiper Belt objects in meteorites*, 40th Lunar and Planetary Science Conference, March 23-27 2009, The Woodlands, Texas (USA)

G. Briani, M. Gounelle, Y. Marrocchi, S. Mostefaoui, F. Robert, H. Leroux, A. Meibom, *Ultra-pristine extra-terrestrial material with unprecedented nitrogen isotopic variation*, 40th Lunar and Planetary Science Conference, March 23-27 2009, The Woodlands, Texas (USA)

G. Briani, M. Gounelle, *Carbonaceous chondritic microclasts in meteorites: samples of the Late Heavy Bombardment?* LPI Contribution No. 1439, p. 21-22, 2009, Workshop on the early solar system impact bombardment, November 19-20, Houston, Texas, (USA)

M. E. Zolensky, M. Gounelle, G. Briani, W. Bottke, E. Young, K. Dyl, M. K. Weisberg, *Pieces of Kuiper Belt bodies in meteorites*, Meteoritics and Planetary Science Supplement, abstract # 5265, 43, A177, 2008

G. Briani, G. Pupillo, S. Aiello, E. Pace, S. N. Shore, A. Passaro, *Study of the Interaction of Micrometeoroids with Earth Atmosphere*, Memorie della Società Astronomica Italiana Supplementi, 11, 89, 2007

### Submitted papers

G. Briani, E. Pace, S. N. Shore, G. Pupillo, A. Passaro, F. Selsis and S. Aiello, *Study of the Interaction of Micrometeoroids with Earth's Atmosphere*.  
submitted to Astronomy & Astrophysics.

### In preparation

G. Briani, M. Gounelle, M. Bourot-Denise, M. E. Zolensky, *Systematic search for new xenoliths and microxenoliths in H chondrites*.

G. Briani, E. Quirico, M. Gounelle, G. Montagnac, *Characterization of organic matter in Isheyevo microxenoliths by Raman spectroscopy*.

G. Briani, A. Morbidelli, M. Gounelle, D. Nesvorný, *Origin of microxenoliths in meteorites: asteroids or comets?*.

# Bibliography

- Aboudan, A., Colombatti, G., Ferri, F., and Angrilli, F. (2008). Huygens probe entry trajectory and attitude estimated simultaneously with Titan atmospheric structure by Kalman filtering. *Planetary and Space Science*, **56**, 573–585.
- Alexander, C. M. O., Newsome, S. N., Fogel, M. L., and Cody, G. D. (2009). Deuterium enrichments – parent body products or a question of preservation? *40th Lunar and Planetary Science Conference (abstract 2546)*.
- Alexander, C. M. O. D., Fogel, M., Yabuta, H., and Cody, G. D. (2007). The origin and evolution of chondrites recorded in the elemental and isotopic compositions of their macromolecular organic matter. *Geochimica et Cosmochimica Acta*, **71**, 4380–4403.
- Becker, R. H. and Epstein, S. (1982). Carbon, hydrogen and nitrogen isotopes in solvent-extractable organic matter from carbonaceous chondrites. *Geochimica et Cosmochimica Acta*, **46**, 97–103.
- Beny-Bassez, C. and Rouzaud, J. N. (1985). Characterization of carbonaceous materials by correlated electron and optical microscopy and raman microspectroscopy. *Scanning electron microscopy*, **12**, 119–132.
- Bernstein, M. P., Elsila, J. E., Dworkin, J. P., Sandford, S. A., Allamandola, L. J., and Zare, R. N. (2002). Side Group Addition to the Polycyclic Aromatic Hydrocarbon Coronene by Ultraviolet Photolysis in Cosmic Ice Analogs. *Astrophysical Journal*, **576**, 1115–1120.
- Beysac, O., Goff, B., Chopin, C., and Rouzaud, J. N. (2002). Raman spectra of carbonaceous material in metasediments: a new geothermometer. *Journal of Metamorphic Geology*, **20**, 859–871.
- Binzel, R. P. and Xu, S. (1993). Chips off of asteroid 4 Vesta - Evidence for the parent body of basaltic achondrite meteorites. *Science*, **260**, 186–191.
- Bischoff, A., Scott, E. R. D., Metzler, K., and Goodrich, C. A. (2006). *Nature and Origins of Meteoritic Breccias*, pages 679–712.

- Bland, P. A., Cintala, M. J., Hörz, F., and Cressey, G. (2001). Survivability of meteorite projectiles – results from impact experiments. *32nd Lunar and Planetary Science Conference (abstract 1764)*.
- Bonal, L., Quirico, E., Bourot-Denise, M., and Montagnac, G. (2006). Determination of the petrologic type of CV3 chondrites by Raman spectroscopy of included organic matter. *Geochimica et Cosmochimica Acta*, **70**, 1849–1863.
- Bonal, L., Bourot-Denise, M., Quirico, E., Montagnac, G., and Lewin, E. (2007). Organic matter and metamorphic history of CO chondrites. *Geochimica et Cosmochimica Acta*, **71**, 1605–1623.
- Bonal, L., Huss, G. R., Krot, A. N., and Nagashima, K. (2008). Lithic clasts of cb/ch-like carbonaceous chondrite isheyev: Diversity revealed by mineralogy, structure of organic matter and oxygen isotopic composition of carbonates. *39th Lunar and Planetary Science Conference (abstract 1506)*.
- Bonny, P. and Balageas, D. (1990). Entry corridor of micrometeorites containing organic material. *21st Lunar and Planetary Science Conference*, pages 111–112.
- Bouvier, A., Blichert-Toft, J., Moynier, F., Vervoort, J. D., and Albarède, F. (2007). Pb Pb dating constraints on the accretion and cooling history of chondrites. *Geochimica et Cosmochimica Acta*, **71**, 1583–1604.
- Bradley, J. P. (2003). Interplanetary Dust Particles. *Treatise on Geochemistry*, **1**, 689–711.
- Brearley, A. J. and Papike, J. J. (1993). Carbonaceous chondrite clasts in the kapoeta howardite. *24th Lunar and Planetary Science Conference*, pages 183–184.
- Brearley, A. J. and Prinz, M. (1992). CI chondrite-like clasts in the Nilpena polymict ureilite - Implications for aqueous alteration processes in CI chondrites. *Geochimica et Cosmochimica Acta*, **56**, 1373–1386.
- Briani, G. and Gounelle, M. (2008). Carbonaceous Chondritic Microclasts in Meteorites: Samples of the Late Heavy Bombardment? *LPI Contributions*, **1439**, 21–22.
- Brinton, K. L. F., Engrand, C., Glavin, D. P., Bada, J. L., and Maurette, M. (1998). A Search for Extraterrestrial Amino Acids in Carbonaceous Antarctic Micrometeorites. *Origins of Life and Evolution of the Biosphere*, **28**, 413–424.

- Bronshnten, V. (1983). *Physics of meteoric phenomena*. D. Reidel Publishing Company.
- Brosch, N., Schijvarg, L. S., Podolak, M., and Rosenkrantz, M. R. (2001). Meteor observations from Israel. In *Meteoroids 2001 Conference*, volume 495 of *ESA Special Publication*, pages 165–173.
- Buchanan, P. C. and Zolensky, M. E. (2003). Carbonaceous chondrite fragments in the polymict eucrite yamato 791834. *24th Lunar and Planetary Science Conference (abstract 1299)*.
- Buchanan, P. C., Zolensky, M. E., and Reid, A. M. (1993). Carbonaceous chondrite clasts in the howardites Bholghati and EET87513. *Meteoritics*, **28**, 659–669.
- Bunch, T. E. and Rajan, R. S. (1988). *Meteorites and the Early Solar System*, chapter Meteorite regolithic breccias, pages 144–164.
- Bunch, T. E., Chang, S., Frick, U., Neil, J. M., and Moreland, G. (1979). Carbonaceous chondrites. I - Characterization and significance of carbonaceous chondrite CM xenoliths in the Jodzie howardite. *Geochimica et Cosmochimica Acta*, **43**, 1727–1729.
- Busemann, H., Young, A. F., O’D. Alexander, C. M., Hoppe, P., Mukhopadhyay, S., and Nittler, L. R. (2006). Interstellar Chemistry Recorded in Organic Matter from Primitive Meteorites. *Science*, **312**, 727–730.
- Campbell-Brown, M. D. and Koschny, D. (2004). Model of the ablation of faint meteors. *Astronomy & Astrophysics*, **418**, 751–758.
- Campins, H. and Swindle, T. D. (1998). Expected characteristics of cometary meteorites. *Meteoritics and Planetary Science*, **33**, 1201–1211.
- Ceplecha, Z., Borovicka, J., Graham elford, W., Revelle, D. O., Hawkes, R. L., and Porubcan, V. Simek, M. (1998). Meteor phenomena and bodies. *Space Science Review*, **84**, 327–471.
- Chapman, C. R., Cohen, B. A., and Grinspoon, D. H. (2007). What are the real constraints on the existence and magnitude of the late heavy bombardment? *Icarus*, **189**, 233–245.
- Chappelow, J. E. and Sharpton, V. L. (2006). Atmospheric variations and meteorite production on Mars. *Icarus*, **184**, 424–435.
- Clayton, R. N. (2002). Solar System: Self-shielding in the solar nebula. *Nature*, **415**, 860–861.

- Clemett, S. J., Chillier, X. D. F., Gillette, S., Zare, R. N., Maurette, M., Engrand, C., and Kurat, G. (1998). Observation of Indigenous Polycyclic Aromatic Hydrocarbons in ‘Giant’ carbonaceous Antarctic Micrometeorites. *Origins of Life and Evolution of the Biosphere*, **28**, 425–448.
- Cody, G. D., O’D Alexander, C. M., Fogel, M., Araki, T., and Kilcoyne, D. (2005). The History of Early Solar System Processes Recorded in the Structure of Meteoritic Organic Solids. *Meteoritics and Planetary Science Supplement*, **40**, 5163.
- Cody, G. D., Alexander, C. M. O., Yabuta, H., Kilcoyne, A. L. D., Araki, T., Ade, H., Dera, P., Fogel, M., Militzer, B., and Mysen, B. O. (2008). Organic thermometry for chondritic parent bodies. *Earth and Planetary Science Letters*, **272**, 446–455.
- Cody, G. D., Heying, E., and Alexander, C. M. O. (2009). A post accretionary origin for meteoritic and cometary organic solids? *40th Lunar and Planetary Science Conference (abstract 2325)*.
- Coulson, S. G. (2002). Resistance of motion to a small, hypervelocity sphere, sputtering through a gas. *Monthly Notices of the Royal Astronomical Society*, **332**, 741–744.
- Coulson, S. G. and Wickramasinge, N. C. (2003). Frictional and radiation heating of micron-sized meteoroids in the earth’s upper atmosphere. *Monthly Notices of the Royal Astronomical Society*, **343**, 1123–1130.
- Dartois, E. and Muñoz-Caro, G. M. (2007). Carbonaceous dust grains in luminous infrared galaxies. Spitzer/IRS reveals a-C:H as an abundant and ubiquitous ISM component. *Astronomy & Astrophysics*, **476**, 1235–1242.
- Derenne, S. and Robert, F. (2009). A Molecular Model of Chemical Structure of Insoluble Organic Matter in Carbonaceous Chondrites. *Meteoritics and Planetary Science Supplement*, **72**, 5119.
- Dobrică, E., Engrand, C., Quirico, E., Montagnac, G., and Duprat, J. (2008). New Clues on Composition and Structure of Carbonaceous Matter in Antarctic Micrometeorites. *Meteoritics and Planetary Science Supplement*, **43**, 5202.
- Dobrică, E., Engrand, C., Quirico, E., Montagnac, G., and Duprat, J. (2009). Immature carbonaceous matter in concordia antarctic micrometeorites. *40th Lunar and Planetary Science Conference (abstract 1688)*.
- Dodd, R. T. and Jarosewich, E. (1979). Incipient melting in and shock classification of L-group chondrites. *Earth and Planetary Science Letters*, **44**, 335–340.

- Draine, B. T. and Salpeter, E. E. (1979). On the physics of dust grain in hot gas. *Astrophysical Journal*, **231**, 77–94.
- Duprat, J., Engrand, C., Maurette, M., Kurat, G., Gounelle, M., and Hammer, C. (2007). Micrometeorites from central antarctic snow: the concordia collection. *Advances in Space Research*, **39**, 605–611.
- Ehrenfreund, P., Robert, F., D’Hendencourt, L., and Behar, F. (1991). Comparison of interstellar and meteoritic organic matter at 3.4 microns. *Astronomy & Astrophysics*, **252**, 712–717.
- English, M. A., Lara, L. M., Lorenz, R. D., Ratcliff, P. R., and Rodrigo, R. (1996). Ablation and chemistry of meteoric materials in the atmosphere of Titan. *Advances in Space Research*, **17**, 157–160.
- Engrand, C. and Maurette, M. (1998). Carbonaceous micrometeorites from antarctica. *Meteoritics and Planetary Science*, **33**, 565–580.
- Eugster, O. (1988). Cosmic-ray production rates for  $^3\text{He}$ ,  $^{21}\text{Ne}$ ,  $^{38}\text{Ar}$ ,  $^{83}\text{Kr}$ , and  $^{126}\text{Xe}$  in chondrites based on  $^{81}\text{Kr}$ - $^{81}\text{Kr}$  exposure ages. *19th Lunar and Planetary Science Conference*, pages 311–312.
- Eugster, O., Herzog, G. F., Marti, K., and Caffee, M. W. (2006). *Irradiation Records, Cosmic-Ray Exposure Ages, and Transfer Times of Meteorites*, pages 829–851.
- Eugster, O., Lorenzetti, S., Krähenbühl, U., and Marti, K. (2007). Comparison of cosmic-ray exposure ages and trapped noble gases in chondrule and matrix samples of ordinary, enstatite, and carbonaceous chondrites. *Meteoritics and Planetary Science*, **42**, 1351–1371.
- Farinella, P., Froeschle, C., and Gonczi, R. (1993). Meteorites from the asteroid 6 Hebe. *Celestial Mechanics and Dynamical Astronomy*, **56**, 287–305.
- Ferrari, A. C. and Robertson, J. (2000). Interpretation of Raman spectra of disordered and amorphous carbon. *Physical Review B*, **61**, 14095–14107.
- Ferrari, A. C. and Robertson, J. (2001). Resonant Raman spectroscopy of disordered, amorphous, and diamondlike carbon. *Physical Review B*, **64**(7), 075414.
- Ferrari, A. C., Rodil, S. E., and Robertson, J. (2003). Interpretation of infrared and Raman spectra of amorphous carbon nitrides. *Physical Review B*, **67**(15), 155306.
- Ferraro, J. R., Nakamoto, K., and Brown, C. W. (2003). *Introductory Raman spectroscopy*. Elsevier.

- Floss, C., Stadermann, F. J., Bradley, J. P., Dai, Z. R., Bajt, S., Graham, G., and Lea, A. S. (2006). Identification of isotopically primitive interplanetary dust particles: A NanoSIMS isotopic imaging study. *Geochimica et Cosmochimica Acta*, **70**, 2371–2399.
- Flynn, G. J. (1992). Atmospheric entry survival of large micrometeorites: Implications for their sources and for the cometary contribution to the zodiacal cloud. In A. W. Harris & E. Bowell, editor, *Asteroids, Comets, Meteors 1991*, pages 195–199.
- Flynn, G. J. (1995a). Atmospheric Entry Heating of Large Interplanetary Dust Particles. *Meteoritics*, **30**, 504.
- Flynn, G. J. (1995b). Thermal gradients in interplanetary dust particles: The effect of an endothermic phase transition. *26th Lunar and Planetary Science Conference*, pages 405–406.
- Flynn, G. J., Keller, L. P., Jacobsen, C., and Wirrick, S. (2004). The Origin of Organic Matter in the Solar System: Evidence from the Interplanetary Dust Particles. In R. Norris & F. Stootman, editor, *Bioastronomy 2002: Life Among the Stars*, volume 213 of *IAU Symposium*, pages 275–280.
- Fodor, R. V. and Keil, K. (1976). Carbonaceous and non-carbonaceous lithic fragments in the Plainview, Texas, chondrite - Origin and history. *Geochimica et Cosmochimica Acta*, **40**, 177–189.
- Fredriksson, K., Jarosewich, E., and Nelen, J. (1968). *Meteorite Research*, pages 155–165. D. Reidel Publishing Company.
- Fuchs, H. L., Olsen, E., and Jensen, K. J. (1973). Mineralogy, mineral-chemistry and composition of the murchison (c2) meteorite. *Smithsonian Contribution to the Earth Science*, **10**.
- Fulchignoni, M., Ferri, F., Angrilli, F., Ball, A. J., Bar-Nun, A., Barucci, M. A., Bettanini, C., Bianchini, G., Borucki, W., Colombatti, G., Coradini, M., Coustenis, A., Debei, S., Falkner, P., Fanti, G., Flamini, E., Gaborit, V., Grard, R., Hamelin, M., Harri, A. M., Hathi, B., Jernej, I., Leese, M. R., Lehto, A., Lion Stoppato, P. F., Lopez-Moreno, J. J., Makinen, T., McDonnell, J. A. M., McKay, C. P., Molina-Cuberos, G., Neubauer, F. M., Pirronello, V., Rodrigo, R., Saggin, B., Schwingenschuh, K., Seiff, A., Simoes, F., Svedhem, H., Tokano, T., Towner, M. C., Trautner, R., Withers, P., and Zarnecki, J. C. (2005). In situ measurements of the physical characteristics of titan's environment. *Nature*, **438**, 785–791.
- Gaffey, M. J. and Gilbert, S. L. (1998). Asteroid 6 Hebe: The probable parent body of the H-Type ordinary chondrites and the IIE iron meteorites. *Meteoritics and Planetary Science*, **33**, 1281–1295.

- Genge, M., Engrand, C., Gounelle, M., and Taylor, S. (2008). The classification of micrometeorites. *Meteoritics and Planetary Science*, **43**, 497–515.
- Genge, M. J. (2006a). Igneous rims on micrometeorites. *Geochimica et Cosmochimica Acta*, **70**, 2603–2621.
- Genge, M. J. (2006b). Ordinary chondrite micrometeorites from the koronis asteroids. *37th Lunar and Planetary Institute Science Conference (abstract 1759)*.
- Genge, M. J., Grady, M. M., and Hutchison, R. (1997). The textures and compositions of fine-grained Antarctic micrometeorites - Implications for comparisons with meteorites. *Geochimica et Cosmochimica Acta*, **61**, 5149.
- Girich, A. L. and Semenenko, V. P. (2001). Magnetite-bearing Fragments in the Krymka Chondrite. *Meteoritics and Planetary Science Supplement*, **36**, 66.
- Glavin, D. B. and Bada, J. L. (2001). Survival of amino acids in micrometeorites during atmospheric entry. *Astrobiology*, **1**, 259–269.
- Gomes, R., Levison, H. F., Tsiganis, K., and Morbidelli, A. (2005). Origin of the cataclysmic Late Heavy Bombardment period of the terrestrial planets. *Nature*, **435**, 466–469.
- Gordon, S. H., Hammond, S. J., Howard, L. E., and Bland, P. A. (2009). Dark inclusions: Clasts of cm-type material within allende. *40th Lunar and Planetary Science Conference (abstract 1713)*.
- Goswami, J. N., Lal, D., and Wilkening, L. L. (1984). Gas-rich meteorites - Probes for particle environment and dynamical processes in the inner solar system. *Space Science Reviews*, **37**, 111–159.
- Gounelle, M., Zolensky, M. E., Liou, J.-C., Bland, P. A., and Alard, O. (2003). Mineralogy of carbonaceous chondritic microclasts in howardites: identification of C2 fossil micrometeorites. *Geochimica et Cosmochimica Acta*, **67**, 507–527.
- Gounelle, M., Engrand, C., Alard, O., Bland, P. A., Zolensky, M. E., Russell, S. S., and Duprat, J. (2005). Hydrogen isotopic composition of water from fossil micrometeorites in howardites. *Geochimica et Cosmochimica Acta*, **69**, 3431–3443.
- Gounelle, M., Spurný, P., and Bland, P. A. (2006). The orbit and atmospheric trajectory of the Orgueil meteorite from historical records. *Meteoritics and Planetary Science*, **41**, 135–150.

- Gounelle, M., Morbidelli, A., Bland, P. A., Spurny, P., Young, E. D., and Sephton, M. (2008). *Meteorites from the Outer Solar System?*, pages 525–541.
- Gounelle, M., Chaussidon, M., Morbidelli, A., Barrat, J. A., Engrand, C., Zolensky, M. E., and McKeegan, K. D. (2009). From the Cover: A unique basaltic micrometeorite expands the inventory of solar system planetary crusts. *Proceedings of the National Academy of Science*, **106**, 6904–6909.
- Graf, T. and Marti, K. (1995). Collisional history of H chondrites. *Journal of Geophysical Research*, **100**, 21247–21264.
- Greshake, A., Kloeck, W., Arndt, P., Maetz, M., Flynn, G. J., Bajt, S., and Bischoff, A. (1998). Heating experiments simulating atmospheric entry heating of micrometeorites: Clues to their parent body sources. *Meteoritics and Planetary Science*, **33**, 267–290.
- Greshake, A., Krot, A. N., Meibom, A., Weisberg, M. K., Zolensky, M. E., and Keil, K. (2002). Heavily-hydrated lithic clasts in CH chondrites and the related, metal-rich chondrites Queen Alexandra Range 94411 and Hammadah al Hamra 237. *Meteoritics and Planetary Science*, **37**, 281–293.
- Grimm, R. E. (1985). Penecontemporaneous metamorphism, fragmentation, and reassembly of ordinary chondrite parent bodies. *Journal of Geophysical Research*, **90**, 2022–2028.
- Grimm, R. E., Bottke, W. F., Durda, D. D., Enke, B., Scott, E. R. D., Asphaug, E., and Richardson, D. (2005). Joint thermal and collisional modeling of the h-chondrite parent body. *36th Lunar and Planetary Science Conference (abstract 1798)*.
- Grün, E., Zook, H. A., Fichtig, H., and Giese, R. H. (1985). Collisional balance of meteoritic complex. *Icarus*, **62**, 244–272.
- Grün, E., Baguhl, M., Svedhem, H., and Zook, H. A. (2001). *Interplanetary dust*, chapter In situ measurements of cosmic dust, pages 295–346. Springer.
- Grün, E., Dikarev, V., Frisch, P. C., Graps, A., Kempf, S., Krüger, H., Landgraf, M., Moragas-Klostermeyer, G., and Srama, R. (2004). Dust in Interplanetary Space and in the Local Galactic Environment. **309**, 245–263.
- Gustafson, B. A. S. (1994). Physics of Zodiacal Dust. *Annual Review of Earth and Planetary Sciences*, **22**, 553–595.

- Haqq-Misra, J. D., Domagal-Goldman, S. D., Kasting, P. J., and Kasting, J. F. (2008). A Revised, Hazy Methane Greenhouse for the Archean Earth. *Astrobiology*, **8**, 1127–1137.
- Hauser, M. G., Gillett, F. C., Low, F. J., Gautier, T. N., Beichman, C. A., Aumann, H. H., Neugebauer, G., Baud, B., Boggess, N., and Emerson, J. P. (1984). IRAS observations of the diffuse infrared background. *Astrophysical Journal*, **278**, L15–L18.
- Hedin, A. (1991). Extension of the msis thermosphere model into the middle and lower atmosphere. *Journal of Geophysical Research*, **96**, 1159–1172.
- Hiroi, T., Zolensky, M. I., and Pieters, C. M. (1997). Characterization of unusual CI/CM/CR meteorites from reflectance spectroscopy. *28th Lunar and Planetary Science Conference (abstract 1463)*.
- Hood, L. L. and Horanyi, M. (1991). Gas dynamic heating of chondrule precursor grains in the solar nebula. *Icarus*, **93**, 259–269.
- Housen, K. R. and Wilkening, L. L. (1982). Regoliths on small bodies in the solar system. *Annual Review of Earth and Planetary Sciences*, **10**, 355–376.
- Ikeda, Y., Kita, N. T., Morishita, Y., and Weisberg, M. K. (2003). Primitive clasts in the Dar al Gani 319 polymict ureilite: Precursors of the ureilites. *Antarctic Meteorite Research*, **16**, 105–127.
- Ip, W. (1990). Meteoroid ablation processes in Titan's atmosphere. *Nature*, **345**, 511.
- Ivanov, A. V., Ulyanov, A. A., Skripnic, A. Y., and Konokona, N. N. (1984). The kaidun polymict carbonaceous breccia: the mixture of incompatible types of meteorites. *15th Lunar and Planetary Science Conference*, pages 393–394.
- Ivanova, M. A., Kononkova, N. N., Krot, A. N., Greenwood, R. C., Franchi, I. A., Verchovsky, A. B., Tieloff, M., Korochantseva, E. V., and Brandstätter, F. (2008). The Isheyevo meteorite: Mineralogy, petrology, bulk chemistry, oxygen, nitrogen, carbon isotopic compositions, and  $^{40}\text{Ar}$ - $^{39}\text{Ar}$  ages. *Meteoritics and Planetary Science*, **43**, 915–940.
- Johnson, C. A. and Prinz, M. (1993). Carbonate compositions in CM and CI chondrites, and implications for aqueous alteration. *Geochimica et Cosmochimica Acta*, **57**, 2843–2852.
- Jull, A. J. T. (2001). *Accretion of extraterrestrial matter throughout Earth's history*, chapter Terrestrial ages of meteorites, pages 241–266. Kluwer Academic.

- Jurac, S., Johnson, R. E., and Donn, B. (1998). Monte carlo calculation of the sputtering of grains: enhanced sputtering of small grains. *Astrophysical Journal*, **503**, 247–252.
- Kasting, J. F. (1993). Earth's early atmosphere. *Science*, **259**, 920.
- Keil, K. (1982). Composition and origin of chondritic breccias. In G. J. Taylor & L. L. Wilkening, editor, *Workshop on Lunar Breccias and Soils and their Meteoritic Analogs*, page 65. Lunar and Planetary Institute.
- Keller, L. P., Messenger, S., Flynn, G. J., Clemett, S., Wirick, S., and Jacobsen, C. (2004). The nature of molecular cloud material in interplanetary dust. *Geochimica et Cosmochimica Acta*, **68**, 2577–2589.
- Klacka, J. (1992). Poynting-Robertson effect. I - Equation of motion. *Earth Moon and Planets*, **59**, 41–59.
- Kortenkamp, S. J. and Dermott, S. F. (1998). Accretion of Interplanetary Dust Particles by the Earth. *Icarus*, **135**, 469–495.
- Krot, A. N., Brearley, A. J., Ulyanov, A. A., Biryukov, V. V., Swindle, T. D., Keil, K., Mittlefehldt, D. W., Scott, E. R. D., Clayton, R. N., and Mayeda, T. K. (1999). Mineralogy, petrography and bulk chemical, iodine-xenon, and oxygen-isotopic compositions of dark inclusions in the reduced CV3 chondrite Efremovka. *Meteoritics and Planetary Science*, **34**, 67–89.
- Krot, A. N., Ivanova, M. A., and Ulyanov, A. A. (2007). Chondrules in the cb/ch-like carbonaceous chondrite isheyevo: Evidence for various chondrule-forming mechanisms and multiple chondrule generations. *Chemie der Erde - Geochemistry*, **67**(4), 283 – 300.
- Kuehner, S. M., Irving, A. J., Rumble, D., Nicklin, I., and Gregory, D. A. (2009). Exotic, primitive micrometeorite clasts related to cm chondrites in polymict eucrite breccia northwest africa 5232. *40th Lunar and Planetary Science Conference (abstract 2315)*.
- Kulikov, Y. N., Lammer, H., Lichtenegger, H. I. M., Penz, T., Breuer, D., Spohn, T., Lundin, R., and Biernat, H. (2007). A comparative study of the influence of the active young sun on the early atmospheres of earth, venus, and mars. *Space Science Review*, **129**, 207–243.
- Kurat, G., Koeberl, C., Presper, T., Brandstätter, F., and Maurette, M. (1994). Petrology and geochemistry of Antarctic micrometeorites. *Geochimica et Cosmochimica Acta*, **58**, 3879–3904.
- Leinert, C., Roser, S., and Buitrago, J. (1983). How to maintain the spatial distribution of interplanetary dust. *Astronomy & Astrophysics*, **118**, 345–357.

- Leitch, C. A. and Grossman, L. (1977). Lithic clasts in the Supuhee chondrite. *Meteoritics*, **12**, 125–139.
- Levison, H. F. and Duncan, M. J. (1997). From the Kuiper Belt to Jupiter-Family Comets: The Spatial Distribution of Ecliptic Comets. *Icarus*, **127**, 13–32.
- Levison, H. F., Bottke, W., Gounelle, M., Morbidelli, A., Nesvorný, D., and Tsiganis, K. (2008a). Chaotic Capture of Planetesimals into Regular Regions of the Solar System. II: Embedding Comets in the Asteroid Belt. In *AAS/Division of Dynamical Astronomy Meeting*, volume 39 of *AAS/Division of Dynamical Astronomy Meeting*, page 12.05.
- Levison, H. F., Morbidelli, A., Vanlaerhoven, C., Gomes, R., and Tsiganis, K. (2008b). Origin of the structure of the Kuiper belt during a dynamical instability in the orbits of Uranus and Neptune. *Icarus*, **196**, 258–273.
- Levison, H. F., Bottke, W. F., Gounelle, M., Morbidelli, A., Nesvorný, D., and Tsiganis, K. (2009). Contamination of the asteroid belt by primordial trans-Neptunian objects. *Nature*, **460**, 364–366.
- Liou, J.-C., Zook, H. A., and Dermott, S. F. (1996). Kuiper Belt Dust Grains as a Source of Interplanetary Dust Particles. *Icarus*, **124**, 429–440.
- Lipschutz, M. E., Gaffey, M. J., and Pellas, P. (1989). Meteoritic parent bodies - Nature, number, size and relation to present-day asteroids. In R. P. Binzel, T. Gehrels, & M. S. Matthews, editor, *Asteroids II*, pages 740–777.
- Lodders, K. and Osborne, R. (1999). Perspectives on the Comet-Asteroid-Meteorite Link. *Space Science Reviews*, **90**, 289–297.
- Lorenz, C. A., Ivanova, M. A., Kurat, G., and Brandstätter, F. (2005). Feo-rich xenoliths in the staroye pesyanoe aubrite. *36th Lunar and Planetary Science Conference (abstract 1612)*.
- Love, S. G. and Brownlee, D. E. (1991). Heating and thermal transformation of micrometeoroids entering the earth's atmosphere. *Icarus*, **89**, 26–43.
- Love, S. G. and Brownlee, D. E. (1993). A direct measurement of the terrestrial mass accretion rate of cosmic dust. *Science*, **262**, 550–553.
- Low, F. J., Young, E., Beintema, D. A., Gautier, T. N., Beichman, C. A., Aumann, H. H., Gillett, F. C., Neugebauer, G., Boggess, N., and Emerson, J. P. (1984). Infrared cirrus - New components of the extended infrared emission. *Astrophysical Journal*, **278**, L19–L22.

- Lyons, J. R. and Young, E. D. (2005). CO self-shielding as the origin of oxygen isotope anomalies in the early solar nebula. *Nature*, **435**, 317–320.
- MacPherson, G. J., Jarosewich, E., and Lowenstein, P. (1993). Magombedze - A new H-chondrite with light-dark structure. *Meteoritics*, **28**, 138–142.
- Martin, H., Claeys, P., Gargaud, M., Pinti, D., and Selsis, F. (2006). From Suns to Life: A Chronological Approach to the History of Life on Earth 6. Environmental Context. *Earth Moon and Planets*, **98**, 205–245.
- Marty, B., Robert, P., and Zimmermann, L. (2005). Nitrogen and noble gases in micrometeorites. *Meteoritics and Planetary Science*, **40**, 881.
- Mason, B. and Nelen, J. (1968). The weatherford meteorite. *Geochimica et Cosmochimica Acta*, **32**, 661–662.
- Matrajt, G., Flynn, G. J., Bradley, J., and Maurette, M. (2001). Ftir and stxm detection of organic carbon in scoriaceous-type antarctic micrometeorites. *32th Lunar and Planetary Science Conference (abstract 1336)*.
- Matrajt, G., Taylor, S., Flynn, G., Brownlee, D., and Joswiak, D. (2003). A nuclear microprobe study of the distribution and concentration of carbon and nitrogen in murchison and tagish lake meteorites, antarctic micrometeorites, and idps: Implications for astrobiology. *Meteoritics and Planetary Science*, **38**, 1585–1600.
- Matrajt, G., Pizzarello, S., Taylor, S., and Brownlee, D. (2004). Concentration and variability of the aib amino acid in polar micrometeorites: Implications for the exogenous delivery of amino acids to the primitive earth. *Meteoritics and Planetary Science*, **39**, 1849–1858.
- Maurette, M. (2006). *Micrometeorites and the Mysteries of Our Origins*. Springer.
- Maurette, M. (2009). Six Models for the Formation of the Earth's Atmosphere. *Meteoritics and Planetary Science Supplement*, **72**, 5057.
- Maurette, M., Duprat, J. and Engrand, C., Gounelle, M., Kurat, G., Matrajt, G., and Toppani, A. (2000). Accretion of neon, organics, co<sub>2</sub>, nitrogen and water from large interplanetary dust particles on the early earth. *Planetary and Space Science*, **48**, 1117–1137.
- Maurette, M., Matrajt, G., Gounelle, M., Engrand, C., and Duprat, J. and Kurat, G. (2001). Emma and the early earth's hydrosphere. *Lunar and Planetary Institute Science Conference Abstracts*, **32**, 1586.

- May, P. W., Pineau des Forts, G., Flower, D. R., Field, D., Allan, N. L., and Purton, J. A. (2000). Sputtering of grains in c-type shocks. *Monthly Notices of the Royal Astronomical Society*, **318**, 809–816.
- McAuliffe, J. P. and Christou, A. A. (2006). Modelling meteor ablation in the venusian atmosphere. *Icarus*, **180**, 8–22.
- McCall, G. J. (1973). *Meteorites and their origins*. Wiley & Sons, NY.
- Meibom, A. and Clark, B. E. (1999). Evidence for the insignificance of ordinary chondritic material in the asteroid belt. *Meteoritics and Planetary Science*, **34**, 7–24.
- Meibom, A., Krot, A. N., Robert, F., Mostefaoui, S., Russell, S. S., Petaev, M. I., and Gounelle, M. (2007). Nitrogen and Carbon Isotopic Composition of the Sun Inferred from a High-Temperature Solar Nebular Condensate. *Astrophysical Journal Letters*, **656**, L33–L36.
- Melosh, H. J. and Goldin, T. J. (2008). Heat and drag coefficients for reentry of impact ejecta. *39th Lunar and Planetary Science Conference (abstract 2457)*.
- Migliorini, F., Manara, A., Scaltriti, F., Farinella, P., Cellino, A., and di Martino, M. (1997). Surface Properties of (6) Hebe: A Possible Parent Body of Ordinary Chondrites. *Icarus*, **128**, 104–113.
- Mittlefehldt, D. W. (1994). The genesis of diogenites and HED parent body petrogenesis. *Geochimica et Cosmochimica Acta*, **58**, 1537–1552.
- Morbidelli, A., Levison, H. F., Tsiganis, K., and Gomes, R. (2005). Chaotic capture of Jupiter’s Trojan asteroids in the early Solar System. *Nature*, **435**, 462–465.
- Moses, J. I. (1992). Meteoroid ablation in Neptune’s atmosphere. *Icarus*, **99**, 368–383.
- Nakamura-Messenger, K., Messenger, S., Keller, L. P., Clemett, S. J., and Zolensky, M. E. (2006). Organic Globules in the Tagish Lake Meteorite: Remnants of the Protosolar Disk. *Science*, **314**, 1439–1442.
- Nakashima, D., Nakamura, T., and Noguchi, T. (2003). Formation history of CI-like phyllosilicate-rich clasts in the Tsukuba meteorite inferred from mineralogy and noble gas signatures. *Earth and Planetary Science Letters*, **212**, 321–336.
- Nakles, M. R. (2004). *Experimental and modelling studies of low-energy ion sputtering for ion thrusters*. Ph.D. thesis, Virginia Polytechnic Institute and State University.

- Nazarov, M. A. and Ariskin, A. A. (1993). The erevan howardite: Petrology of glassy clasts and mineral chemistry. *24th Lunar and Planetary Science Conference (abstract 1049)*.
- Nazarov, M. A., Brändstatter, F., and Kurat, G. (1993). Carbonaceous Xenoliths from the Erevan Howardite. In *Lunar and Planetary Institute Science Conference Abstracts*, volume 24 of *Lunar and Planetary Inst. Technical Report*, page 1053.
- Nazarov, M. A., Brandstätter, F., Kurat, G., Spettel, B., and Palme, H. (1994). Chemistry of Carbonaceous Xenoliths from the Erevan Howardite. In *Lunar and Planetary Institute Science Conference Abstracts*, volume 25 of *Lunar and Planetary Inst. Technical Report*, page 981.
- Nesvorný, D. and Vokrouhlický, D. (2009). Chaotic Capture of Neptune Trojans. *Astronomical Journal*, **137**, 5003–5011.
- Nesvorný, D., Vokrouhlický, D., Bottke, W. F., and Sykes, M. (2006). Physical properties of asteroid dust bands and their sources. *Icarus*, **181**, 107–144.
- Nesvorný, D., Jenniskens, P., Levison, H. F., Bottke, W. F., and Vokrouhlický, D. (2010). Cometary Origin of the Zodiacal Cloud and Carbonaceous Micrometeorites. *The Astrophysical Journal*, **713**, 816–836.
- Nittler, L. R. (2003). Presolar stardust in meteorites: recent advances and scientific frontiers. *Earth and Planetary Science Letters*, **209**, 259–273.
- Noguchi, T., Nakamura, T., Nakashima, D., Inada, A., and Nagao, K. (2003). CI-like chondrite clasts in ordinary chondrite regolith breccias and their implication to the investigation of the surface material of asteroids. *Geochimica et Cosmochimica Acta Supplement*, **67**, 341.
- Noonan, A. F., Nelen, J., and Fredriksson, K. (1976). Mineralogy and chemistry of xenoliths in the Weston chondrite - ordinary and carbonaceous. *Meteoritics*, **11**, 344.
- O'D. Alexander, C. M., Russell, S. S., Arden, J. W., Ash, R. D., Grady, M. M., and Pillinger, C. T. (1998). The origin of chondritic macromolecular organic matter: A carbon and nitrogen isotope study. *Meteoritics and Planetary Science*, **33**, 603–622.
- Olsen, E. J., Davis, A. M., Clayton, R. N., Mayeda, T. K., and Grossman, L. (1988). Murchison xenoliths. *Geochimica et Cosmochimica Acta*, **52**, 1615–1626.
- Palme, H. and Jones, A. (2005). *Meteorites, Comets and Planets: Treatise on Geochemistry, Volume 1*, chapter Solar System Abundances of the Elements, page 41. Elsevier.

- Pearson, V. K., Sephton, M. A., Franchi, I. A., Gibson, J. M., and Gilmour, I. (2006). Carbon and nitrogen in carbonaceous chondrites: Elemental abundances and stable isotopic compositions. *Meteoritics and Planetary Science*, **41**, 1899–1918.
- Piani, L., Derenne, S., Robert, F., Thomen, A., Mostefaoui, S., Marrocchi, Y., and Meibom, A. (2009). Molecular and Isotopic Study of the Insoluble Organic Matter Isolated from a Primitive Enstatite Chondrite. *Meteoritics and Planetary Science Supplement*, **72**, 5134.
- Pizzarello, S., Cooper, G. W., and Flynn, G. J. (2006). *Meteorites and the Early Solar System II*, chapter The Nature and Distribution of the Organic Material in Carbonaceous Chondrites and Interplanetary Dust Particles, pages 625–651. University of Arizona Press.
- Popova, O. P., Strelkov, A. S., and Sidneva, S. N. (2007). Sputtering of fast meteoroid's surface. *Advances in Space Research*, **39**, 567–573.
- Quirico, E., Raynal, P. I., and Bourot-Denise, M. (2003). Metamorphic grade of organic matter in six unequilibrated ordinary chondrites. *Meteoritics and Planetary Science*, **38**, 795–811.
- Quirico, E., Borg, J., Raynal, P., Montagnac, G., and D'Hendecourt, L. (2005). A micro-Raman survey of 10 IDPs and 6 carbonaceous chondrites. *Planetary and Space Science*, **53**, 1443–1448.
- Quirico, E., Montagnac, G., Rouzaud, J., and Reynard, B. (2008a). Carbon thermometry applied to chondrites and terrestrial rocks: Effect of organic precursor. *39th Lunar and Planetary Science Conference (abstract 1261)*.
- Quirico, E., Szopa, C., Cernogora, G., Lees, V., Derenne, S., McMillan, P. F., Montagnac, G., Reynard, B., Rouzaud, J., Fray, N., Coll, P., Raulin, F., Schmitt, B., and Minard, B. (2008b). Tholins and their relevance for astrophysical issues. In S. Kwok & S. Sandford, editor, *IAU Symposium*, volume 251 of *IAU Symposium*, pages 409–416.
- Quirico, E., Montagnac, G., and Reynard, B. (2008c). UV Raman Spectroscopy as a Powerful Tool for Investigating Insoluble Organic Matter of Chondrites and Cometary Dust. *Meteoritics and Planetary Science Supplement*, **43**, 5226.
- Quirico, E., Montagnac, G., Rouzaud, J., Bonal, L., Bourot-Denise, M., Duber, S., and Reynard, B. (2009a). Precursor and metamorphic condition effects on Raman spectra of poorly ordered carbonaceous matter in chondrites and coals. *Earth and Planetary Science Letters*, **287**, 185–193.

- Quirico, E., Bourot-Denise, M., Bonal, L., Orthous-Daunay, F., Beck, P., and Montagnac, G. (2009b). Structural and Chemical Characterization of the Organic Matter in Metamorphosed CM Carbonaceous Chondrites. *Meteoritics and Planetary Science Supplement*, **72**, 5208.
- Reid, A. M., Buchanan, P., Zolensky, M. E., and Barrett, R. A. (1990). The Bholghati howardite - Petrography and mineral chemistry. *Geochimica et Cosmochimica Acta*, **54**, 2161–2166.
- Remusat, L., Derenne, S., and Robert, F. (2005). New insight on aliphatic linkages in the macromolecular organic fraction of Orgueil and Murchison meteorites through ruthenium tetroxide oxidation. *Geochimica et Cosmochimica Acta*, **69**, 4377–4386.
- Remusat, L., Palhol, F., Robert, F., Derenne, S., and France-Lanord, C. (2006). Enrichment of deuterium in insoluble organic matter from primitive meteorites: A solar system origin? *Earth and Planetary Science Letters*, **243**, 15–25.
- Ribas, I., Guinan, E. F., Güdel, M., and Audard, M. (2005). Evolution of the Solar Activity over Time and Effects on Planetary Atmospheres. I. High-Energy Irradiances (1-1700 Å). *Astrophysical Journal*, **622**, 680–694.
- Robert, F. and Derenne, S. (2006). The Molecular Structure and Isotopic Compositions of the Insoluble Organic Matter in Chondrites. *Meteoritics and Planetary Science Supplement*, **41**, 5259.
- Robert, F. and Epstein, S. (1982). The concentration and isotopic composition of hydrogen, carbon and nitrogen in carbonaceous meteorites. *Geochimica et Cosmochimica Acta*, **46**, 81–95.
- Roberts, H., Herbst, E., and Millar, T. J. (2003). Enhanced Deuterium Fractionation in Dense Interstellar Cores Resulting from Multiply Deuterated H<sub>3</sub><sup>+</sup>. *Astrophysical Journal Letters*, **591**, L41–L44.
- Rodgers, S. D. and Charnley, S. B. (2008). Nitrogen superfractionation in dense cloud cores. *Monthly Notices of the Royal Astronomical Society*, **385**, L48–L52.
- Rogers, L. A., Hill, K. A., and Hawkes, R. L. (2005). Mass loss due to sputtering and thermal processes in meteoroid ablation. *Planetary and Space Science*, **53**, 1341–1354.
- Rotundi, A., Ferrini, G., Baratta, G. A., Palumbo, M. E., Palomba, E., and Colangeli, L. (2007). Combined Micro-Infrared (IR) and Micro-Raman Measurements on Stratospheric Interplanetary Dust Particles. *Dust in Planetary Systems*, **643**, 149–153.

- Rotundi, A., Baratta, G. A., Borg, J., Brucato, J. R., Busemann, H., Colangeli, L., D'Hendecourt, L., Djouadi, Z., Ferrini, G., Franchi, I. A., Fries, M., Grossemy, F., Keller, L. P., Mennella, V., Nakamura, K., Nittler, L. R., Palumbo, M. E., Sandford, S. A., Steele, A., and Wopenka, B. (2008). Combined micro-Raman, micro-infrared, and field emission scanning electron microscope analyses of comet 81P/Wild 2 particles collected by Stardust. *Meteoritics and Planetary Science*, **43**, 367–397.
- Rubin, A. E. and Bottke, W. F. (2009). On the origin of shocked and unshocked cm clast in h-chondrite regolith breccias. *Meteoritics and Planetary Science*, **44**, 701–724.
- Rubin, A. E., Scott, E. R. D., and Keil, K. (1982). Microchondrule-bearing clast in the Piancaldoli LL3 meteorite - A new kind of type 3 chondrite and its relevance to the history of chondrules. *Geochimica et Cosmochimica Acta*, **46**, 1763–1776.
- Russel, S. S., Zolensky, M. E., Righter, K., Folco, L., Jones, R., Connolly Jr., H., Grady, M. M., and N., G. J. (2005). The meteoritical bulletin, no. 89, 2005 september. *Meteoritics and Planetary Science Supplement*, **40**, A201–A263.
- Sadezky, A., Muckenhuber, H., Grothe, H., Niessner, R., and Pschl, U. (2005). Raman microspectroscopy of soot and related carbonaceous materials: Spectral analysis and structural information. *Carbon*, **43**(8), 1731 – 1742.
- Sandford, S. A., Aléon, J., Alexander, C. M. O. D., Araki, T., Bajt, S., Baratta, G. A., Borg, J., Bradley, J. P., Brownlee, D. E., Brucato, J. R., Burchell, M. J., Busemann, H., Butterworth, A., Clemett, S. J., Cody, G., Colangeli, L., Cooper, G., D'Hendecourt, L., Djouadi, Z., Dworkin, J. P., Ferrini, G., Fleckenstein, H., Flynn, G. J., Franchi, I. A., Fries, M., Gilles, M. K., Glavin, D. P., Gounelle, M., Grossemy, F., Jacobsen, C., Keller, L. P., Kilcoyne, A. L. D., Leitner, J., Matrajt, G., Meibom, A., Mennella, V., Mostefaoui, S., Nittler, L. R., Palumbo, M. E., Papanastassiou, D. A., Robert, F., Rotundi, A., Snead, C. J., Spencer, M. K., Stadermann, F. J., Steele, A., Stephan, T., Tsou, P., Tyliczszak, T., Westphal, A. J., Wirick, S., Wopenka, B., Yabuta, H., Zare, R. N., and Zolensky, M. E. (2006). Organics Captured from Comet 81P/Wild 2 by the Stardust Spacecraft. *Science*, **314**, 1720–1724.
- Scarsi, P. (2004). Uv meteor observation from a space platform. *Il Nuovo Cimento C*, **27**, 359–381.
- Scholl, H. and Froeschle, C. (1991). The  $v(6)$  secular resonance region near 2 AU - A possible source of meteorites. *Astronomy & Astrophysics*, **245**, 316–321.

- Schrag, D. P., Berner, R. A., Hoffman, P. F., and Halverson, G. P. (2002). On the initiation of a snowball Earth. *Geochemistry, Geophysics, Geosystems*, page 1.
- Schultz, L. and Weber, H. W. (1995). Noble gases in chondrites from a proposed meteoroid stream. *26th Lunar and Planetary Science Conference (abstract 1247)*.
- Selsis, F., Despois, D., and Parisot, J.-P. (2002). Signature of life on exoplanets: Can darwin produce false positive detections? *Astronomy & Astrophysics*, **388**, 985–1003.
- Semenenko, V. P., Girich, A. L., and Nittler, L. R. (2004). An exotic kind of cosmic material: graphite-containing xenoliths from the Krymka (LL3.1) chondrite 1. *Geochimica et Cosmochimica Acta*, **68**, 455–475.
- Semenenko, V. P., Jessberger, E. K., Chaussidon, M., Weber, I., Stephan, T., and Wies, C. (2005). Carbonaceous xenoliths in the Krymka LL3.1 chondrite: Mysteries and established facts. *Geochimica et Cosmochimica Acta*, **69**, 2165–2182.
- Sigmund, P. (1981). *Sputtering by particle bombardment*, chapter Sputtering by ion bombardment: theoretical concepts, pages 9–71. Berlin: Springer-Verlag.
- Sleep, N. H. and Zahnle, K. (2001). Carbon dioxide cycling and implications for climate on ancient Earth. *Journal of Geophysical Research*, **106**, 1373–1400.
- Sorasio, G., Mendis, G. A., and Rosemberg, M. (2001). The reole of thermionic emission in meteor physics. *Planetary and Space Science*, **49**, 1257–1264.
- Stöffler, D., Keil, K., and Scott, E. R. D. (1991). Shock metamorphism of ordinary chondrites. *Geochimica et Cosmochimica Acta*, **55**, 3845–3867.
- Suzuki, A., Kebukawa, Y., Nakashima, S., Keller, L. P., Zolensky, M. E., and Nakamura, T. (2005). Infrared micro-spectroscopy of organic and hydrous components in some antarctic micrometeorites. *36th Lunar and Planetary Science Conference (abstract 1176)*.
- Taylor, S. and Lever, J. H. (2001). *Accretion of extraterrestrial matter throughout Earth's history*, chapter Seeking unbiased collections of modern and ancient micrometeorites, pages 205–240. Kluwer Academic.
- Thiemens, M. H. and Heidenreich, III, J. E. (1983). The mass-independent fractionation of oxygen - A novel isotope effect and its possible cosmochemical implications. *Science*, **219**, 1073–1075.

- Thomen, A., Robert, F., and Derenne, S. (2008). Hydrogen isotopic exchange rates between deuterium-rich sources (uv irradiated molecular hydrogen and liquid water) and an organic molecule: Implications for the conditions of formation of the insoluble organic matter in the early solar system. *39th Lunar and Planetary Science Conference (abstract 2001)*.
- Thomen, A., Robert, F., Mostefaoui, S., Piani, L., Marrocchi, Y., and Meibom, A. (2009). Spatial Relations Between D/H and N Isotopic Anomalies in Orgueil and Murchison Insoluble Organic Matter: A NanoSIMS Study. *Meteoritics and Planetary Science Supplement*, **72**, 5284.
- Tielens, A. G. G., McKee, C. F., Seab, C. G., and Hollenbach, D. J. (1994). The physics of grain-grain collisions and gas-grain sputtering in interstellar shocks. *Astrophysical Journal*, **431**, 321–340.
- Tomeoka, K. and Buseck, P. R. (1988). Matrix mineralogy of the Orgueil CI carbonaceous chondrite. *Geochimica et Cosmochimica Acta*, **52**, 1627–1640.
- Tonui, E. K., Zolensky, M. E., Hiroi, T., Wang, M., and Lipschutz, M. E. (2002). Petrographic, chemical and spectroscopic data on thermally metamorphosed carbonaceous chondrites. *33rd Lunar and Planetary Science Conference (abstract 1288)*.
- Toppani, A., Libourel, G., Engrand, C., and Maurette, M. (2001). Experimental simulation of atmospheric entry of micrometeorites. *Meteoritics and Planetary Science*, **36**, 1377–1396.
- Trieloff, M., Jessberger, E. K., Herrwerth, I., Hopp, J., Fiéni, C., Ghéllis, M., Bourot-Denise, M., and Pellas, P. (2003). Structure and thermal history of the H-chondrite parent asteroid revealed by thermochronometry. *Nature*, **422**, 502–506.
- Tsiganis, K., Gomes, R., Morbidelli, A., and Levison, H. F. (2005). Origin of the orbital architecture of the giant planets of the Solar System. *Nature*, **435**, 459–461.
- Ueno, Y., Johnson, M. S., Danielache, S. O., Eskebjerg, C., Pandey, A., and Yoshida, N. (2009). Geological sulfur isotopes indicate elevated  $\delta^{34}\text{S}$  in the Archean atmosphere, solving faint young sun paradox. *Proceedings of the National Academy of Science*, **35**, 14784–14789.
- van Schmus, W. R. (1967). Polymict structure of the Mezö-Madaras chondrite. *Geochimica et Cosmochimica Acta*, **31**, 2027–2028.
- van Schmus, W. R. and Wood, J. A. (1967). A chemical-petrologic classification for the chondritic meteorites. *Geochimica et Cosmochimica Acta*, **31**, 747–747.

- von Paris, P., Rauer, H., Lee Grenfell, J., Patzer, B., Hedelt, P., Stracke, B., Trautmann, T., and Schreier, F. (2008). Warming the early earth - CO<sub>2</sub> reconsidered. *Planetary and Space Science*, **56**, 1244–1259.
- Wahl, W. (1952). The brecciated stony meteorites and meteorites containing foreign fragments. *Geochimica et Cosmochimica Acta*, **2**, 91–117.
- Walker, J. C. G., Hays, P. B., and Kasting, J. F. (1981). A negative feedback mechanism for the long-term stabilization of Earth's surface temperature. *Journal of Geophysical Research*, **86**, 9776–9782.
- Wang, M. and Lipschutz, M. E. (1998). Thermally metamorphosed carbonaceous chondrites from data for thermally mobile trace elements. *Meteoritics and Planetary Science*, **33**, 1297–1302.
- Weisberg, M. K., Prinz, M., Clayton, R. N., and Mayeda, T. K. (1993). The CR (Renazzo-type) carbonaceous chondrite group and its implications. *Geochimica et Cosmochimica Acta*, **57**, 1567–1586.
- Weisberg, M. K., Prinz, M., Zolensky, M. E., and Ivanov, A. V. (1994). Carbonates in the Kaidun chondrite. *Meteoritics*, **29**, 549–550.
- Wetherill, G. W. (1967). Collisions in the Asteroid Belt. *Journal of Geophysical Research*, **72**, 2429–2444.
- Wilkening, L. L. (1973). Foreign inclusions in stony meteorites—I. Carbonaceous chondritic xenoliths in the Kapoeta howardite. *Geochimica et Cosmochimica Acta*, **37**, 1985–1986.
- Wilkening, L. L. (1976). Carbonaceous chondritic xenoliths and planetary-type noble gases in gas-rich meteorites. *7th Lunar and Planetary Science Conference*, pages 3549–3559.
- Wilkening, L. L. (1977a). Meteorites in meteorites - Evidence for mixing among the asteroids. In A. H. Delsemme, editor, *IAU Colloq. 39: Comets, Asteroids, Meteorites: Interrelations, Evolution and Origins*, pages 389–395.
- Wilkening, L. L. (1977b). Meteorites in meteorites - Evidence for mixing among the asteroids. In A. H. Delsemme, editor, *IAU Colloq. 39: Comets, Asteroids, Meteorites: Interrelations, Evolution and Origins*, pages 389–395.
- Wilkening, L. L. and Clayton, R. N. (1974). Foreign inclusions in stony meteorites—III. Rare gases and oxygen isotopes in a carbonaceous chondritic xenolith in the Plainview gas-rich chondrite. *Geochimica et Cosmochimica Acta*, **38**, 937–938.

- Wilson, R. C., Dobrica, E., Pearson, V. K., Turner, D. C., and Gilmour, I. (2008). Comprehensive organic analysis of antarctic micrometeorites. *39th Lunar and Planetary Science Conference (abstract 1763)*.
- Wopenka, B. (1988). Raman observations on individual interplanetary dust particles. *Earth and Planetary Science Letters*, **88**, 221–231.
- Yabuta, H., Alexander, C. M. O., Fogel, M. L., Kilcoyne, A. L. D., and Cody, G. D. (2008). The mildly-heated c2 wis 91600 evaluated through complementary analyses of the insoluble organic matter. *39th Lunar and Planetary Science Conference (abstract 2273)*.
- Yang, J. and Epstein, S. (1983). Interstellar organic matter in meteorites. *Geochimica et Cosmochimica Acta*, **47**, 2199–2216.
- Yurimoto, H. and Kuramoto, K. (2004). Molecular Cloud Origin for the Oxygen Isotope Heterogeneity in the Solar System. *Science*, **305**, 1763–1766.
- Zolensky, M., Barrett, R., and Burkett, P. J. (1993a). Chondritic Interplanetary Dust Particles: Mineral Compositions and Petrofabrics. *Meteoritics*, **28**, 469–470.
- Zolensky, M., Barrett, R., and Browning, L. (1993b). Mineralogy and composition of matrix and chondrule rims in carbonaceous chondrites. *Geochimica et Cosmochimica Acta*, **57**, 3123–3148.
- Zolensky, M., Nakamura-Messenger, K., Rietmeijer, F., Leroux, H., Mikouchi, T., Ohsumi, K., Simon, S., Grossman, L., Stephan, T., Weisberg, M., Velbel, M., Zega, T., Stroud, R., Tomeoka, K., Ohnishi, I., Tomioka, N., Nakamura, T., Matrajt, G., Joswiak, D., Brownlee, D., Langenhorst, F., Krot, A., Kearsley, A., Ishii, H., Graham, G., Dai, Z. R., Chi, M., Bradley, J., Hagiya, K., Gounelle, M., and Bridges, J. (2008). Comparing Wild 2 particles to chondrites and IDPs. *Meteoritics and Planetary Science*, **43**, 261–272.
- Zolensky, M. E., Barrett, R. A., and Gooding, J. L. (1989). C11, c12, and cm2 clasts in the bholghati howardite and the ai rais chondrite. *20th Lunar and Planetary Science Conference (abstract 1247)*.
- Zolensky, M. E., Hewins, R. H., Mittlefehldt, D. W., Lindstrom, M. M., Xiao, X., and Lipschutz, M. E. (1992). Mineralogy, petrology and geochemistry of carbonaceous chondritic clasts in the LEW 85300 polymict eucrite. *Meteoritics*, **27**, 596–604.
- Zolensky, M. E., Krot, A. N., Weisberg, M. K., Buchanan, P. C., and Prinz, M. (1996a). Fine-grained inclusions in type 3 ordinary and carbonaceous chondrites. *27th Lunar and Planetary Science Conference (abstract 1507)*.

- Zolensky, M. E., Weisberg, M. K., Buchanen, P. C., and Mittlefehldt, D. W. (1996b). Mineralogy of carbonaceous chondrite clasts in HED achondrites and the Moon. *Meteoritics and Planetary Science*, **31**, 518–537.
- Zolensky, M. E., Nakamura, K., Gounelle, M., Mikouchi, T., Kasama, T., Tachikawa, O., and Tonui, E. (2002). Mineralogy of Tagish Lake: An ungrouped type 2 carbonaceous chondrite. *Meteoritics and Planetary Science*, **37**, 737–761.
- Zolensky, M. E., Clayton, R. N., Mayeda, T., Chokai, J., and Norton, O. R. (2003). Carbonaceous Chondrite Clasts in the Halite-bearing H5 Chondrite Zag. *Meteoritics and Planetary Science Supplement*, **38**, 5216.
- Zolensky, M. E., Zega, T. J., Yano, H., Wirick, S., Westphal, A. J., Weisberg, M. K., Weber, I., Warren, J. L., Velbel, M. A., Tsuchiyama, A., Tsou, P., Toppani, A., Tomioka, N., Tomeoka, K., Teslich, N., Taheri, M., Susini, J., Stroud, R., Stephan, T., Stadermann, F. J., Snead, C. J., Simon, S. B., Simionovici, A., See, T. H., Robert, F., Rietmeijer, F. J. M., Rao, W., Peronnet, M. C., Papanastassiou, D. A., Okudaira, K., Ohsumi, K., Ohnishi, I., Nakamura-Messenger, K., Nakamura, T., Mostefaoui, S., Mikouchi, T., Meibom, A., Matrajt, G., Marcus, M. A., Leroux, H., Lemelle, L., Le, L., Lanzirrotti, A., Langenhorst, F., Krot, A. N., Keller, L. P., Kearsley, A. T., Joswiak, D., Jacob, D., Ishii, H., Harvey, R., Hagiya, K., Grossman, L., Grossman, J. N., Graham, G. A., Gounelle, M., Gillet, P., Genge, M. J., Flynn, G., Ferroir, T., Fallon, S., Ebel, D. S., Dai, Z. R., Cordier, P., Clark, B., Chi, M., Butterworth, A. L., Brownlee, D. E., Bridges, J. C., Brennan, S., Brearley, A., Bradley, J. P., Bleuet, P., Bland, P. A., and Bastien, R. (2006). Mineralogy and Petrology of Comet 81P/Wild 2 Nucleus Samples. *Science*, **314**, 1735–1739.
- Zolensky, M. E., Briani, G., Gounelle, M., Mikouchi, T., Ohsumi, K., Weisberg, M. K., Le, L., Satake, W., and Kurihara, T. (2009). Searching for chips of kuiper belt objects in meteorites. *40th Lunar and Planetary Science Conference (abstract 2162)*.



## RÉSUMÉ

Les micrométéorites, échantillons extraterrestres de taille submillimétrique, dominent le flux de matière extraterrestre qui entre dans l'atmosphère terrestre. Toute micrométéorite est inévitablement altérée par son passage atmosphérique. Mais elles peuvent être trouvées enchâssées dans des météorites plus grandes, sous forme de microxénolithes. Les microxénolithes sont des micrométéorites anciennes, ils permettent d'étudier des époques passées de l'histoire du Système Solaire, pas accessibles par les micrométéorites. Des nouveaux microxénolithes ont été découverts et étudiés dans les chondrites H et dans la chondrite carbonée Isheyev. Plusieurs techniques expérimentales (microscopie électronique à balayage et à transmission, spectroscopie Raman, spectrométrie de masse) ont été utilisées pour les caractériser, et des simulations numériques ont été réalisées pour étudier leur origine et les effets qu'ils subissent lors de leur passage dans l'atmosphère de la Terre.

**Mots clés :** micrométéorites ; xénolithes ; astéroïdes ; comètes ; dynamique des poussières ; entrée atmosphérique.

## SUMMARY

Micrometeorites are sub-millimetric extraterrestrial samples, which dominate the flux of extraterrestrial matter entering the Earth atmosphere. Every micrometeorite is altered by the interaction with the atmosphere. However, they can be found embedded in larger meteorites, in which case they are called microxenoliths. Microxenoliths are ancient micrometeorites, and they allow the study of past epochs of the Solar System, not accessible by studying micrometeorites. New microxenoliths have been discovered and studied in H chondrites and in the carbonaceous chondrite Isheyev. Many different techniques (scanning and transmission electron microscopy, Raman spectroscopy, mass spectrometry) have been applied to characterize them. Also, numerical simulations have been performed to investigate their origin and the effects they suffer during the passage through the Earth atmosphere.

**Keywords:** micrometeorites; xenoliths; asteroids; comets; dust dynamics; atmospheric entry.